

Plasmonic metal nanoparticle films for solar cells with ultra-thin absorber layers- low temperature synthesis and application

Inaugural Dissertation
to obtain the academic degree
Doctor rerum naturalium (Dr. rer. nat.)

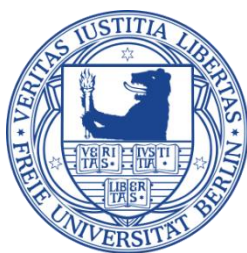
Submitted to the Department of
Biology, Chemistry and Pharmacy
of Freie Universität Berlin

by

Yang Liu

from Shandong, China

December, 2016



HZB Helmholtz
Zentrum Berlin

This work has been carried out at Helmholtz-Zentrum Berlin für Materialien und Energie during the period from September 2013 to December 2016.

1st Reviewer: Prof. Dr. Christian-Herbert Fischer

2nd Reviewer: Prof. Dr. Ulrich Abram

Date of Defense: February 2nd, 2017

Acknowledgement

During the journey of finishing my Ph.D. work and realizing this thesis, many challenges existed. My supervisors, colleagues, friends and family always supported me to overcome all of them. Here I would like to express my acknowledgement to them:

First and foremost, I would like to thank my supervisor Prof. Dr. Christian-Herbert Fischer. He is very wise, responsible and patient on supervising my work and reading all of my writings during this period. Without his supervision I cannot finish this thesis. We had many nice discussions which solved my problems not only on research but also in life. I also learned much from him. I deeply appreciate him for all the work, help and support.

I am very grateful to my 2nd supervisor of this thesis Prof. Dr. Ulrich Abram, who gave me not only very helpful advises but also constant support. I would also like to thank him for fruitful discussions and help in this work.

I would also like to thank Prof. Dr. Martha Ch. Lux-Steiner for giving me the opportunity to work in her department in Helmholtz-Zentrum Berlin. I appreciate her for the nice discussions and encouragements during the Montalks. Thanks a lot to her also for the supports she provided.

Many thanks to Prof. Dr. Martina Schmid for being my supervisor on this work and for accepting me to finish this thesis in her group. I appreciate it that she led me to the fascinating field of plasmonic and supervised me on the related part of this work. I want to thank her also for the responsible discussions and strong support to help me improve this work.

Special thanks to Dr. Thomas Dittrich for being my supervisor on this work and introducing me to SPV measurements. I would like to thank him for the fruitful discussions and interpretation of SPV measurement results. Thanks also for his reading of my writing and his responsibility, I learned a lot from him.

Special thanks also to Dr. Yanpeng Fu for introducing me to the ILGAR group and for very useful assistance especially at the beginning of my work.

Many thanks to Paul Plate for the cooperation in silver nanoparticle preparation, to Felix Lang for the cooperation on perovskite solar cells and many useful discussions, to Dr. Andreas Ott for the preparation of gold nanorods.

I'm grateful to Dr. Phillip Manley for his support of the optical simulation program and many discussions, as well as his help. The simulation results were obtained at the Berlin Joint Lab for Optical Simulations for Energy Research (BerOSE) of Helmholtz-Zentrum Berlin für Materialien und Energie, Zuse Institute Berlin, and Freie Universität Berlin.

Special thanks go to the former ILGAR-group members for very helpful discussions, lots of help in many aspects and very nice work environment, particularly: Tristan Köhler, Dr. Rodrigo S áez Araoz, Martin Krüger and Johanna Krammer.

I am thankful to Dr. Iver Lauermann and Dr. Alexander Steigert for helping me with the XPS measurement and the related discussions. I would also like to thank Dr. Volker Hinrichs for his great help on LA-ICP-MS. Many thanks to Prof. Dr. Sebastian Fiechter for measurements and helpful discussions. Thanks to Dr. Daniel Abou-Ras for the SEM measurements. Thanks to Dr. Jaison Kavalakkatt and Dr. Xianzhong Lin for XRD measurements and their help in many aspects.

I would like to thank Dr. Jörg Rappich, Dr. Marin Rusu, Dr. Konstantinos Fostiropoulos and Dr. Reiner Klenk for letting me work in their labs and supports they provided.

I would like to thank Dr. Guanchao Yin and Min Song for helping me and for discussions on optical stimulations.

Many thanks go to all of my colleagues in Institute for Heterogeneous Material Systems and Nanooptical concepts for PV as well as the rest of HZB who helped me to finish this thesis and to enjoy the stay in HZB.

I am very grateful to China Scholarship Council for sponsoring me to study in Helmholtz-Zentrum Berlin. I would also like to thank Helmholtz-Zentrum Berlin for its support.

Finally, I want to express my deep gratitude to my family who always support my life. Very, very special thanks to my wife, Fangfang Chu, without her love, support and encouragement I cannot come to this point.

Content

Chapter 1 Introduction	1
Chapter 2 Fundamentals and theory	5
2.1 Solar cells with ultra-thin absorber layers	5
2.1.1 <i>J-V</i> characteristics of solar cells	5
2.1.2 Extremely thin absorber solar cells.....	7
2.1.3 Ultra-thin perovskite solar cells.....	8
2.2 Plasmonic silver and gold nanoparticles	10
2.2.1 Localized surface plasmon resonances	10
2.2.2 Synthesis of silver and gold nanoparticles.....	11
2.2.3 Application for light trapping of solar cells.....	12
2.2.4 Optical simulations for plasmonic solar cells	14
2.3 Background of this Thesis	15
Chapter 3 Deposition of Ag NPs by spray-CVD method	17
3.1 Chemical vapor deposition	17
3.2 Deposition of Ag nanoparticles by spray-CVD.....	21
3.2.1 Fundamentals of spray-CVD for Ag nanoparticle deposition	21
3.2.2 Influence of the deposition parameters	24
3.2.2.1 Influence of N ₂ flow rate	24
3.2.2.2 Influence of concentration of precursor solution.....	25
3.2.2.3 Influence of deposition time	27
3.2.2.4 Influence of substrate temperature	30
3.2.3 Size and density controlled Ag nanoparticles.....	31
3.2.4 Mechanism of the deposition of Ag NPs	34
3.2.4.1 Deposition mechanism	35
3.2.4.2 Growth mechanism of Ag NPs	38

3.3 Summary	41
Chapter 4 Deposition of plasmonic silver nanoparticles on top of extremely-thin In₂S₃ layer	45
4.1 Preparation of extremely-thin In ₂ S ₃ layer by spray-ILGAR	45
4.2 Deposition of Ag NPs on top of extremely-thin In ₂ S ₃ layers by spray-CVD	48
4.3 Influence of the process parameter on the deposition of Ag NPs on top of In ₂ S ₃ layers	49
4.3.1 Concentration of precursor solution	50
4.3.2 Deposition time	54
4.4 Mechanism of the deposition process	61
4.5 Application in extremely-thin absorber solar cells	63
4.6 Summary	65
Chapter 5 Application of Ag nanoparticles in ultra-thin perovskite solar cells	67
5.1 Fabrication of ultra-thin perovskite solar cells.....	67
5.2 Simulated incorporation of Ag NPs in ultra-thin perovskite solar cells.....	72
5.2.1 Incorporation of Ag NPs between perovskite layer and spiro-OMeTAD layer .	73
5.2.2 Incorporation of Ag NPs between TiO ₂ layer and perovskite layer	77
5.2.3 Incorporation of Ag NPs between FTO and TiO ₂ layer	78
5.3 Experimental incorporation of Ag NPs in ultra-thin perovskite solar cells	78
5.3.1 Deposition of Ag NPs on top of ultra-thin perovskite layer.....	79
5.3.2 Deposition of Ag NPs on top of the TiO ₂ layer.....	81
5.3.3 Deposition of Ag NPs on top of the FTO layer	84
5.4 Summary	93
Chapter 6 Application of Au@SiO₂ core-shell nanorods in perovskite solar cells	95
6.1 Simulated incorporation of Au@SiO ₂ core-shell nanorods in perovskite solar cells	95
6.2 Experimental incorporation of Au@SiO ₂ core-shell nanorods into perovskite solar cells.....	98
6.3 Summary	103
Chapter 7 Summary.....	105
Appendix A	109
Appendix B.....	113
References	119

Contents

List of publications	129
Curriculum Vitae.....	131
Statement	133

Contents

Kurzreferat

Plasmonische Silber- und Gold-Nanopartikel sind von besonderem, aktuellem Interesse, da sie zur Absorptions- und Leistungssteigerung von Solarzellen verwendet werden können, ohne die Dicke der Absorberschichten zu erhöhen. Es ist vielversprechend, solche Nanopartikel in Solarzellen mit extrem dünnem Absorber (ETA SCs) und ultradünnen Perovskit-Solarzellen (UTPSCs) einzubauen. Beide Typen leiden unter geringer Leistungsfähigkeit hervorgerufen durch ineffiziente Lichtabsorption. Besondere Herausforderungen bestehen beim Einbau der Nanopartikel, weil zum einen die Abscheideverfahren von plasmonischen Nanopartikeln entweder zu komplex sind oder zum anderen unter anormalen Bedingungen durchgeführt werden müssen. Z.B. sind für die Synthese und den Einbau von kolloidalen Silbernanopartikeln mehrstufige Prozessschritte erforderlich und deren Fixierung sowie die Entfernung der Stabilisatoren sind kritisch. Probleme bereiten die Auflösung von Silber in Sulfid Absorbern, die thermische Instabilität der Perovskitschicht usw. Schwierig gestaltet sich außerdem die Herstellung von homogenen Nanopartikelschichten mit enger Größenverteilung. Daher konzentriert sich diese Arbeit auf die Entwicklung eines einfachen Verfahrens zur Abscheidung von Silbernanopartikeln (Ag NPs) und untersucht den Einbau von plasmonischen Nanopartikeln in ETA SCs und UTPSCs zur plasmonischen Absorptionsverstärkung.

Ein neues Sprüh-Verfahren (Spray-CVD) wurde entwickelt, um Ag-NPs bei Substrattemperaturen sogar unterhalb von 100 °C herzustellen, was wesentlich niedriger als bei den meisten anderen Abscheidemethoden ist. Es ist auch ein sehr reproduzierbares, sehr einfaches und kostengünstiges Verfahren, das Trimethylphosphin (Hexafluoracetylacetonato) Silber als Ausgangsstoff in alkoholischer Lösung verwendet. Durch die Kontrolle der Prozessparameter wie Temperatur, Konzentration der Ausgangslösung und Abscheidezeit, können unabhängig voneinander Größe und Dichte der Ag-NPs auf verschiedenen Substraten gesteuert werden. Die Ag-NPs sind in ihrer Größe, Form und Verteilung sehr homogen. Durch systematische Variation der Depositionsparameter und klassische chemische Experimente konnten die Mechanismen des Teilchenwachstums und der Abscheideprozesse bei unterschiedlichen Temperaturen sowie die außerordentlich niedrige Zersetzungstemperatur des Precursors sogar unterhalb seines Schmelzpunktes erklärt werden.

Dieses neue Spray-CVD Verfahren wurde zum Abscheiden von plasmonischen Ag-NPs auf extrem dünnen halbleitenden Schichten verwendet. Während der Abscheidung von Ag-NPs auf In_2S_3 -Vorläuferschichten konnte eine Reihe von Phasenübergängen zu ternären AgIn_xS_y Verbindungen vor der Bildung von Ag-NPs auf der Oberfläche beobachtet werden. Gleichzeitig mit den Ag-NPs werden AgIn_5S_8 und orthorhombisches AgInS_2 in der Ausgangsschicht gebildet. Die Bildung von Ag_2S an der Grenzfläche zwischen Ag-NPs und der Halbleiterschicht konnte ebenfalls beobachtet werden. Die

Oberflächenphotospannungsspektroskopie zeigt die Ladungstrennung und die elektronischen Übergänge in den Bandlückenbereichen der entsprechenden Verbindungen an. Die gebildeten extrem dünnen Halbleiterschichten mit Ag-NPs wurden in ETA-SCs angewendet.

In UTPSCs wurden sowohl Ag NPs als auch Au@SiO₂ –Kern-Schale-Nanostäbe (Au NRs) eingebaut, um die Lichtabsorption und -leistung zu verbessern. Vor der experimentellen Einbettung wurden in beiden Fällen optische Simulationen mit der Finite-Element-Methode durchgeführt und zur Vorhersage und zum Verständnis des Einflusses von Ag-NPs und Au-NRs auf die Lichtabsorption von Perovskit-Absorberschichten verwendet. Es zeigte sich, dass Absorptionsverbesserungen für den Einbau von Ag-NPs an den Grenzflächen zwischen der Perovskit und der spiro-OMeTAD-Schicht sowie zwischen der TiO₂- und der Perovskitschicht auftreten. Dies ist auf die Kopplung sowohl des Streueffekts als auch der Nahfeldverstärkung von Ag-NPs in den Perovskitschichten zurückzuführen. Durch den Einbau von Au-NRs zwischen TiO₂ und der Perovskit-Schicht wird die Absorption der Perovskit-Schicht bei Wellenlängen zwischen 580 nm und 760 nm verstärkt. Bei Wellenlängen kürzer als 580 nm wird in Perovskitschichten aufgrund der Bandübergänge im Au die Absorption nicht verbessert.

Experimentell wurden plasmonische Ag-NPs erfolgreich an der Grenzfläche zwischen FTO-Substrat und TiO₂-Schicht in ultradünnen Perovskit-Solarzellen eingebaut. Dies führt zu einer signifikanten Verbesserung von 22,2% für die durchschnittliche Kurzschlussstromdichte (J_{sc}) und zu einer relativen Verbesserung von 22,5% für den durchschnittlichen Leistungswandlungswirkungsgrad. Bei der Charakterisierung durch Oberflächen-Photospannung und Photolumineszenz zeigte sich, dass die implementierten Silber-Nanopartikel die Ladungstrennung und das Einfangen von Elektronen in die TiO₂-Schicht an der CH₃NH₃PbI₃ / TiO₂-Grenzfläche verbessern können. Die Anwendung dieser Silber-Nanopartikel ist daher sehr vielversprechend, um die ultradünnen Perovskit-Solarzellen zu deutlich verbessern. Beim Einbau von Au-NRs in Perovskit-Solarzellen lässt sich mit zunehmender Dichte der Au NRs von 3% auf 11,8% ebenfalls ein klarer Anstieg der J_{sc} erkennen.

Abstract

Plasmonic silver and gold nanoparticles have attracted tremendous interests because they can be used for absorption and performance enhancement of solar cells without increasing the thickness of absorber layers. It is promising to incorporate such nanoparticles into extremely thin absorber solar cells (ETA SCs) and ultra-thin perovskite solar cells (UTPSCs) since both of them suffer from the low performance caused by inefficient light absorption. Several challenges exist during the incorporation of nanoparticles, like the deposition methods of plasmonic nanoparticles are either too complex or must be operated under abnormal conditions, e.g., multi steps are required for the synthesis and incorporation of colloidal silver nanoparticles, dissolving of silver in sulfide absorbers, thermal instability of perovskite layer etc. Moreover, the preparation of homogenous nanoparticle films with narrow size distribution is still a difficult task. Therefore, this thesis concentrates on the development of a simple method for depositing silver nanoparticles (Ag NPs) and the studies on the incorporation of plasmonic nanoparticles in ETA SCs and UTPSCs for plasmonic enhancement.

A novel spray chemical vapor deposition method (spray-CVD) has been developed for producing Ag NPs at substrate temperatures even below 100 °C which is much lower than many other techniques. It is a highly reproducible, very simple and low-cost process which uses Trimethylphosphine (hexafluoroacetylacetonato) silver as precursor in alcoholic solution. By controlling the process parameters, such as temperature, concentration of precursor solution and deposition time, independently size and density controlled Ag NPs can be obtained on different substrates. The Ag NPs are highly homogenous in size and shape. By systematic variation of deposition parameters and classic chemical experiments, the mechanisms of particle growth and of deposition processes at different temperatures as well as the extraordinarily low decomposition temperature of the precursor even below its melting point could be explained.

This novel spray-CVD can be used for depositing plasmonic Ag NPs on top of extremely thin semiconducting layers. However, during the deposition of Ag NPs on In_2S_3 precursor layers a sequence of phase transitions are observed due to the generation of AgIn_xS_y ternary compounds before the formation of Ag NPs on the surface. The formation of Ag NPs set on concomitant with the formation of AgIn_5S_8 in the bulk layer. The growth of Ag NPs is accompanied by the evolution of orthorhombic AgInS_2 . The formation of Ag_2S at the interface between Ag NPs and the semiconductor layer is observed. Surface photovoltage spectroscopy indicates charge separation and electronic transitions in the band gap ranges of corresponding compounds. The formed extremely thin semiconducting layers with Ag NPs on top were applied in ETA SCs.

For UTPSCs, both Ag NPs and Au@SiO_2 core shell nanorods (Au NRs) are

incorporated to enhance the light absorption and performance. In both cases, optical simulations (performed by finite element method) are employed prior to the experimental embedding for predicting and understanding the influence of Ag NPs and Au NRs on the light absorption of perovskite absorber layers. It revealed that absorption enhancements are observed for incorporation of Ag NPs at the interfaces between the perovskite and the spiro-OMeTAD layer as well as between the TiO_2 and the perovskite layer. This is due to the coupling of both scattering effect and near-field enhancement of Ag NPs in the perovskite layers. By incorporating Au NRs between the TiO_2 and the perovskite layer the absorption of the perovskite layer is enhanced at wavelengths between 580 nm and 760 nm. Due to the interband transitions of Au, the absorption in the perovskite layer at wavelengths shorter than 580 nm is not improved.

In experiment, plasmonic Ag NPs are successfully incorporated at the interface between FTO substrate and TiO_2 layer in the ultra-thin perovskite solar cells. This leads to a significant enhancement of 22.2% for the average short-circuit current density (J_{sc}) and resulted in a relative improvement of 22.5% for the average power conversion efficiency. Characterization by surface photovoltage and photoluminescence give the evidence that the implemented silver nanoparticles can enhance the charge separation and the trapping of electrons into the TiO_2 layer at the $\text{CH}_3\text{NH}_3\text{PbI}_3/\text{TiO}_2$ interface. The application of these silver nanoparticles is therefore very promising to improve the ultra-thin perovskite solar cells. Incorporation of Au NRs also leads to an obvious rise of J_{sc} of perovskite solar cells. A clear increase trend of J_{sc} is obtained with increasing density of Au NRs from 3% to 11.8% which gives strong evidence for the influence of Au NRs.

Chapter 1

Introduction

At the end of 2015, worldwide installed photovoltaic (PV) capacity increased to 228 gigawatts (GW) and the total power output from PV meets 1.2% of worldwide electricity demand [1]. By 2050, 16% of the world electricity demand is expected to come from PV [2]. Till now, most of the established PV technologies are based on crystalline silicon and around 10% of the productions rely on thin-film technologies [3]. For both cases, price of the electricity from PV is still not competitive compared to that from traditional energy due to the high production cost. Since the absorber layer accounts for a large part of the cost, reducing the thickness and therefore the material amount of the absorber layer or using low cost deposition methods can be very useful for decreasing the high production cost [4].

Extremely thin absorber solar cells (ETA SCs) use inorganic absorbers with a thickness of less than 100 nm which reduces significantly the thickness of absorber layers [5, 6]. By using such extremely thin absorbers, ETA SCs can reduce also the recombination loss and thus enhance the collection of charge carriers at interfaces [7]. Therefore, even materials with higher defect states than normal can be used for absorbers and such absorbers can be deposited by low cost processes [8]. Hence, ETA SC is a choice for decreasing the high production cost of solar cells. Perovskite solar cells (PSCs) could be another promising candidate for solving the cost problem, since they can be processed by very simple, low cost methods and in parallel they have excellent electrical and optical properties [9, 10]. Power conversion efficiency (PCE) of the PSCs has sharply improved from 3.81% first reported in 2009 to 22.1% in 2016 [11, 12]. Among the PSCs, ultra-thin perovskite solar cells (UTPSCs) which have much thinner absorber layers than that in normal PSCs attract a lot of interest because they can be used in tandem solar cells and building-integrated photovoltaics [13-16]. However, ETA SCs and UTPSCs suffer from the same problem, i.e., the incomplete absorption of incident light due to the ultra-thin absorber thickness [13, 17]. Therefore, it will be very promising to enhance the light absorption without thickness increase of absorber layers.

Research on plasmonic enhancement of solar cells has attracted high interest in recent years. The implementation of plasmonic nanostructures can cause absorption enhancement of different kinds of solar cell absorbers which allows either decreasing the physical thickness of an absorber layer while keeping the optical thickness constant, e.g., for Cu(In,Ga)Se_2 , CdTe, or improving absorption in poorly absorbing materials like Si [4]. Optical simulation can help understanding the mechanism of plasmonic enhancement and predicting the optimum design [18, 19]. Among the well-studied plasmonic nanostructures,

silver nanoparticles (Ag NPs) have been widely used in several types of solar cells, e.g., thin film silicon solar cells [20, 21], thin film Cu(In,Ga)Se₂ solar cells [22, 23], organic solar cells [24, 25] and perovskite solar cells [26, 27]. By tuning the Ag NPs' size, geometry, density and surrounding medium, the resonance peaks can be controlled [28, 29]. Therefore, it is promising to incorporate designed Ag NPs with proper size and shape into ETA SCs and UTPSCs for absorption enhancement of light without thickness increase of absorber layers. However, the integration of Ag NPs especially into solar cells with chalcopyrite or sulfide absorbers (in ETA SCs) remains challenging, for example, due to dissolving of silver in the matrix [22], and perovskite layers are not stable under high temperatures [30]. In addition, controlled particle sizes and a good homogeneity of the particle films are crucial for application in ETA SCs and UTPSCs [17, 31]. Therefore, to elaborate the deposition method for Ag NPs with size and density control at low temperature, including understanding the mechanisms of Ag NPs' deposition and growth. After the study of deposition of Ag NPs, their application in ETA SCs and UTPSCs is not trivial. Method development of tailored Ag NPs, optical modeling, stable incorporation of Ag NPs in ETA SCs and UTPSCs as well as the characterization of the structure and devices are the main topics of this interdisciplinary work. It is also reported that direct contact between metal nanoparticles and perovskite layers may cause the formation of recombination centers [32]. Gold nanoparticles (Au NPs) can also be used for plasmonic enhancement due to their outstanding optical properties and good stability [32-34]. Thus, to find more possibilities for performance improvement of UTPSCs, the incorporation of Au NPs with dielectric shells in UTPSCs was also investigated.

The structure of this thesis and the contents of each chapter are given below.

Chapter 2 starts with a brief introduction of the most important characterization method for a solar cell (current-voltage characteristics) and then introduces fundamentals of ETA SCs and UTPSCs. It is followed by the basics of plasmonic Ag NPs and Au NPs, including basics of localized surface plasmon resonance, brief overview on the reported preparation methods of Ag NPs and Au NPs, application of both nanoparticles in plasmonic solar cells and optical simulation method for the application. At last, the background of this thesis is presented.

Chapter 3 describes the development of spray chemical vapor deposition method (spray-CVD) for depositing Ag NPs. A brief overview of chemical vapor deposition is introduced first. Secondly, influence of different parameters on the deposition process is studied in detail. The parameters include flow rate of carrier gas, volume and concentration of precursor solution, deposition time and substrate temperature. This broad study is the base for the application of tailored Ag NPs in solar cells. Thereafter, deposition mechanism of the process and growth mechanism of Ag NPs are investigated.

In chapter 4, deposition of Ag NPs on top of an In₂S₃ layer is investigated which is the first step of incorporation of plasmonic Ag NPs in ETA SCs. Studies of the change of morphology and coverage of Ag NPs as well as phase transitions during the deposition process are presented. Mechanisms behind the changes are also studied.

Chapter 5 presents the application of plasmonic Ag NPs produced by spray-CVD in UTPSCs. To start with, the fabrication and characterization of UTPSCs is introduced. Afterwards, optical simulations of the incorporation of Ag NPs at different positions of UTPSCs are reported. Then, Ag NPs are incorporated into UTPSCs experimentally to study the effects on absorption and performance of UTPSCs.

Chapter 6 reports the studies on the implementation of Au@SiO₂ core-shell nanorods into PSCs for enhancement of photocurrent and power conversion efficiency. Both optical simulation and experimental results are shown.

A summary of the results presented in this thesis is given in chapter 7.

A short description of the main characterization methods used in this thesis is presented in Appendix A.

Chapter 2

Fundamentals and theory

This chapter begins with a brief overview on solar cells with ultra-thin absorber layers, such as extremely thin absorber solar cells (ETA SCs) and ultra-thin perovskite solar cells (UTPSCs), also including fundamentals of the current density-voltage (J - V) characteristics of solar cells. Afterwards, basics of plasmonic metal nanoparticles, e.g., theory of plasmonic extinction of metal nanoparticles, fabrication of silver (Ag) and gold (Au) nanoparticles (NPs), experimental and simulated application of Ag NPs and Au NPs are introduced. The background of this thesis is depicted at the end of this chapter.

2.1 Solar cells with ultra-thin absorber layers

A solar cell is an electrical device which can convert the energy of sunlight to electricity directly by photovoltaic effect. To achieve these photovoltaic effects, the first requirement is the absorption of optical photons which happens in the absorber layer of a solar cell [35]. Currently, most of the commercial solar cells are using absorbers based on crystalline silicon wafers with thicknesses in the range of 180 μm and 300 μm which spend most of the cost in silicon material and processing. To reduce the high cost, solar cells with absorber thicknesses between hundreds of nanometer and 2 μm are of great interest. Semiconductors used for the absorber layers in these kinds of solar cells can be amorphous and polycrystalline Si, GaAs, CdTe, CuInSe₂ and organic semiconductors, as well as organic-inorganic tri-halide perovskite. [10, 36, 37] Due to the usage of many scarce materials in these absorber layers, costs of such solar cells are still high. [38, 39] Thus, research on solar cells with ultra-thin absorber layers, thicknesses of which are around 100 nm or less, raises more interest [16, 40, 41]. Advantages of solar cells with ultra thin absorber layers are [7, 16]: (1) reduction of material volume used for production of absorber layers; (2) capable usage of materials with lower purity and higher defect densities which can be produced by inexpensive solution based processes because of the reduction of bulk recombination and enhancement of charge separation at interface; (3) capable application in building-integrated photovoltaics. Solar cells with extremely thin absorbers (ETA SCs) and ultra-thin perovskite solar cells (UTPSCs) belong to such kind of solar cells and will be introduced in detail.

2.1.1 J - V characteristics of solar cells

To understand the ETA SCs and UTPSCs better, J - V characteristic which is the most important characterization method for solar cells will be introduced first [42]. More details

can be found in textbooks. [43, 44] A p-n junction, which is formed by joining p-type and n-type semiconductors, is the core part of a solar cell. In a p-n junction, an internal electric field can be formed without an external applied voltage. Under illumination of light, absorption of optical photons and charge separation will happen. Charge separation is driven by the internal electric field so that the electron is pushed toward the n side and the hole is pushed toward the p side. When an external load is connected to a p-n junction, the separated charge carriers can be collected and electricity can be generated. Under this condition, the current density flowing through the p-n junction can be written as:

$$J(v) = J_0 \left[\exp \left(\frac{qv}{AkT} \right) - 1 \right] - J_{ph} \quad \text{Eq.2.1}$$

In the equation, J_0 is the saturation current density, q is the elementary charge, v is the applied voltage across the p-n junction, A is the diode ideality factor of the p-n junction, k is the Boltzmann's constant, T is the absolute temperature and J_{ph} is the photo-generated current density.

The most important parameters for the property of a solar cell are power conversion efficiency (η), short-circuit current density (J_{sc}), open-circuit voltage (V_{oc}) and fill factor (FF). Among these four parameters, J_{sc} , V_{oc} and FF can be obtained from the J - V characteristics and η is derived from the other three parameters.

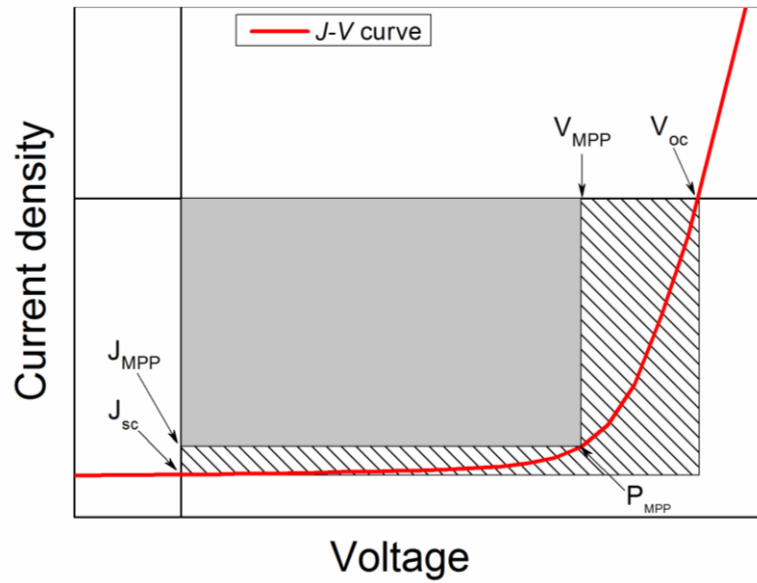


Figure 2.1: Current density voltage characteristics of a solar cell under AM 1.5 illumination. The parameters indicated in this figure are short current density (J_{sc}), open circuit voltage (V_{oc}), maximum power point (P_{MPP}), the current density and voltage at the maximum power point (J_{MPP} and V_{MPP}).

Figure 2.1 shows the J - V curve under illumination obtained from J - V characteristics. The short-circuit current density, J_{sc} , and open-circuit voltage, V_{oc} , are shown on the J - V curve. The J_{sc} is the maximum current density from a solar cell and happens only at the condition that the voltage across the solar cell is zero. J_{sc} is originated in the generation and collection of photo-generated charge carriers in a solar cell. It depends on different factors, like (1) the number of photons, (2) the spectrum of the incident light, (3) the optical properties of a solar cell and (4) the collection probability of the charge carriers. Since J_{sc} is

the largest current density which can be obtained from a solar cell, it is a significant important parameter for the performance of a solar cell.

The open-circuit voltage, V_{oc} , is the maximum voltage from a solar cell which happens when the net current density $J_{(v)}$ flowing through the solar cell is zero. An equation of V_{oc} can be given by applying the condition to Eq.2.1:

$$V_{oc} = \frac{AkT}{q} \ln \left(\frac{J_{ph}}{J_0} + 1 \right) \quad \text{Eq.2.2}$$

From the equation, V_{oc} is mainly influenced by the saturation current density, J_0 which depends on recombination of charge carriers in a solar cell. Therefore, V_{oc} is a measure of recombination in the solar cell.

The fill factor, FF, in conjunction with J_{sc} and V_{oc} , determines the maximum power from a solar cell. Thus, FF is defined as:

$$FF = \frac{P_{MPP}}{V_{oc} * J_{sc}} = \frac{V_{MPP} * J_{MPP}}{V_{oc} * J_{sc}} \quad \text{Eq.2.3}$$

In the equation, P_{MPP} is the maximum power point of the solar cell, V_{MPP} and J_{MPP} are the voltage and current density at the maximum power point, respectively.

The power conversion efficiency of a solar cell is defined as the ratio of energy of output from the solar cell to input energy from the sunlight. It is the most common used parameter for the comparison between different solar cells. It can be described by Eq.2.4.

$$\eta = \frac{P_{MPP}}{P_{in}} = \frac{V_{oc} * J_{sc} * FF}{P_{in}} \quad \text{Eq.2.4}$$

Here, P_{in} is the input energy from the sunlight. In general, the solar cells are measured under AM1.5 conditions (Air Mass 1.5: standard test conditions for testing solar cells or modules) and at a temperature of 25 °C.

2.1.2 Extremely thin absorber solar cells

The extremely thin absorber solar cells, ETA SCs, are a kind of solar cell using a nanostructured substrate coated with a very thin inorganic absorber and completed with a solid state hole collector. ETA SCs have very good stability at high temperature because of the application of inorganic absorbers and other solid state components. Due to the extremely thin absorber layer, diffusion length of the charge carriers is smaller than the local thickness of absorber layer which leads to the easy reduction of recombination losses and enhancement of the collection of charge carriers at interfaces [41]. Therefore, even materials with lower defect states can be used for absorbers which can significantly lower the processing cost for absorber layers. [7, 8] The structure of ETA SCs is based on the extremely thin absorber layer (thickness less than 100 nm) sandwiched between transparent electron and hole transport layers. A schematic structure of the cross section of an ETA SC is shown in Figure 2.2. Details of the information of each layer are listed following [5, 6, 41, 45, 46]:

TCO/glass substrate

In ETA SCs, a transparent conductive oxide (TCO) coated glass is used as substrate. The most common applied TCOs are indium tin oxide (ITO) and fluorine doped tin oxide (FTO). Due to the conductivity and transparency to visible light, TCOs can be used as electrode in ETA SCs and are valuable for the capability of ETA SCs' superstrate structure.

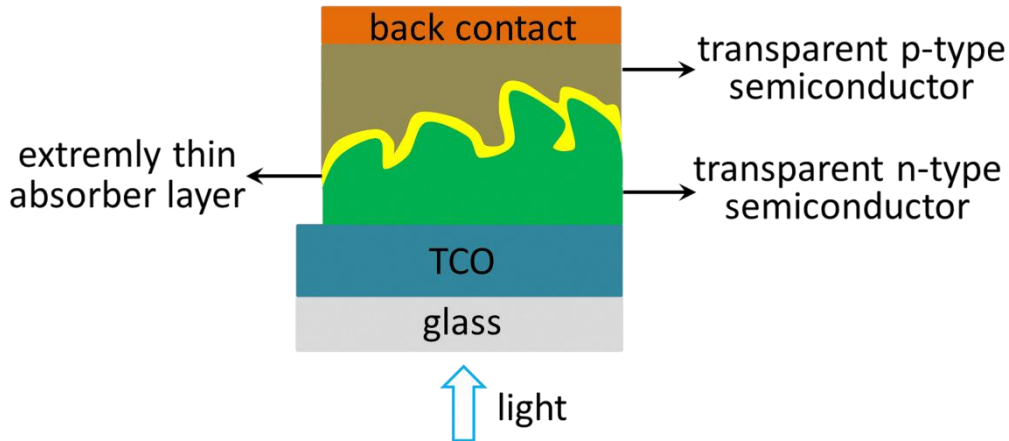


Figure 2.2: Schematic structure of an extremely thin absorber solar cell.

Transparent n-type semiconductor

A transparent n-type semiconductor is used for the collection of electrons and transportation of them to the electrode. Normally, the morphology is designed as highly structured in nano-size which is advantageous for light trapping in absorber layers. Titanium dioxide (TiO_2) and zinc oxide are commonly used as the transparent n-type semiconductor [6, 46]. Fabrication methods can be doctor blade technique [47], electrophoretic deposition [48], sol-gel process [49], dipping process [50], spray pyrolysis [51] for nanoporous layer of TiO_2 , and chemical bath deposition [52], electrodeposition [53] for ZnO nanorods.

Extremely thin absorber layer

The absorber layer is deposited on top of the highly structured transparent n-type semiconductor. CuInS_2 , CdS , CdTe , In_2S_3 can be used as the absorber for ETA SCs and deposition methods for these absorbers are atomic layer deposition [54], chemical bath deposition [51], electrochemical deposition [55], ion layer gas reaction (ILGAR) [6], respectively.

Transparent p-type semiconductor

Transparent p-type semiconductor is used for transporting holes to the metal back contact [41]. CuSCN is an often used p-type semiconductor in ETA SCs and it can be deposited by solution casting [40, 45].

Metal back contact

Silver or gold are normally evaporated on top of transparent p-type semiconductor to serve as metal back contact in test devices [56].

2.1.3 Ultra-thin perovskite solar cells

Perovskite is the name of a class of compounds with the same type of crystal structure as CaTiO_3 and the structure of perovskite (ABX_3) is known as perovskite structure [9, 10]. In perovskite solar cells, a hybrid organic-inorganic lead or tin halide based material with perovskite structure is most commonly used as absorber layer [37].

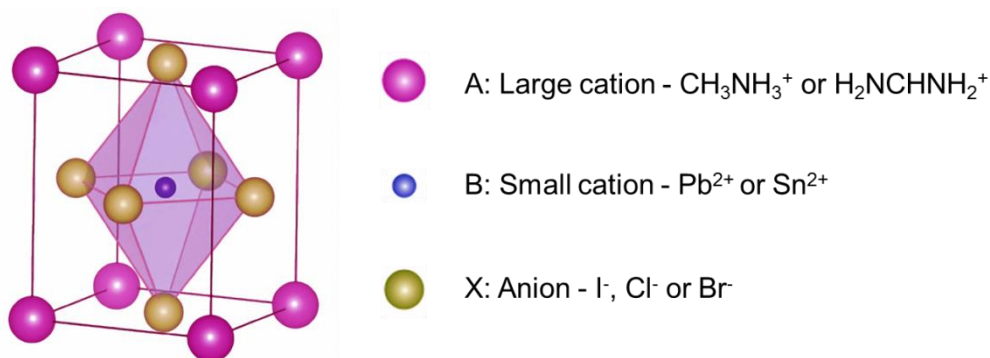


Figure 2.3: Crystal structure of the perovskite absorber with the ABX_3 form, where A is organic cation, B is Pb^{2+} or Sn^{2+} and X is I^- , Br^- or Cl^- . Adapted after Ref: [37].

The crystal structure of an organic-inorganic tri-halide perovskite material is shown in Figure 2.3. In this perovskite structure ABX_3 , methylammonium (CH_3NH_3^+) and formamidinium ($\text{H}_2\text{NCHNH}_2^+$) are most commonly used organic cations A, Pb^{2+} and Sn^{2+} are mostly studied small cations B, I^- , Cl^- and Br^- are halogen used as anions X [57]. By selecting different combinations of cations and anions, the band gap of the perovskite layer can be tuned between 1.2 and 2.2 eV which broadens the application of perovskite absorber layers [58, 59]. Perovskite layers can be fabricated by low cost, solution based processes, which is a significant advantage compared to many traditional solar cells. In addition, perovskite layers have excellent optical properties and long charge carrier diffusion length [10, 60, 61]. All of those advantages of perovskite layers attracted significant research interests. Different configurations can be used for fabrication of perovskite solar cells, like PSCs with nanostructured electron transport layer, regular planar and inverted planar ones [62, 63]. Ultra-thin perovskite absorber layers have much thinner thickness than the absorbers in normal PSCs. They attract more and more interest, because they can be widely used in semitransparent PSCs and tandem solar cells [13-16]. The PSCs with ultra-thin perovskite layers are called ultra-thin perovskite solar cells (UTPSCs). Figure 2.4 depicts the structure of PSCs and UTPSCs with regular planar configuration.

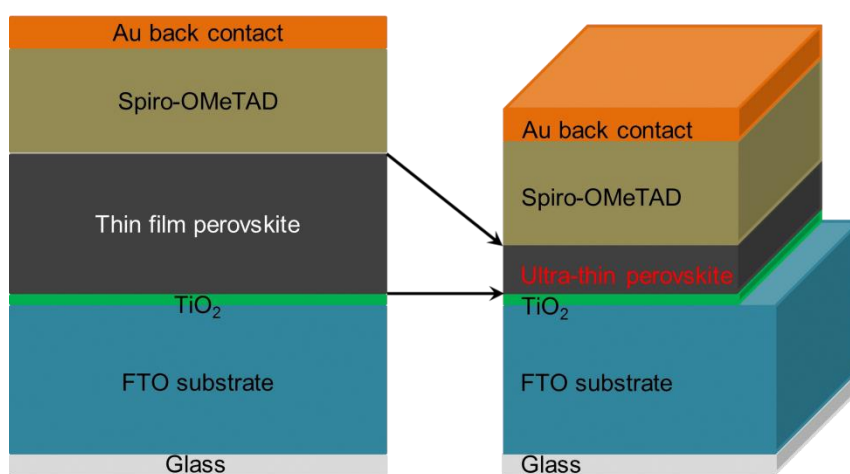


Figure 2.4: Schematic structure of perovskite solar cell and ultra-thin perovskite solar cell with regular planar configuration.

As shown in Figure 2.4, a typical regular planar PSC contains FTO coated glass substrate, TiO_2 layer, perovskite layer, 2,2',7,7'-tetrakis(N,N-di-4-methoxy-phenyl-amino)-9,9'-spirobifluorene (spiro-OMeTAD) layer and Au back contact. In these layers: a FTO front and an Au back contacts are used as electrodes; a TiO_2 layer and a spiro-OMeTAD layer are electron and hole transport layer, respectively; the perovskite layer is the absorber. The thickness of a typical perovskite layer is more than 300 nm while in UTPSCs the thickness is thinner than 150 nm [31, 64]. Due to the decrease of the absorber layer thickness, UTPSCs can be semi-transparent which is very attractive for using in building-integrated PV applications [16].

A drawback for UTPSCs or ultra-thin perovskite layer is the decreased absorption of sunlight [31]. This will reduce the J_{sc} generated by the UTPSCs, thus decrease power conversion efficiency. From theoretical calculation, the maximum PCE of PSCs depends on the thickness of the perovskite layer [65]. It is reported that PSCs with a thickness more than 300 nm can achieve PCEs larger than 29% while UTPSCs with a thickness less than 150 nm can only achieve PCEs smaller than 25%. For the usual thickness of PSCs, the highest efficiency of 22.1% has been obtained [12]. For the UTPSCs, a perovskite layer with around 140 nm thickness, the highest PCE is still lower than 15% [16, 31].

2.2 Plasmonic silver and gold nanoparticles

In recent years, the field of plasmonics for photovoltaics has emerged as a rapidly increasing area for research on materials and devices. Plasmonics can achieve light trapping in different kinds of solar cells by using metallic nanostructures to excite collective oscillations of electrons in the nanostructures or at the interface between metal and dielectric. These metallic nanostructures can be modified to couple or concentrate light into an absorber layer to enhance the absorption of incident light. [36, 66] Among the metallic nanostructures, Ag NPs and Au NPs are most popular because [67, 68]: (1) they have high density of free electrons in the particles; (2) they can support resonance in the visible and NIR region which are suitable for many kinds of solar cells; (3) both of them have low losses in inter-band transitions; (4) they are relatively stable. Therefore, in this section, the fundamentals on plasmonic Ag NPs and Au NPs will be introduced.

2.2.1 Localized surface plasmon resonances

Localized surface plasmon resonances (LSPRs) are collective electron charge oscillations in metallic nanoparticles that are excited by light [69]. LSPRs can be generated by the interaction between metallic nanoparticles and the electric field of incident light. When metallic nanoparticles are subjected in the electric field, the free conduction electrons are driven to the opposite direction of the electric field and positive charges accumulate on the other side of the nanoparticle. The formation of a dipole induces restoring forces in the nanoparticle which leads to oscillations. These oscillations are referred to localized surface plasmon. (see, Figure 2.5) LSPRs can be excited by direct light illumination and lead to amplification of electric field in the near-field area outside the nanoparticle. [70]

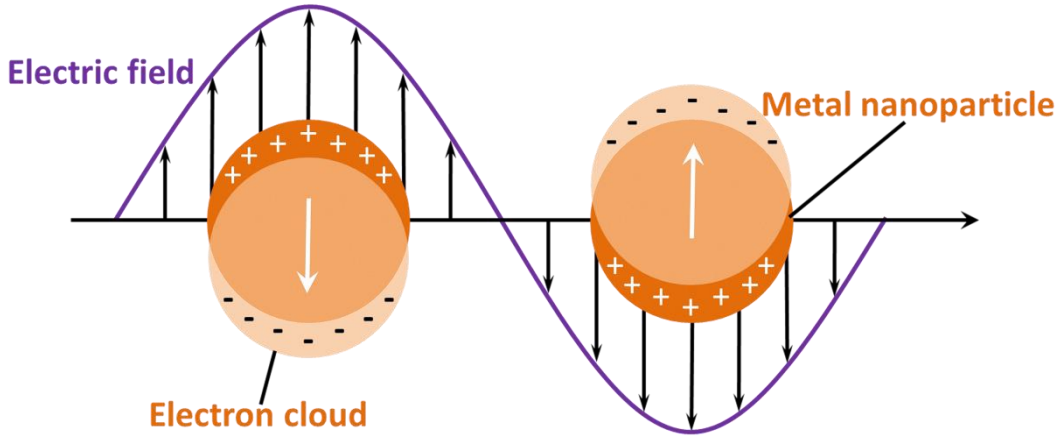


Figure 2.5: Schematic diagram of a localized surface plasmon of metal nanoparticles.

To characterize the LSPR, one simple quasi-static approximation in which the nanoparticle is much smaller than the wavelength of incident light can be used. Under this condition, the electric field over the whole volume of the spherically assumed nanoparticle is constant that the spatial field distribution can be calculated and the assumption of an ideal dipole mode is valid. By solving Maxwell's equation, the polarizability (α) of the spherical metal nanoparticle caused by the electric field can be obtained:

$$\alpha = 4\pi a^3 \frac{\varepsilon - \varepsilon_m}{\varepsilon + 2\varepsilon_m} \quad \text{Eq.2.5}$$

Here, a is the radius of metal nanoparticle, ε is the dielectric function of the metal nanoparticle and ε_m is the dielectric function of the medium surrounding the nanoparticle. In LSPRs, the metal nanoparticle can both absorb and scatter light and the related cross-sections -- absorption cross-section (C_{abs}) and scattering cross-section (C_{sca}) -- can be calculated based on the polarizability:

$$C_{sca} = \frac{k^4}{6\pi} |\alpha|^2 = \frac{8\pi}{3} k^4 a^6 \left| \frac{\varepsilon - \varepsilon_m}{\varepsilon + \varepsilon_m} \right|^2 \propto a^6 \quad \text{Eq.2.6}$$

$$C_{abs} = k \text{Im}[\alpha] = 4\pi k a^3 \text{Im} \left[\frac{\varepsilon - \varepsilon_m}{\varepsilon + \varepsilon_m} \right] \propto a^3 \quad \text{Eq.2.7}$$

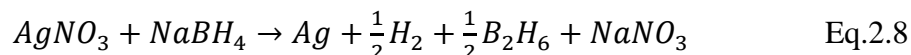
In these two equations, $k = 2\pi/\lambda$ is the wave vector in the surrounding medium and λ is the wavelength of incident light. From the three equations, useful information can be extracted: (1) the polarizability, C_{sca} and C_{abs} of metal nanoparticle experience the maximum under the condition that ε equals to $-2\varepsilon_m$; (2) the absorption of a metal nanoparticle scales with a^3 while scattering scales with a^6 which means absorption of light dominates for smaller nanoparticle and scattering dominates for bigger ones. It has to be mentioned that only quasi-static approximation and dipole mode are mentioned here as an example to explain LSPR of metal nanoparticle. Other approximations can be used for more complex conditions and high order modes also exist, more details can be found elsewhere [70].

2.2.2 Synthesis of silver and gold nanoparticles

Due to the outstanding optical properties, Ag NPs and Au NPs are the most commonly used plasmonic metal nanoparticles. Ag NPs and Au NPs can be prepared by many kinds

of methods and most of them can be attributed to chemical or physical methods [71-73]. Among chemical methods, chemical vapor deposition and the solution based method which involves reduction of metal salts are widely used; in physical methods, surface-tension-induced agglomeration, substrate-conformal imprint lithography, electron-beam lithography and pulsed laser deposition have been reported for fabrication of Ag NPs and Au NPs [17, 28, 74-78].

For the synthesis of Ag NPs, reduction of silver nitrate by ice-cold sodium borohydride is one of the most popular methods [79, 80]. During the process, small nuclei or clusters are first formed and then reduction of silver ions happens on the surface of the clusters to let them grow larger. The reduction reaction can be written as [74]:



Chemical vapor deposition (CVD) is also a popular method. During the deposition process, a vapor phase of silver precursor decomposes directly on top of a hot substrate and small nuclei can be formed and grow to Ag NPs [17, 75]. Details of the mechanism of CVD can be found in chapter 3.

In surface-tension-induced agglomeration method, a thin silver layer is first evaporated on a substrate by thermal evaporation and then the substrate is annealed at temperatures higher than 200 °C for several minutes. Due to the surface tension, silver layer cannot maintain and shrinks to form Ag NPs. By controlling the layer thickness, annealing temperature and annealing time, Ag NPs of different size and density can be obtained. [23, 76]

For the synthesis of Au NPs, the colloidal method is mostly used. The first researcher used this method was Faraday in 19th century and the technique he used is the basis of colloidal method applied nowadays [81]. In general, a metal salt is first dissolved in a solvent and then reduced by a proper reducing agent. When the metal ion is reduced to zero valence state, small nuclei are generated and grow to bigger Au NPs. During the fabrication process, capping a material is also required to stabilize the formed Au NPs. In addition, capping materials can also be used for the control of size, shape and size-distribution of the obtained Au NPs. Mono-dispersed spherical Au NPs were first produced by Turkevich et al., in 1951 [82] by using sodium citrate to reduce chloroauric acid in boiling water. The size of the obtained Au NPs is around 10-20 nm. There was also further development of the Turkevich process by other researchers which can produce Au NPs with size between 5-100 nm [83]. However, using the same process to obtain larger, mono-dispersed Au NPs is impossible because the overlap of nucleation and growth of Au NPs makes the control of size-distribution very hard. In this case, seed mediated growth was developed. In the process, seed particles are first produced by the reduction of gold salt by strong reducing agents (like NaBH₄) and then are added into a solution with gold salt and weak reducing agent (like, ascorbic acid or hydrazine) [84]. As with weak reducing agent, reduction of gold salts happens only on the surface of seed particles, hence, larger mono-disperse Au NPs can be obtained. It has to be mentioned that the seed mediated growth can also be used for production of Au NPs with different shapes, e.g., Au nanorods [85, 86], Au cubes [87, 88] or Au tubes [89].

2.2.3 Application for light trapping of solar cells

Light trapping in solar cells can make the optical path length of the incident light several times longer than the thickness of the absorber layer to increase the absorption of light.

Initially, micro-sized structuring of the surface was used for thick solar cells (thickness bigger than 1 μm), but the structures are too large for thin-film solar cell and solar cells with ultra-thin absorbers [90]. In this case, a promising solution is the integration of Ag NPs and Au NPs into the solar cells which can enhance the absorption of nearly all kinds of solar cells. By using Ag NPs and Au NPs, three different mechanisms can be used for absorption enhancement of light in solar cells which are [36]: (a) scattering, (b) near-field enhancement, (c) excitation of surface plasmon polaritons (see, Figure 2.6).

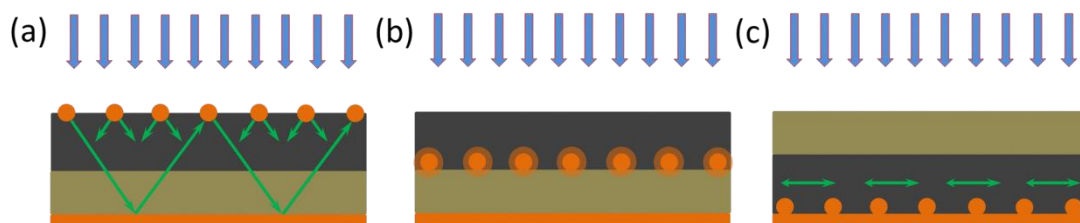


Figure 2.6: Three mechanisms for light trapping of solar cells by silver or gold nanoparticles: (a) high-angle scattering, (b) near-field enhancement, (c) excitation of surface plasmon polaritons. Adapted after Ref: [36].

Light scattering by plasmonic silver and gold nanoparticles

Ag NPs and Au NPs can enhance the absorption of light in solar cells by high-angle scattering. This absorption enhancement can be realized by placing nanoparticles nearby the absorber layer. [18] The light is preferentially scattered to the absorber layer since refractive indexes of many absorber layers are bigger than those of the other layers. [91] Therefore, light can have longer optical path through the absorber. Moreover, if a reflective back contact is present, light can pass through the absorber layer several times which will increase the absorption probability effectively [23]. In addition, for big enough nanoparticles, e.g., 150 nm Ag NPs, the scattering cross section is much bigger than the geometric cross section of nanoparticles which lead to nearly full capture of incident light by 10% coverage of nanoparticles [36].

For the application of Ag NPs and Au NPs for light scattering, several parameters should be considered and well designed to fit the requirement of different absorbers [92-94]. On one hand, parasitic absorption of nanoparticles should be avoided because it leads to ohmic loss and cannot contribute to the charge separation in absorber layer. This can be solved by increase of the size of nanoparticles because larger nanoparticles scatter light stronger than absorb them [91]. On the other hand, the scattering region of light wavelength should be designed to fit the requirement of absorbers. Plasmon resonance of Ag NPs and Au NPs is mainly in the visible light region and it can be influenced by particles' size, shape and surrounding medium [28, 92]. Therefore, the scattering wavelength of light should be controlled by the mentioned three parameters.

Near-field enhancement by plasmonic silver and gold nanoparticles

Ag NPs and Au NPs can also cause the absorption enhancement of light in the absorber layer by near-field effect. [95] The near-field is the region of the electromagnetic field around the nanoparticle in nanoscale environment. When light incidents to a metal nanoparticle, a very strong electromagnetic field will be generated around the nanoparticle. The strong electromagnetic field can interact with the surrounding medium. If the metal nanoparticle is put in the absorber material, the strong electromagnetic field can increase absorption and charge generation in the absorber materials surrounding the nanoparticle.

For the absorber layers with short diffusion length of charge carriers, near-field enhancement is useful in particular and can be realized by putting Ag NPs or Au NPs nearby the collection junction area. Near-field enhancement has been used in different kinds of solar cells for enhancement of performance, e.g., perovskite solar cells [96], ultra-thin organic solar cell [97], dye-sensitized solar cell [98, 99] and inorganic solar cells [100].

Light trapping by surface plasmon polaritons

Ag NPs and Au NPs can also be used for light trapping by the generation of surface plasmon polaritons (SPP). SPP are electromagnetic waves which travel along the interface between metal back contact and the semiconductor absorber layer [36]. The excitation of SPP at the interface by metal grating (Ag or Au nanostructure) can turn the incident light by 90°, which means the light will travel along the lateral direction of the solar cell. Therefore, the optical path of the incident light in the absorber layer is enlarged for orders that absorption of light can be enhanced significantly.

Exploitation of SPP for light trapping of absorber layer requires that the absorption of the SPP in the semiconductor is stronger than in the metal. It is reported that for different absorber materials, the absorption fraction between semiconductor and metal can be different in different wavelengths, e.g., at a GaAs/Ag interface the semiconductor absorption fraction is high in the wavelength range between 600 nm and 870 nm while at a Si/Ag interface plasmon losses dominate over the entire spectral range. Therefore, plasmon absorption which can couple with the metal should be avoided by design of the parameters of metal film and nanostructure. SPP have also been used for light trapping in different kinds of solar cells. [101-103]

2.2.4 Optical simulations for plasmonic solar cells

It has been mentioned in section 2.2.3 that different parameters should be considered to get optimum plasmonic Ag NPs or Au NPs for light trapping. In addition, understanding how the light trapping of nanoparticles works is very important. Due to the above two reasons, theoretical optical simulation for plasmonic solar cells is necessary. The Finite Element Method (FEM) performed by JCMsuite was used for the optical simulation. [104-106] JCMsuite is a complete Finite Element software package for the computation of electromagnetic waves, elasticity and heat conduction. Because optical simulation of plasmonic solar cells is related to the computation of electromagnetic waves, details of this computation will be discussed. The FEM is a numerical technique for approximating the solutions of Maxwell's equations to the exact solutions in the computational domain. For the computation, the domain is first subdivided into smaller, simpler parts which are called finite elements. Each of these small parts or finite elements is defined with a small polynomial space and connected with the tangential continuity. Thus, the electromagnetic field can spread across the boundaries of the small parts. Finally, these simple equations that model each of the small parts are assembled into Maxwell's equations and the desired approximation solutions can be obtained. The FEM has many advantages compared to other simulation methods: (a) complex geometries, like irregular and curved surfaces, can be represented very accurately; (b) the resolution of the elements at different positions can be controlled separately which increases the efficiency and accuracy of the computation; (c) the small parts (finite elements) can be set very tiny that even weak effects of nanoparticles can be distinguished very well. [107-109]

2.3 Background of this Thesis

ETA solar cells have attracted a lot of interests due to many advantages like [8, 41]: (1) good stability under high temperature; (2) usage of absorber layer with very thin thickness; (3) reduction of recombination loss and enhancement of charge collection probability; (4) application of low cost solution based processes for fabrication of absorber layers. Research on ultra-thin perovskite solar cells (UTPSCs) is also a hot topic in recent years due to the excellent optical and electron properties of organic-inorganic halide perovskite absorbers [10, 16]. UTPSCs can be used in tandem solar cells, ultra-lightweight solar cells or building-integrated photovoltaics. However, for both ETA solar cells and UTPSCs weak absorption of light (especially at the wavelengths near the band gap) is a significant shortcoming due to the ultra-thin thickness of absorber layers [17, 32]. To overcome this disadvantage, integration of plasmonic silver nanoparticles or gold nanoparticles is a promising solution since it can enhance the absorption of light without increase the thickness of absorber layers.

For the fabrication of silver nanoparticles, different methods have been introduced in section 2.2.2. But for the application of plasmonic Ag NPs in ETA solar cells and UTPSCs, different parameters should be considered: (1) size and density of Ag NPs should be controlled separately to obtain the resonance at desired wavelengths; (2) synthesis and integration of Ag NPs should be simple enough and low cost for potential large scale performance; (3) temperature during fabrication and integration of Ag NPs should be as low as possible because of the thermal instability of some kinds of absorber materials. For the reported synthesis methods, the colloidal method requires a second step for integration of Ag NPs into solar cells, the known spray pyrolysis method needs operation temperatures higher than 400 °C, surface-tension-induced agglomeration method, and atomic layer deposition require vacuum environment which increases cost significantly. The spray ion layer gas reaction (spray-ILGAR) method and its setup have been used for deposition of many kinds of layers and nanoparticles. It can be operated under atmospheric pressure.

Based on the discussed items and the spray-ILGAR setup, a simple spray chemical vapor deposition method (spray-CVD) for deposition of size and density controlled Ag NPs directly on substrates or films is developed in this thesis. Mechanisms of the deposition process and growth of Ag NPs are studied in detail. The Ag NPs deposited by spray-CVD have been applied in ETA SCs and UTPSCs to study the influence of Ag NPs on these two kinds of solar cells. Integration of Au nanorods in UTPSCs is also studied.

Chapter 3

Deposition of Ag NPs by spray-CVD method

Development of spray-CVD method for deposition of silver nanoparticles (Ag NPs) and mechanism of the deposition process are described in this chapter.

In section 3.1, the chemical vapor deposition (CVD) is introduced briefly as the basis for the following sections. Advantages and disadvantages as well as different mechanisms of the aerosol assisted chemical vapor deposition (AACVD) are presented.

Deposition of silver nanoparticles (Ag NPs) by spray-CVD method is introduced in section 3.2. Details of the process are described in section 3.2.1. Effect of the deposition parameters on sizes and densities of Ag NPs are studied in detail in section 3.2.2, e.g., influence of flow rate of carrier gas, concentration of precursor solution, deposition time and substrate temperature. Based on the systematical variation of deposition parameters, size and density controlled Ag NPs can be achieved. This part of content will be described in section 3.2.3. In section 3.2.4, the deposition and Ag NPs growth mechanisms during the deposition by spray-CVD method are investigated.

A summary of the substance in this chapter is described in section 3.3.

3.1 Chemical vapor deposition

Chemical vapor deposition (CVD) can be defined as the deposition of a stable solid product on a heated surface from a chemical reaction of gaseous reactants transported in the vapor phase [110]. In 1893, de Lodyguine had published a patent literature using CVD to deposit W which is the first industrial exploitation of CVD [111]. At that time, CVD was mainly used for the production of refractory metals. A deep understanding of CVD and expanded application of the process happened in past 50 years. Nowadays, the CVD process has been used in a wide range of applications, e.g., coating, deposition of films, powder and nanostructured materials, producing free standing shapes, rapid prototyping, and etc. [112]

In a conventional CVD process, seven steps can be separated to clearly understand the process. The seven steps are [113]:

- (1) Feed of precursor gaseous to the reactor;
- (2) Diffusion of precursor material through boundary layer to the substrate;

- (3) Adsorption of precursor material on the substrate;
- (4) Surface reaction of precursor material;
- (5) Desorption of by-products generated during the reaction;
- (6) Diffusion of by-products through boundary layer to main flow region;
- (7) Transport of by-products and unreacted precursor material.

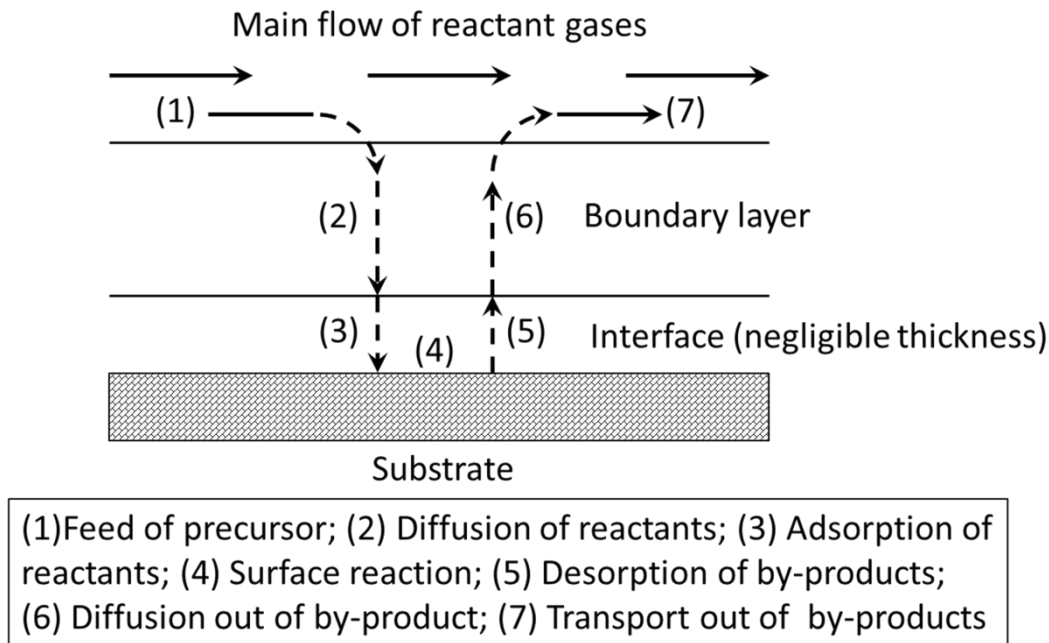


Figure 3.1: Steps during chemical vapor deposition. Adapted after Ref: [113].

Figure 3.1 shows the sequence of events of a conventional CVD process. To realize the steps of the CVD process, three main components are normally used, which are vapor precursor supply system, CVD reactor and gas handling system. Hence, the CVD equipment consists of these three main components. By varying the supply system or the energy sources used for activating the chemical reactions, variant CVD methods were developed, such as thermal activated CVD (TACVD), plasma enhanced CVD (PECVD), photo-assisted CVD (PACVD), Atomic Layer Epitaxy (ALE), metal organic CVD (MOCVD), Flame assisted vapor deposition (FAVD), Electrochemical vapor deposition (EVD), Chemical vapor infiltration (CVI) and aerosol assisted CVD (AACVD). Details of the variant CVD methods can be found in many works [113, 114].

Among those CVD methods, AACVD is very special as it makes use of aerosol precursors. In general, the aerosol is generated by atomizing the chemical precursors into liquid droplets, size of the liquid droplets are in the order of micro meters. The generated aerosol will be carried to a heated zone, where the solvent will be evaporated completely. The chemical precursor undergoes subsequent chemical reaction or decomposition to deposit desired films on the substrate. Compared to the conventional CVD, advantages of AACVD are [110]:

- (1) Deposition of multicomponent films
- (2) Controlled stoichiometry
- (3) Simplicity
- (4) Wide variety of materials

- (5) Oriented or epitaxial films
- (6) High deposition rate
- (7) Many choices for precursors
- (8) Extended range of thermal stability for volatile precursors
- (9) Possibility of doping
- (10) Conformal coverage
- (11) Reproducible, constant delivery rates for multicomponent systems

Like the conventional CVD, the AACVD process is not an equilibrium one but a complex chemical system. This is due to the continuous supply of the precursor materials, different places where the chemical reactions can take place, transport and adsorption of precursor materials, etc. Correspondingly, research on the kinetics of AACVD process should involve all the possible effects on the chemical reactions. In general, the deposition rate of AACVD processes can be limited by (1) feed rate of precursor material; (2) diffusion or transport of precursor material to substrate; (3) surface reaction rate. Feed rate limitation is mainly due to the very few supply amount of precursor material, as this will cause the low partial pressure of the vaporized precursor material. When the partial pressure of the vaporized precursor is high enough, deposition rate is limited by transport of material or surface reaction rate. [115, 116]

With variation of the limitation mechanism, the deposition rate can be given by Eq.3.1-3.5 [114]:

$$\text{rate} = \frac{F_r M}{(A_s \rho)} = \frac{C_r Q M}{(A_s \rho)} = C_T \exp\left(\frac{-\Delta H_{vap}}{RT}\right) \left[\frac{Q M_m}{(A_s \rho)}\right] \quad \text{Eq.3.1}$$

$$\text{rate} = k_s C_r v = k_0 C_r v \exp\left(\frac{-E_A}{RT}\right) \quad \text{Eq.3.2}$$

$$\text{rate} = k_0 C_r v \exp\left(\frac{-E_A}{RT}\right) = v C_T \exp\left(\frac{-\Delta H_{vap}}{RT}\right) k_0 \exp\left(\frac{-E_A}{RT}\right) \quad \text{Eq.3.3}$$

$$\text{rate} = \frac{v D C_r}{L} = \left(\frac{v D_0}{L}\right) \left(\frac{p_0}{p}\right) \left(\frac{T}{T_0}\right)^{3/2} \left(\frac{p_r}{RT}\right) \quad \text{Eq.3.4}$$

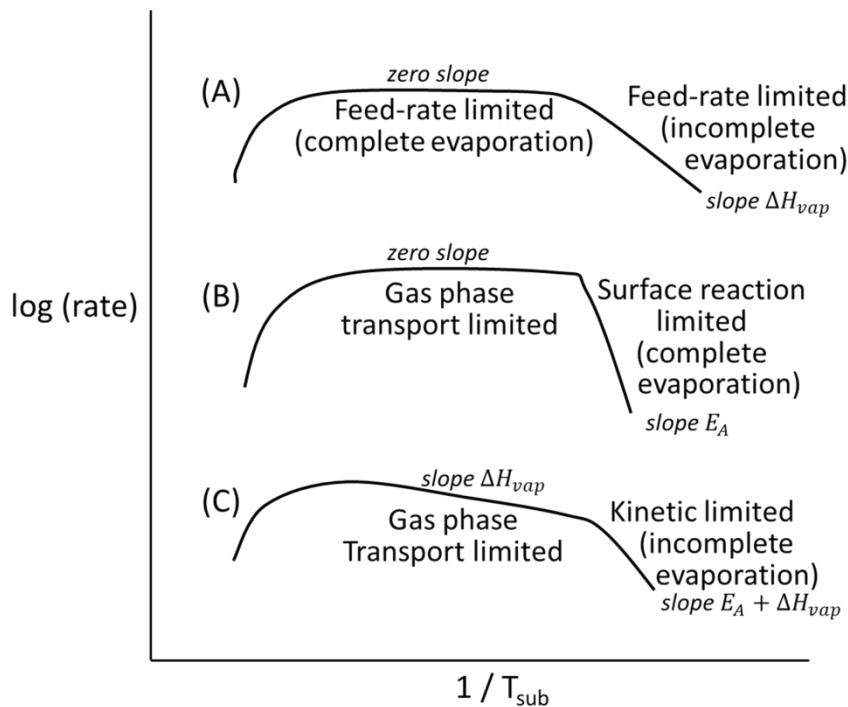
$$\text{rate} = B \left(\frac{T}{T_0}\right)^{3/2} \exp\left(\frac{-\Delta H_{vap}}{RT}\right) \quad \text{Eq.3.5}$$

Here C_r is the molar concentration of gaseous reactant outside the boundary layer, F_r the feed rate of the reactant, M the atomic weight of depositing species, A_s the heated area over which the deposition happens, ρ the density of the deposited film, Q the gas flow rate in volume, C_T the pre-exponential term for the temperature-dependent form of the precursor vapor pressure, ΔH_{vap} the enthalpy of evaporation of the precursor, T the substrate surface temperature, k_s the surface reaction rate constant, v the volume of deposited species, k_0 the pre-exponential constant, R the gas constant, E_A the activation energy, D the diffusion coefficient, D_0 the diffusion coefficient at reference conditions, L the thickness of the boundary layer, p_0 the total pressure at reference conditions, p the total pressure, p_r the reactant partial pressure outside the boundary layer, T_0 the reference temperature for the gas above the substrate, B a constant.

Eq.3.1 describes the situation that the deposition rate is limited by the low feed rate of the precursor. In this situation, the partial pressure of the reactant can be affected by substrate temperature. At low temperatures, with increase of the substrate temperature, the gas is heated up and more precursors can be evaporated into the gas phases. This leads to the increase of deposition rate. Thus the dependence of deposition rate on temperature at low temperature regime is given by the evaporation enthalpy. When the substrate

temperature is higher, the precursor evaporated completely, the deposition rate will not increase with temperature from this point as the precursor partial pressure is constant. At even higher temperatures, particle can be formed by gas phase reaction above the boundary layer, thus lead to reduction of precursor concentration in the gas phase. Hence, this will lead to the decrease of deposition rate. The described condition is shown in plot A in Figure 3.2.

When the feed-rate of the precursor is high enough and the precursor is evaporated completely before entering the reactor, the deposition rate is limited only by surface reaction rate at low substrate temperatures. Eq.3.2 depicts this case. At low temperature regime, with increase of substrate temperature, surface reaction accelerates which leads to the exponential increase of the deposition rate. Thus the dependence of deposition rate on the temperature is given by the activation energy E_A . At higher temperatures, transport of the precursor from gas phase to the surface of substrate cannot afford the requirement in surface reaction. In this case, the deposition rate keeps nearly constant and the dependence on temperature is very weak. At this high temperature regime, the deposition rate is limited by gas phase transport. At even higher temperature, gas phase reaction can reduce the deposition rate which is similar as the case described in the former paragraph.



- | |
|---|
| (A) Feed-rate limited with incomplete evaporation of precursor at low temperature
(B) No feed-rate limitation and complete evaporation of precursor
(C) No feed-rate limitation and incomplete evaporation of precursor |
|---|

Figure 3.2: Plots of the logarithm of the deposition rate depends on the inverse of the substrate temperature, showing three possible dependencies of deposition rate on temperature in AACVD. Adapted after Ref: [114].

When the feed-rate of precursor is high enough to overcome the limitation on the deposition rate but the precursor is not evaporated completely, the dependence of

deposition rate on temperature will be complex. At lower temperatures, the increase of the deposition rate with increase of temperature can be attributed to the rise of surface reaction rate and more precursor material is evaporated into gas phases. The related equation is described in Eq.3.3. Hence, the dependence of deposition rate on temperature is given by the sum of the activation energy for surface reaction E_A and the enthalpy of evaporation of the precursor ΔH_{vap} . At higher temperatures, the deposition rate is limited by transport of precursor, which is depicted in Eq.3.4. As the evaporation of precursor is still not complete, increase of temperature can improve the precursor partial pressure in the gas phase. The transport limited regime can be also expressed as Eq.3.5, which shows clearly the influence of evaporation of precursor on the deposition rate. So in the transport limited regime, the dependence of deposition rate is given by the enthalpy of evaporation of the precursor ΔH_{vap} . At even higher temperatures, the gas phase reaction will reduce the deposition rate. The complex dependence of deposition rate on temperature is illustrated in plot C in Figure 3.2.

3.2 Deposition of Ag nanoparticles by spray-CVD

In this section, a spray-CVD process is developed for depositing Ag nanoparticles (Ag NPs) on different kind of substrates. Fundamentals of the process, effect of different deposition parameters, size and density control of Ag NPs and investigation on the deposition mechanism will be shown in this section.

3.2.1 Fundamentals of spray-CVD for Ag nanoparticle deposition

From section 3.1, compared to the conventional CVD process AACVD has many advantages, e.g., higher deposition rate, lower temperature and simpler deposition conditions. These advantages benefit from the special precursor supply system, which nebulizes the precursor solution to form an aerosol.

The spray-ILGAR is a sequential and cyclic technique including a CVD step which uses an ultrasonic generator to nebulize the precursor solution to form an aerosol. This technique has been widely used to deposit various kinds of layers and nanoparticles [117]. When adapting the setup from spray-ILGAR for a special kind of CVD deposition process, the spray-CVD for Ag NPs was developed. Figure 3.3 shows the scheme of the spray-CVD setup.

The spray-CVD setup contains an ultrasonic generator, a glass vessel, a flexible tube, a 90° bent glass tube, a straight glass tube, a heater and a copper block. The ultrasonic generator is connected to the glass vessel which contains the precursor solution. The ultrasonic generator can nebulize the precursor solution to form the aerosol with droplets size around 2 μm . The glass vessel has one gas inlet plus one for solution and one outlet. The gas inlet is for N_2 carrier gas and the outlet is for the aerosol flow. The outlet connects to the flexible tube which follows the 90° bent glass tube. The flexible tube enables the aerosol flowing through an increasing slope part which can trap big size. The other side of the bent glass tube connects with the straight glass tube, in which the steel heater and copper block are located. The copper block is fixed on top of the heater by kapton tape. The substrate is placed on top of the copper block.

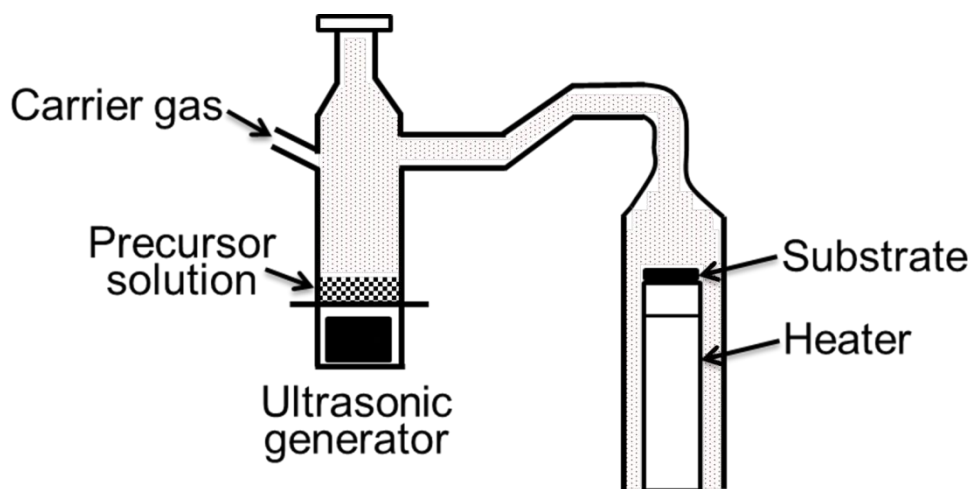


Figure 3.3: Schematic sketch of spray-CVD set up.

During the deposition, the ultrasonic generator nebulizes the precursor solution to form an aerosol which will be carried by N_2 gas through the tubes to the place above the heated substrate. Thereby the precursor in the aerosol will be evaporated and the precursor can diffuse to the surface of the substrate and participate in surface reaction. The desired nanoparticles or films are deposited on the surface of the substrates.

For deposition of Ag NPs by spray-CVD at low temperature, stable at room temperature and volatile silver complexes are required [116]. $AgNO_3$ has been used as precursor in Ag NP deposition by spray pyrolysis [118, 119]. However, the deposition temperatures are more than 400 °C, which is a significant disadvantage for incorporating Ag NPs on thermally unstable layers or materials. Trimethylphosphine (hexafluoroacetylacetonato) silver ($Ag(hfacac)PMe_3$) has good volatility and is stable against air, moisture and light [120]. It has been used in CVD processes to deposit Ag film at around 300 °C. So in this work, $Ag(hfacac)PMe_3$ is chosen as precursor for depositing Ag NPs. Figure 3.4 shows the molecular formula of $Ag(hfacac)PMe_3$.

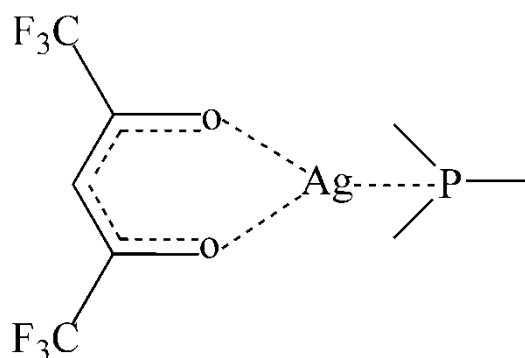


Figure 3.4: Molecular formula of $Ag(hfacac)PMe_3$.

To deposit size and density controlled Ag NPs at low temperature on different substrates by spray-CVD, several deposition parameters have to be taken into account, like N_2 flow rate, precursor solution volume and concentration, deposition time and substrate temperature. Systematic variation of these parameters can help getting the proper condition for the desired Ag NPs. Table 3.1 shows the fundamental deposition parameters of spray-CVD for producing Ag NPs. In general, 20 mL 10 mM ethanolic $Ag(hfacac)PMe_3$ solution

was used as precursor solution. N_2 flow rate was 1 L/min, substrate temperature was 110 °C and deposition time was 5 min. Figure 3.5a presents a SEM image of the produced Ag NPs on FTO substrate under this condition. Size distribution of the Ag NPs is shown in Figure 3.5b. Both figures show that the Ag NPs are homogeneous in size distribution. Average size of the achieved Ag NPs is 21 ± 4 nm and the density of the Ag NPs is about $6.8 \times 10^9 \text{ cm}^{-2}$. It has to be mentioned that the Ag NPs dispersed homogeneous on the substrate which is proper for further application. Another point worth mentioning is that the substrate temperature is below 230 °C (mostly around 110 °C), which is a notable advantage for application in thermally unstable material.

The influence of the deposition parameters on the formation of Ag NPs will be discussed in the next section.

Table 3.1 Process parameters of deposition Ag NPs on substrates.

Flow rate of N_2 carrier gas	1 L/min
Precursor material	Ag(hfacac)PMe ₃
Solvent	EtOH
Concentration of precursor solution	10 mM
Volume of solution	20 mL
Substrate temperature	110 °C
Deposition time	5 min

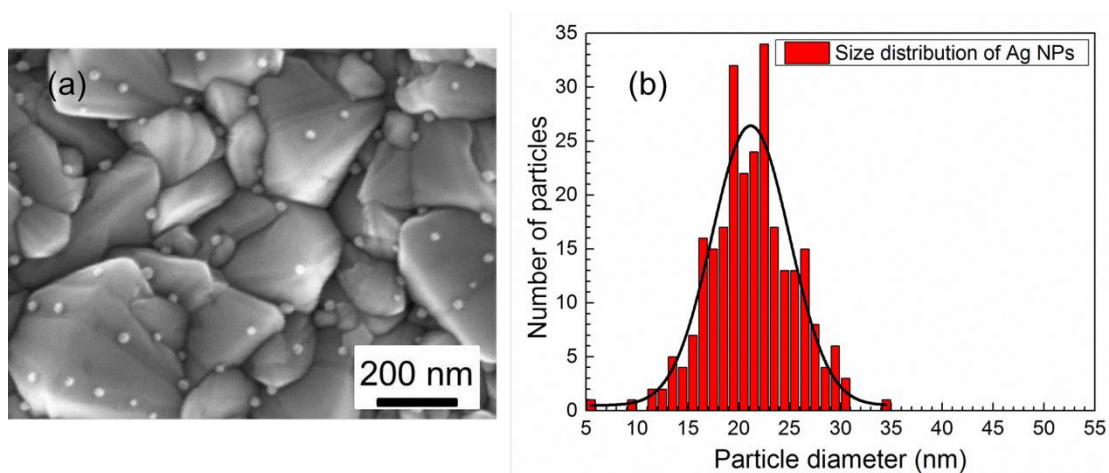


Figure 3.5: (a) SEM image of Ag NPs on FTO obtained by spray-CVD with parameters in Table 3.1; (2) size distribution of the achieved Ag NPs extracted from Figure 3.5a.

3.2.2 Influence of the deposition parameters

Variation of deposition parameters can impact the growth mechanism of Ag NPs directly and therefore influence the particle size and density. Systematic variation of deposition parameters can firstly influence the formation of Ag NPs. Moreover, it can give the external information to optimize the deposition process to control size and density of Ag NPs. Last but not least, it is helpful for studying the deposition and growth mechanism of Ag NPs.

The reference sample was obtained under the condition: substrate temperature 110 °C, N₂ flow rate 1 L/min, precursor solution volume 20 mL, concentration of precursor solution 10 mM and deposition time 5 min. During the systematic variation of deposition parameters, one parameter was varied and analyzed while the other ones were kept constant. Effect of the parameters like N₂ flow rate (in section 3.2.2.1), concentration of precursor solution (in section 3.2.2.2), deposition time (in section 3.2.2.3) and substrate temperature (in section 3.2.2.4) were discussed in detail.

3.2.2.1 Influence of N₂ flow rate

N₂ flow rate is one of the most important parameters in the deposition of Ag NPs, because it determines the transported amount of precursor material to the heated substrate. For this experiment, different N₂ flow rates were used, keeping other parameters constant as shown in section 3.2.1 except the precursor solution volume was kept as 25 mL. The substrates used in this series were FTO.

Figure 3.6 shows SEM images of the Ag NPs achieved using 0.5, 1, 2, 3 and 5 L/min N₂ flow rate. Figure 3.7 presents the average particle size of the Ag NPs extracted from the SEM images shown in Figure 3.6. It is observed that both the average particle size and the density of Ag NPs achieved with 0.5 L/min N₂ is nearly the lowest most likely because the precursor amount transported by such a low N₂ gas flow rate to the substrate is very small. From 0.5 L/min to 1 L/min, both size and density of the obtained Ag NPs increased significantly, which is attributed to the increased amount of precursor material to the substrate. From 1 L/min to higher N₂ flow rate, both size and density of the obtained Ag NPs decrease compared to the 1 L/min sample. This means the precursor material is strongly diluted and the residence time over the substrate is also very short.

If the droplets of the precursor solution would land directly onto the substrate and decompose, the deposited amount of Ag NPs will increase accordingly with increase of N₂ flow rate. In contrary, the trend is decrease after 1 L/min. Hence, these interesting results give the evidence that investigated process does not run “liquid to solid” process but “vapor to solid process”. In the vapor to solid process, the transported precursor material was evaporated first and then diffused to the surface of substrate. In this case, the increased N₂ flow rate decreased the evaporation time and diffusion chance of precursor material, which decreased the deposited amount of Ag NPs on FTO substrates.

From the above discussion, 1 L/min N₂ flow rate give the biggest particle size and highest density of Ag NPs. Thus, it was chosen as standard N₂ flow rate for the further investigation of other parameters.

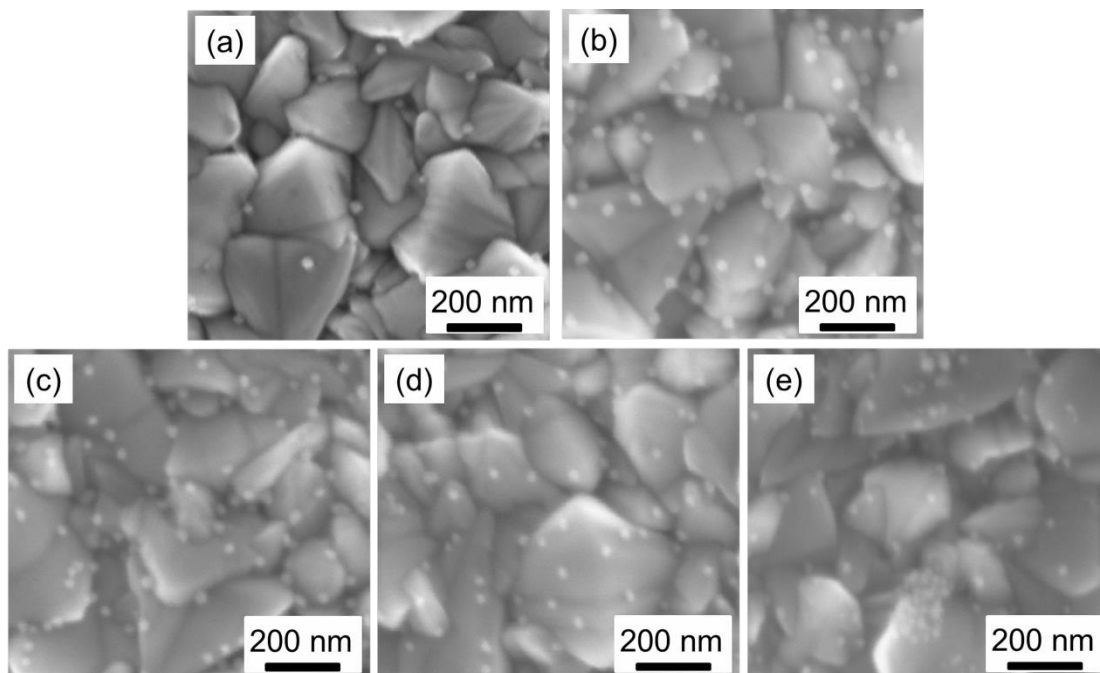


Figure 3.6: SEM images of the achieved Ag NPs using different N_2 flow rate: (a) 0.5 L/min, (b) 1 L/min, (c) 2 L/min, (d) 3 L/min, (e) 5 L/min.

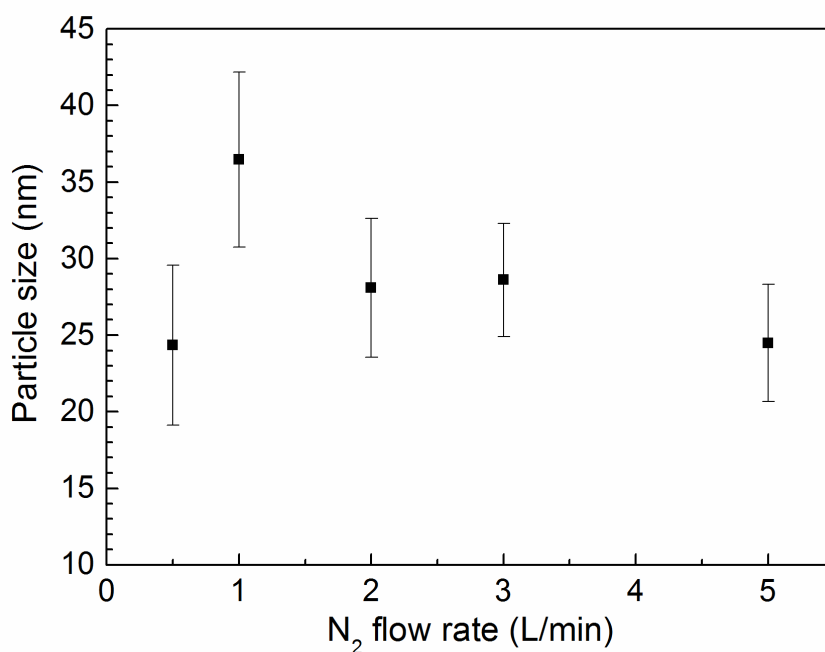


Figure 3.7: Dependence of particle size of Ag NPs on the flow rate of N_2 gas.

3.2.2.2 Influence of concentration of precursor solution

Six concentrations of the precursor solution (5, 10, 20, 50, 75 and 100 mM) were used to study the influence of them on the formation of Ag NPs on FTO coated glass substrate. N_2 flow rate, precursor solution volume, deposition time and substrate temperature were kept as 1 L/min, 20 mL, 5 min and 110 °C, respectively.

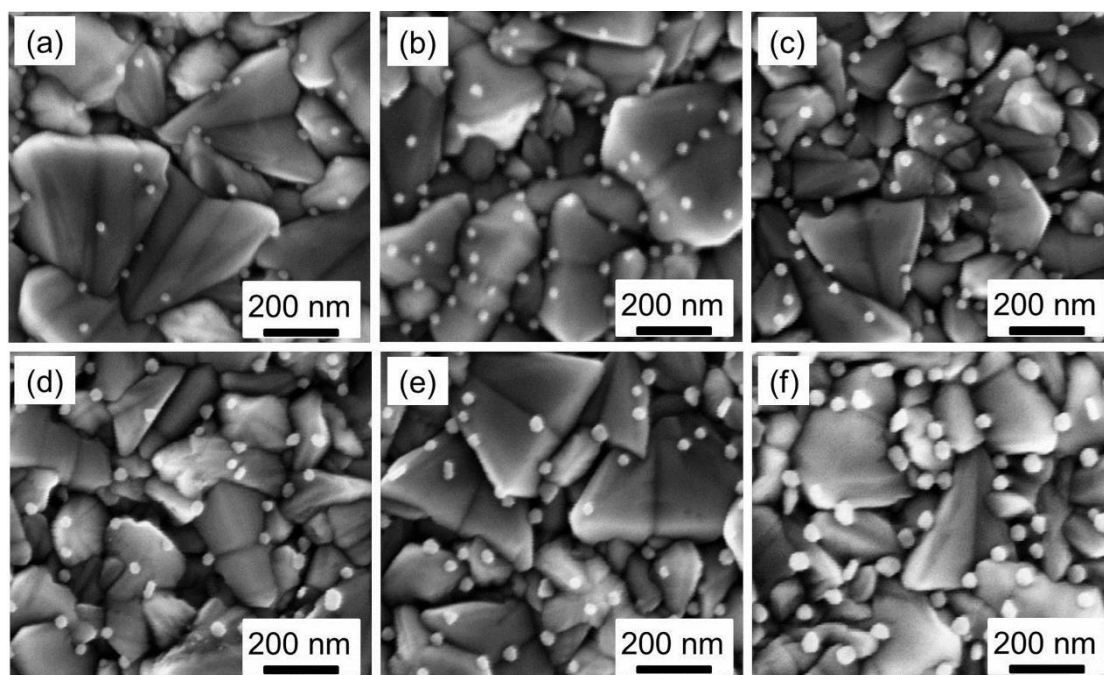


Figure 3.8: SEM images of the obtained Ag NPs using different concentrations of precursor solution: (a) 5 mM, (b) 10 mM, (c) 20 mM, (d) 50 mM, (e) 75 mM, (f) 100 mM.

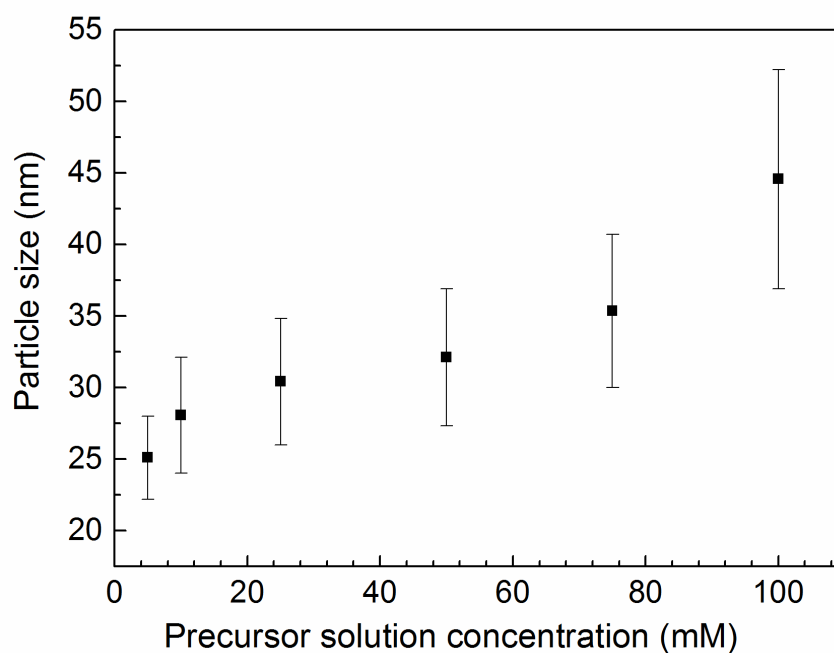


Figure 3.9: Dependence of particle size of the obtained Ag NPs on the concentration of precursor solution.

Figure 3.8 shows the SEM images of the obtained Ag NPs using the mentioned different concentrations of precursor solution. Figure 3.9 depicts the dependence of average particle size (extracted from the SEM images in Figure 3.8) on the variation of the concentration of precursor solution.

It is observed from the two figures that with increase of concentration the particle size increases continuously. With increase of concentration, the transported precursor material contained in aerosol per unit time increases, leading to the improvement of the precursor material amount which participates in the surface reaction, thus cause the Ag NPs grow bigger.

3.2.2.3 Influence of deposition time

For this experiment, Ag NPs were deposited with different deposition times (during different spray durations) at two different substrate temperatures - 110 °C and 230 °C, keeping all other parameters constant.

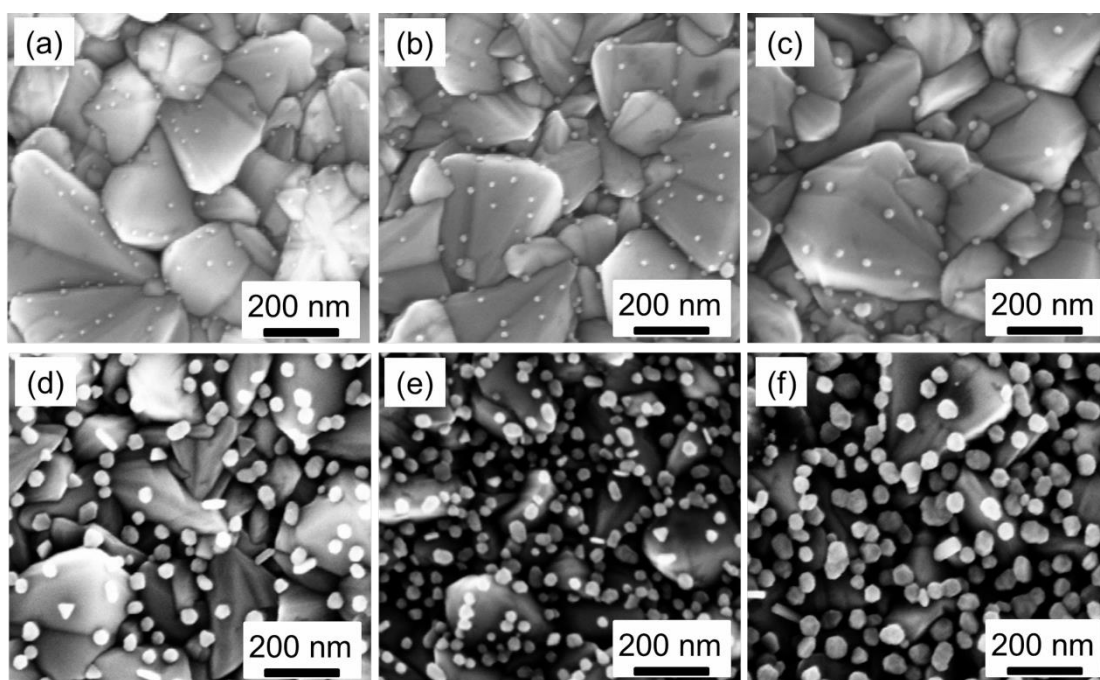


Figure 3.10: SEM images of Ag NP films deposited with variation of deposition time: (a) 0.5 min, (b) 1 min, (c) 5 min, (d) 7.5 min, (e) 10 min and (f) 15 min. Substrate temperature was 110 °C for all samples.

Figure 3.10 shows the SEM images of Ag NPs with deposition times from 0.5 min to 15 min at a substrate temperature of 110 °C. The big grains are FTO. With increasing deposition time up to 10 min, the small Ag NPs grew bigger and kept separated. Then, some Ag NPs touched each other or grew on a neighbor particle. At all times the particles were relatively mono-dispersed. They are not ideally spherical, but have edges; some exhibit clear geometric shapes like triangles or icosahedra. A closer inspection shows that at least during the first 5 min the particles formed preferentially within FTO valleys.

From SEM images shown in Figure 3.11, the Ag NPs obtained at 230 °C substrate temperature look quite different. Due to higher reaction rate the deposited material increases, thus coverage and density of Ag NPs are bigger. The particle size is smaller; because of high nucleation rate the incoming material is distributed on many more species. The generally increased polydispersity and after 10 min more frequent aggregation and multi-layer structures are striking, but the original particles are still visible, i.e., they were not fused completely. Also the grains in a higher level were not merged. Obviously, big

particles which are grown quickly in a position inappropriate for crystal fusion are not able anymore to rearrange at 230 °C. The deposition seems favored on protruding surfaces manifested by much bigger particles at the very surface as compared to those visible between the big grains in a lower level. Most gaseous precursor molecules are fast deposited and consumed just where they reach the hot surface first. Similar effects were observed in the CVD coating of nanorods where mushroom like structures were found at high deposition rates [121].

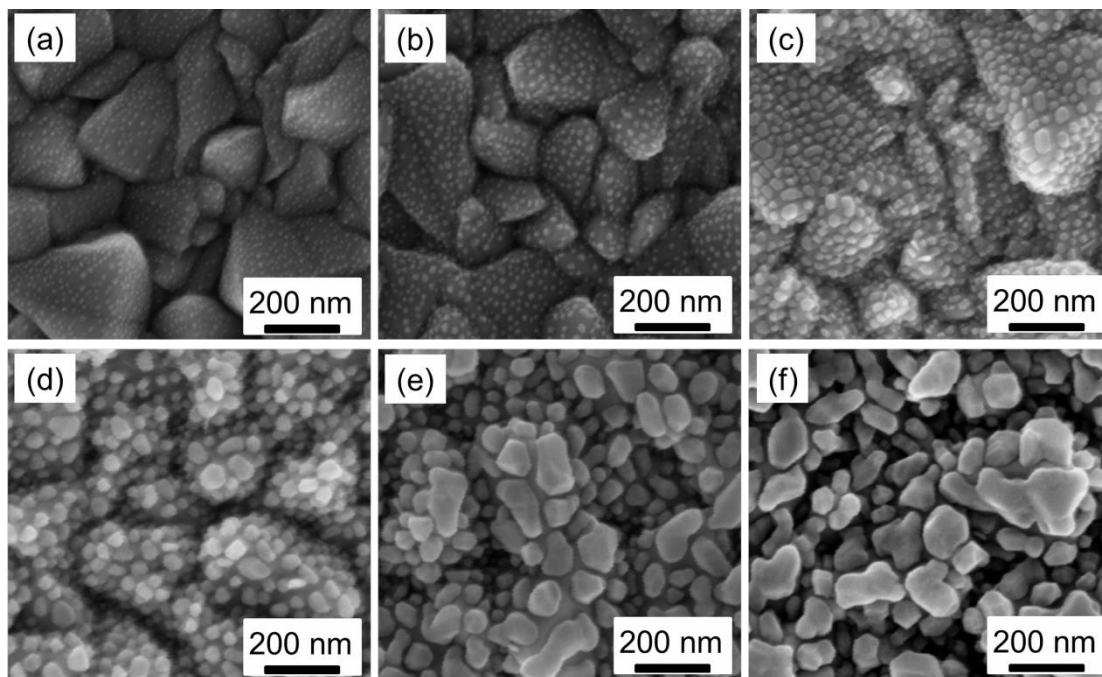


Figure 3.11: SEM images of Ag NP films deposited with variation of deposition time: (a) 0.5 min, (b) 1 min, (c) 5 min, (d) 7.5 min, (e) 10 min and (f) 15 min. Substrate temperature was 230 °C for all samples.

For a detailed and quantitative discussion, the synopsis of the results for deposited mass, particle density, substrate coverage and particle size for the two substrate temperatures 110 °C and 230 °C (Figure 3.12a and 3.12b) is helpful. After a short induction period, until a stationary precursor concentration over the substrate has been built up, the deposition rates (slope of the mass curves) for both temperatures are rather constant for the first 5 or 6 min, respectively. In this time range the deposition at 230 °C is about 6 times faster than at 110 °C due to faster diffusion of educt molecules to the surface, faster decomposition reaction and faster diffusion of gaseous organic products away from the reaction site. Thereafter the rates increase considerably.

But why the deposition is strongly accelerated in both series after a certain time? A change of the flow mode by the increasing number of particles and therefore roughness was also ruled out. The flow conditions (linear flow rate about 50 cm/min) indicate laminar flow where an increase in surface roughness does not have an influence on friction or heat transfer. However, instabilities in the flow field due to buoyancy might occur (Rayleigh-Benard convection) triggering a transition to turbulent flow. Assuming that the effect of surface roughness on deposition rate is in the same order of magnitude as on friction one can estimate that a wall roughness far beyond the particle height would be required to cause a significant effect on the near wall flow. Therefore, the observed effect could be explained by an impact of the already formed Ag particles. This might result in a better

adsorption of the precursor, a locally higher temperature due to much less heat emission of Ag than of the FTO (emissivity $\epsilon_{\text{Ag}} \approx 0.01 - 0.03$ [122], $\epsilon_{\text{FTO}} \approx 0.38$ [123]) or an autocatalytic effect. For the latter an exponential increase of the reaction rate is reported [124]. The non-perfect exponential curves could be due to a superposition of several effects. The onset of the strong acceleration begins at very different coverage values, about 5 % for 110 °C and 50 % for 230 °C. That the lower deposition rate is more sensitive to the catalyst seems plausible.

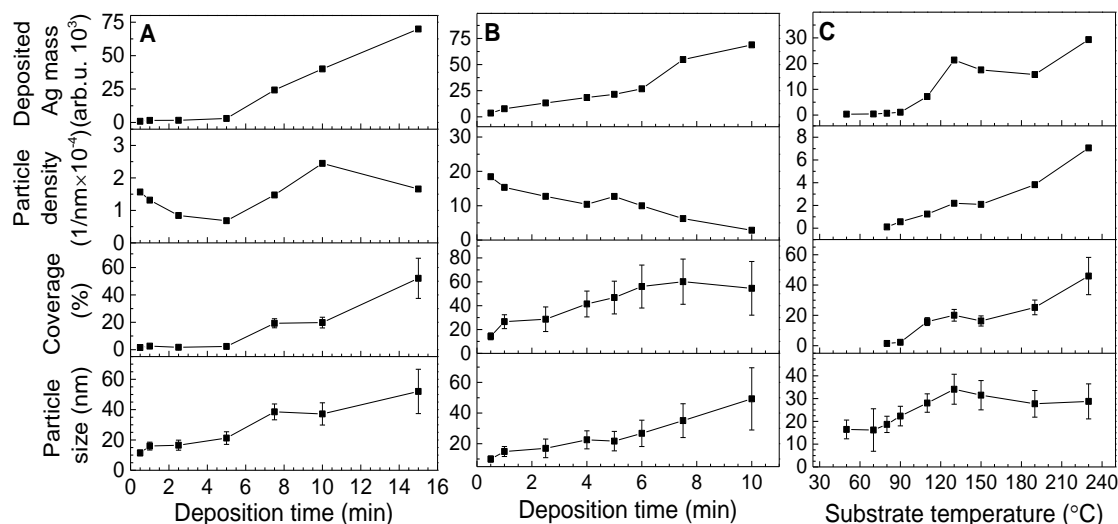


Figure 3.12 Synoptic plots of crucial parameters of the obtained Ag NP films: deposited Ag mass, particle density, coverage and size. The error of deposited Ag mass is too small to visualize. Figure 3.12a (extracted from Figure 3.10) and Figure 3.12b (extracted from Figure 3.11) show the parameters dependent on the deposition time. Figure 3.12c (extracted from Figure 3.14) presents the parameters dependent on substrate temperatures.

The trend of the coverage, calculated from average particle diameter and density, goes to some extent parallel to the deposited Ag mass as it does not distinguish between size and density. The saturation of the coverage for the 230 °C sample after 7.5 min despite increase of both particle size and deposited mass (Figure 3.14e and 3.13f) is explained by partial multi-layer formation due to rare free substrate area, the fast process with process control by material transport and lack of time for a fitting crystalline orientation in the nucleation or small crystallite state.

Variation of deposition time is helpful not only in the study on the effect of Ag NPs formation but also in the growth mechanism of Ag NPs. Investigation on the growth mechanism of Ag NPs and mechanism of the deposition process will be discussed in section 3.2.4.

The resonance band of Ag NPs is a very crucial property in applications. To investigate the optical properties of Ag NPs deposited on FTO substrates, reflection and transmission of the samples with different deposition times (shown in Figure 3.13 and Figure 3.14) as well as the FTO substrate were measured and the absorption of each sample was calculated (in Figure 3.13). For both the 110 °C and 230 °C series samples, two

absorption peaks at around 380 nm and 420 nm can be observed, but the FTO substrate shows absorption peak at around 380 nm. Therefore, the peak at around 380 nm can be attributed to the absorption enhancement of FTO substrate by deposition of Ag NPs. Thus, the absorption peak at around 420 nm belongs to Ag NPs. For both series samples, with increase of deposition time the intensity of the absorption spectra increases. This is due to the increase of particle size and density of the achieved Ag NPs with increase of deposition time. For the same deposition time, the absorption intensity of Ag NPs obtained at 230 °C was higher than that at 110 °C. This can be assigned to the same reason. For the Ag NPs with longer deposition time, absorption at longer wavelength can be explained by the interaction of neighbored Ag NPs.

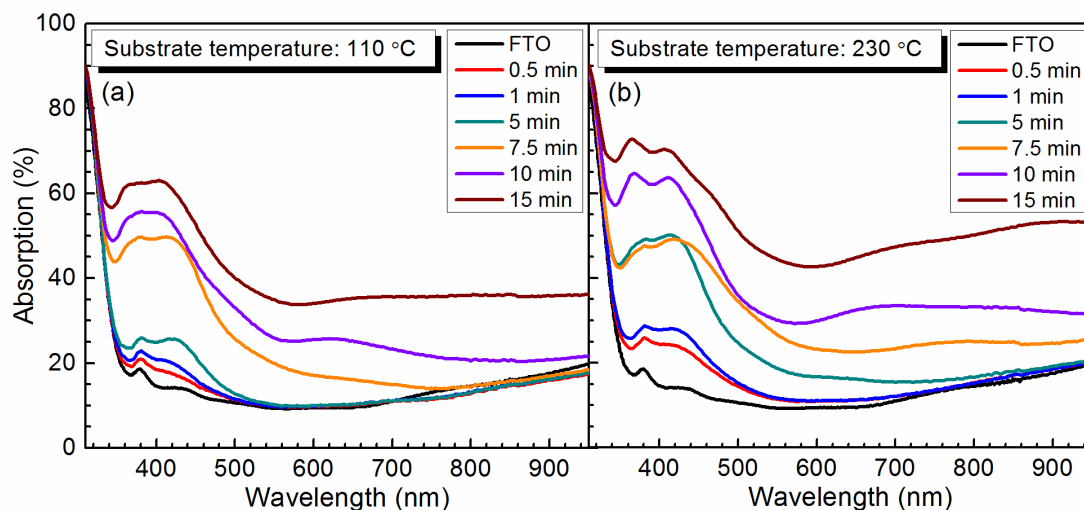


Figure 3.13: Absorption spectra of FTO substrate without and with Ag NPs obtained with different deposition time – 0.5, 1, 5, 7.5, 10 and 15 min at two different substrate temperatures: (a) 110 °C and (b) 230 °C.

3.2.2.4 Influence of substrate temperature

From the substance shown in section 3.2.2.3, it is seen that the substrate temperature has a significant effect on the size and density of the formed Ag NPs. Therefore, a systematic variation of substrate temperature can help understanding how the substrate temperature influences the formation of Ag NPs. In this part, 9 different substrate temperatures (50, 70, 80, 90, 110, 130, 150, 190 and 230 °C) were varied while other deposition parameters were kept constant.

The SEM images of these samples are shown in Figure 3.14. A few, small particles (marked by red circles) are formed already at temperatures as low as 50 °C and 70 °C, which is much lower than the reported temperature of 400 °C in common silver pyrolysis processes [118, 119]. But merely with the substrate temperature of 80 °C or higher, a significant amount of Ag NPs can be deposited in a reasonable time. Only these samples with a statistically meaningful number of particles are considered for discussions of particle size, density and coverage. Both size and density of the formed particles are dramatically increased till a substrate temperature of 130 °C. Above this temperature only the density increases while the particle size is practically constant, because the nucleation rate is higher. This and the first growth of the nuclei consume more material per time, thus limiting the particle size. The deposition rate now stagnates more or less because the process becomes feed rate limited (see below, section 3.2.4 Deposition mechanism).

Moreover, there is no preference of the particle positions at edges and kinks observed above 110 °C. It could be explained by the high substrate temperature letting the general energy of the system overcome this preference [125].

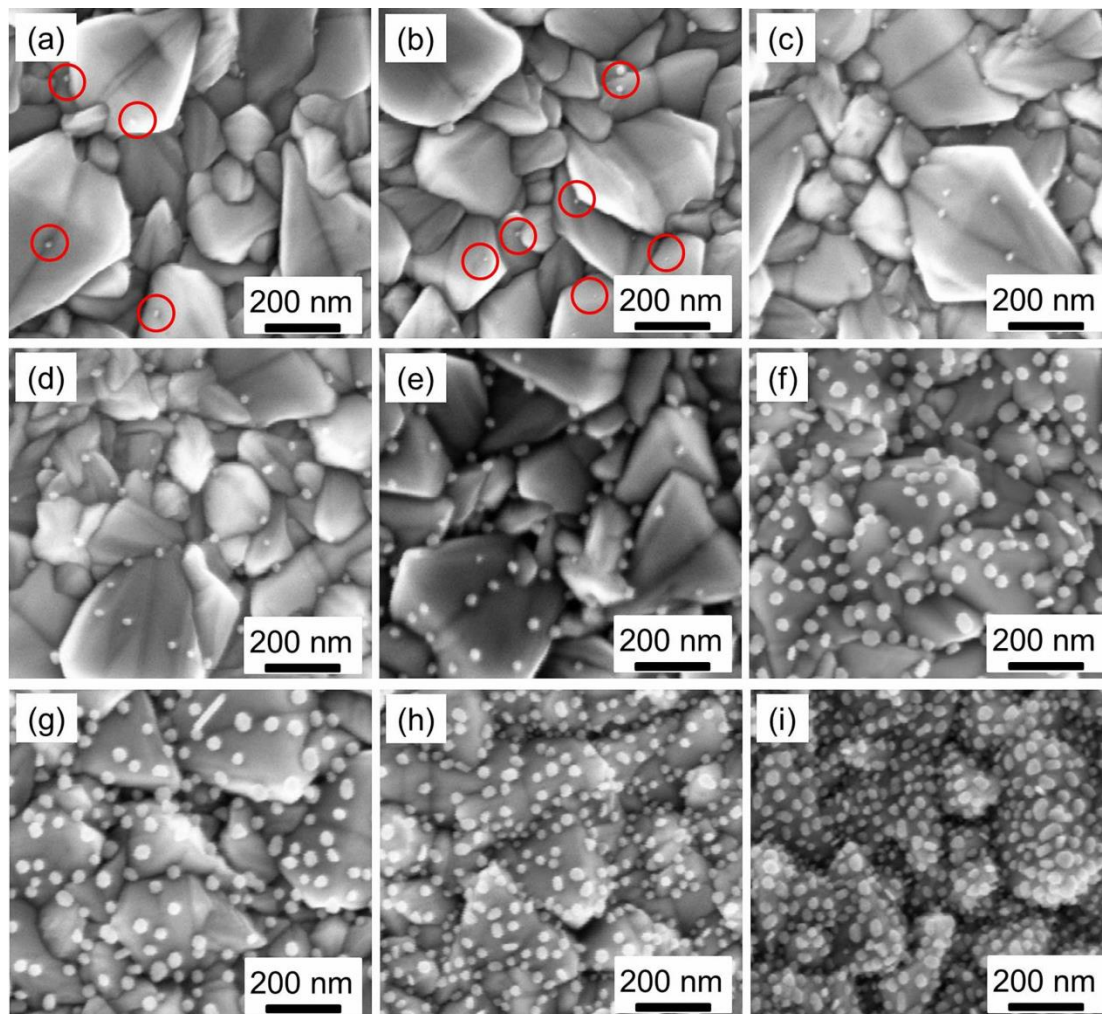


Figure 3.14: SEM images of Ag NPs deposited with variation of substrate temperatures: (a) 50 °C, (b) 70 °C, (c) 80 °C, (d) 90 °C, (e) 110 °C, (f) 130 °C, (g) 150 °C, (h) 190 °C and (i) 230 °C.

The deposited silver amount shown in Figure 3.12 is almost temperature independent in the range from 50 °C to 90 °C. Then up to 130 °C the increase is exponential. At the higher investigated temperature ranges up to 230 °C the deposited mass goes almost into saturation. This might be due to the complete evaporation of the precursor material. Details of the explanation can be found in the deposition mechanism part.

3.2.3 Size and density controlled Ag nanoparticles

From the features shown above, it is clear that variation of deposition parameters influences the formation of Ag NPs and the mechanism of deposition. Therefore, by simple variation and combination of different deposition parameters, size and density of the obtained Ag NPs can be controlled. In this section, the size and density controlled Ag NPs based on the combination of deposition parameters will be shown.

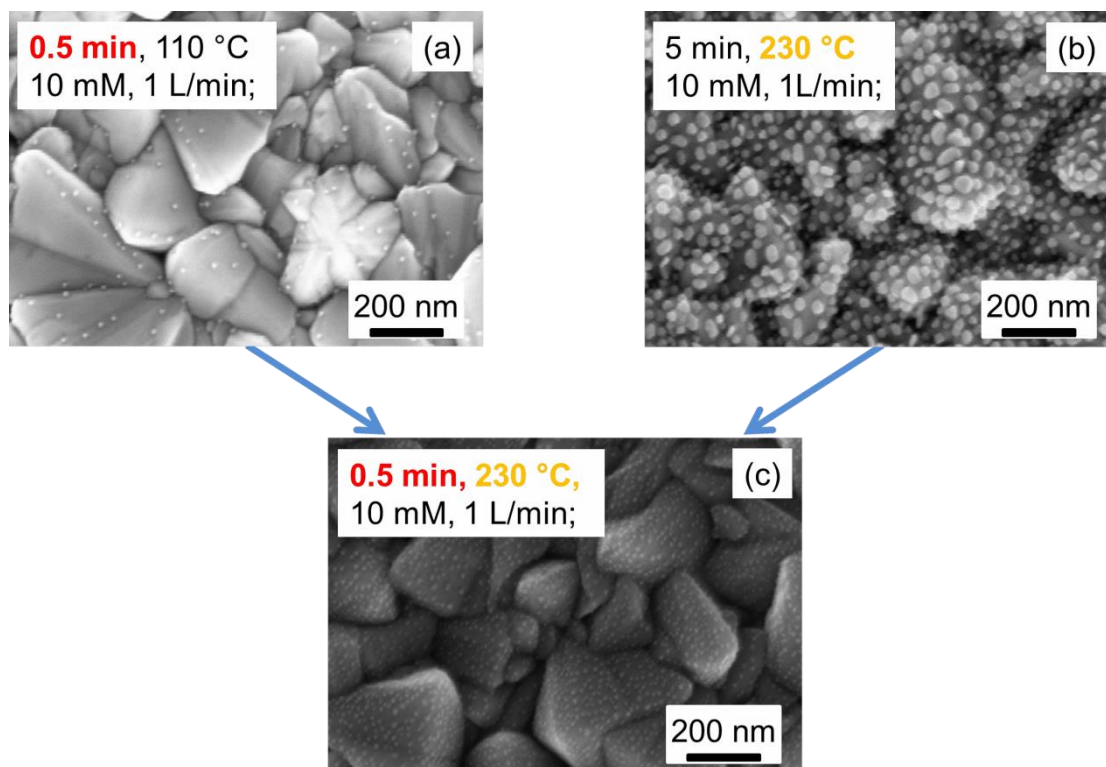


Figure 3.15: SEM images of deposited Ag NPs using a precursor solution with a concentration of 10 mM in ethanol and 1 L/min N_2 gas. Substrate temperature and deposition time were 110 °C and 0.5 min for (A), 230 °C and 5 min for (B), 230 °C and 0.5 min for (C), respectively.

Table 3.2: Average diameters and densities of Ag NPs calculated from SEM images shown in Figure 3.15. Deposition times of the Ag NPs were 0.5, 5 and 0.5 min for the samples in Figure 3.15a, Figure 3.15b and Figure 3.15c, respectively. Substrate temperatures for the three samples were 110, 230 and 230 °C, respectively. The concentration of precursor solution for Ag NPs deposition was 10 mM.

Samples	Diameter of Ag NPs (nm)	Density of Ag NPs (nm^{-2})
Figure 3.15a	11.4 ± 1.9	1.6×10^{-4}
Figure 3.15b	21.7 ± 6.3	1.3×10^{-3}
Figure 3.15c	9.9 ± 2.0	1.8×10^{-3}

Figure 3.15 gives a very striking example, in which SEM images of three Ag NPs samples obtained with different sets of temperature / time parameters are shown. The Ag NPs of Figure 3.15a was obtained after 0.5 min deposition time at 110 °C substrate temperature. The Ag NPs have small particle size and low density. After deposition for 5 min at 230 °C the Ag NPs exhibit bigger particles with higher density (Figure 3.15b). When we combine the deposition time of the first sample and the temperature of the second one, Ag NPs with roughly the size of one sample (Figure 3.15a) and the density of

the other (Figure 3.15b) were produced (Table 3.2). Details of the size and density of Ag NPs in Figure 3.15 are shown in Table 3.2. This demonstrates that particle size and density of Ag NPs can be controlled independently by this spray-CVD method.

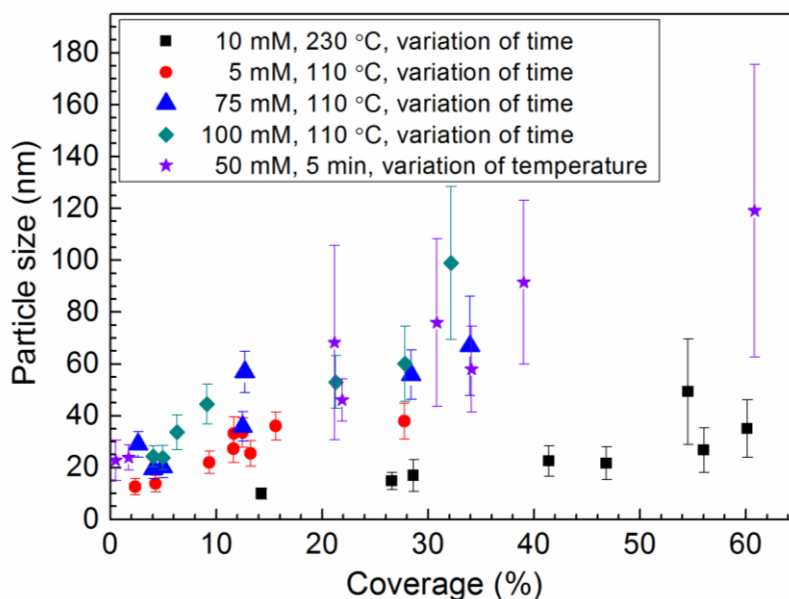


Figure 3.16: Plot of average size and coverage of Ag NPs obtained by spray-CVD method.

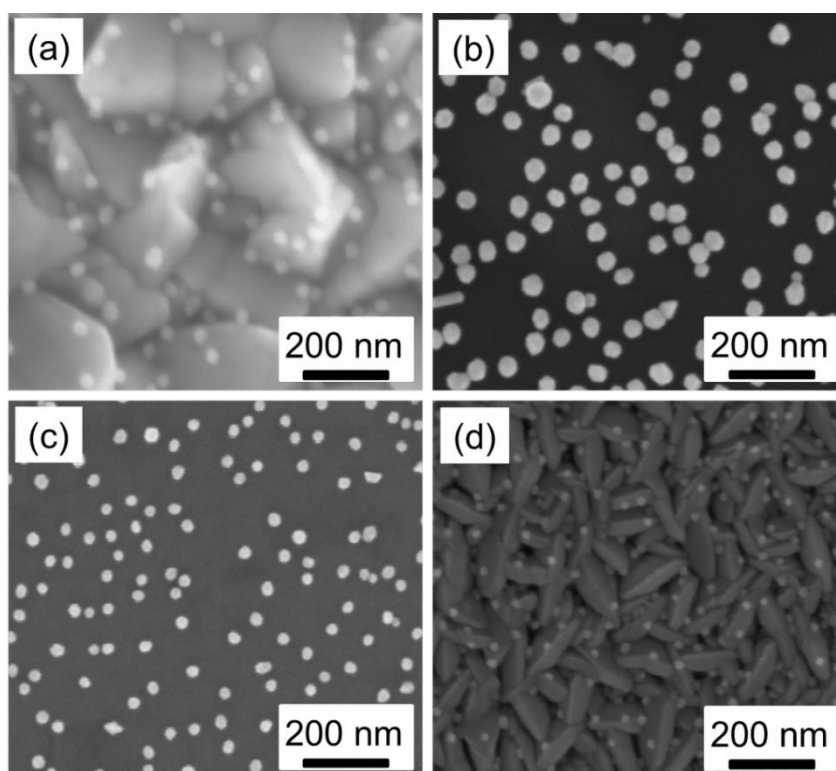


Figure 3.17: SEM images of deposited Ag NPs on different kind of substrates: (a) FTO, (b) c-Si, (c) ITO, (d) Mo. All the deposition parameters were kept the same as 10 mM precursor solution concentration, 1 L/min N_2 gas flow rate, 110 °C substrate temperature and 5 min deposition time.

Table 3.3: Average diameters and coverage of Ag NPs extracted from SEM images shown in Figure 3.17.

Samples	Diameter of Ag NPs (nm)	Coverage of Ag NPs (%)
Figure 3.17a_FTO	36.5 ± 5.7	9.3
Figure 3.17b_c-Si	62.3 ± 14.2	24.9
Figure 3.17c_ITO	32.7 ± 4.1	11.4
Figure 3.17d_Mo	18.1 ± 9.7	4.9

Figure 3.16 shows a summary plot of average size and coverage of all Ag NPs deposited in this work by spray-CVD method. Different symbols in the plot show different series of samples which means one parameter was varied while other parameters were constant. It's observed that average size of the achieved Ag NPs can be controlled between 5 nm and 120 nm while the coverage of the Ag NPs between 1% and 60%. This plot confirms again the independent control of size and density of the Ag NPs by spray-CVD method in a wide range.

The content shown above uses FTO coated glass substrate. But the spray-CVD method is not limited to this substrate material. It can be used to deposit Ag NPs on different kinds of substrates and materials. Figure 3.17 shows SEM images of the deposited Ag NPs on four kinds of substrate which are FTO, c-Si, ITO and Mo. All the deposition parameters were the same for these four samples. The concentration of precursor solution was 10 mM, substrate temperature was 110 °C, N₂ gas flow rate was 1 L/min and deposition time was 5 min.

Table 3.3 shows the average size and coverage of the Ag NPs from Figure 3.17. The average size and coverage are quite different for these four samples. This is due to the different surface structure and material of the different substrate. The formation and growth of the Ag NPs during the deposition process can be influenced strongly by the surface properties of the substrate. But the most important point is that the low temperature spray-CVD method can be used in different substrate which greatly expands the application field of it.

3.2.4 Mechanism of the deposition of Ag NPs

In addition to the control of size and density, the mechanism of the Ag NP deposition and growth processes are very important for understanding and further development of the method. In this part, the deposition mechanism is studied based on the results shown above as well as a special kind of Arrhenius plot and classic chemical experiments. A scheme of the deposition mechanism will summarize the results (Figure 3.19). For the growth mechanism of Ag NPs, the information extracted from the SEM images shown above and the deposited amount of Ag were mainly used for the investigation.

3.2.4.1 Deposition mechanism

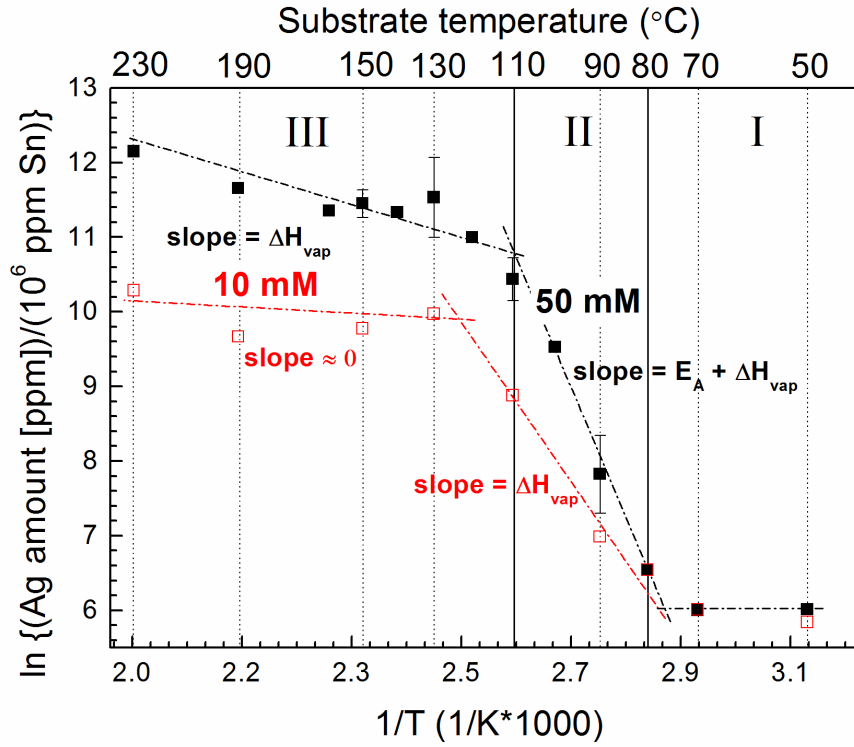


Figure 3.18: Arrhenius plot of two sample series which were prepared with 10 mM and 50 mM precursor solution, respectively. Deposition time was 5 min for all the samples. Ag masses are relative values based on the internal standard Sn.

The deposited amount of silver within five minutes gives a deposition rate which is proportional to the rate constant. Eq.3.6 was used for a kind of Arrhenius-plot, where δ is the deposition rate, E_A the activation energy, R the universal gas constant, A the pre-exponential constant and T the substrate temperature.

$$\ln \delta = -\frac{1}{T} \frac{E_A}{R} + \ln A \quad \text{Eq.3.6}$$

Plotting the logarithmized deposition rate over the reciprocal temperature leads to the special kind of Arrhenius plot shown in Figure 3.18 where the deposition rate bases on the Ag to Sn ratio but not on the absolute deposition rate. However, as the Sn amount is constant in the commercial FTO substrates it can be used for relative considerations. There the already discussed temperature series are used together with another one prepared with a 5 times higher precursor concentration of 50 mM resulting in a clearly higher deposition rate. Generally, in each series three sections can be distinguished. The first one is located in a temperature range from 50 to 80 °C, where the deposition rate of silver is very low and nearly constant. The second section ranges from 80 °C to 110 °C or 130 °C, respectively, where the deposition rate of Ag increases sharply with increase of substrate temperature. In the third section up to 230 °C, the slope is much smaller. The shape of the plots is typical for aerosol assisted chemical vapor deposition (AACVD) with incomplete evaporation in the beginning [114]. Only the horizontal part at extremely low temperatures is special and will be explained later in this section. However, it's hard to confirm the deposition mechanism by this plot alone. Therefore, classic experiments were carried out.

During the deposition of In_2S_3 from alcoholic $\text{In}(\text{acac})_3$ solution by ILGAR it was shown by mass spectrometry that ethanol forms complexes with $\text{In}(\text{acac})_3$ thereby enhancing the volatility dramatically [126]. Therefore, it's worth investigating whether ethanol is responsible also here for the extraordinarily low deposition temperature way below the literature value of $220\text{ }^\circ\text{C}$ [127]. Ethanol could have several benefits for the reaction. In addition to the improving of volatility by complex formation it could act also as a reducing agent for the silver precursor from Ag (I) to Ag (0). Ethanol would get oxidized to formaldehyde or acetic acid.

To detect the by-products during the deposition of Ag NPs, another set up was used to indicate a possible formation of acetic acid (pH experiments). A glass tube with middle part filled with $\text{Ag}(\text{hfacac})\text{PMe}_3$ powder was placed in a copper block. A wet pH test stripe (sensitivity range from pH 4.0 to pH 7.0) was placed into the end of the glass tube. During this experiment, the heaters were heated up to $150\text{ }^\circ\text{C}$. Both pure and ethanol saturated nitrogen gas was purged through the glass tube and bubble in the solution.

Independently, whether pure nitrogen was blown over the dry crystals or ethanol saturated nitrogen over crystals wetted with ethanol, upon heating to $150\text{ }^\circ\text{C}$ the powder turns brownish and the pH stripes indicated acid evolution. Therefore, it is concluded that in any case the $(\text{hfacac})\text{PMe}_3$ ligand acts as reduction agent forming acidic decomposition products, but no evidence of the participation of ethanol in the redox reaction was obtained.

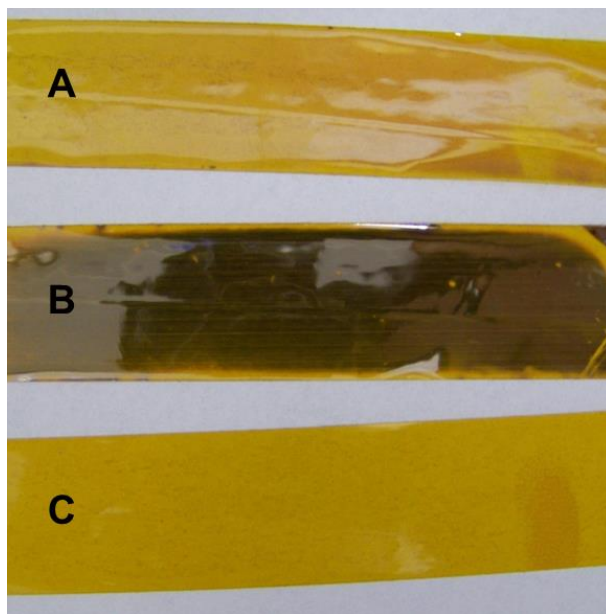


Figure 3.19 Kapton tape stripes after the decomposition experiment of $\text{Ag}(\text{hfacac})\text{PMe}_3$ powder. Figure 3.19a and Figure 3.19b show the tapes after experiment without and with ethanol, respectively. Figure 3.19c shows the untreated reference tape.

Two decomposition experiments were carried out to help understanding the mechanism in terms of the potential role of ethanol for enhancing volatility in addition to the pH experiment. In the decomposition experiments, the precursor material was placed on a clean FTO substrate located on the copper block of the standard set-up (shown in Figure 3.2) which was purged with nitrogen flow rate of 1 L/min . The copper block was fixed on the heater using a kapton tape and kept at $110\text{ }^\circ\text{C}$ for 30 min. In the first

experiment, the Ag precursor powder was put on the substrate before heating and dry nitrogen flow over the powder with flow rate of 1 L/min. In the second experiment, the same amount of Ag precursor was put on the substrate but a droplet of ethanol was dripped on the powder and an ethanol saturated nitrogen flow was used which was obtained by bubble the nitrogen through a washing bottle filled with ethanol. Other experiment parameters were kept constant. After each experiment, the kapton tape which was used to fix the copper block was removed and inspected.

For the first experiment, after pure N_2 flow for 30 min, the color of the precursor material changed to brown and most of it seemed to melt. But on the kapton tape nearly no change was observed. A significant difference was observed when ethanol saturated nitrogen was used (the second experiment). The melting and color change of the precursor material occurred much faster than with pure nitrogen. In parallel, some visible vapor over the precursor was generated. After 30 min the kapton tape was covered with a dark brownish and mirror-like layer, which is obviously silver. Figure 3.19 shows the tapes after the experiments. As a remark, the tapes didn't have direct contact with the precursor material. Thus, a new volatile compound, likely an alcoholic Ag hfacac complex, is formed in the presence of ethanol above the precursor powder at a temperature lower than its melting point of 140-142 °C. The formed Ag complex was transported by ethanol over a few centimeters through the gas phase to the kapton tape directly on the heater. There, the decomposition of Ag complex and the deposition of the Ag took place. The exact composition of the complex needs further investigation. However, the results give the strong evidence that at 110 °C the process follows a CVD mechanism [110].

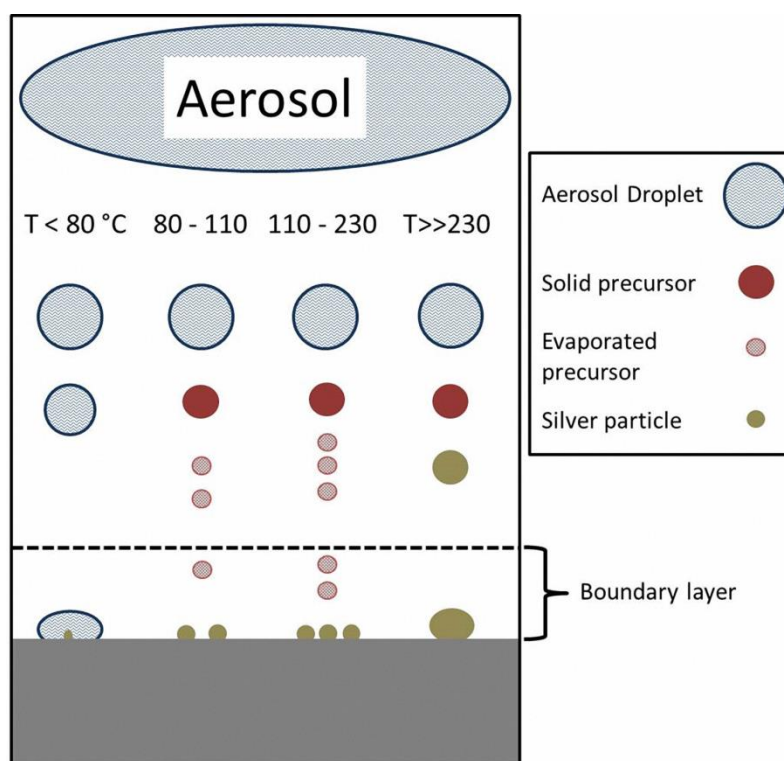


Figure 3.20: Schematic illustration of the deposition mechanisms with variation of substrate temperature.

Based on all the results shown above, the deposition mechanism was summarized in a scheme (Figure 3.20). Evident from the Arrhenius plot, (Figure 3.18) the mechanism is

influenced by the substrate temperature. In the first section below 80 °C, the temperature is not high enough to evaporate the ethanol of the aerosol completely during the short residence time. Only a few little droplets can land on the substrate. In this section, the deposition rate and the slope are both very low, since the precursor has not been evaporated. The mechanisms in this regime are the same for 10 mM and 50 mM series samples.

The second regime ranges from 80 °C to 110 °C for the 50 mM series samples, in which the solvent evaporates completely. Solid precursor particles arrive over the substrate and evaporate partly, while the rest remains solid (but with increasing temperature diminishing), does not adhere and is blown away by N₂ gas. The gaseous fraction got transported through the boundary layer, which separates the reaction zone over the substrate from the remaining reaction room, adsorb and decompose on the substrate to form Ag nuclei or on existing particles to be integrated in, respectively. With increasing temperature the deposition rate is accelerated due to increasing of both precursor vapor pressure and decomposition rate. Still the evaporated material transported through the boundary layer is sufficient enough for the surface reaction. Thus, here the deposition rate is kinetically controlled and the slope is the sum of evaporation enthalpy ΔH_{vap} and decomposition activation energy E_A . For the 10 mM series, the mechanism of the second regime (80 °C - 130 °C) is different. Due to the low precursor material concentration, mainly the feed rate limits the deposition rate. Therefore, the slope of the second regime reflects mainly the enthalpy of evaporation of the precursor material. Therefore, the slope is smaller than that of 50 mM series samples.

The change to a smaller slope at 110 °C for the 50 mM series marks the start of the third section. Here, the precursor material is still not completely evaporated, but the surface reaction rate is high enough to decompose all the gaseous precursor material arriving on the substrate surface. Hence, in this range the overall deposition rate is transport controlled and the slope of the plot is mainly determined by precursor evaporation enthalpy ΔH_{vap} . (The contribution of the diffusion coefficient can be neglected). [110, 114]

In general, it can be predicted that at even higher temperatures, the deposition rate will decrease due to the evaporation and decomposition of precursor material and formation of Ag NPs already above the boundary layer. Only a few of those Ag NPs can land on the substrate and are easily blown away.

3.2.4.2 Growth mechanism of Ag NPs

Despite the deposition mechanism, growth mechanism of the Ag NPs is crucial to understand the morphology and size of the achieved Ag NPs under different deposition parameters. From the deposition mechanism shown in section 3.2.4.1, the deposition rate of Ag NPs can be limited by the substrate temperature, feed-rate, surface reaction kinetics and transport of gaseous precursor material. Growth of the Ag NPs is also influenced by the deposition mechanism. According to the different limitations of deposition mechanism, three different temperature regimes can be divided. The growth mechanism will be discussed also based on these different temperature regimes.

Before the discussion on the growth mechanism of Ag NPs, the general growth modes of chemical vapor deposition should be mentioned [128]. Compared to the homogeneous growth of Ag NPs in colloid synthesis, heterogeneous reaction takes place in the CVD process which means not only the precursor material but also other considerations like wetting properties, surface defects and interdiffusion between substrate and deposited

material should be taken into account into the growth of particles or films. In general, during the CVD processes there are three possible growth modes of the crystals on surface (shown in Figure 3.21). Figure 3.21a shows the layer or Frank-van der Merwe mode in which the deposited material forms a layer directly during the CVD process. Figure 3.21b presents the layer plus island or Stranski-Krastanov mode in which the deposited material first forms a layer hence on top of the layer particles can be generated. Figure 3.21c displays the island or Volmer-Weber mode in which particles are produced directly on the surface. These three modes can be used as the basis for the explanation of the particles or films growth during the CVD processes.

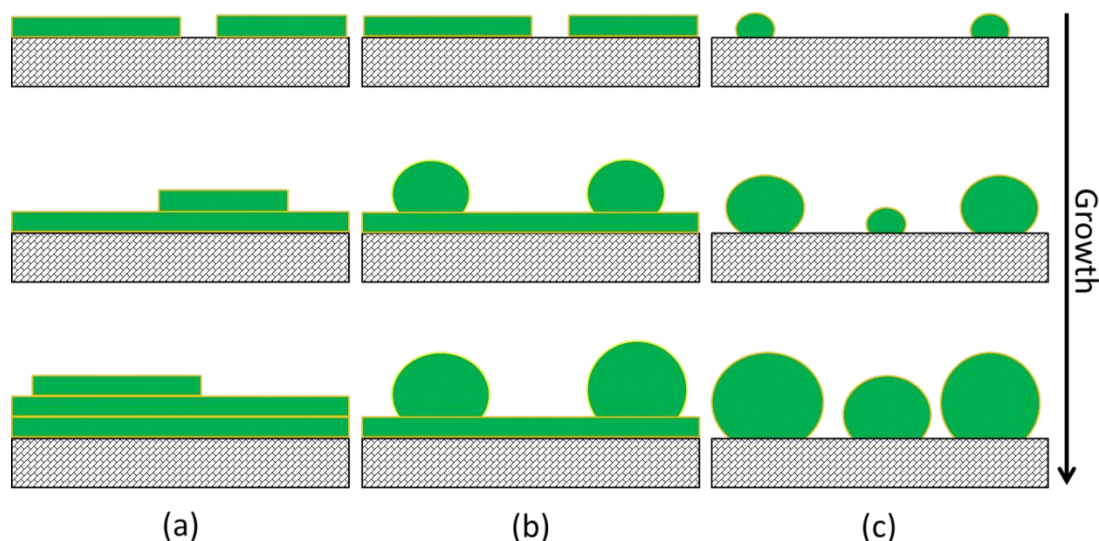


Figure 3.21: Schematic representation of the three chemical vapor deposition growth modes: (a) layer or Frank-van der Merwe mode, (b) layer plus island or Stranski-Krastanov mode, (c) island or Volmer-Weber mode. Adapted after Ref: [128].

From the results discussed above, growth of Ag NPs in spray-CVD process mainly followed the island or Volmer-Weber mode. However, the growth mechanism can change when the deposition mechanism changes.

In the very low temperature regime (below 80 °C), only a few droplets containing the precursor material land on the surface directly. There, the solvent evaporates and the precursor material decomposes to form nuclei and grow to Ag NPs. Since the landed droplets are too few, even after longer deposition time, number of the formed Ag NPs doesn't visibly increase.

In the second temperature regime (between 80 °C and around 110 °C), the deposition rate of Ag is limited by surface reaction kinetics and/or feed-rate. At the very beginning, due to the low substrate temperature, the vaporized precursor material transports to the surface of substrate and preferentially diffuses to the preferential adsorption and decomposition sites and decomposes there to form nuclei. These adsorption and decomposition sites need lowest energy for nucleation. On FTO substrate surface, the valleys and kinks of the FTO grains are these nucleation friendly positions, as nearly all the Ag NPs were generated at those places. With ongoing deposition time, the freshly arriving precursor material has two path ways to grow, one is to diffuse to the surface of the already

formed nuclei of Ag NPs and decompose there, the other is to find another nucleation friendly position and form new nuclei there. Since the substrate temperature is constant, those kinds of nucleation friendly positions are limited and there also Ostwald Ripening (OR) happens, density of the Ag NPs stays nearly constant but the size grows bigger and bigger.

In the third temperature regime (between 110 °C and 230 °C), the deposition rate of Ag is limited by transportation of the precursor material and/or feed-rate. At the very beginning, precursor material decomposes directly to form nuclei. With the time goes on, due to the high substrate temperature, the gaseous precursor material decomposes subsequently when it arrives on the surface of substrate, this leads to either formation of new nuclei or growth of the existing particles. Since the density of the Ag NPs is too high for the generation and growth of isolated Ag NPs, they can touch each other when they grow bigger. In addition, the OR and possible particle migration and subsequent coalescence (PMC) process let the density of Ag NPs decrease which can be seen from Figure 3.12b.

Despite of the growth models of Ag NPs discussed above, a few questions have to be clarified. In the following, two specific problems will be discussed to make the growth of Ag NPs clearer.

The complete absence of much smaller particles and the narrow size distribution point to a pronounced OR, though in addition PMC cannot be excluded. Preferentially very small particles undergo OR, losing smallest units or atoms which diffuse over the surface and attach to bigger ones. The remaining even smaller species shrink even faster and disappear completely. In contrast to PMC the growth is gradual and under a certain thermodynamic control leading to quite homogenous particle sizes. Thus, the energy of the complete system is improved. Many experimental and theoretical studies on OR of solid particles on substrates are reported. Sintering of immobilized nanoparticle catalysts for steam reforming and automotive exhaust conversion results in a loss of their activity by Ostwald ripening at 550 °C [129]. Sn clusters on Si(111) at 300 °C showed a pronounced trend to large interparticle distances during OR [130]) as the Ag NP films in this work. Such spatial ordering was explained as local ripening, a special case of OR comprising both, size and spatial distribution by self-similar evolution [131]. There the diffusion gradient is developed between two neighboring clusters resulting in the preferential elimination of near cluster pairs. It is expected that nuclei move much faster than particles and smaller particles faster than bigger ones. Particles “attract” coalescing nuclei from all directions. However, species close to another one have a reduced area of attraction; the smaller the distance, the more shielded and reduced is this area. Therefore, these particles grow more slowly and finally aggregate with a near neighbor.

For the higher temperature the particle size distribution is clearly wider (see standard deviation). Here, OR and PMC towards a relatively stable uniform size are partially outbalanced by the fast arrival of new material. This is confirmed by the different relative decreases in particle density from 0.5 min to 5 min which are 30% and 60% for 230 °C and 110 °C, respectively (shown in Figure 3.12ab). The situation for solid NPs films is more complex than for colloidal particles. The latter are surrounded by only one liquid medium and their size is controlled by crystalline properties as well as kinetic factors, such as the competitive reactions of particle growth and shielding by stabilizer molecules [132]. In contrast, for film particles also the interaction with the substrate (adsorption, wetting, lattice match etc.) plays an important role. Moreover, unlike for reactions in a vessel with limited educt, spray pyrolysis provides a continuous educt supply and is a complex action

involving evaporation of solvent and precursor, material transport to and from reaction site, adsorption and decomposition.

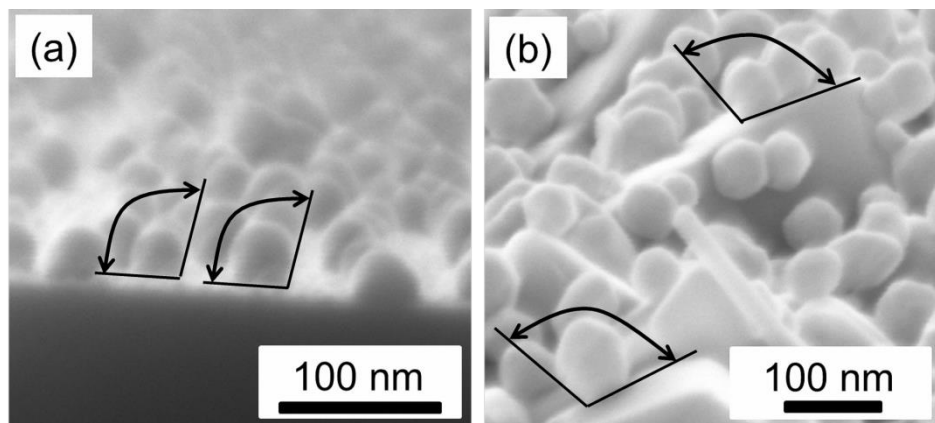


Figure 3.22: Cross section of the obtained Ag NPs on (a) c-Si substrate and on (b) FTO substrate. Deposition parameters for (a) were 5 min deposition time, 110 °C substrate temperature, 10 mM precursor solution concentration, 5 L/min N₂ flow rate and 25 mL precursor solution volume which for (b) were 5 min, 110 °C, 20 mL 100 mM precursor solution and 1 L/min N₂ flow rate.

What hinders the growth at an ongoing average particle size before all other species reach that? SEM cross-sections of a film with ~60 nm Ag NPs (shown in Figure 3.22) demonstrate a contact angle bigger than 90 ° indicating a repulsion from the FTO surface and a low free surface energy of the latter. Only in the first minutes the small species with high energy search a stabilization in substrate valleys, for the bigger, more stable particles the contact with the FTO is energetically not favored anymore and the bigger a particle, the larger its contact area resulting in a preferential formation of new species which grow in average to just that size. Thus, the system energy is minimized. But more material is continuously added and the equilibrium of the system is readjusted according to Le Chatelier's principle. In other words, there is interplay between precursor concentration, material feed, the amount of already deposited material and of temperature.

As bad wetting and high surface tension let compact Ag films disintegrate into particles at about 200 °C [133], this might reduce the driving force for coalescence also for our films at a certain stage. Moreover, then instead of forming a compact layer particles are created in a second level.

3.3 Summary

In this chapter, the development of a spray-CVD method for the deposition of Ag NPs is described. The deposition mechanism and the growth mechanism of Ag NPs in this spray-CVD process are presented in detail.

Using the spray-CVD method, size and density controlled Ag NPs can be produced at low temperatures with rather homogenous size distribution which can be used for further application in photocurrent enhancement of perovskite solar cells. This is done by adapting the spray-ILGAR setup and choosing a high volatility precursor material Ag(hfacac)PMe₃. The size and density of the Ag NPs are controlled by variation of different deposition parameters such as N₂ flow rate, concentration of precursor solution, deposition time and substrate temperature. The details are shown in the following:

- The lowest temperature for the production of Ag NPs can be 50 °C and at 80 °C already a very nice Ag NP film was obtained. Ag NPs with most of the sizes and densities could be achieved at around 110 °C. These temperatures are much lower than that of previous reported CVD methods which is a significant advantage for application in the thermal non stable materials.
- Varying the deposition parameters, size and density of Ag NPs can be controlled independently. The average size of the achieved Ag NPs can be controlled between 5 nm and 120 nm while the coverage of the Ag NPs between 1% and 60%. This is very helpful for the optical application which needs to tune the size and density of Ag NPs to get the desired optical properties.
- Deposition of Ag NPs by spray-CVD is not limited to certain substrate materials. It is proved that the method can be used not only in FTO substrate but also on several other substrates, such as ITO, Mo, c-Si and kapton tape. Hence, the application scope of the developed spray-CVD is broad.

Based on the systematical variation of deposition parameters and a few additional classic chemical experiments, the deposition mechanism of the spray-CVD process was investigated.

- It was found that a vapor phase formation takes place even at temperatures lower than the melting point of the precursor material. By simple experiments with the precursor powder a CVD mechanism involving the ethanol evidently explained the high volatility and low decomposition temperature of the precursor in the process.
- Three temperature sections are clearly distinguished by their slope in the Arrhenius plot. These are with increasing temperature for a high precursor concentration droplets landing regime (liquid-solid pyrolysis), kinetically controlled regime and transport controlled regime (both gas-solid pyrolysis), and for lower concentration droplets landing regime, feed rate limited regime (incomplete evaporation) and feed rate limited regime (complete evaporation), respectively. The respective determining energies such as evaporation enthalpy and activation energy are attributed to the particular Arrhenius slopes.

In general, the growth mechanism of Ag NPs follows the island or Volmer-Weber mode. Three growth mechanisms based on the deposition mechanism are described.

- In the very low temperature regime (below 80 °C), very few droplets can land on the substrate surface and decompose to form nuclei. With ongoing time, density of the formed Ag NPs keeps nearly constant.
- In the second temperature regime (between 80 °C and around 110 °C), surface reaction kinetics or feed-rate limit the deposition rate of Ag. Due to the low substrate temperature, the vapor phase precursor solution which is diffused to the substrate surface can only decompose at the adsorption and decomposition sites which need low energy for nucleation. These sites are named as nucleation friendly positions. Since decomposition on the already existing Ag NPs needs even lower energy than the nucleation, the arriving precursor material preferentially decompose on the existing Ag NPs leading to growth of Ag NPs. However, there are still new nuclei formed in nucleation friendly positions with ongoing time. But due to the OR and PMC processes, only big size Ag NPs can be achieved.
- In the third temperature regime (between 110 °C and 230 °C), precursor material transport and feed-rate limit the deposition rate of the Ag. Due to the high substrate

temperature, all gaseous precursor material decomposes when it arrives on the substrate surface. This leads to the high density of Ag NPs at beginning. With ongoing time, decompose to help growth of existing Ag NPs and decompose to form new nuclei happen in parallel, size distribution of Ag NPs becomes wider. Still the OR and PMC processes play a role, they cause the disappearance of the very small Ag NPs and merge growth of the Ag NPs which are very near to each other. This reduced the density of Ag NPs with increase of deposition time.

- The interplay between nucleation and growth by integration of fresh material or Ostwald Ripening are discussed with respect to narrow size distribution, absence of much smaller particles and quite homogenous distances to the next neighbors.

Chapter 4

Deposition of plasmonic silver nanoparticles on top of extremely-thin In_2S_3 layer

This chapter presents the deposition of silver nanoparticles (Ag NPs) on top of In_2S_3 layers. The In_2S_3 layers were deposited by spray-ILGAR method and details of the deposition of In_2S_3 layer are described in section 4.1. In section 4.2, the parameters of the deposition process of Ag NPs by spray-CVD are introduced, including the deposition time, substrate temperature, N_2 flow rate, etc. The influence of the deposition parameters, e.g., concentration of precursor solution and deposition time, on the surface morphology and coverage as well as on the phase transition of the precursor In_2S_3 layer is analyzed in section 4.3. In section 4.4, the mechanism of the deposition of Ag NPs on top of the In_2S_3 layer and phase transitions during the process are studied in detail based on the content in section 4.3. Ag NPs deposited on an In_2S_3 layer are intended to be applied in the investigation of their plasmonic effect on extremely thin absorber solar cells. A brief study of such effect is introduced in section 4.4.

4.1 Preparation of extremely-thin In_2S_3 layer by spray-ILGAR

In_2S_3 layer is a promising candidate for application in photovoltaics because of its photosensitivity, stability and relatively wide band gap [134]. It has been widely used as an alternative buffer layer to replace CdS in CIGS based solar cells [135-138]. In comparison to CdS, In_2S_3 has the following advantages: (1) non-toxic, (2) higher transmission in the blue wavelength region and (3) can be prepared by different methods, most of which are suitable for in-line processing [139]. Methods used for In_2S_3 deposition are atomic layer deposition (ALD) [140], sputtering [141], physical vapor deposition (PVD) [142], metal organic chemical vapor deposition (MOCVD) [143], spray pyrolysis [135] and spray ion layer gas reaction (spray-ILGAR) [126, 139]. Among these deposition methods, the spray-ILGAR technique has high deposition rates, high layer quality and good layer homogeneity [117]. In_2S_3 layer deposited by spray-ILGAR can also be used as precursor layers for the absorber of extremely thin absorber solar cell [6, 40].

The spray-ILGAR method, which is used in this part, was modified from the ILGAR technique. Originally, a substrate was dipped into the metal precursor solution to integrate the precursor material on the substrate first. Secondly, the substrate was taken out from the

solution and dried by N_2 flow, leaving a precursor material film on the substrate. Thirdly, the remaining precursor material was sulfurized or hydrolyzed by H_2S gas or wet ammonia, respectively. As the precursor material was integrated on the substrate by dipping process, this ILGAR technique was named as “dip-ILGAR”, details of the dip-ILGAR process can be found elsewhere [144-146]. The dip-ILGAR technique had been successfully used in production of ZnO and ZnS buffer layers [147, 148]. However, it's very hard to integrate the dip-ILGAR into an in-line process and the deposition rate of each cycle is limited. Thus, the spray version of ILGAR was developed and optimized, and then established as the standard spray-ILGAR process which is used in this work. The schematic sketch of the spray-ILGAR set up is shown in Figure 4.1(a). It has to be mentioned that Figure 4.1(a) only shows the lab-scale set up. The spray-ILGAR can be also up-scaled to perform on in-line process [117, 149]. The spray-ILGAR technique has been successfully used in the deposition of various kinds of materials, for example In_2S_3 , Sb_2S_3 , ZnS, MnS, $CuInS_2$ and so on [117, 126, 150, 151]. The spray pyrolysis process based on the spray-ILGAR technique and set up can be used without sulfurization step for production of many materials, such as ZnO, Al_2O_3 , VO_2 , TiO_2 , Ag NPs, Au NPs, and Cu NPs [17, 75, 117, 152].

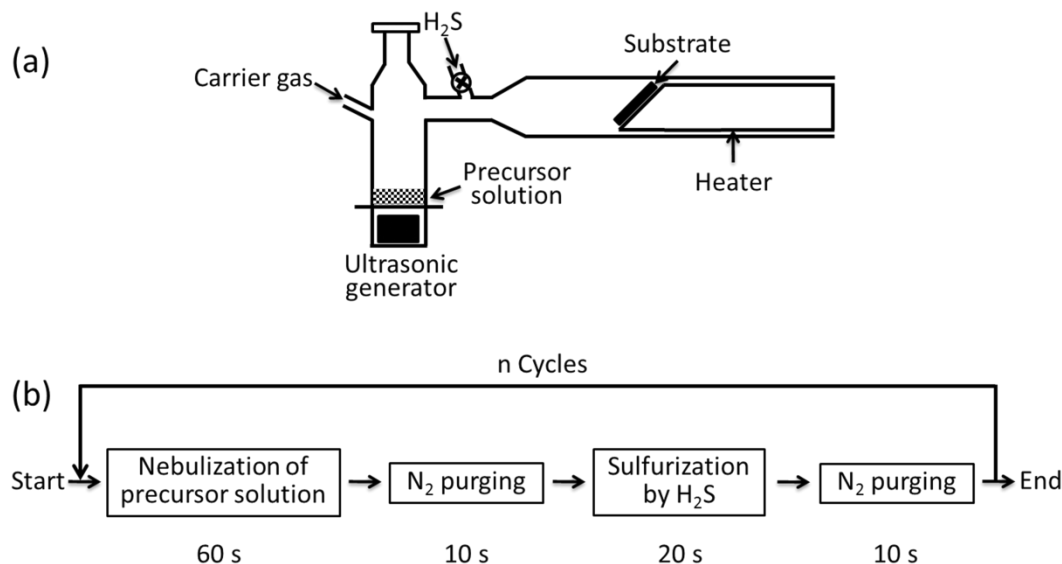


Figure 4.1: (a) Schematic sketch of the lab-scale spray-ILGAR set up; (b) Schematic diagram of spray-ILGAR process.

In the spray-ILGAR set up a glass vessel is used for containing the precursor solution. The glass vessel is connected to an ultrasonic generator which is used for nebulizing the precursor solution in the mist. Average size of the droplets of the precursor solution in the mist is around $2\ \mu m$ when EtOH is used as solvent. The glass vessel contains two gas inlets, one is for N_2 carrier gas and the other one is for H_2S . Near the inlet for H_2S , the glass vessel has an outlet which is connected to a horizontal glass tube. A steel heater is inside the glass tube and a substrate holder is connected with the heater. The substrate can be heated up to $500\ ^\circ C$. The substrate holder is designed to have 45° angle, this enables the homogeneous flow of the precursor material in the mist to the surface of substrate. The N_2 carrier gas is used for carrying the mist or H_2S to the surface of the heated substrate. The H_2S is used for sulfurizing the layer generated by decomposing the precursor material to form metal sulfide layer.

Table 4.1: Experimental parameters applied for the deposition of In_2S_3 layers by spray-ILGAR process

Flow rate of N_2 carrier gas	5 L/min
Flow rate of H_2S gas	1 L/min
Precursor material	$\text{In}(\text{acac})_3$
Solvent	EtOH
Cocentration of precursor solution	25 mM
Substrate temperature	225 °C
Cycles repeated	7, 14

The spray-ILGAR is a sequential and cyclic process. In a typical spray-ILGAR deposition process, each cycle can be divided into 4 steps. Figure 4.1(b) shows the schematic diagram of the spray-ILGAR process. In the first step, the precursor solution is nebulized by the ultrasonic generator to form an aerosol which is carried by the N_2 carrier gas to the surface of heated substrate. The substrate lies on the substrate holder. The precursor material contained in the aerosol will decompose on the surface of the substrate and form an $\text{In}(\text{OH},\text{O})$ layer. In the second step, the nebulization is stopped and the N_2 gas continues purging to remove the entire aerosol from the glass vessel and glass tube. In the third step, H_2S is introduced from the inlet of the glass vessel and carried by the N_2 gas to the surface of the substrate. The $\text{In}(\text{OH},\text{O})$ layer will be sulfurized by the H_2S gas to form the desired metal sulfide layer. The H_2S will be switched off at the end of this step. In the fourth step, the N_2 gas purges to remove the H_2S gas left in the entire set up. These four steps will be repeated until the desired thickness is obtained. The lasted time for each step used in this work is 60 s, 10 s, 20 s and 10 s, respectively. Other parameters applied for the spray-ILGAR deposition in this work are listed in Table 4.1.

In_2S_3 layer thickness deposited per cycle during the spray-ILGAR process is an important factor, because deposition rate should be efficient for both lab and industrial application. The thickness deposited per cycle is related to the deposition rate. The deposition rate of the spray-ILGAR process can be influenced by concentration of precursor solution, substrate temperature, gas flow rate. Details of the deposition rate had been studied by N.A. Allsop [153]. From Allsop's work, substrate temperatures have influence on the thickness of In_2S_3 layer which was deposited per cycle. It's observed that at around 100 °C nearly no In_2S_3 can be deposited, and with the increase of the temperature to 300 °C, the thickness deposited per cycle increases as well. This is due to the increase of reaction rate with improvement of temperature.

By applying the experimental parameters in Table 4.1, two In_2S_3 layers with different thicknesses were obtained. The cycles applied were 7 cycles and 14 cycles, SEM images of which are shown in Figure 4.2 (a) and Figure 4.2 (b), respectively. It's observed that both In_2S_3 layers are dense and continuous, but with slight roughness. By calculating the thickness in different positions, the obtained thicknesses of 7 cycles and 14 cycles sample

are 44 ± 6 nm and 85 ± 11 nm, respectively. The relation between obtained thickness and deposition cycles fit very well with the previous work [153]. The obtained In_2S_3 layers with different thicknesses will be used in the following investigation. For different investigation methods, different kinds of substrates were applied to deposit In_2S_3 layers. The substrates used in this section were c-Si substrate (SEM, EDX, LA-ICP-MS), glass substrate (XRD, UV-Vis), Mo/glass substrate (SEM, SPV).

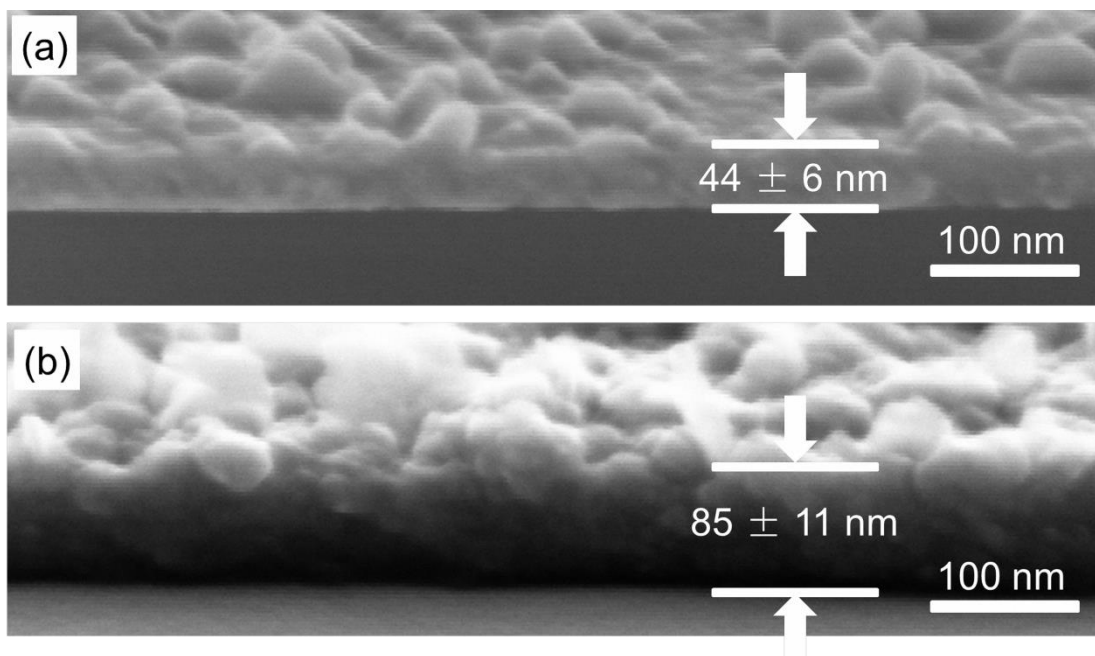


Figure 4.2: SEM images of In_2S_3 layer deposited by spray-ILGAR for (a) 7 cycles and (b) 14 cycles. Other experimental parameters are the same as in the Table 4.1

4.2 Deposition of Ag NPs on top of extremely-thin In_2S_3 layers by spray-CVD

In this section, silver nanoparticles (Ag NPs) are deposited on In_2S_3 layers which were deposited by the spray-ILGAR on different substrates. The spray-ILGAR set up is applied for the deposition of Ag NPs. Precursor for the deposition was Trimethylphosphine (hexafluoroacetylacetonato) silver ($\text{Ag}(\text{hfacac})\text{PMe}_3$) and the solvent for the precursor was Ethanol (EtOH). As the details of the deposition of Ag NPs have been discussed in Chapter 3, we will only describe the parameters used here for the deposition of Ag NPs on top of In_2S_3 layer.

Ag NPs were deposited on top of In_2S_3 layer by the spray-CVD method. Before the deposition process, 20 mL 10 mM alcoholic solution of $\text{Ag}(\text{hfacac})\text{PMe}_3$ was added into the glass vessel, In_2S_3 layer on different substrates were heated to 200°C , N_2 flow rate was set to 5 L/min. During the process, the alcoholic solution was nebulized to form dense mist by the ultrasonic generator at the frequency of 1.6 MHz for 2 min. The formed dense mist was carried by the N_2 gas to the surface of the In_2S_3 layer. The Ag precursor was evaporated from the mist and decomposed at the surface of In_2S_3 layer and form Ag NPs.

The deposition parameters for the deposition of Ag NPs in this chapter are shown in Table 4.2.

Table 4.2: Process parameters of depositing Ag NPs on top of In_2S_3 layers.

Carrier gas	5 L/min N_2
Precursor material	$\text{Ag}(\text{hfacac})\text{PMe}_3$
Solvent	EtOH
Concentration of precursor solution	10 mM
Substrate temperature	200 $^\circ\text{C}$
Deposition time	2 min

It has been described in chapter 3 that the precursor solution and deposition time are important factors to obtain different sizes of Ag NPs on FTO substrate. In this case, these two parameters were also varied to deposit Ag NPs on top of In_2S_3 to study their influence on the deposition process. The concentration of precursor solution applied were 5 mM, 10 mM and 20 mM (shown in section 4.3.1) while the deposition time used were 0.5 min, 1 min, 2 min, 4 min, 8 min, 16 min and 32 min (shown in section 4.3.2).

After the Ag deposition on In_2S_3 layers on different kinds of substrates, properties of morphology and silver to indium ratio of $\text{Ag}/\text{In}_2\text{S}_3/\text{c-Si}$ were characterized by scanning electron microscopy (SEM), energy-dispersive X-ray emission (EDX) and laser ablation inductively coupled plasma mass spectrometry (LA-ICP-MS), the $\text{Ag}/\text{In}_2\text{S}_3/\text{Glass}$ layers' crystalline and optical properties were studied by X-ray diffraction (XRD) and UV-Vis spectroscopy, the surface morphology and electronic properties of Ag NPs/ $\text{In}_2\text{S}_3/\text{Mo}/\text{Glass}$ were investigated by SEM and modulated surface photovoltage (SPV) spectroscopy.

4.3 Influence of the process parameter on the deposition of Ag NPs on top of In_2S_3 layers

Variation of the process parameters can directly influence the deposition mechanism and therefore influence the size and density of Ag NPs. This has been confirmed in the work dealing with deposition of Ag NPs on top of FTO substrate (Chapter 3). In the process of the deposition of Ag NPs on top of In_2S_3 layer, systematic variation of the parameters is helpful to (1) understanding the influence of parameters on the formation of Ag NPs which can be used for further understanding of the deposition mechanism of Ag NPs on In_2S_3 layer; (2) obtain different sizes and densities of Ag NPs on In_2S_3 layer which can be used for further study of the plasmonic effect of Ag NPs on In_2S_3 based extremely thin absorber solar cell.

The In_2S_3 layer deposited by the spray-ILGAR process under the condition shown in Table 4.1 is set as reference sample. To investigate the influence of concentration of precursor solution, deposition of Ag NPs followed the parameters in Table 4.2, the solution concentration was set as 5 mM, 10 mM and 20 mM, other parameters are constant. The reference sample was kept as pure In_2S_3 layer. Results will be shown in Section 4.3.1.

Similarly, the deposition time was varied from 0.5 min to 32 min to study the influence of deposition time in detail. This will be shown in Section 4.3.2.

4.3.1 Concentration of precursor solution

Figure 4.3 shows the top view SEM images of the reference sample in Figure 4.3a (pure In_2S_3 without Ag NPs deposition process), 5 mM sample in Figure 4.3b (In_2S_3 with Ag NPs deposition process by using 5mM $\text{Ag}(\text{hfacac})\text{PMe}_3$ solution), 10 mM sample in Figure 4.3c (In_2S_3 with Ag NPs deposition process by using 10 mM $\text{Ag}(\text{hfacac})\text{PMe}_3$ solution) and 20 mM sample in Figure 4.3d (In_2S_3 with Ag NPs deposition process by using 20mM $\text{Ag}(\text{hfacac})\text{PMe}_3$ solution). Deposition time was 2 min for the three samples shown in Figure 4.3b-d. For the reference In_2S_3 layer sample, clear roughness could be found from the image, the sizes of the grains of In_2S_3 were in the reange of 20 – 70 nm. With deposition of 5 mM alcoholic $\text{Ag}(\text{hfacac})\text{PMe}_3$ solution, the roughness of the layer was clearly reduced, apart from this there was nearly no other effects observed from the image. From Figure 4.3(c), few white dots with bright contrast were obtained on top of In_2S_3 layer, their diameters were in the order of 10 nm. With deposition of 20 mM Ag precursor solution, bigger particles with sizes varying from 10 to 200 nm with bright contrast were produced. The observed images are very differnent from the former introduced phenomenon in chapter 3, i.e., even with 5 mM $\text{Ag}(\text{hfacac})\text{PMe}_3$ solution Ag NPs were obtained within 2 min on FTO substrate, which can be because of the different deposition mechanism between deposition of Ag NPs on FTO substrate and deposition of Ag NPs on In_2S_3 layer.

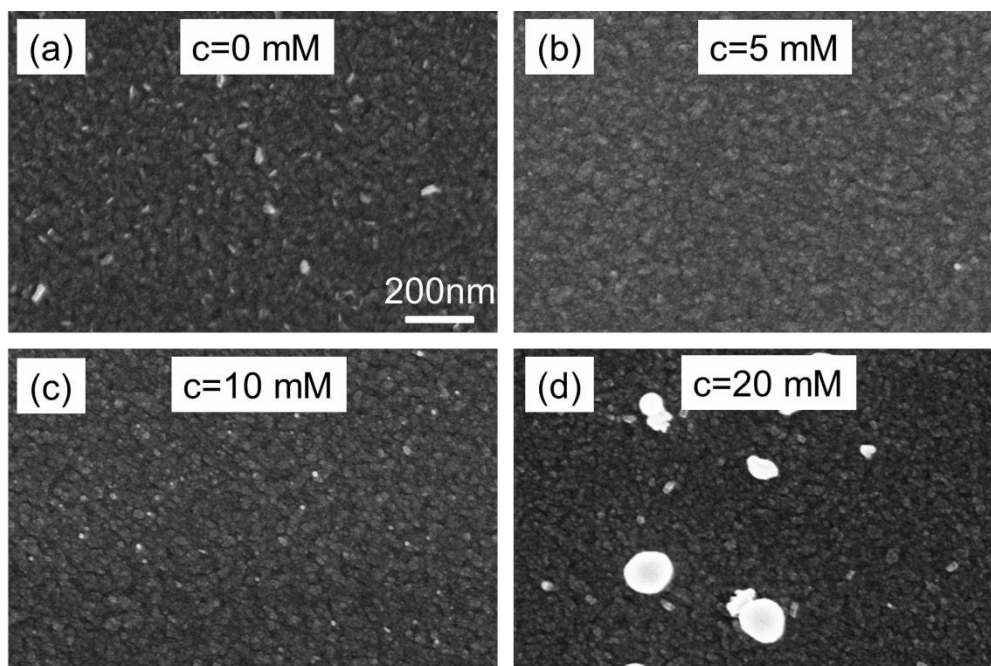


Figure 4.3 Top view SEM images of (a) pure In_2S_3 layer and In_2S_3 layer with deposition of Ag NPs by (b) 5 mM, (c) 10 mM and (d) 20 mM precursor solution concentration for 2 min.

To investigate the influence of Ag deposition on the electronic properties of In_2S_3 layers, SPV measurements were carried on. The SPV amplitudes of $\text{In}_2\text{S}_3/\text{Mo}/\text{Glass}$ layers before and after spray-CVD deposition of 5 mM, 10 mM and 20 mM $\text{Ag}(\text{hfacac})\text{PMe}_3$ solution are shown in Figure 4.4. Photon flux spectrum is also included in the figure. After

deposition of 5 mM precursor solution, the SPV amplitude increased from 0.43 mV to 1.35 mV. However, when the concentration of precursor solution increased to 10 mM and 20 mM, the SPV amplitudes started to drop (compare to the 5 mM sample) to 0.51 mV and 0.09 mV. It has to be mentioned that for all three samples with deposition of Ag precursor solution, the SPV amplitudes shifted to lower photon energies compare to the bare In_2S_3 sample. This indicates the possible electronic properties of the layers changed during the deposition of Ag.

Normalized SPV amplitudes of the samples are shown in Figure 4.5 for a better understanding on the influence of Ag deposition. From this figure, the onset energy of SPV amplitude is introduced. The onset energy of the SPV signal (E_{abs}) is consistent with the mobility gap. The intensity of SPV signal increases strongly from the mobility gap to bigger photon energies. The E_{abs} values were determined by extrapolating the increasing edge (at smaller photon energy side) of the normalized SPV amplitude to the baseline of y axis ($y = 0$ mV), the value of photon energy at the intersection point is E_{abs} (shown in Figure 4.5). The values of E_{abs} were 1.9 eV, 1.72 eV, 1.70 eV and 1.53 eV for the bare In_2S_3 sample, 5 mM sample, 10 mM sample and 20 mM sample, respectively. The onset energies of SPV amplitude shifted to lower photon energies with increase of the concentration of precursor solution. The increase of the concentration of precursor solution leads to the improvement of deposited amount of Ag and the shift of E_{abs} concomitants with the shift of band gap. Therefore, with the increase of deposited amount of Ag, the band gap of the In_2S_3 layers shifted to narrower ones. It has to be mentioned that the SPV signals in the region below the onset energy originated from participation of the defect states below the band gap in the charge separation. Shifting of the E_{abs} values may referred to the difference of electronic properties of the layer, this has been reported [154]. However, it's hard to determine the causes of the change of electronic properties by only the SPV measurement. Thus, further measurements on the same samples and different conditions for the deposition of Ag should be done to understand the effect of deposition Ag on top of In_2S_3 layers.

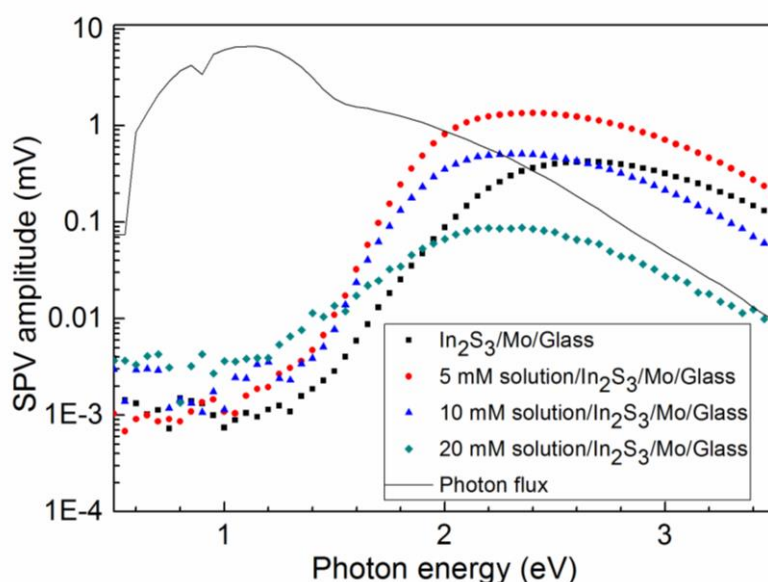


Figure 4.4: SPV amplitudes for $\text{In}_2\text{S}_3/\text{Mo}/\text{Glass}$ layers before (squares) and after 5 mM (circles), 10 mM (triangles), 20 mM (diamonds) $\text{Ag}(\text{hfacac})\text{PMe}_3$ solution deposition for 2 min.

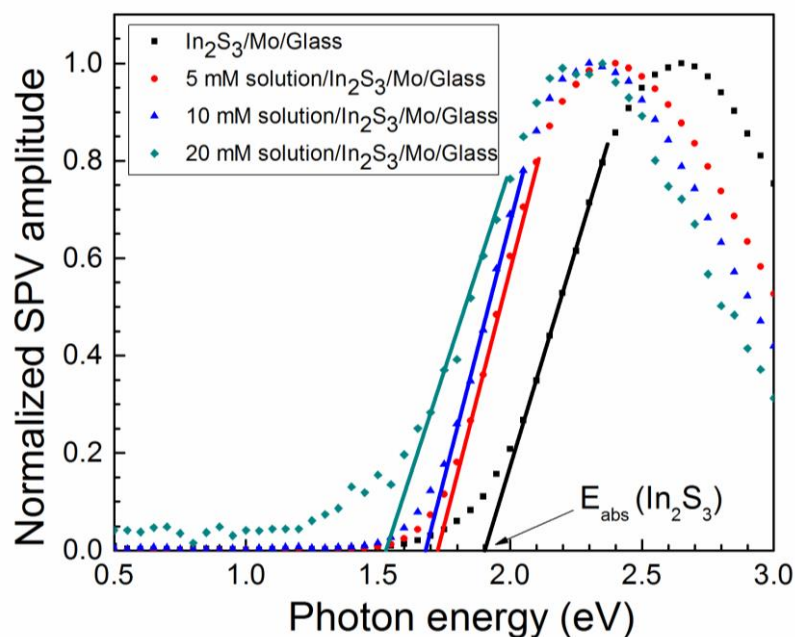


Figure 4.5: Normalized SPV amplitudes for In₂S₃/Mo/Glass layers before (squares) and after 5 mM (circles), 10 mM (triangles), 20 mM (diamonds) Ag(hfacac)PMe₃ solution deposition for 2 min.

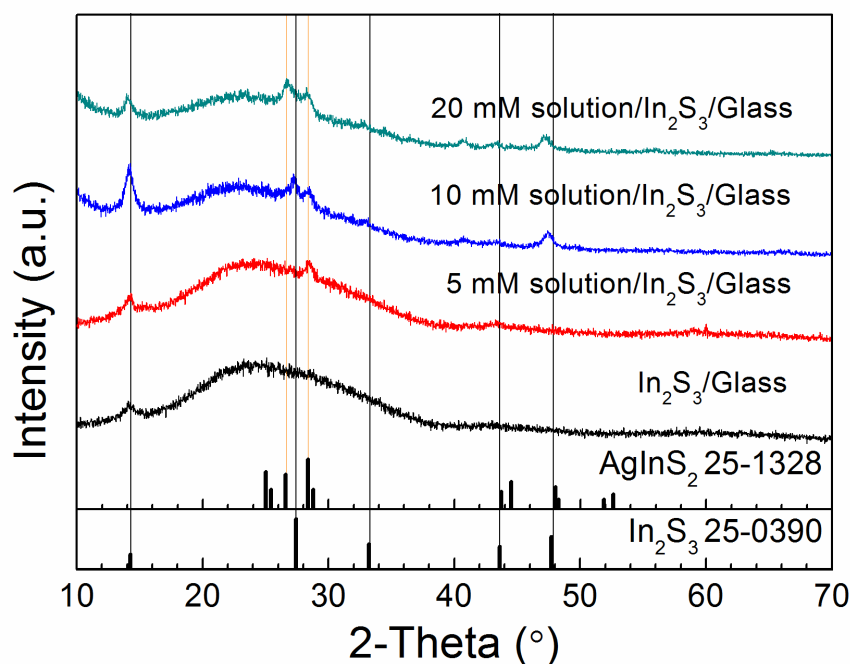


Figure 4.6: X-ray diffraction spectra of the In₂S₃/Glass layers before and after 5 mM, 10 mM, 20 mM Ag(hfacac)PMe₃ solution deposition for 2 min. Characteristic peaks of AgInS₂ and β -In₂S₃ from JCPDS File 25-1328 and 25-0390 are also shown.

XRD patterns of In₂S₃ layers on glass substrates before and after deposition of 5 mM, 10 mM, 20 mM Ag(hfacac)PMe₃ solution for 2 min are shown in Figure 4.6. Characteristic

peaks of β - In_2S_3 (JCPDS File No. 25-0390) and orthorhombic AgInS_2 (JCPDS File No. 25-1328) are also shown in the figure. The diffraction peak at $2\theta = 14.26^\circ$ was assigned to β - In_2S_3 . This peak could be observed for all the four samples. But for the 20 mM sample, the peak shifted slightly to smaller 2θ angles. For the pure In_2S_3 layer, no other peaks could be detected, probably because the layer thickness was too small for the detection of all the peaks by XRD. With deposition of Ag precursor solution, characteristic peaks for the orthorhombic AgInS_2 are observed. This indicates a chemical reaction between Ag and In_2S_3 during the deposition of Ag precursor solution. Characteristic peaks of β - In_2S_3 can still be detected which means the In_2S_3 layer didn't react completely during the 2 min deposition process. Thus, longer deposition time can be applied to understand further reactions during the deposition of Ag precursor solution on In_2S_3 layer. This part of work will be shown in Section 4.3.2.

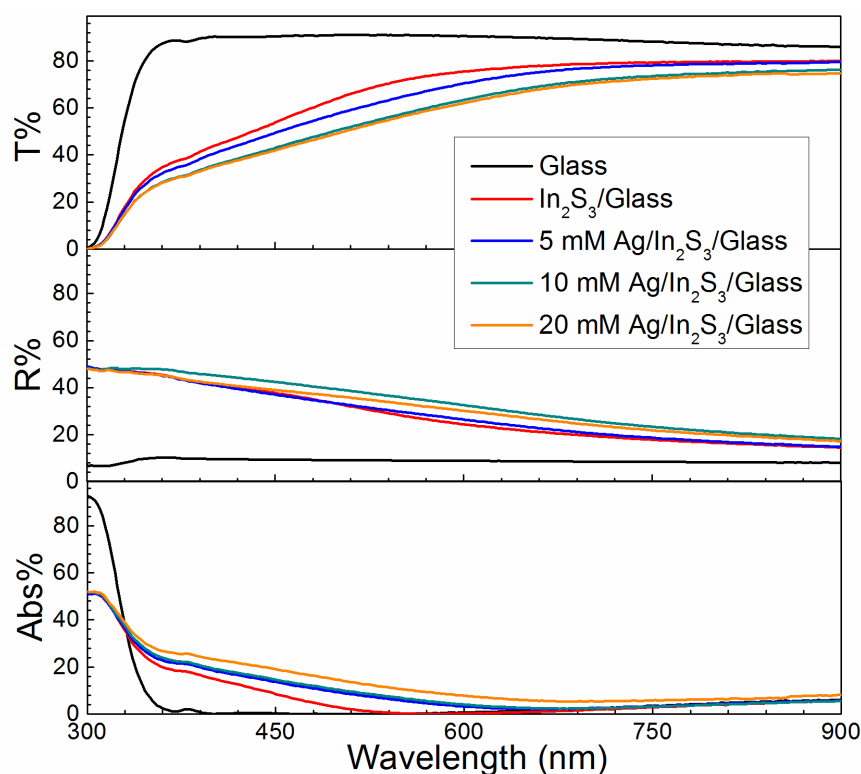


Figure 4.7: Transmission, reflection and absorption spectra for the In_2S_3 /Glass layers before and after deposition of 5 mM, 10 mM, 20 mM Ag(hfacac)PMe_3 solution for 2 min.

Optical properties of the In_2S_3 /Glass layers before and after deposition of 5 mM, 10 mM and 20 mM Ag(hfacac)PMe_3 solution for 2 min were investigated. Figure 4.7 shows the transmission, reflection and absorption spectra of the samples. It is observed that transmission of the 5 mM sample is less than the pure In_2S_3 sample nearly in the whole wavelength range from 300 nm to 900 nm. With increase of the concentration of precursor solution used in deposition, the transmission of the obtained layers further decreased. When we have a look at the reflection and absorption spectra, we can find that the decrease of transmission of the layers is results from the increase of reflection and absorption. Hence we can conclude that the deposition of Ag(hfacac)PMe_3 solution enhanced the absorption and reflection of the resulting layer, this leading to the decrease of the transmission.

It is observed from the previous characterization methods (SEM, XRD, SPV) that during the Ag deposition process white dots on the In_2S_3 layer surface and new phases were generated. This leads to the change of the electronic and optical properties of the In_2S_3 layers. Although the concentration of precursor solution was varied during the deposition process which may lead to the variation of deposition amount of Ag, 2 min deposition time is too short for the complete reaction and a maximum change of the layers' properties. Thus, it's hard to understand the mechanism and deposition process very well by only variation of the concentration of precursor solution. Thus, variation of deposition time is necessary to study the deposition process.

4.3.2 Deposition time

In this set of experiments, the deposition time of silver was varied from 0.5 min to 32 min while other deposition parameters were kept constant (as shown in Table 4.2).

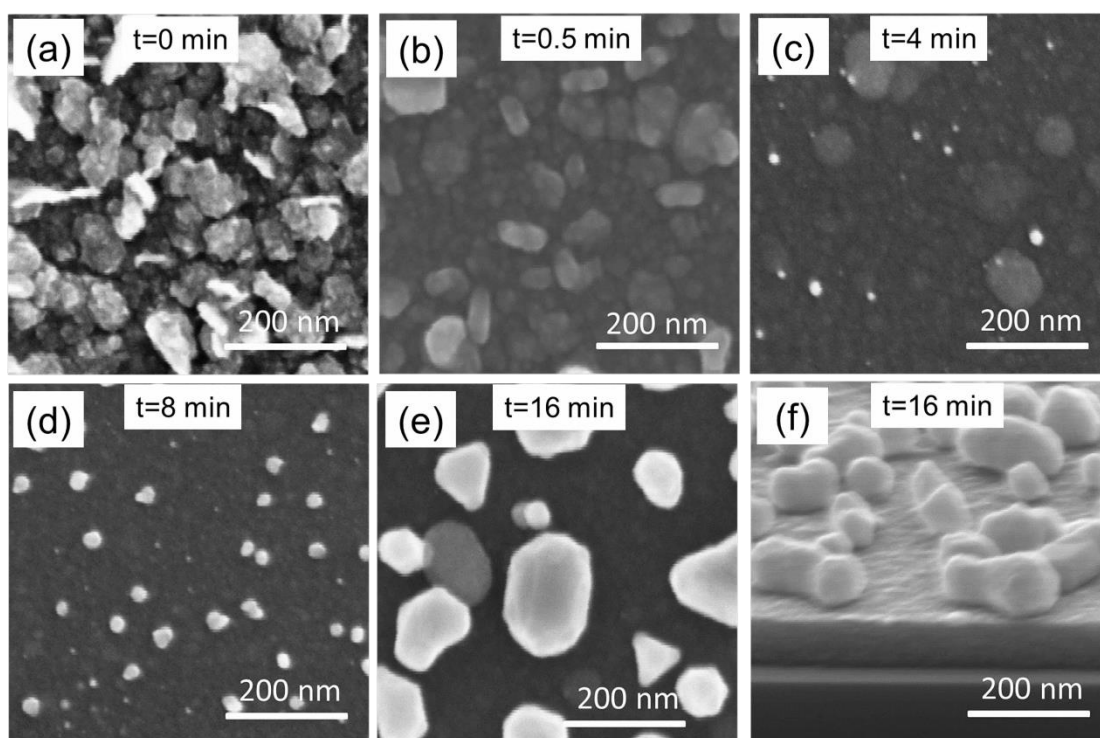


Figure 4.8: Top (a–e) and cross section (f, tilt angle 30 °) view SEM images of In_2S_3 precursor layers on c-Si substrates after deposition of Ag from an $\text{Ag}(\text{hfacac})\text{PMe}_3$ source for deposition times of 0 min (a), 0.5 min (b), 4 min (c), 8 min (d) and 16 min (e and f).

Figure 4.8 shows SEM images of the sample surfaces before (a) and after deposition of silver (b–f) for different times. Figure 4.8(a) shows a top view of an In_2S_3 layer deposited on c-Si. The In_2S_3 layer is comprised by agglomerates, sizes of which are around 50-100 nm. Due to this the layers is relatively rough. After the deposition of silver for 0.5 min the layer is more homogeneous (Figure 4.8b). Moreover, the very small grains in the original In_2S_3 layer (Figure 4.8a) nearly cannot be distinguished.

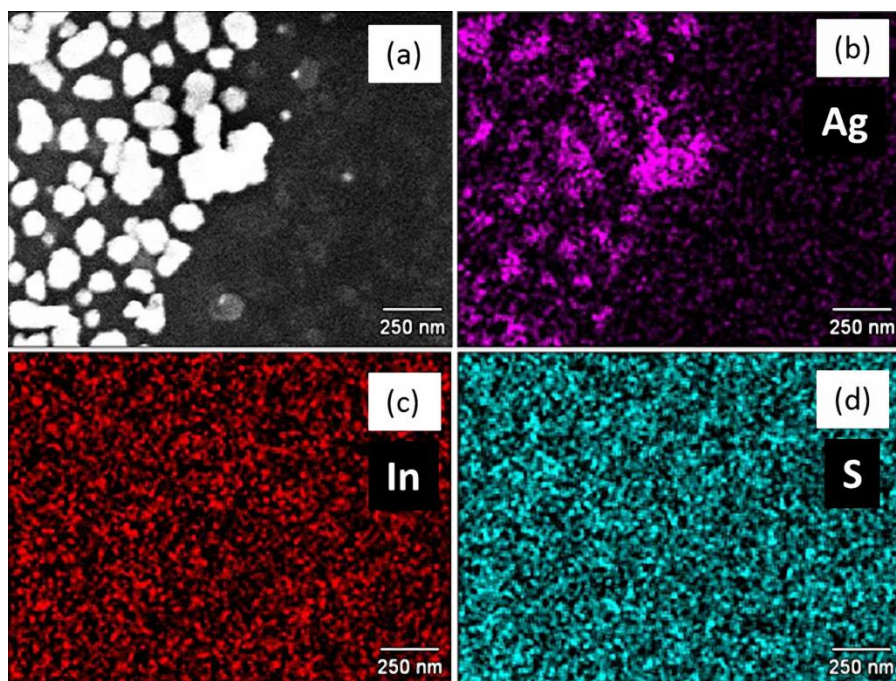


Figure 4.9: Top view (a) and maps of Ag (b), In (c) and S (d) for the In₂S₃/c-Si sample after deposition of Ag for 16 min [17].

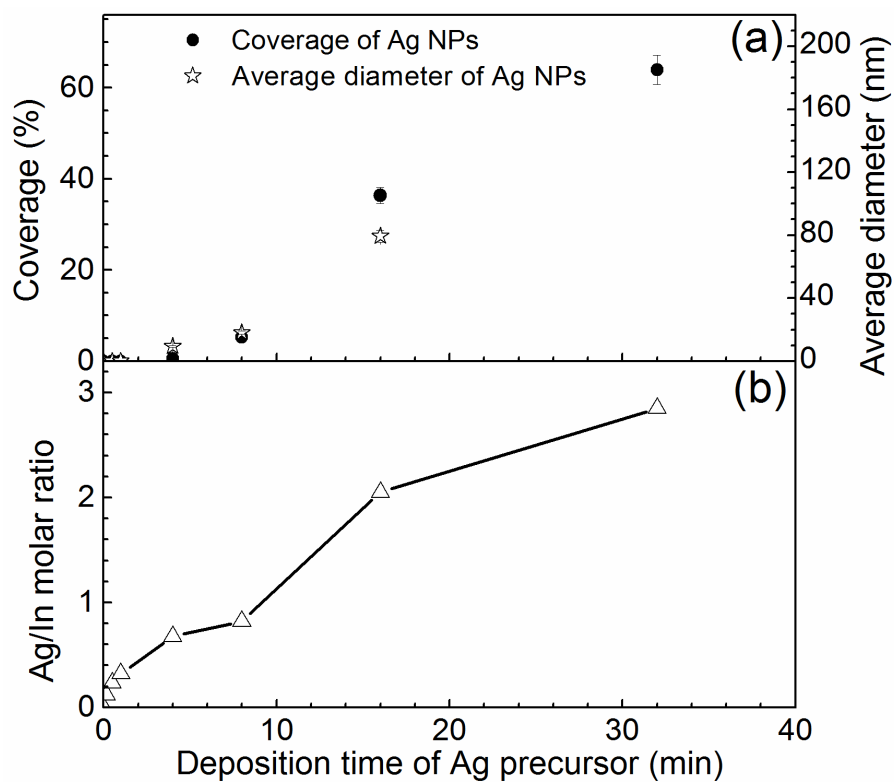


Figure 4.10: The coverage of Ag nanoparticles (a, circles), the average diameter of Ag nanoparticles (a, stars) and the overall molar ratio between silver and indium (b, triangles) depend on the deposition time of Ag.

After the deposition of silver for 4 min, the sample surface shown in Figure 4.8c becomes more homogeneous and small dots (diameters around 10 nm) with bright contrast appeared. After the deposition of silver for 8 min, the diameter and the density of these dots increased (Figure 4.8(d)). Deposition of silver for 16 min (e and f) leads to a very smooth layer (f) covered by particles with bright contrast (e) and the size of the particles was about 100–200 nm.

The SEM images showed above were obtained using a field emission gun microscope with an in-lens detector. For the EDX measurements, the distributed element maps (Ag, In and S) were obtained by analysis of the Ag–L, In–L and S–K signals. Both SEM and EDX analyses were performed on a Thermo Noran X-ray detector equipped LEO GEMINI 1530 scanning electron microscope.

EDX mapping of the sample with deposition of silver for 16 min is shown in Figure 4.9. The intensity of silver signals matches very well with the shape of nanoparticles with bright contrast. To the opposite, the signals intensities of the indium and sulfur do not correlate with these nanoparticles. Therefore, the nanoparticles consisted of silver and were situated on top of the homogeneous In_2S_3 layer.

The coverage and particle size of silver nanoparticles (Ag NPs) are very useful for understanding the deposition process. The area covered by the Ag NPs has been calculated by ImageJ software from SEM images with an area of $1.50 \times 1.04 \mu\text{m}^2$. ImageJ software uses the contrast difference between Ag NPs and the In_2S_3 layer. The average diameter of the Ag NPs was obtained from the diameter of each Ag NP which was calculated from its coverage area using the equation:

$$A = \pi\left(\frac{d}{2}\right)^2 \quad \text{Eq.4.1}$$

Here, A is the coverage area and d is the diameter of the Ag NP. This calculation presumes a spherical shape of Ag NPs. The clear contrast between Ag NPs and the layer underneath in all the images allowed for the calculation by the software, the results are demonstrated in Figure 4.10.

Ag NPs were first observed after the deposition of Ag for 4 min from the SEM images (Figure 4.8(c)). With the Ag deposition time increased to 16 min, the average diameter and coverage of Ag NPs were increased from 9.5 nm and 0.53% (4 min sample) to 79 nm and 36.4% (16 min sample), respectively. After the deposition of Ag for 32 min, Ag NPs' coverage increased to 64%, average diameter is not shown for this sample because many of the Ag NPs connected to each other, to distinguish every Ag NP is very hard and to calculate the average diameter is meaningless. For the samples with deposition of Ag for 4, 8 and 16 min, on the defined area the numbers of Ag NPs were 76, 204 and 78, respectively. From the SEM images and calculated data one can conclude that by varying the deposition time, size controlled Ag NPs (between ten(s) and hundred(s) nm) can be deposited on transformed In_2S_3 precursor layers. This enables the incorporation of plasmonic Ag NPs into devices with application of transformed In_2S_3 precursor layers.

Figure 4.10(b) shows the dependence of the overall Ag/In molar ratio on the deposition time. The molar ratio was obtained by LA-ICP-MS for the samples deposited on c-Si substrates. For each sample, laser ablation was performed in multiple lines scan with enough laser power to reach the surface of c-Si substrate. The Ag/In ratio was calibrated using the NIST612 reference material which contains 23 ppm Ag and 38 ppm In [155]. A standard deviation of around 2.4% of the indium signal was obtained for all samples, which indicated the In_2S_3 precursor layers of all the samples were homogeneous.

The Ag/In molar ratio should depend on the deposition time linearly if the deposition rate of silver is constant. However, between 1 min and 8 min the slope of the Ag/In molar ratio depends on the deposition time. It decreased strongly. The reducing of the deposition rate happened together with the smoothening of the layer because of the phase transitions. On the other hand, between 8 and 16 min the slope of the Ag/In molar ratio increased with deposition time. This is because of the increase of the surface area with the nucleation and growth of Ag NPs. Finally, between 16 and 32 min the slope of the Ag/In molar ratio decreased due to the formation of a compact silver layer.

Table 4.3: Deposition of Ag from an 10 mM alcoholic Ag(hfacac)PMe₃ solution at 200 °C. The dependency of coverage of silver nanoparticles (Ag NPs), average of diameter of Ag NPs, density of Ag NPs (in an area of $1.50 \times 1.04 \mu\text{m}^2$) and silver to indium overall molar ratio on the deposition time of Ag from an alcoholic Ag(hfacac)PMe₃ solution.

Deposition time of Ag (min)	Coverage of Ag NPs(%)	Average diameter of Ag NPs(nm)	Density of Ag NPs	Ag / In molar ratio
0	--	--	0	0.00
0.17	--	--	0	0.12
0.5	--	--	0	0.24
1	--	--	0	0.32
4	0.53	9.5	76	0.68
8	5.2	18	204	0.82
16	36.4	79	78	2.05
32	64	--	--	2.85

Table 4.3 comprises all the results described above which were obtained from the SEM images and LA-ICP-MS measurements, including coverage of Ag NPs, average diameter of Ag NPs, density of Ag NPs and silver to indium overall molar ratio.

Obviously, the stoichiometry changed strongly due to the deposition of Ag NPs on In₂S₃ layers which will very likely lead to the transformation of the layer. Figure 4.11 presents XRD spectra of In₂S₃ layer before and after silver deposition for 0.5, 4, 8, 16 and 32 min. Characteristic peaks of β -In₂S₃ (JCPDS File No.: 25-0390), AgIn₅S₈ (JCPDS File No.: 25-1329), orthorhombic AgInS₂ (JCPDS File No.: 25-1328), Ag (JCPDS File No.: 04-0783) and Ag₂S (JCPDS File No.: 02-0998) are marked by different symbols in the figure. For the In₂S₃ layer and the sample after deposition of Ag for 0.5 min, only β -In₂S₃ peaks are detected. After deposition of Ag for 4 min, both β -In₂S₃ and AgIn₅S₈ peaks are observed from the spectra. After 8 min Ag deposition the β -In₂S₃ peaks vanished and peaks of AgIn₅S₈ appeared. Interestingly, although Ag NPs were already observed in the SEM images of 4 min and 8 min samples, XRD peaks of Ag did not appear for both of them. This is due to the limited sensitivity of XRD measurement. After Ag deposition for 16 and 32 min, peaks of AgIn₅S₈, orthorhombic AgInS₂, Ag and Ag₂S were detected. From the XRD analysis, it is confirmed that the achieved nanoparticles on top of the layers are truly

pure silver nanoparticles. Compared to the 16 min sample, the XRD peak of silver of the 32 min sample increased by 8 times.

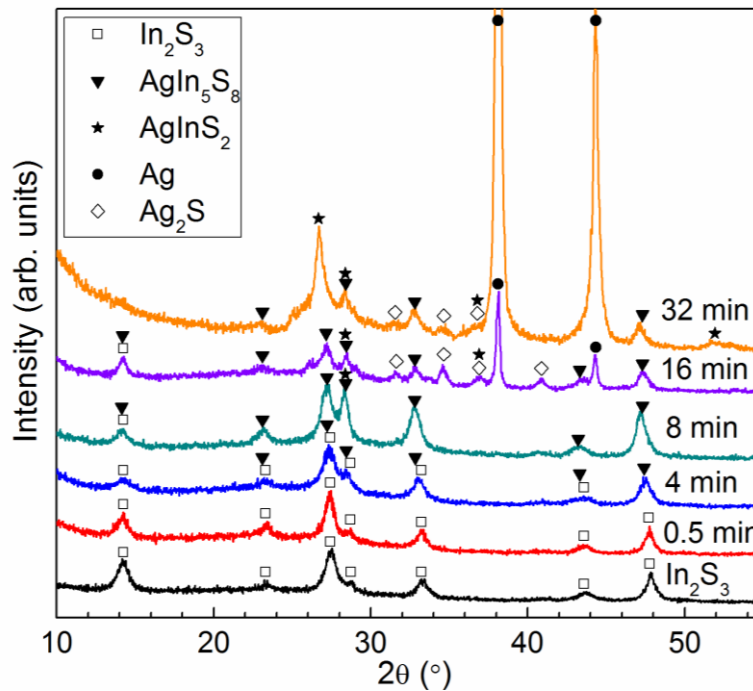


Figure 4.11: X-ray diffraction spectra of the In_2S_3 layer deposited on glass before and after deposition of Ag for 0.5, 4, 8, 16 and 32 min. The symbols mark the characteristic peaks of $\beta\text{-In}_2\text{S}_3$ (open squares), AgIn_5S_8 (filled triangles), orthorhombic AgInS_2 (stars), Ag (circles) and Ag_2S (open diamonds).

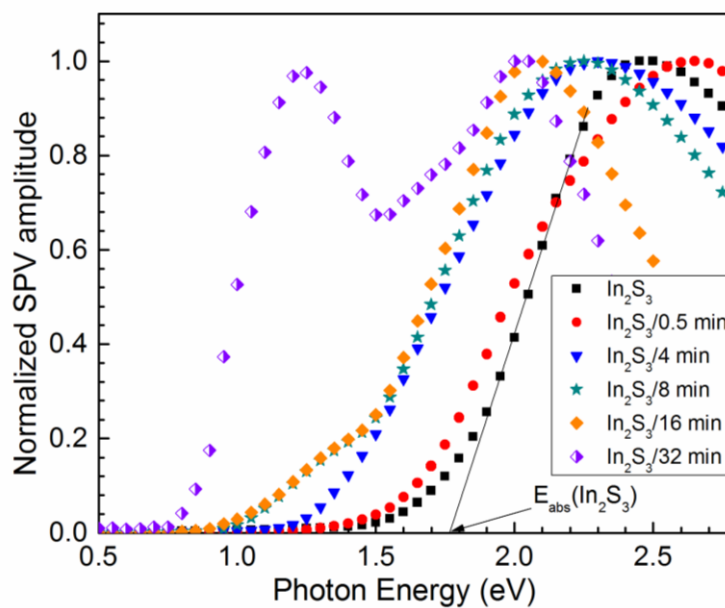


Figure 4.12: Normalized SPV amplitudes for $\text{In}_2\text{S}_3/\text{Mo}/\text{Glass}$ layers before (squares) and after deposition of Ag for 0.5 (circles), 4 (triangles), 8 (stars), 16 (filled diamonds) and 32 (half filled diamonds) min.

To check the electronic properties of the In_2S_3 layer before and after deposition of Ag for 0.5, 4, 8, 16 and 32 min, modulated SPV of the samples were measured. The normalized SPV amplitudes of the samples are shown in Figure 4.12 to focus on the investigation of the changes on the onset energy of SPV signal (E_{abs}). The values of E_{abs} are 1.77 eV, 1.63 eV, 1.36 eV, 1.34 eV, 1.33 eV and 1.11 eV for the bare In_2S_3 sample, 0.5 min sample, 4 min sample, 8 min sample, 16 min sample and 32 min sample, respectively. The E_{abs} values point to an obvious trend that the onset energies of SPV amplitude shift to lower photon energies with increase of deposition time of Ag. This indicates the strong change of band gap of the obtained layers as the E_{abs} value related to the band gap. For the samples with Ag deposition for 8 min and 16 min, clear tails below the E_{abs} are observed which means more defect states were generated in this two deposition time than other shorter deposition times. For the 32 min sample, despite the E_{abs} value of 1.11 eV another E_{abs} value 0.84 eV can be extracted from the spectra. If we relate the change of E_{abs} value with the XRD results shown above, we can attribute the shift of E_{abs} value to new compounds generated during the deposition of Ag. It has to be mentioned that the band gap of the compounds shown in XRD are 2.0...2.2 eV for In_2S_3 [156], 0.9...1.1 eV for Ag_2S [157, 158], 1.7...1.9 eV for the AgIn_5S_8 phase, and 1.86...2.01 eV for the AgInS_2 phase [159-161]. Based on the band gap of the compounds, formation of the compounds with narrower band gaps can explain roughly the change of electronic properties. However, more details are needed from the analysis of SPV spectra to understand the change of electronic properties during the deposition process.

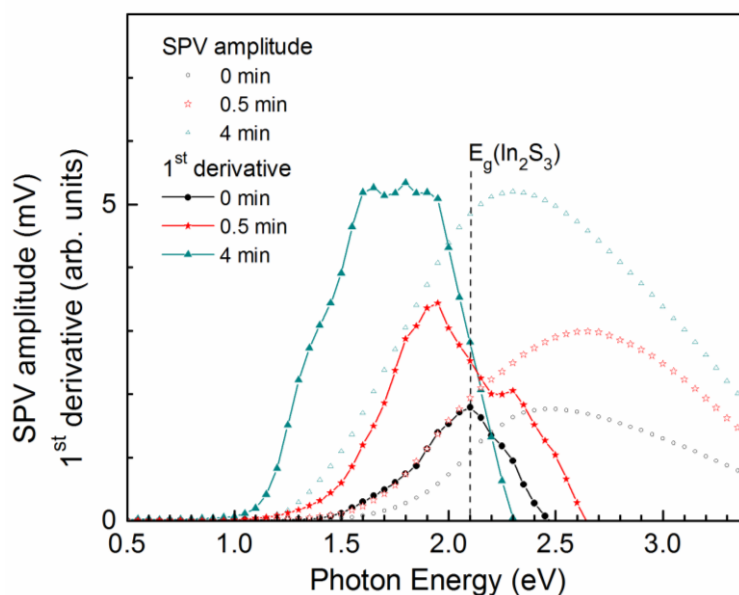


Figure 4.13: SPV amplitudes (open symbols) and the first derivative for the increasing part of the SPV amplitudes (filled symbols with lines) spectra of the bare In_2S_3 layer (circles) and of the layers after Ag deposition for 0.5 min (stars) and for 4 min (triangles). The dashed line shows the band gap of $\beta\text{-In}_2\text{S}_3$.

The in-phase SPV signals' sign of all the samples was positive along the whole spectral range (not shown) which means that the modulated charge separation direction was the same for all samples. In this case, the SPV spectra can be used for the analysis of characteristic transition energies. Figure 4.13 shows the SPV amplitude spectra and the first derivative of the In_2S_3 sample, the 0.5 min sample and the 4 min sample. Interestingly,

shoulders could be distinguished in the increasing part of the SPV spectra, e.g., for the sample with a silver deposition time of 4 min. In the first derivative spectra, the shoulders appeared as maxima value. Characteristic transition energies can be extracted from the peak positions in the first derivative spectra (energy of derivative peak analysis: E_{dpa}). By fitting the first derivative of SPV spectra in the increasing signals range with a minimum number of Gaussians, the values of E_{dpa} could be obtained. The first derivatives of the In_2S_3 sample, 0.5 min sample and 4 min sample shown in Figure 4.13 were fitted with 1, 2 and 3 Gaussians, respectively. Figure 4.14 gives examples for the analysis of derivative peak by fitting with two and three Gaussians for the 1st derivative spectra of the samples after deposition of Ag for 0.5 and 4 min, respectively.

The peak positions obtained from the analysis of the derivative spectra can be used for the comparison with the optical band gaps of pure compounds. Like, the E_{dpa} value of the In_2S_3 layer was 2.1 eV which correlated well with the optical band gap of $\beta\text{-In}_2\text{S}_3$ [156]. However, the defect states below the band gap can also contribute to the E_{dpa} . Therefore, we cannot get the direct information about phase transitions from the E_{dpa} values of the samples with different deposition time of Ag, but the E_{dpa} values give very sensitive information of the formation of new phases during the phase transitions.

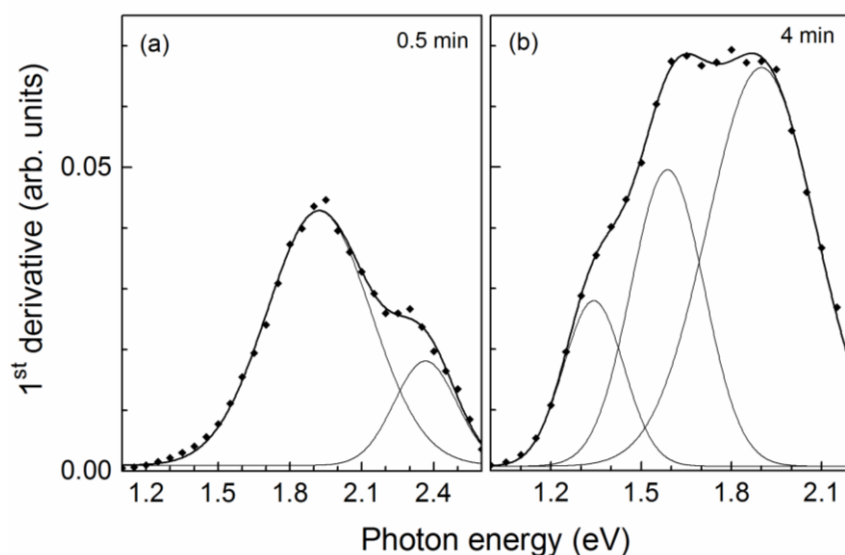


Figure 4.14: The first derivatives of the increasing part of the SPV amplitude fit with Gaussians for samples after Ag deposition for 0.5 min (a) and for 4 min (b).

Ag NPs can be used for plasmonic absorption enhancement by different effects, like far-field effect, near-field effect and the wave-guide effect [36]. For the use of these different effects, the required optimum Ag NPs vary significantly with respect to the size and particle density [4, 21, 25, 162]. Optical properties of the In_2S_3 layer before and after deposition of Ag were characterized which are also helpful for investigating the plasmonic responses of the Ag NPs formed during the phase transition processes. Figure 4.15 shows the absorption properties of In_2S_3 layer before and after Ag deposition for 16 min and 32 min. In the 16 min sample absorption spectrum, an obvious absorption peak at 380nm is observed which is attributed to Ag NPs [163]. For longer wavelengths, their absorption is stronger than that of the In_2S_3 layer. This indicates the obvious absorption enhancement caused by the deposition of Ag NPs on In_2S_3 layer. For the samples with Ag deposition for

shorter time (up to 8 min), no plasmonic absorption peaks was observed. For the sample with deposition of Ag for 32 min, the plasmonic peak signature was still observed and broadened. As AgInS_2 can be used as an absorber material in extremely thin absorber solar cells, the observed absorption enhancement by Ag NPs is important for improving the performance of such kind of solar cells.

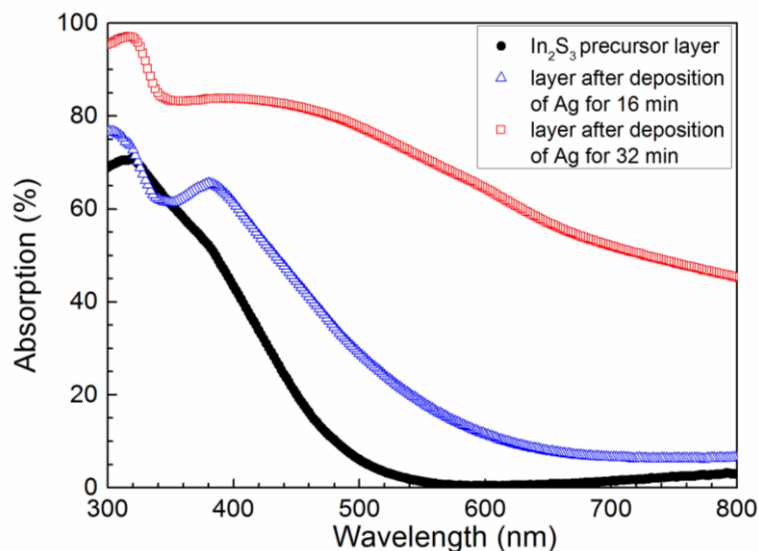


Figure 4.15: Absorption spectra of the In_2S_3 layer before (filled circles) and after Ag deposition of 16 min (open triangles) and 32 min (open squares).

From the results shown in this section, Ag NPs with different sizes and densities were deposited on In_2S_3 layer by simple variation of the deposition time. The AgIn_5S_8 , orthorhombic AgInS_2 and Ag_2S phases were detected with increasing deposition time. After the appearance of Ag NPs on top, the layers still showed semiconducting properties, which enables the further application as absorbers in solar cells. Absorption enhancement of the In_2S_3 layers after Ag deposition for 16 min and 32 min was illustrated. This Ag NPs deposition approach opens the opportunity to tune the size or density of Ag NPs as well as solves the problem of stable implementation of Ag NPs on top of sulfide absorber layers.

4.4 Mechanism of the deposition process

In this section, the results obtained from all the investigations on the deposition time series are summarized to study the deposition mechanism of integrating Ag NPs on In_2S_3 layer. A growth model is shown to illustrate the deposition process.

Figure 4.16 summarizes the analysis of phase (XRD and SEM) and of the first derivative peak (SPV) as a function of the deposition time of silver. For the pure In_2S_3 layer, only one peak at 2.1 eV was observed which correlates to the band gap of $\beta\text{-In}_2\text{S}_3$ layer. For the sample with Ag deposition for 0.17 min, two peaks at 1.96 eV and 2.2 eV are obtained. However, from SEM or XRD no new phases were observed yet. After deposition of Ag for 0.5 min, two peaks were still identified but they shifted to 1.92 and 2.36 eV, respectively. For the 1 min sample, a third peak was fitted and the obtained three peaks were at 1.4, 1.85 and 2.34 eV. By fitting analysis of the first derivative of the 4 min sample, three Gaussians peaked at 1.34, 1.58 and 1.9 eV were determined. For the 8, 16 and 32 min samples, the low energy peak shifted to 1.17, 1.18 and 1.0 eV, respectively, while the peak at around 1.6 eV was nearly constant. From the XRD and SEM

investigations, AgIn_5S_8 and Ag appeared as new phases between 1 and 4 min. While in analysis of E_{dpa} , the 2.3 eV peak disappeared and an intermediate peak at around 1.6 eV appeared. The emerging of the new phases could be correlated with the change of the peaks. The appearance of the Ag_2S phase could be correlated with the shift of the low energy peak towards 1 eV as the Ag_2S phase band gap is between 0.9 and 1.1 eV [157, 158]. The peak between 1.8 and 1.9 eV can be attributed to a defect band which could convert to the band gap of orthorhombic AgInS_2 (band gap around 1.96 eV [159, 160]) and/or of AgIn_5S_8 (between 1.7 and 1.8 eV [157]). It has to be mentioned that the peak between 1.8 and 1.9 eV disappeared for the samples with Ag deposition time longer than 4 min. This is due to the decrease of the SPV amplitude in this spectral range. As a remark, the peak around 1.6 eV is very likely not related to the band gap of given phases but to a defect band.

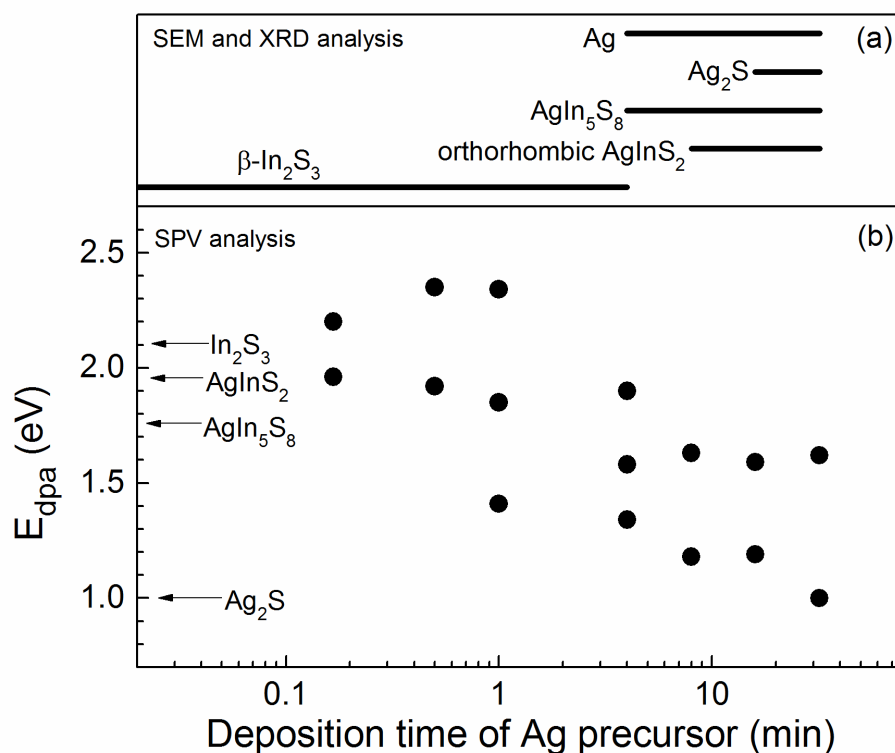


Figure 4.16 Phases (a) and the peak positions extracted from the first derivatives of the SPV amplitude spectra in the increasing part (b) as a function of the Ag deposition time. The arrows show the band gaps of $\beta\text{-In}_2\text{S}_3$, AgIn_5S_8 , orthorhombic AgInS_2 and Ag_2S .

Based on all the analysis shown above in this chapter, the phase transitions during the deposition of Ag on an In_2S_3 precursor layer were summarized to form a scheme (shown in Figure 4.17). In the beginning, silver diffused into the In_2S_3 layer and a silver doped $\text{In}_2\text{S}_3\text{:Ag}$ layer was formed and the surface started to become smooth. During the diffusion or doping process, defect states which are close to form AgIn_5S_8 were developed. With further Ag deposition, the AgIn_5S_8 phase was generated and the $\text{In}_2\text{S}_3\text{:Ag}$ and AgIn_5S_8 phases coexisted. And the Ag NPs started to form on top of saturated AgIn_5S_8 . Subsequently, the $\text{In}_2\text{S}_3\text{:Ag}$ phase was transformed fully to the composite of AgIn_5S_8 and the orthorhombic AgInS_2 . The formation and the growth of Ag NPs didn't stop and the Ag_2S phase appeared at the interface between Ag NPs and AgIn_5S_8 and/or AgInS_2 . The

The diagram illustrates the synthesis of the $\text{AgIn}_5\text{S}_8/\text{AgInS}_2$ heterostructure. It begins with an In_2S_3 layer on a substrate. The introduction of gaseous $\text{Ag}(\text{hfacac})(\text{PMe}_3)/\text{EtOH}$ leads to the formation of an $\text{In}_2\text{S}_3:\text{Ag}$ layer. Subsequent steps involve the growth of an Ag Nanoparticle layer, which then transforms into an Ag_2S layer. The final structure is a heterostructure of AgIn_5S_8 and AgInS_2 layers.

4.5 Application in extremely-thin absorber solar cells

A schematic diagram of a device structure. The layers, from top to bottom, are: Au Back Contact (grey), Spiro-OMeTAD (orange), Extremely-thin In_2S_3 layer (green) containing Ag NPs (indicated by white dots and an arrow), TiO_2 (white), FTO (white), and Glass (white). The layers are separated by horizontal lines.

Figure 4.18 shows the architecture of the solar cells used in this section. Fluorine-doped tin oxide (FTO) glasses ($2.35\text{ cm} \times 2.35\text{ cm}$) were used as substrates. They were cleaned by sonication in de-ionized water, acetone and ethanol for 20 min in each solvent and dried at room temperature afterwards. A dense and thin TiO_2 compact layer was deposited on top of the cleaned FTO glass substrates by spray pyrolysis method. Titanium diisopropoxide bis(acetylacetonate) was used as precursor and concentration of the precursor solution was 6.8 mM. The TiO_2 layer acted as electron transport layer in the solar cell. After the deposition of TiO_2 compact layer, an In_2S_3 layer was deposited by the spray-

ILGAR method following the deposition parameters shown in Table 4.1. Afterwards the Ag NPs deposition process was used on one sample following the deposition parameters listed in Table 4.2 but with 8 min deposition time. Later a 2,2',7,7'-tetrakis(N,N-di-4-methoxy-phenyl-amino)-9,9'-spirobifluorene (spiro-OMeTAD) layer was deposited on top of the layer stacks by spin coating. This layer was used as a hole transport layer. Details of the method used to form spiro-OMeTAD layer can be found elsewhere [14]. Finally, gold back contacts with a thickness of 80 nm were deposited by thermal evaporation to complete the solar cells.

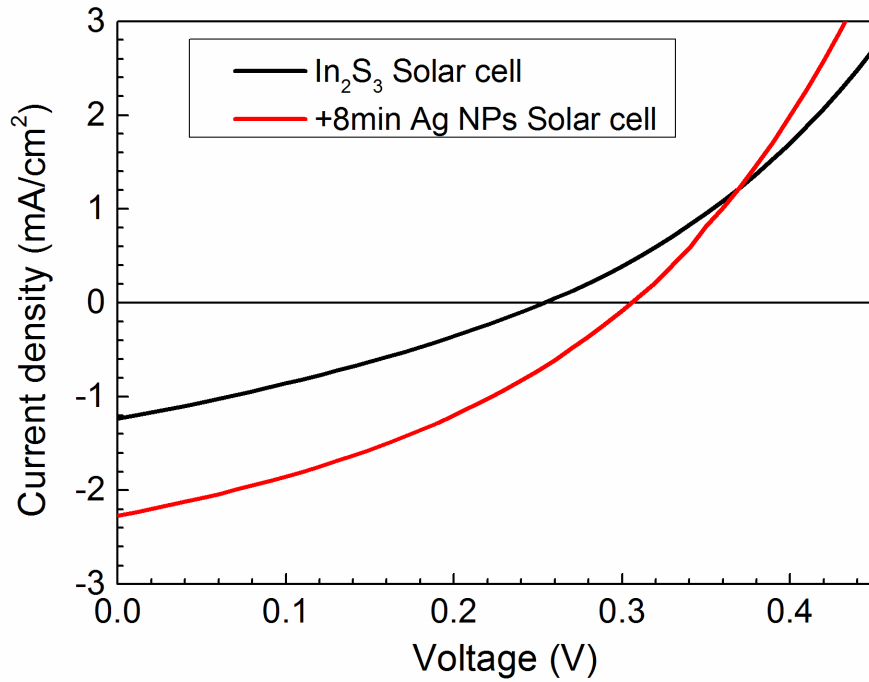


Figure 4.19: Current density-voltage curves for the best devices of solar cell based on In_2S_3 layer and 8 min Ag NPs deposited In_2S_3 layer.

Table 4.4: Device performance for solar cells using In_2S_3 layers before and after deposition of Ag NPs for 8 min, averaged from 5 devices for each condition.

Solar cell	V_{oc} (V)	J_{sc} (mA/cm ²)	FF	PCE (%)
In_2S_3	0.21 ± 0.04	1.4 ± 0.1	0.29 ± 0.02	0.1 ± 0.02
In_2S_3 +8 min Ag NPs	0.26 ± 0.04	2.1 ± 0.1	0.34 ± 0.03	0.2 ± 0.05

Figure 4.19 shows the I-V curves of the solar cells with best performance based on pure In_2S_3 layer before and after Ag deposition for 8 min. The solar cell based on In_2S_3 layer exhibited $V_{oc} = 0.25$ V, $J_{sc} = 1.5$ mA/cm², and FF = 0.31, leading to a PCE of 0.1%. The solar cell based on In_2S_3 layer with Ag deposition for 8 min exhibited a PCE of 0.2% with $V_{oc} = 0.31$ V, $J_{sc} = 2.3$ mA/cm², and FF = 0.35. The performance of solar cell based on 8 min Ag deposited In_2S_3 layer is better in all parameters than the solar cell based on In_2S_3 layer. The same phenomenon was observed when we compare the average performance of 5 devices (shown in Table 4.4) for each condition. There is no doubt that the performance of solar cells based on In_2S_3 layer with and without deposition of Ag

needs more work for further improvement and optimization. However, the results showed already the application potential of plasmonic Ag NPs in solar cells based on In_2S_3 layers.

4.6 Summary

In this chapter, the development of a process for the deposition of Ag NPs on top of In_2S_3 layer is described.

In_2S_3 layers were deposited by spray-ILGAR method. The spray-ILGAR method is a sequential and cyclic method. One cycle In_2S_3 layer deposition can be divided into four steps. Firstly the alcoholic $\text{In}(\text{acac})_3$ solution is nebulized for 60 s by an ultrasonic nebulizer to form aerosol which is carried by N_2 carrier gas to the surface of heated substrate. A precursor layer will be formed on the surface. After 10 s N_2 purging, H_2S is introduced and carried by N_2 to the substrate surface to sulfurize the precursor layer and form In_2S_3 layer. At last step, H_2S flow will be stopped and N_2 purging is lasted for 10 s. The four steps will be repeated for different cycles to get desired In_2S_3 layer thickness. Two thicknesses (44 ± 6 nm and 85 ± 11 nm) were applied.

Using the spray-CVD method described in Chapter 3, Ag NPs with controlled size and coverage can be deposited on top of the In_2S_3 layer, which are very useful for the further application of plasmonic Ag NPs in ETA solar cells with In_2S_3 layers. During the deposition process of Ag NPs on top of In_2S_3 , a variation of deposition parameters such as the concentration of precursor solution and deposition time has significant influence on the layer properties, i.e. electronic, optical and compositional one. Details of the influence of these two parameters and related deposition mechanism are shown below:

- With increase of the concentration of precursor solution, the band gap of the layers obtained from the E_{abs} (from SPV measurement) shifted to smaller photon energy. This is due to the generation of new compounds during the deposition process. Ag NPs could be observed only under 10 mM precursor solution deposition, for the sample with smaller concentration (5 mM) no Ag NPs were generated. Due to the formation of new compounds and Ag NPs, the absorption of the layers also increased with increase of the concentration of precursor solution. However, with the short deposition time (2 min), it was hard to observe the complete reaction during the deposition.
- With variation of deposition time from 0.5 min to 32 min, much clearer changes of the layer properties during the deposition process were observed. For process times shorter than 4 min, only doping of Ag and planarization of the In_2S_3 layer happened. Ag NPs were first observed on the 4 min deposition sample. With further increase of the deposition time, Ag NPs grew up and at some point connected to each other and formed big clusters. For the optical properties of the layer, absorption enhancement by the new formed compounds and Ag NPs were observed. The change of electronic properties of the layers happened similarly to the variation of the concentration of precursor solution experiment. The generated new compounds (AgIn_5S_8 , orthorhombic AgInS_2 and Ag_2S) were identified by XRD.
- Based on the variation of the two parameters, the deposition mechanism was studied. During the deposition process, silver doped In_2S_3 :Ag layer is first formed and the previously rough layer is becoming planar. Later, AgIn_5S_8 is generated and coexisted with In_2S_3 :Ag. With ongoing deposition, Ag NPs were produced on top of saturated AgIn_5S_8 layer. In the following, the In_2S_3 :Ag phase was transformed fully to the composite of AgIn_5S_8 and the orthorhombic

AgInS₂. Ag NPs grow continually and the Ag₂S phase appeared at the interface between Ag NPs and AgIn₅S₈ and/or AgInS₂. Ag NPs became bigger with increase of deposition time that the neighboring Ag NPs started to agglomerate. At last, the agglomerated Ag NPs merged with the neighboring ones and formed irregular silver islands which resulted in the disappearance of isolated Ag NPs.

In₂S₃ layer with and without deposition of Ag NPs were applied to fabricate solar cells. From the performance of the solar cells, there is no doubt that they need further work to improve and optimize the performance. However, the results already show clearly the potential of the application of plasmonic Ag NPs coupled In₂S₃ layers into solar cells.

Chapter 5

Application of Ag nanoparticles in ultra-thin perovskite solar cells

In this chapter Ag nanoparticles (Ag NPs) deposited by the spray-CVD method were applied into ultra-thin perovskite solar cells for enhancement of photocurrent and power conversion efficiency.

The process for the fabrication of ultra-thin perovskite solar cells is presented in section 5.1. Different characterization methods were used to characterize the fabricated ultra-thin perovskite layer and solar cells. Results of which are also shown in this section.

Section 5.2 shows the optical simulation results of incorporating Ag nanoparticles at three different positions of ultra-thin perovskite solar cells.

Experimentally incorporation of Ag NPs at the same positions as described in section 5.2 leads to different effects on the performance of ultra-thin perovskite solar cells. This part of content is shown in section 5.3.

Results of the three sections are summarized in section 5.4.

5.1 Fabrication of ultra-thin perovskite solar cells

In recent years, the inorganic-organic hybrid perovskites have attracted extremely high attention [10]. They have many advantages, e.g., they can be processed by very simple, low cost methods and in parallel they have excellent electrical and optical properties [57]. Early-stage PSCs had a similar architecture as dye-sensitized solar cells, employing a mesoporous metal oxide (normally TiO_2) layer for electron transfer [164]. Later, Snaith et al. found electrons can be transported through the perovskite absorber layer [165]. This opened the gate for developing the planar heterojunction PSCs which further expanded the scope of application of PSCs [37, 166]. Based on the development of planar heterojunction PSCs, ultra-thin perovskite absorber layers which are much thinner than the perovskite absorber layers in normal PSCs became widely used and find application in semitransparent PSCs and tandem solar cells [13-16]. However, due to the decrease of the layer thickness, the ultra-thin perovskite solar cells (UTPSCs) cannot give PCEs comparable to the bulk PSCs [16, 166].

To improve the PCE of solar cells without increasing the thickness of the absorber layer, the implementation of plasmonic nanoparticles has proved beneficial [36, 66]. Therefore, it is a promising way to use the same method to improve the PCE of ultra-thin

perovskite solar cells. The first step for the investigation of the improvement is fabrication of UTPSCs.

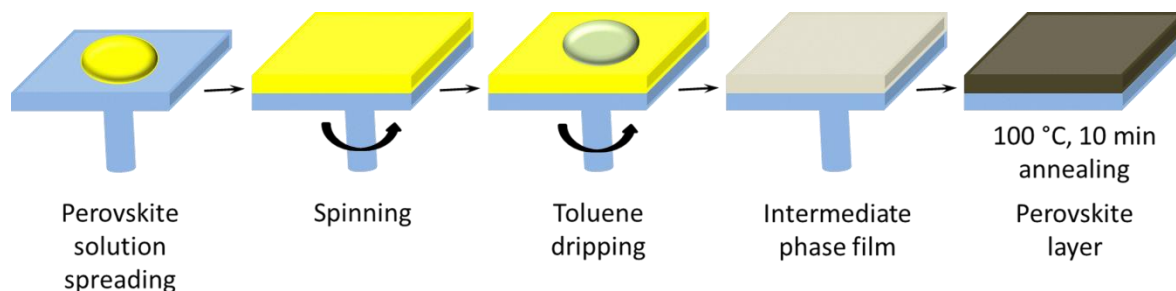


Figure 5.1: Schematic process of ultra-thin perovskite layer deposition. Adapted after Ref: [63].

In the fabrication process, the most important step is the deposition of the ultra-thin perovskite layer. Hence, deposition and characterization of ultra-thin perovskite layers will be introduced first. Figure 5.1 shows a schematic diagram of the deposition of ultra-thin perovskite layer by spin-coating. The deposition process is carried out in a N_2 filled glove box in which the O_2 and H_2O levels are both less than 0.1 ppm. During the process, a stoichiometric $CH_3NH_3PbI_3$ precursor solution with a concentration of 0.8 M is prepared by dissolving lead iodide (PbI_2) and methylammonium iodide in 1 mL mixed solvent from 0.7 mL γ -butyrolactone and 0.3 mL dimethyl sulfoxide. The solution is then stirred at 60 °C for 12 h. A $CH_3NH_3PbI_3$ layer is deposited by spin coating the $CH_3NH_3PbI_3$ solution on a substrate at 1000 rpm for 10 s and 5000 rpm for 20 s, respectively. For each speed, there are both 5 s for increasing from 0 or 1000 rpm to the desired speed. At 35 s of the spin coating step, 150 μ L of toluene is dripped onto the samples. The obtained intermediate layer was annealed on a hot plate at 100 °C for 10 min. The ultra-thin perovskite layer is obtained after the annealing. Details of the corresponding process can be found elsewhere [63].

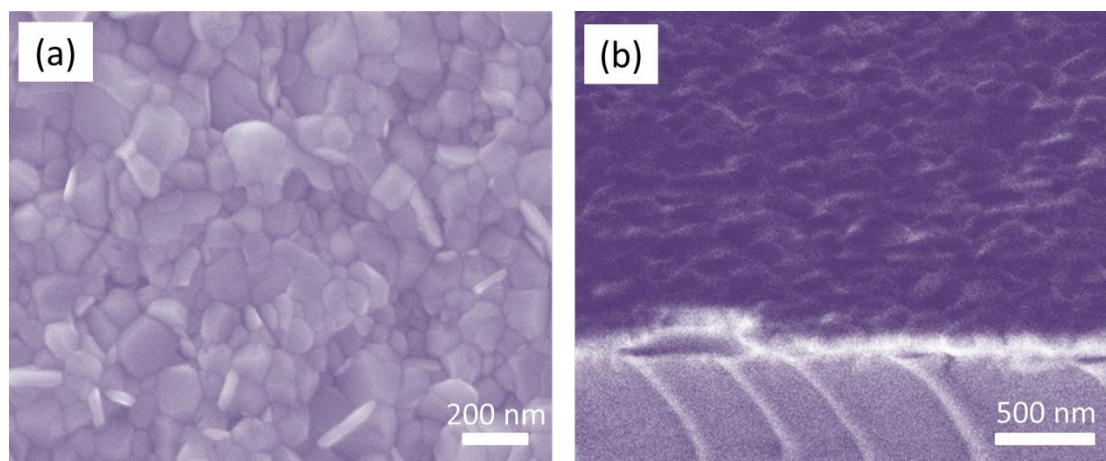


Figure 5.2: (a) Top view SEM image of ultra-thin perovskite layer. (b) Cross sectional SEM image of ultra-thin perovskite layer on glass substrate.

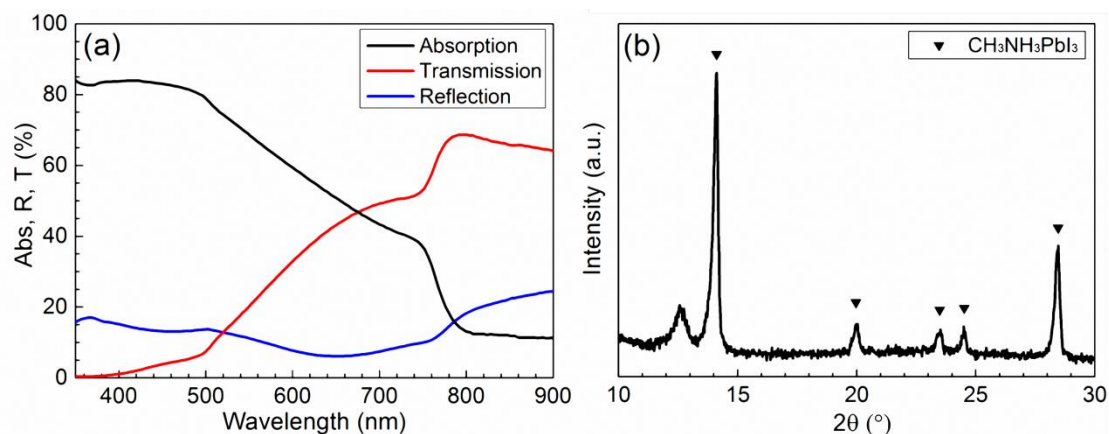


Figure 5.3: (a) Absorption, transmission and reflection of the achieved perovskite layer on glass substrate. (b) XRD pattern of the obtained perovskite layer coated on glass substrate.

Figure 5.2 shows the top view and cross section view SEM images of the achieved ultra-thin perovskite layers on glass substrate. The perovskite layer is highly uniform and nearly pin-hole free which is very important for the fabrication of solar cells [167]. The cross section SEM images give the information that the average thickness of the obtained perovskite layer is around 140 nm.

Figure 5.3a presents the measured optical responses of the achieved ultra-thin perovskite layer on glass substrate, i.e., transmission, reflection and absorption (absorption = 100% - transmission - reflection). The absorption of the layer between 350 nm and 500 nm is around 82%, which is very sufficient. However, from 500 nm to around 780 nm (band gap of perovskite), absorption decreases significantly which is due to the thickness of the perovskite layer is too thin for full absorption of the incident light in this wavelength range [168]. Figure 5.3b depicts the X-ray diffraction (XRD) pattern of the deposited ultra-thin perovskite layer. Characteristic peaks of CH₃NH₃PbI₃ marked by filled triangle in the figure confirm the deposited layer is perovskite.

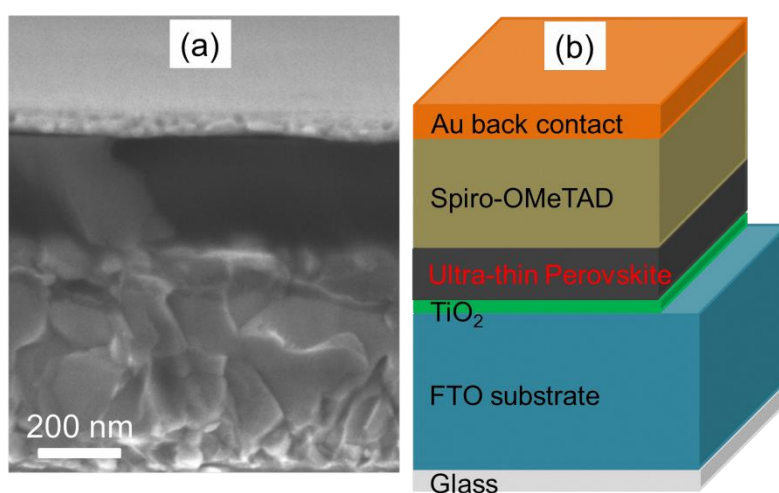
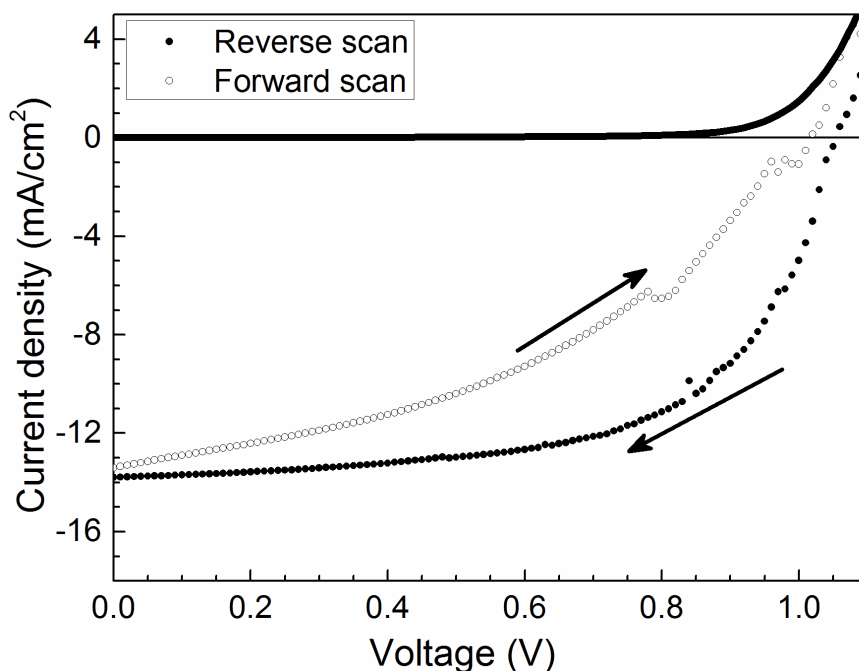


Figure 5.4: (a) Cross sectional SEM image of ultra-thin perovskite solar cell. (b) Schematic device structure of ultra-thin perovskite solar cell.



Scan direction	J_{sc} (mA/cm ²)	V_{oc} (V)	FF (%)	PCE
Forward	13.4	1.02	40.98	5.6
Reverse	13.8	1.05	61.35	8.9

Figure 5.5 J - V curve and performance of the best PCE ultra-thin perovskite solar cell. Filled circle and open circle curves are reverse scan and forward scan J - V curve of the solar cell, respectively. The upper black curve is the dark J - V curve of the solar cell.

Using the recipe described above, ultra-thin perovskite layers can be deposited for the fabrication of UTPSCs. Figure 5.4a shows the cross sectional SEM image of UTPSC and Figure 5.4b illustrates the schematic structure of the UTPSCs. In the UTPSC structure, FTO acts as substrate and front contact while the TiO_2 layer is the electron transport layer. The ultra-thin perovskite layer is the absorber of the UTPSC and the 2,2',7,7'-tetrakis(N,N-di-4-methoxy-phenyl-amino)-9,9'-spirobifluorene (spiro-OMeTAD) layer is the hole transport layer. Au acts as back contact of the UTPSC.

For the fabrication of UTPSC, FTO glass substrates (2.35 cm \times 2.35 cm) are first cleaned by sonication in de-ionized water, acetone and ethanol for 20 min in each solvent and blown dry with nitrogen afterwards. The substrates are further cleaned by an Ar plasma treatment for 5 min. The compact TiO_2 layer is deposited onto the cleaned FTO glass substrates by spray pyrolysis using titanium diisopropoxide bis(acetylacetonate) as precursor. The concentration of the precursor solution and the substrate temperature are 6.8 mM and 460 $^{\circ}C$, respectively. After the deposition of the compact TiO_2 layer, all samples are transferred into a glove box with a H_2O and O_2 level less than 0.1 ppm. An ultra-thin perovskite layer is deposited on top of a TiO_2 layer by the recipe described above. After the sample cooled down to room temperature, a layer of spiro-OMeTAD is deposited onto the perovskite layer by spin coating at 2000 rpm for 40 s. The spiro-OMeTAD solution is prepared by dissolving 72.3 mg spiro-OMeTAD in 1 mL chlorobenzene, and then adding

17.5 μL tri-*n*-butylphosphine and 46.4 μL bis(trifluoromethane)sulfonimide lithium salt solution (170 mg/mL in acetonitrile). Finally, gold back contacts with a thickness of 80 nm are deposited by thermal evaporation to finish the fabrication of the solar cells. Photocurrent density–voltage (J - V) responses, optical responses and external quantum efficiency (EQE) of the fabricated UTPSCs are characterized by a sun simulator, a Lambda 950 spectrophotometer with an integrating sphere and an EQE system, respectively.

Figure 5.5 presents J - V curve and performance of the best UTPSC selected from more than 40 devices. Measured by reverse scan, the best UTPSC exhibits 1.05 V open circuit voltage (V_{oc}), $J_{sc} = 13.8 \text{ mA/cm}^2$, and $FF = 0.61$, leading to a PCE of 8.9%. In forward scan mode, the same UTPSC exhibits $V_{oc} = 1.02 \text{ V}$, $J_{sc} = 13.4 \text{ mA/cm}^2$, $FF = 0.41$ and PCE = 5.6%. The UTPSC shows obviously a hysteresis which is caused by slowly moving ions (in the perovskite layer) during the J - V measurement [169].

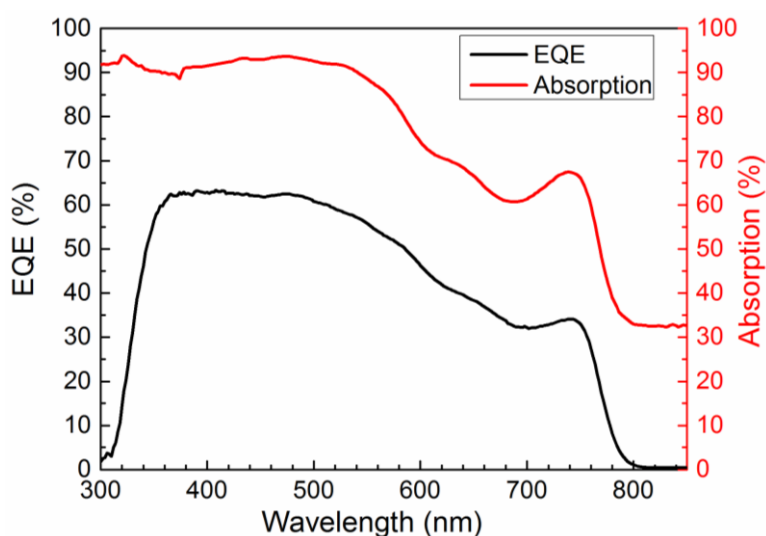


Figure 5.6: EQE (black line) and absorption spectra (red line) of the fabricated UTPSC.

Figure 5.6 shows the EQE and absorption spectra of the fabricated UTPSC. Compared to the absorption of a single perovskite layer shown in Figure 5.3a, the overall absorption of the UTPSC is higher. The increased absorption can be attributed to both the absorption of other layers and the absorption enhancement of the perovskite layer caused by other layers. However, the absorption between 550 nm and 780 nm is still lower than between 300 nm and 550 nm. The EQE spectrum shows the similar shape as the absorption spectrum which means the weak absorption of light at longer wavelength limits the J_{sc} of the UTPSC. Therefore, if absorption of light at the wavelength range between 550 nm and 780 nm of the UTPSCs increases, performance of the UTPSCs can be enhanced. Incorporation of plasmonic nanoparticles into the UTPSCs can be a promising way for this purpose. In the following two sections, the simulated and experimental incorporation of Ag NPs into UTPSCs will be discussed in detail.

5.2 Simulated incorporation of Ag NPs in ultra-thin perovskite solar cells

As introduced previously, Ag NPs can localize and scatter light and in this case can be applied in solar cells for enhancing light absorption as well as performance. However, the possible positions to integrate Ag NPs into the UTPSCs should be considered carefully to exploit the plasmonic effect of Ag NPs as well as the preparative realization. Light intensity near the Ag NPs is much higher than elsewhere which leads to the absorption enhancement of the material surrounding the Ag NPs. In the UTPSCs, the ultra-thin perovskite layer is used for absorbing and converting light into electron and hole pairs. Therefore, Ag NPs should be placed very near or in the perovskite layer to exploit their plasmonic effects. Based on the structure of the UTPSC shown in Figure 5.4b, three positions can be used to integrate Ag NPs into the UTPSCs. Figure 5.7 shows the three possible positions for the integration of Ag NPs, i.e., at the interface between Spiro-OMeTAD and perovskite layer, at the interface between perovskite layer and TiO_2 layer and at the interface between TiO_2 layer and FTO.

Optical simulation is very useful for predicting the influence of different parameters on the absorption of the perovskite layer in the UTPSCs. Therefore, before experimental integration of Ag NPs into the UTPSCs, simulations can help understanding how the Ag NPs can enhance absorption of the perovskite layer. In this section, Finite Element Method (FEM) simulations have been performed by JCMsuite to estimate the theoretical absorption of the perovskite layer in the UTPSCs with integration of Ag NPs in the mentioned three different positions. The FEM can subdivide the computational domain into elements and each element defines a geometrical region. The full solution within the geometrical region can be approximated.

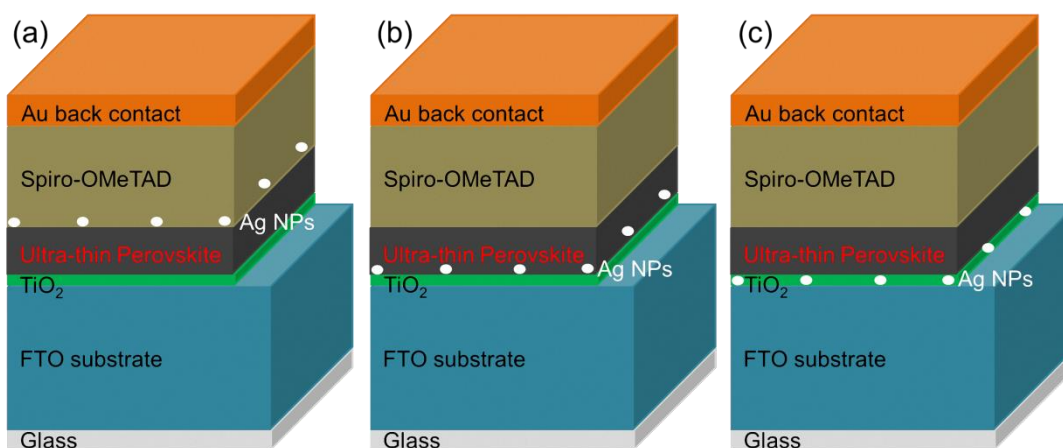


Figure 5.7: Three possible positions to integrate Ag NPs. (a) At the interface between Spiro-OMeTAD and perovskite layer. (b) At the interface between perovskite layer and TiO_2 layer. (c) At the interface between TiO_2 layer and FTO.

The structure of the UTPSCs used in the simulation is Au/spiro-OMeTAD/perovskite/ TiO_2 /FTO and the corresponding layer thicknesses are 80 nm/280 nm/140 nm/35 nm/570 nm. Thickness and structure are taken from the experimentally fabricated UTPSCs (see Section 5.1). The shape of the Ag NPs used in the simulation was

a cropped sphere. The sphere was cropped such that the height of the cropped object was a certain part of the diameter of the sphere, e.g., $1/2$, $2/3$, $5/6$, $7/8$ parts of the diameter of the sphere (upper part). For all simulations periodic boundary conditions were used in the x-y plane, with the unit cell taking a hexagonal shape. Perfectly matched layer boundary conditions were used in the propagation (z) direction. The material data for Ag was taken from Palik [170] while the other material data was obtained from fitting to measurements of own samples [171]. It has to be mentioned that in this section the absorption in perovskite layers and in Ag NPs are extracted and shown to study the effects of Ag NPs on the absorption of perovskite layers.

5.2.1 Incorporation of Ag NPs between perovskite layer and spiro-OMeTAD layer

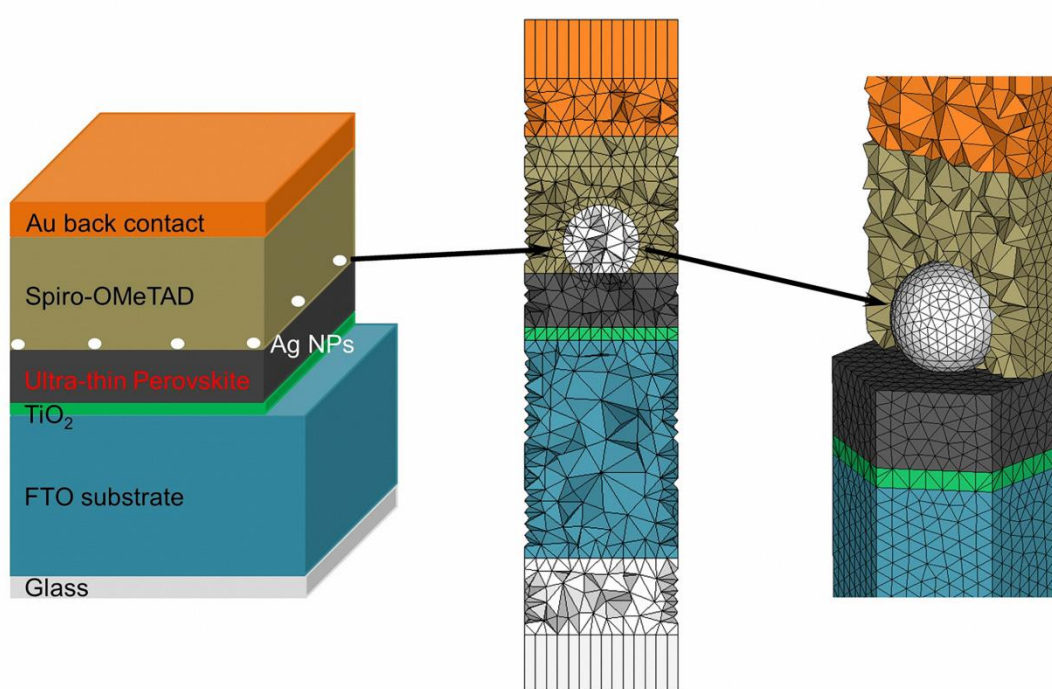


Figure 5.8: Schematic structure for simulated incorporating Ag NPs at the interface between perovskite layer and Spiro-OMeTAD layer.

In this section, simulation results of incorporation Ag NPs into the UTPSCs at the interface between perovskite layer and Spiro-OMeTAD layer are discussed. Figure 5.8 shows the schematic structure of the incorporation of Ag NPs at the interface. To study and predict the application of Ag NPs with certain size, upper part and coverage, systematic studies of these three conditions are shown.

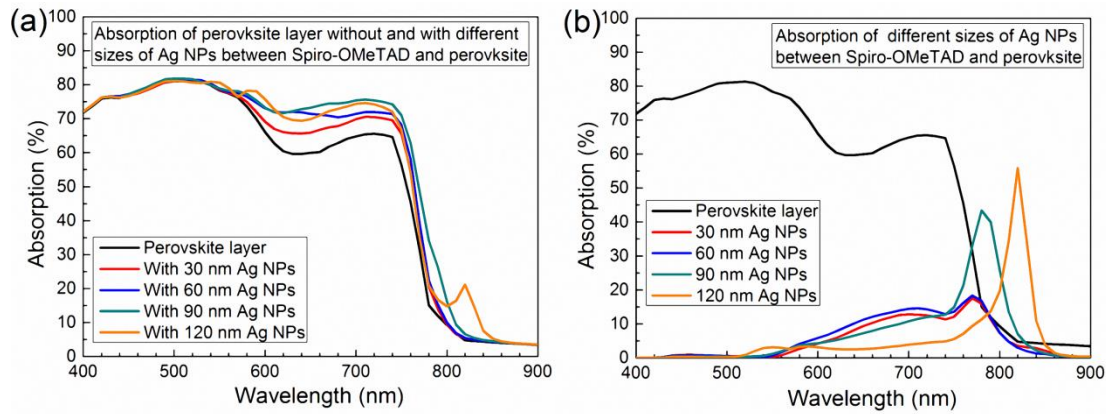


Figure 5.9: Absorption spectra of (a) perovskite layers without and with different size of Ag NPs between Spiro-OMeTAD layer and perovskite layer, (b) different sizes of Ag NPs integrated between Spiro-OMeTAD layer and perovskite layer.

Figure 5.9a shows absorption spectra of perovskite layers without and with different sizes of Ag NPs incorporated at the interface between spiro-OMeTAD and perovskite layer. The shape of Ag NPs used in this series was 2/3 upper part of Ag NPs and the coverage of Ag NPs (density) is 13.4%. From the absorption of only perovskite layer, absorption at the wavelength between 560 nm and 780 nm is significantly lower than that at wavelengths shorter than 560 nm which is consistent with the experimental measured absorption of perovskite single layer (see Figure 5.3a). It's observed that with incorporation of different sizes Ag NPs, the absorption of the perovskite layer was enhanced at the poor absorbing range of the spectrum while the absorption were the same for all samples at the wavelengths shorter than 550 nm. The absorption enhancement of the perovskite layer is caused by the scattering and localized surface plasmon resonance (LSPR). With increase of particle size from 30 nm to 90 nm, absorption of enhancement increase. However, absorption enhancement caused by 120 nm Ag NPs is less than that by 90 nm Ag NPs. This is because the resonance peak of 120 nm Ag NPs red-shifts to the wavelength longer than the band gap of perovskite which decreases the resonance that can be coupled to perovskite layer. Figure 5.9b gives more evidences. The resonance peaks of Ag NPs red-shift with increasing size of Ag NPs from 30 nm to 120 nm. For perovskite layer with 120 nm Ag NPs, a kink appears at the wavelength of 820 nm. This is due to that the resonance of 120 nm Ag NPs at this wavelength (Figure 5.9b) coupled to the absorption of perovskite layer. In principle, perovskite layer has no absorption at the wavelengths longer than the band gap wavelength of perovskite. However, defect states appear in the perovskite layer may cause the absorption at those wavelengths in realistic. Moreover, the material data used in simulation are extracted from our own sample. Thus, the absorption of perovskite layers at the wavelengths longer than band gap is caused by the defect states. The broad resonance peaks can be attributed to the shape of Ag NPs. The resonance peaks' wavelength of Ag NPs is consistent with the enhanced absorption wavelength range of perovskite layer. Based on this simulation, 90 nm Ag NPs can contribute more absorption enhancement to perovskite layer. Therefore, 90 nm Ag NPs will be used for further simulations.

After the study on the influence of the size of Ag NPs, a systematic variation of the cropped upper part of Ag NPs is carried out. Figure 5.10a shows absorption spectra of perovskite layers without and with different upper part of Ag NPs (from 1/2 to 1/1)

between Spiro-OMeTAD layer and perovskite layer. Figure 5.10b shows absorption spectra of the Ag NPs. In this series simulation, 90 nm was set as the particle diameter of all the Ag NPs and the surface coverage of perovskite by Ag NPs was set as 13.4% for all samples.

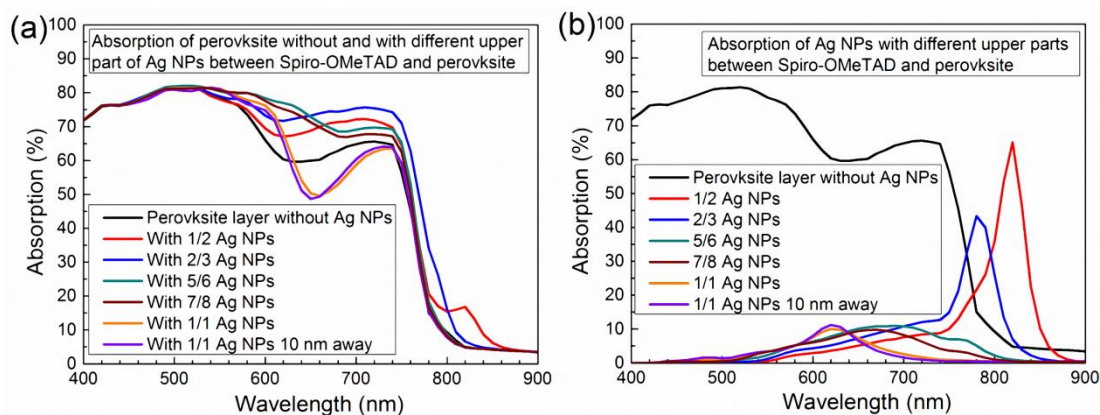


Figure 5.10: Absorption spectra of (a) perovskite layers without and with different upper part of Ag NPs between Spiro-OMeTAD layer and perovskite layer, (b) different upper part of Ag NPs integrated between Spiro-OMeTAD layer and perovskite layer.

For the two samples with full sphere Ag NPs on top of perovskite-1/1 Ag NPs and 1/1 Ag NPs 10 nm away (1/1 Ag NPs 10 nm away means full sphere Ag NPs were set at the position which has 10 nm distance from perovskite layer to the bottom of the sphere), the absorption of perovskite layers is nearly the same and higher than the reference sample at the wavelength between 540 nm and 640 nm, but is less at the wavelengths from 640 nm to 760 nm. Overall absorption of these two samples is nearly equal to the reference perovskite layer. When we look at the resonance peaks of just these two Ag NPs (Figure 5.10b), we can find that they are very similar and have only one resonance peak. From these two Ag NPs to 1/2 upper part Ag NPs, the resonance peak red-shifts with decrease of upper part of Ag NPs. This is due to (1) the change of the size difference of Ag NPs in different directions and (2) the change of contact area between Ag NPs and perovskite layer. Shift of the resonance peak position leads to a change of absorption of perovskite layer. When the Ag NPs have around 5/6 or 2/3 parts on top of perovskite layer, the absorption enhancements of the perovskite layer is larger than for other samples. This is because the resonance peaks of Ag NPs for these two samples are mostly in the poor absorption range of perovskite. 5/6 upper part Ag NPs will be selected for the next simulation step since the resonance of them can most strongly enhance the absorption of perovskite layers.

Particle density is also important for the application of plasmonic Ag NPs. In this simulation series, the coverage and thus the particle density of Ag NPs was varied. 90 nm 5/6 upper part Ag NPs were used in this simulation. Figure 5.11a shows the absorption spectra of perovskite layers without and with different densities of Ag NPs and Figure 5.11b presents absorption spectra of Ag NPs. Absorption of perovskite layers with Ag NPs is in all cases bigger than the reference perovskite layer and the resonance peak positions of Ag NPs are all nearly at the same wavelengths. At 620 nm, the absorption enhancement of perovskite layers increases with increase of particle density while at around 750 nm it decreases with increase of particle density. This means: (1) for higher density Ag NPs, their resonance at longer wavelength can contribute more to the absorption of Ag NPs whereas at shorter wavelengths can contribute more to scattering; (2) for lower density Ag

NPs, their resonance at longer wavelength contributes more to scattering. In this series simulation, Ag NPs with 13.4% density cause the strongest absorption enhancement of perovskite layer.

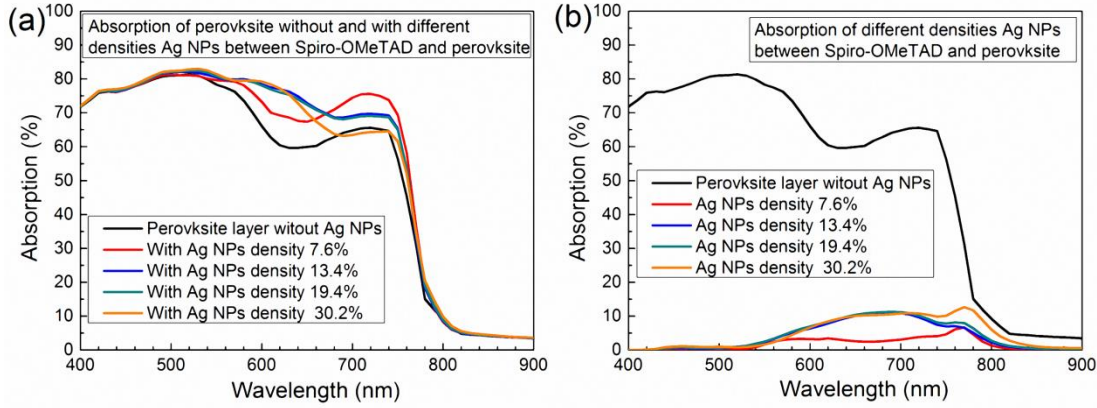


Figure 5.11: Absorption spectra of (a) perovskite layers without and with different densities of Ag NPs between Spiro-OMeTAD layer and perovskite layer, (b) Ag NPs of different density integrated between Spiro-OMeTAD layer and perovskite layer.

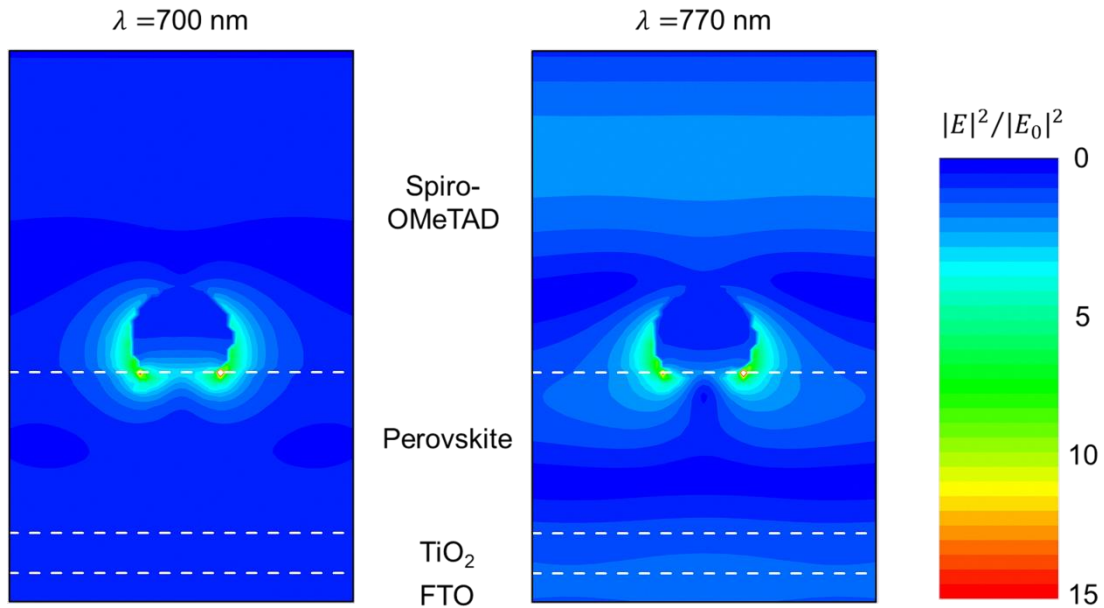


Figure 5.12: The cross sections of electrical field intensity at the middle of the 90 nm Ag NPs (with 5/6 upper part on top of perovskite layer) in x-z planes, at the resonance wavelength ($\lambda = 700$ nm); b) at the resonance wavelength ($\lambda = 770$ nm).

To understand how the absorption enhancement works, the electric field intensity profiles in the middle of the Ag NPs (90 nm, 5/6 upper part, 13.4% particle density) in the (x-z) plane are shown in Figure 5.12. At two different wavelengths (700 nm and 770 nm),

the mechanisms of absorption enhancement of perovskite layer are different. It's observed that at 770 nm wavelength, a Ag NP preferentially scatters the incident light back to the perovskite layer, which can enhance the absorption of the perovskite layer. At 700 nm wavelength, LSPR of Ag NP is generated to enhance the absorption of perovskite surrounding the Ag NP. The electric field at the corner of the contact area between Ag NPs and perovskite is much stronger than elsewhere; this is due to that the charges tend to concentrate at sharp corners.

5.2.2 Incorporation of Ag NPs between TiO_2 layer and perovskite layer

Simulation results of incorporating Ag NPs into the interface between TiO_2 layer and perovskite layer are shown in this section. The schematic structure used for the simulation is shown in Figure 5.7b. The influence of particle size is systematically studied and the absorption spectra of perovskite layers without and with different sizes of Ag NPs are shown in Figure 5.13a. Figure 5.13b shows the absorption spectra of different sizes of Ag NPs. To keep the simulation consistence with the previous section, simulation parameters used in this series samples are: particle coverage 13.4%, particle upper part: 5/6.

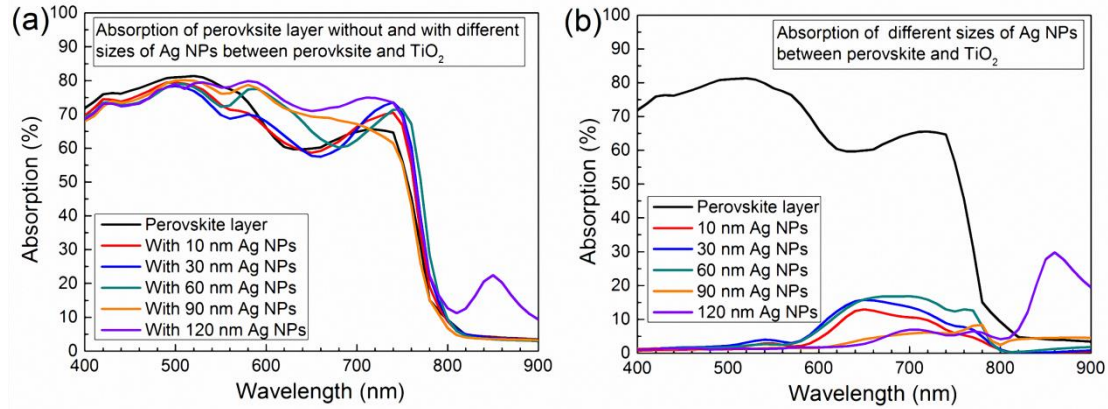


Figure 5.13: Absorption spectra of (a) perovskite layers without and with different size of Ag NPs between perovskite layer and TiO_2 layer, (b) different sizes of Ag NPs integrated between perovskite layer and TiO_2 layer.

It is observed that at short wavelengths between 400 nm and 560 nm, all samples with incorporation of Ag NPs have a weaker absorption than the reference perovskite layer. This can be due to the enhanced absorption of the FTO layer by Ag NPs at short wavelengths. At longer wavelengths till 600 nm, perovskite layers with incorporation of Ag NPs smaller than 60 nm still have less absorption. For perovskite layers with Ag NPs bigger than 30 nm, the absorption of them is higher at longer wavelength. The 120 nm Ag NPs cause the highest absorption enhancement. The difference of the absorption of perovskite layers with different sizes of Ag NPs can be explained by the Mie theory. Smaller particles preferentially absorb more of the incident light while bigger Ag NPs preferentially scatter more of the incident light. The refractive index of perovskite layer is bigger than that of TiO_2 layer. Hence the Ag NPs will preferentially forward scatter the incident light to the perovskite layer to enhance the absorption of it. It should be noted that in both cases the absorbed light in Ag NPs can have localized surface plasmon resonance which can also contribute to the perovskite which surrounds the particles.

5.2.3 Incorporation of Ag NPs between FTO and TiO₂ layer

In this section, Ag NPs are incorporated into the interface between FTO substrate and TiO₂ layer in simulation. The schematic structure used in the simulation is shown in Figure 5.7c. Due to the very thin (35 nm) thickness of TiO₂ layer, the particle size of the incorporated Ag NPs is controlled to be less than 35 nm. Coverage of Ag NPs is varied systematically and the shape of Ag NPs used is 5/6 upper part on top of FTO substrate.

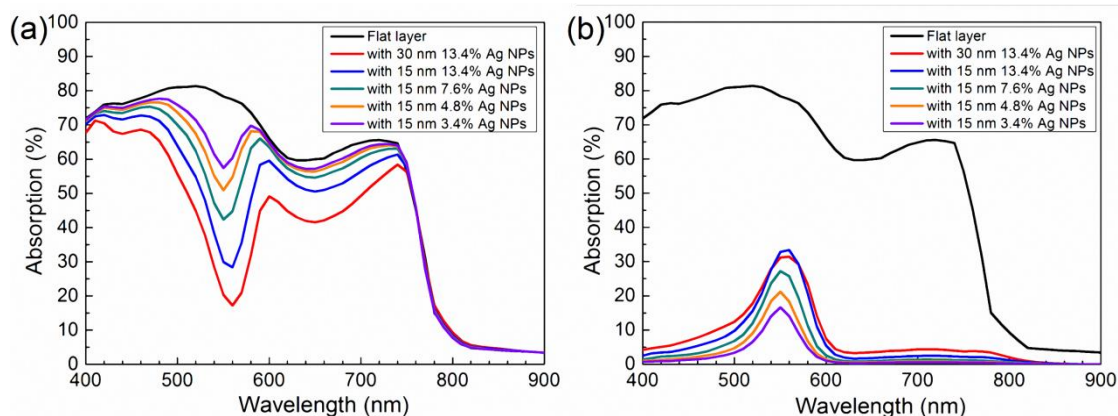


Figure 5.14: Absorption spectra of (a) perovskite layers without and with different size and density of Ag NPs between TiO₂ layer and FTO substrate, (b) different sizes of Ag NPs integrated between TiO₂ layer and FTO substrate.

Figure 5.14a shows absorption spectra of perovskite layers without and with different sizes and densities of Ag NPs and Figure 5.14b presents absorption of Ag NPs. It is observed that for all samples, the absorption of perovskite layers decreases with incorporation of Ag NPs. With increase of particle size from 15 nm to 30 nm, the absorption loss of perovskite layers increases. With decrease of particle density from 13.4% to 3.4%, the absorption loss of perovskite layers decreases. The absorption of Ag NPs decreases with decrease of particle size and density and the absorption peaks of Ag NPs correlate well with the absorption loss peaks of perovskite layers. There are different possible reasons. The light incidents from the glass side and passes through glass, FTO, Ag NPs and TiO₂ layer to perovskite layer which means only the light cannot be absorbed by those layers and Ag NPs can be considered to absorb in the perovskite layer. The sizes of the Ag NPs are too small to scatter the light to the perovskite layer which means the Ag NPs preferentially absorb the incident light. Moreover, LSPR generated by the Ag NPs can be used for enhancing absorption of FTO and TiO₂ which further decrease the light can be absorbed by the perovskite layer. It is also observed that, even with very small particles, if the density of them is very small, e.g., 3.4%, the absorption of perovskite layer at longer wavelength can be nearly equal to the reference perovskite layer. Therefore, for experiment, small size and low density Ag NPs should be investigated for this position.

5.3 Experimental incorporation of Ag NPs in ultra-thin perovskite solar cells

Optical simulation results in section 5.2 show that the absorption of the ultra-thin perovskite layer can be enhanced by incorporation of Ag NPs between spiro-OMeTAD

layer and perovskite layer and between perovskite layer and TiO_2 layer while it is reduced by incorporating Ag NPs at the other position. Since the simulation can only consider the ideal condition, it is worth realizing the simulation conditions to experiment: (1) to check the reality of incorporating Ag NPs into ultra-thin perovskite solar cells; (2) to check the agreement between simulation and experiment; (3) to improve the simulation base on experiments. In this section, Ag NPs are incorporated at different positions in the UTPSCs by the spray-CVD method. The positions are: (1) at the interface between perovskite layer and spiro-OMeTAD layer (see section 5.3.1); (2) at the interface between TiO_2 layer and perovskite layer (see section 5.3.2); (3) at the interface between FTO and TiO_2 layer (see section 5.3.3).

5.3.1 Deposition of Ag NPs on top of ultra-thin perovskite layer

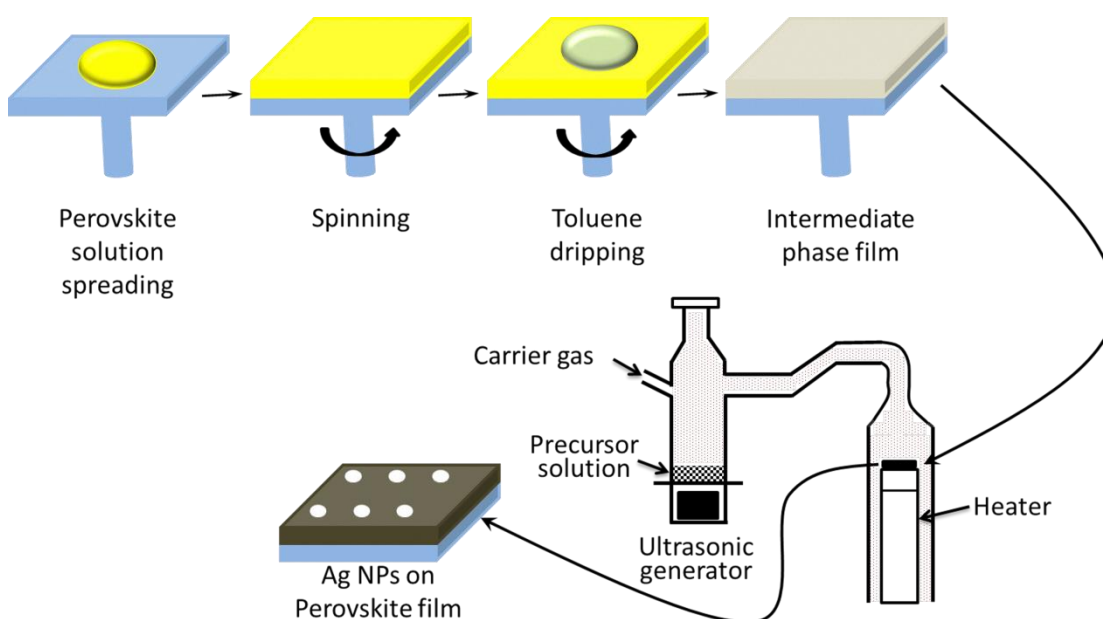


Figure 5.15 Schematic process of depositing Ag NPs on the surface of perovskite layers.

To deposit Ag NPs onto perovskite layer, a modified process is used. Figure 5.15 shows the schematic process of depositing Ag NPs on top of a perovskite layer. Compared to the standard process (see Figure 5.1), the substrate with the intermediate phase film is transferred to the heater in the spray-CVD set up and annealed at $90\text{ }^{\circ}\text{C}$ with N_2 flowing for 10 min. After the annealing step, spray-CVD deposition of Ag NPs starts and lasts for different time. Then the samples are cooled down to room temperature and transferred to a glove box for characterizations.

Photos of the obtained ultra-thin perovskite layers with and without Ag NPs deposition are shown in Figure 5.16. The upper three photos show the perovskite layers after annealing and before deposition of Ag NPs. It is observed that in all of the three samples the perovskite layers show dark brown color which is the same as the perovskite layer prepared by the standard process (see Figure 5.1). The lower three photos show the corresponding samples deposited with Ag NPs for 0 min, 1 min and 2.5 min, respectively. Concentration of precursor solution, substrate temperature and N_2 flow rate were 10 mM,

90 °C and 1 L/min, respectively. After 1 min deposition of Ag NPs, the color of the perovskite layer changes to light brown. With 2.5 min deposition of Ag NPs, the perovskite layer color changes strongly to yellow which is obviously not the color of $\text{CH}_3\text{NH}_3\text{PbI}_3$.

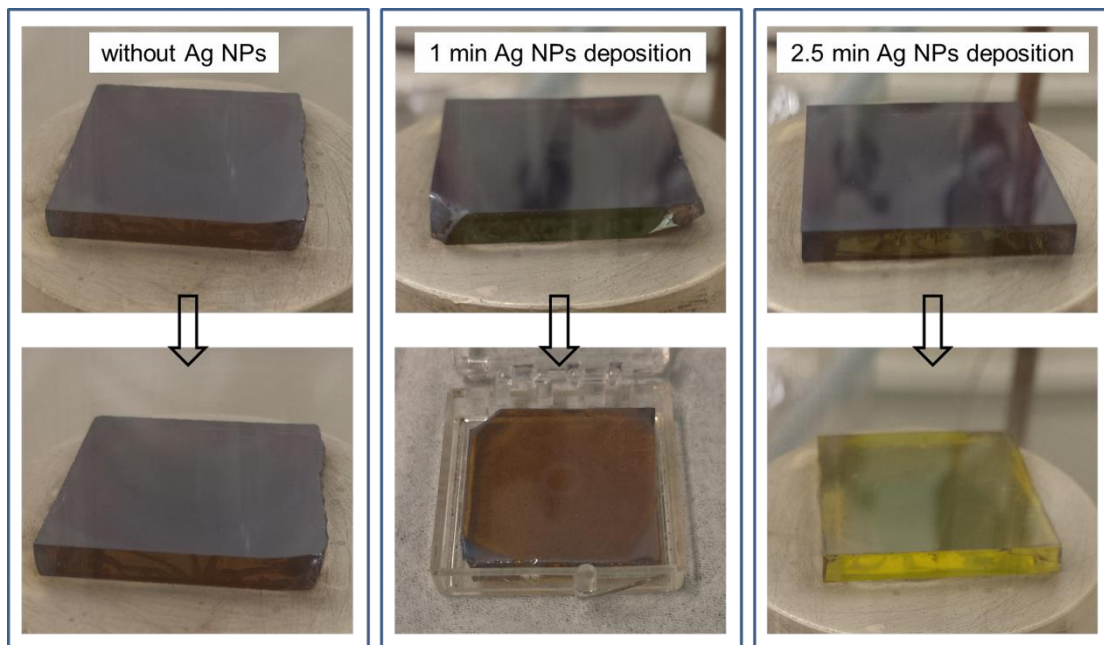


Figure 5.16: Photos of perovskite layers before and after deposition of Ag NPs for 0, 1 and 2.5 min.

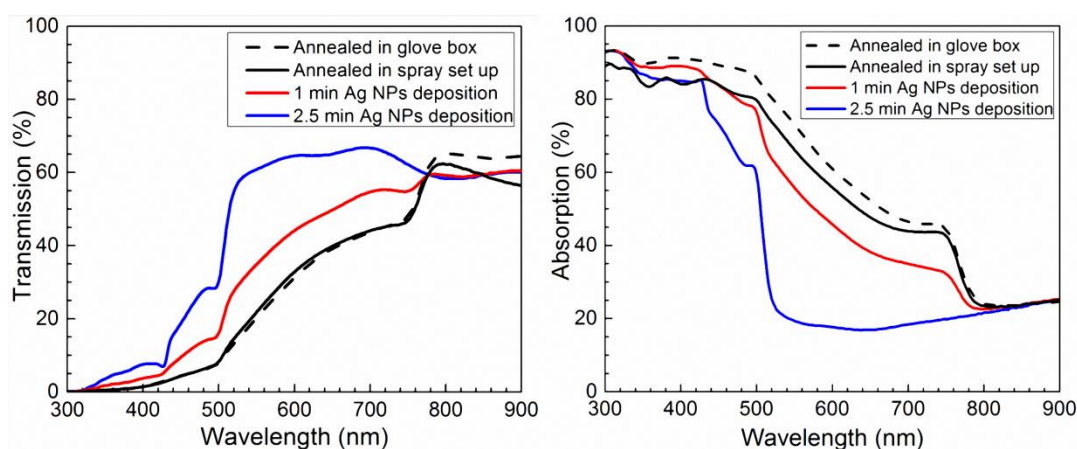


Figure 5.17 Transmission and absorption spectra of perovskite layer (annealed in spray-CVD setup) before and after deposition of Ag NPs for 1 min and 2.5 min. Spectra of a standard process prepared perovskite layer are used as reference.

To compare the optical properties before and after deposition Ag NPs on top of perovskite layer, UV-Vis measurements were carried out. Transmission and absorption spectra of the three samples are shown in Figure 5.17. Spectra of the perovskite layer prepared using the standard process in glove box is shown as reference. From transmission spectra, there is no difference between the perovskite layer prepared in the spray-CVD set up and the standard perovskite layer. However, after deposition of Ag NPs on perovskite layer for 1 min and 2.5 min the transmission increases significantly. In the absorption

spectra, the standard process perovskite layer absorbs more light than the layer prepared in spray-CVD set up in the wavelength from 300 nm to 780 nm, the absorption difference can be due to the reduction of reflection of the standard perovskite layer. The absorption edges of both layers are at 780 nm which is the band gap of $\text{CH}_3\text{NH}_3\text{PbI}_3$ [10]. The absorption of the perovskite layer with 1 min Ag NPs deposition is less than that of perovskite layers without Ag NPs and an extra absorption edge at around 550 nm appears. The extra absorption edge could be attributed to the generation of PbI_2 [172]. After deposition of Ag NPs for 2.5 min, the absorption edge at 780 nm disappears completely and the absorption edge at around 550 nm is very obvious. Absorption of the 2.5 min sample is less than the other three samples. The change of absorption edge and color of the sample indicates the decomposition of $\text{CH}_3\text{NH}_3\text{PbI}_3$ under the environment of Ag NPs deposition. Reason of the decomposition could be the instability of $\text{CH}_3\text{NH}_3\text{PbI}_3$ in ethanol and high temperature environment [30].

In summary, using the spray-CVD method to deposit Ag NPs on top perovskite layers leads to reduction of absorption and decomposition of the layers. The temperature used for Ag NPs deposition was 90 °C which is already very low for Ag NPs deposition. Therefore, it is very hard to use the spray-CVD method to deposit Ag NPs on top of perovskite layers without damaging the layer itself. If the stability problem of perovskite layer under the spray-CVD condition can be resolved, it will be promising to integrate Ag NPs on top of perovskite layer by the spray-CVD method. Since the stability of perovskite layers is challenging in practical application, many researchers are focusing on this problem and resolve it soon [30, 173].

5.3.2 Deposition of Ag NPs on top of the TiO_2 layer

In this section, Ag NPs are first deposited and the perovskite layer is deposited on top of the Ag NPs to study the influence of Ag NPs on the growth of perovskite layers and on the performance of perovskite solar cells. Figure 5.18 shows SEM images of the FTO substrate before and after deposition of Ag NPs for different time. Spray-CVD was used for the deposition of Ag NPs and deposition times were 0.5 min, 2 min and 4 min. Other conditions for the deposition of Ag NPs were: 200 °C substrate temperature, 10 mM precursor solution concentration and 1L/min N_2 flow rate. Using different deposition times, different sizes of Ag NPs are achieved on top of FTO substrates.

After deposition of Ag NPs, perovskite layers were deposited on top of bare FTO substrate and FTO with 4 min Ag NPs to study the effect of Ag NPs on the growth of perovskite. Figure 5.19 shows SEM images of the two samples before and after deposition of perovskite layers on top. It's observed that the perovskite layer grows on top of FTO substrate as a continuous film and nearly no pinhole appears in the film. Grains of perovskite can be also observed from the same sample. For the 4 min Ag NPs sample, there is no continuous compact film of perovskite formed and many holes are generated in the structure. From the comparison, appearance of Ag NPs affects the growth of the perovskite layer strongly.

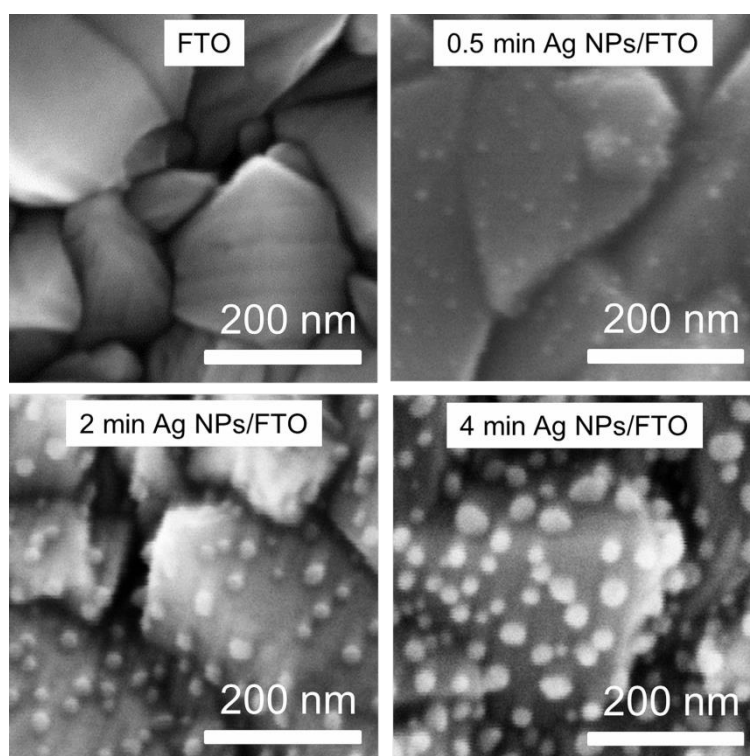


Figure 5.18: SEM images of FTO substrates without and with deposition of Ag NPs. Deposition times are 0.5 min, 2 min and 4 min.

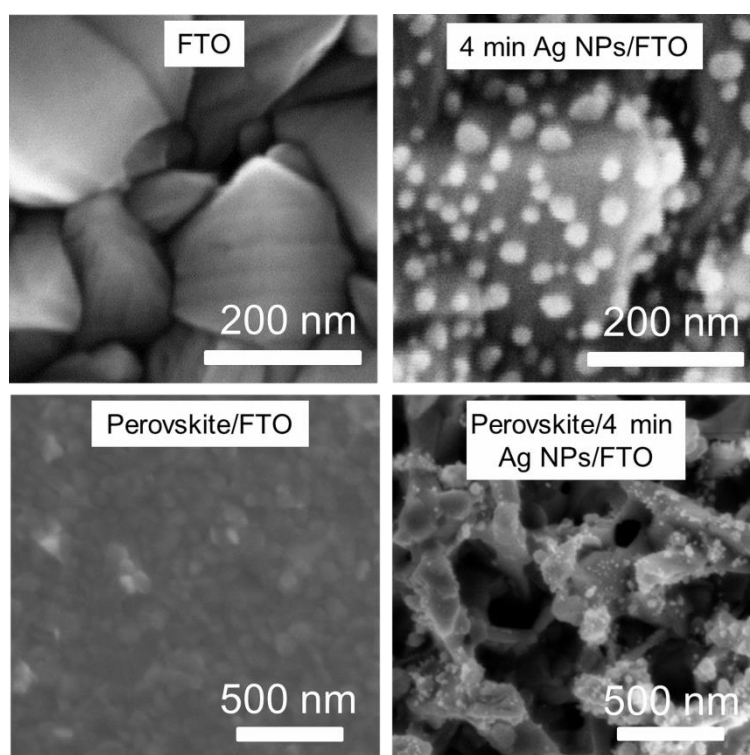


Figure 5.19: SEM images of FTO substrate before and after deposition of Ag NPs for 4 min. SEM images of perovskite layers deposited on top of the two samples are also shown.

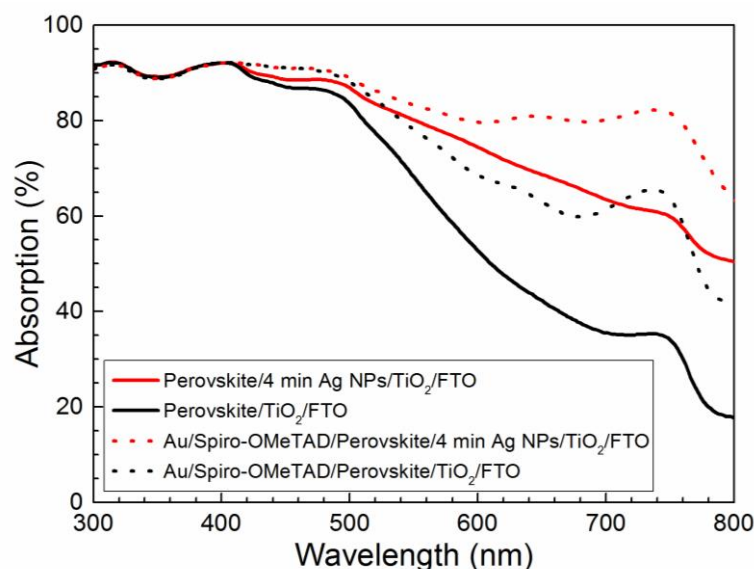
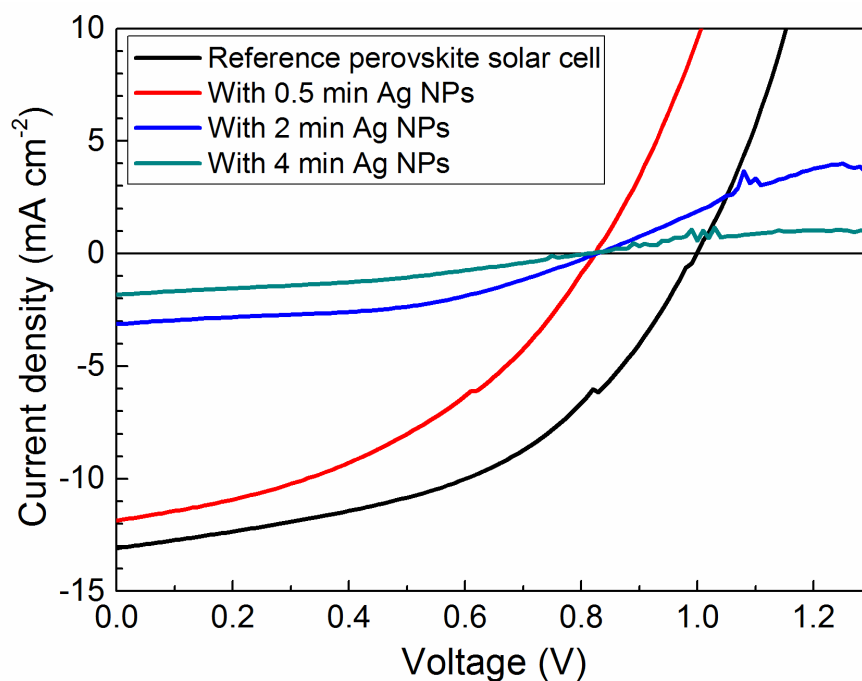


Figure 5.20: Absorption spectra of perovskite/TiO₂/FTO, perovskite/4 min Ag NPs/TiO₂/FTO, Au/Spiro-OMeTAD/perovskite/TiO₂/FTO and Au/Spiro-OMeTAD/perovskite/4 min Ag NPs/TiO₂/FTO.

To investigate the influence of Ag NPs on the optical properties of perovskite layer and whole perovskite solar cell, four new samples were fabricated which are perovskite/TiO₂/FTO, perovskite/4 min Ag NPs/TiO₂/FTO, Au/Spiro-OMeTAD/perovskite/TiO₂/FTO and Au/Spiro-OMeTAD/perovskite/4 min Ag NPs/TiO₂/FTO. Absorption spectra of the four samples are shown in Figure 5.20. It's observed that with incorporation of 4 min Ag NPs, the absorption of perovskite layer and whole perovskite solar cell increase significantly at wavelengths between 450 nm and 800 nm. This gives strong evidence that incorporation of Ag NPs can contribute to absorption enhancement of perovskite solar cells. Interestingly, the absorption of the complete perovskite solar cells are stronger than that of the perovskite layers alone. The absorption difference must be due to the Au back contact layer and the Spiro-OMeTAD layer.

Absorption spectra shown in Figure 5.20 reveal that incorporation of Ag NPs at the interface between perovskite layer and TiO₂ layer leads to absorption enhancement of perovskite solar cells. Although the morphology of the perovskite layer can be influenced strongly by the Ag NPs, it is worth to investigate whether the Ag NPs can enhance the performance of perovskite solar cells. Therefore, four devices without and with incorporation of different time deposited Ag NPs are fabricated and measured. Figure 5.21 shows the *J-V* curves and performances of the four samples. The perovskite solar cell without Ag NPs exhibits J_{sc} 13.1 mA/cm², open circuit voltage (V_{oc}) 0.99 V, fill factor (FF) 0.48, leading to PCE 6.2% which is the best in these four samples. For the solar cells with Ag NPs at the interface between perovskite and TiO₂, all the four parameters are lower than the reference cell. V_{oc} of the three samples with Ag NPs is similar but J_{sc} decreases with increase of deposition time of Ag NPs. Decrease of V_{oc} and FF can be attributed to the formation of recombination centers by Ag, which is mainly due to the direct contact between Ag NPs and perovskite layer [32, 33]. Several reasons can cause the decrease of J_{sc} , e.g., (1) growth and layer properties of perovskite layer influenced by Ag NPs, (2) recombination velocity increased at the interface between perovskite and TiO₂ due to the exist of Ag NPs, (3) parasitic absorption of Ag NPs prior to the absorption of perovskite.



Samples	J_{sc} (mA/cm ²)	V_{oc} (V)	FF	PCE(%)
Reference	13.1	0.99	0.48	6.2
0.5 min Ag NPs	11.9	0.82	0.41	4.0
2 min Ag NPs	3.1	0.82	0.46	1.2
4 min Ag NPs	1.8	0.81	0.36	0.5

Figure 5.21: J - V curves and performances of the perovskite solar cells without and with incorporation of different deposition time Ag NPs at the perovskite/ TiO_2 interface.

Based on the content shown in this section, incorporation of Ag NPs at the interface between perovskite layer and TiO_2 layer (1) affects growth of perovskite layer and leads to a multi hole structure, (2) causes significantly absorption enhancement of perovskite solar cells and (3) decreases performance of perovskite solar cells. Therefore, the perovskite/ TiO_2 interface is not suitable for the incorporation of Ag NPs. Direct contact between Ag NPs and perovskite is an important reason for the bad effects, but the absorption enhancement caused by Ag NPs is still promising. If the Ag NPs can be covered by TiO_2 layer, most of the bad effects of Ag NPs could be avoided. Therefore, the third position which is the interface between FTO and TiO_2 layer is applied for incorporating Ag NPs in further studies.

5.3.3 Deposition of Ag NPs on top of the FTO layer

In this section, different sizes of Ag NPs are deposited on top of FTO substrates and then covered by a compact TiO_2 layer to avoid the direct contact between Ag NPs and the perovskite layer.

Figure 5.22b-e shows SEM images of FTO substrates without and with different sizes of Ag NPs. Ag NPs were deposited on clean FTO substrates by spray-CVD. The precursor solution was prepared by dissolving Ag(hfacac)PMe₃ in ethanol with a concentration of 10

mM. The nitrogen flow rate was controlled to be 1 liter per minute and the substrate temperature was set to 110 °C during the deposition process. The deposition time was adjusted to 0.5, 1 and 5 min in order to vary the size (diameter from SEM) of the Ag NPs. The FTO glass substrates without Ag NP deposition were used as control samples. Figure 5.22a shows the schematic structure of Ag NPs on top of FTO coated glass substrate. Sizes of the Ag NPs are 11 nm (Figure 5.22b, 0.5 min deposition), 16 nm (Figure 5.22b, 1 min deposition) and 36 nm (Figure 5.22b, 5 min deposition). It is observed that in all three cases the sizes of the Ag NPs varied not much, which can be recognized as nearly mono-dispersed.

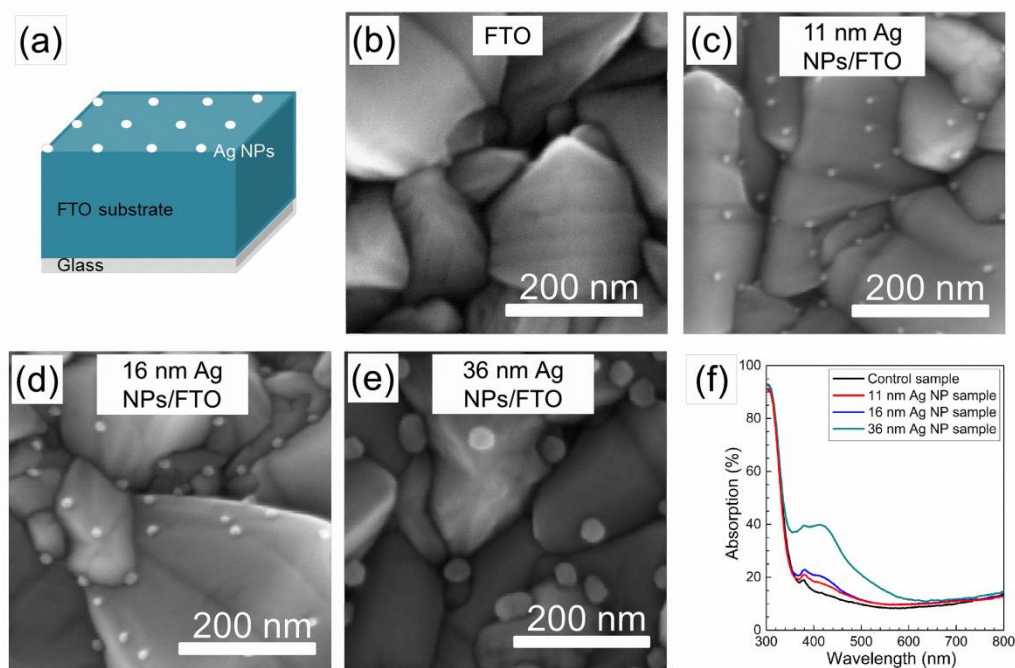


Figure 5.22: (a) Schematic sample structure of Ag NPs on top of FTO coated glass substrate. (b-e) SEM images of FTO coated glass substrates without (b) and with 11 nm Ag NPs (c), 16 nm Ag NPs (d), 36 nm Ag NPs (e) on top. (f) UV-Vis spectra of FTO coated glass substrate and with different sizes of Ag NPs on top.

Optical properties of Ag NPs deposited on FTO substrates were studied by UV-Vis measurements. Reflection and transmission of the three samples were recorded and the absorption of each sample was calculated (shown in Figure 5.22f). Compared to the FTO/glass substrate, the absorption is clearly enhanced for the three Ag NPs samples. The significant absorption enhancement from the 11 nm Ag NP sample to the 36 nm Ag NP sample is due to the increase of both size and coverage. In all three cases with Ag NPs (11nm, 16nm and 36 nm) an absorption peak around 430 nm is observed. As the $\text{CH}_3\text{NH}_3\text{PbI}_3$ perovskite layer can convert light with wavelengths between 300 nm and ~800 nm to electron-hole pairs, plasmonic effects of the Ag NPs with a resonance peak around 430 nm could be exploited to enhance the performance of such perovskite solar cell.

After the characterization of the four samples by SEM and UV-Vis, a compact TiO_2 layer was deposited on top of them by spray pyrolysis. Figure 5.23a presents the structure in which the Ag NPs on top of FTO coated glass substrate is covered by a TiO_2 compact

layer. Figure 5.23b, 5.23c, 5.23d and 5.23f show the SEM images for the samples from Figure 5.22 with covering of an additional TiO_2 thin layer. For all the samples in Figure 5.23b-5.23e, the thin TiO_2 layers were very homogeneous and followed the structure of FTO surface. Almost no Ag NPs can be observed from Figure 5.23c-5.23e, which means that all Ag NPs were covered by the TiO_2 layer. In Figure 5.23e, the distances between the Ag NPs nearly don't change compared to the same sample without TiO_2 coating (Figure 5.22e). This indicates that the Ag NPs on the surface of FTO were stabilized at their original positions by the TiO_2 compact layer.

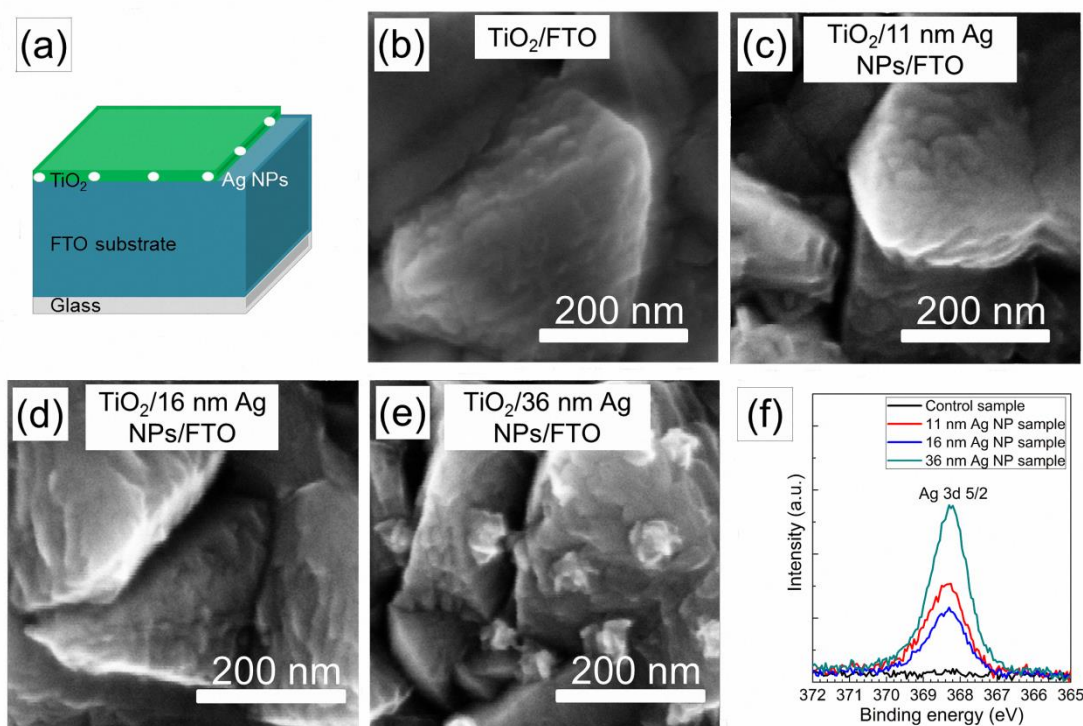


Figure 5.23: (a) Schematic sample structure of $\text{TiO}_2/\text{Ag NPs}/\text{FTO}/\text{glass}$. (b-e) SEM images of TiO_2 layer coated on FTO coated glass substrates without (b) and with 11 nm Ag NPs (c), 16 nm Ag NPs (d), 36 nm Ag NPs (e) on top. (f) XPS spectra of Ag 3d 5/2 core level measured on compact TiO_2 layers, which cover the bare FTO substrate (control sample) and FTO substrates with 11 nm Ag NPs, 16 nm Ag NPs and 36 nm Ag NPs, respectively.

A typical series of XPS spectra is shown in Figure 5.23f. The most interesting peak is the Ag 3d 5/2 core level with a binding energy of 368.3eV which is typically assigned to the pure Ag element. For the samples shown in Figure 5.23b-5.23e, as the TiO_2 layers were very thin (~ 35 nm), XPS measurements were taken to investigate whether the Ag NPs were fully covered by TiO_2 layer. It is observed that there is no Ag signal detected on the control sample, but Ag signals are detected on the surface of TiO_2 for all the samples with Ag NPs. With increase of particle size from 11 nm to 36 nm Ag NPs, the detected Ag signal intensity increases. Interestingly, the Ag signal intensity of the 16 nm Ag NP sample is smaller than that of 11 nm Ag NP sample. According to the XPS results, the Ag NPs are not fully covered by TiO_2 or there is diffusion of Ag to the surface of TiO_2 . Both of the

possibilities can cause the direct contact between perovskite layer and Ag NPs, leading to the formation of recombination centers at the interface between perovskite and TiO_2 layer.

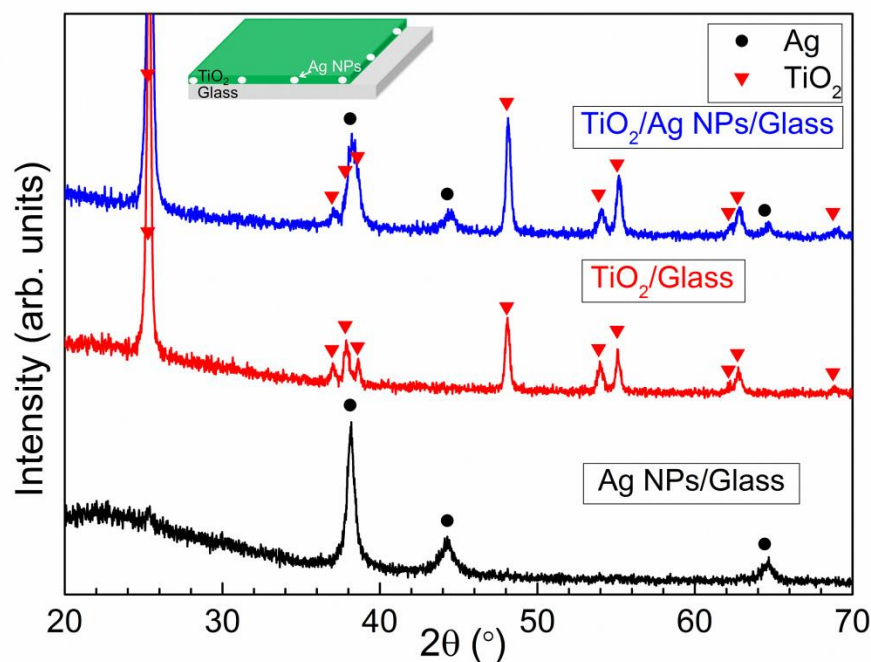


Figure 5.24: XRD spectra of Ag NPs/glass, TiO_2 /glass and TiO_2 /Ag NPs/glass samples.

Although from Figure 5.23c-5.23e it looks like the shape of the Ag NPs doesn't change, it is hard to confirm from SEM images whether the particles underneath TiO_2 are still Ag NPs. To investigate this, XRD measurements were carried out. Figure 5.24 gives XRD spectra for Ag NPs/glass, TiO_2 /glass and TiO_2 covered Ag NPs/glass. Characteristic peaks of Ag (JCPDS Files No.: 04-0783) and TiO_2 (JCPDS Files No.: 21-1272) are marked in the figure. Only peaks of Ag are detected for the Ag NPs/glass sample and only peaks of TiO_2 are observed for the TiO_2 /glass sample. For the sample after deposition of the TiO_2 layer onto the Ag NPs, peaks of both Ag and TiO_2 are observed and all the peaks can be attributed to Ag and TiO_2 . This observation confirms that the Ag NPs still exist after deposition of TiO_2 and no other crystal phase is found. Figure 5.22, Figure 5.23 and Figure 5.24 can provide the information that the deposition of the TiO_2 layer can stabilize the Ag NPs at their location and no defect phases were generated during the deposition.

To understand the effect of Ag NPs on the charge transfer at the $\text{CH}_3\text{NH}_3\text{PbI}_3/\text{TiO}_2$ interface better, SPV measurements were carried out. Figure 5.25a shows the schematic structure of the samples used for the SPV measurements. Figure 5.25b presents spectra of the in-phase and phase-shifted by 90° SPV signals of the control sample and the 11 nm, 16 nm and 36 nm Ag NP samples. The in-phase signals are positive for all the four samples which means that photo generated electrons were separated preferentially towards the $\text{CH}_3\text{NH}_3\text{PbI}_3/\text{TiO}_2$ interface. The in-phase signals and phase-shifted by 90° signals have opposite sign shows that charge separation was caused by only one mechanism. The decrease of both in-phase and phase-shifted by 90° signals with implementation of Ag NPs can be attributed to the increase of recombination. The phase-shifted by 90° signals reduced stronger than in-phase signals indicates the enhancement of de-trapping probability of electrons. This can be due to the increase of contact between Ag NPs and

TiO₂ layer. Moreover, Ag NPs were not fully covered by the TiO₂ layer, which led to a direct contact between Ag NPs and the perovskite layer. Hence, Ag NPs can support the channel for recombination between the de-trapped electrons from TiO₂ layer and holes from the perovskite layer. This could be another reason in addition to the recombination centres for the decrease of V_{oc} in solar cells.

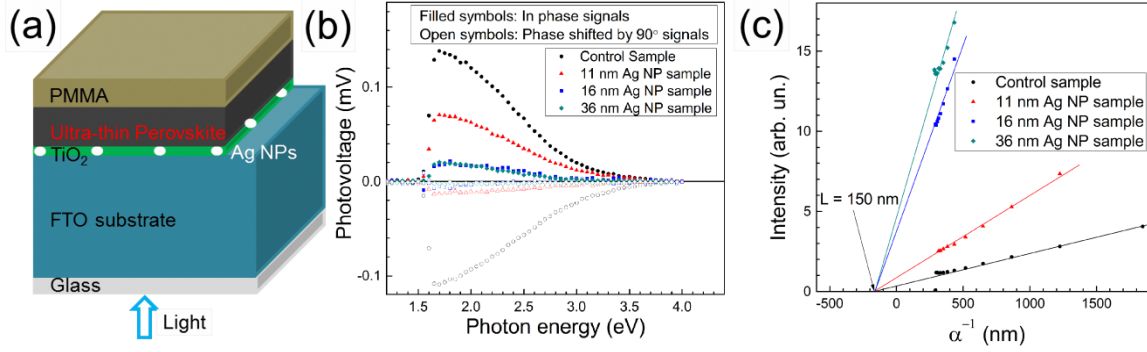


Figure 5.25: (a) Schematic sample structure of PMMA/ultra-thin perovskite layer/TiO₂/Ag NPs/FTO/glass. (b) SPV spectra of the in-phase (filled symbols) and phase shifted by 90° (open symbols) SPV signals of ultra-thin perovskite layers deposited on TiO₂/(with and without) Ag NPs/FTO/Glass and coated with PMMA. (c) Goodman plots measured for constant SPV signals of ultra-thin perovskite layers deposited on TiO₂/(with and without) Ag NPs/FTO/Glass and coated with PMMA.

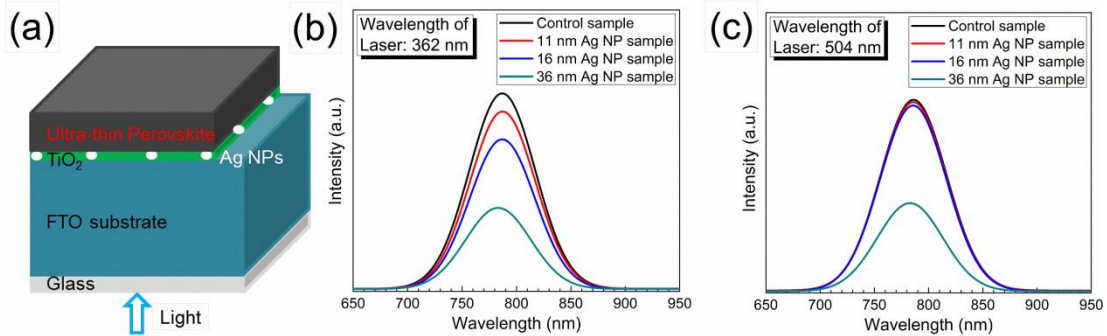


Figure 5.26: (a) Schematic sample structure of ultra-thin perovskite layer/TiO₂/Ag NPs/FTO/glass. (b-c) Photoluminescence spectra of ultra-thin perovskite layers coated on TiO₂/FTO/glass (control sample) and on TiO₂/Ag NPs/FTO/glass (with different size, i.e., 11 nm, 16 nm and 36 nm) samples. PL spectra at the perovskite/TiO₂ interface (b) and at deeper position from interface (c) were measured by laser with wavelengths of 362 nm and 504 nm, respectively.

Figure 5.25c shows the transport lengths of minority charge carriers in the control sample, 11 nm, 16 nm and 36 nm Ag NP samples derived from SPV [60]. For all four samples, the transport lengths are around 150 nm. This means the implementation of Ag NPs will not cause reduction of J_{sc} originating from reduced diffusion lengths of charge carriers. As remark, the layer thickness was equal to the transport length that gives evidence for the formation of an electric field across the whole layer.

To further study the effect of Ag NPs, steady-state photoluminescence (PL) was measured for the control sample and the 11 nm, 16 nm and 36 nm Ag NP samples. There were no spiro-OMeTAD layer and Au back contact layer for the samples used in PL measurement. The schematic structure of the samples used for PL measurements is shown in Figure 5.26a. Lasers with wavelengths of 362 nm and 504 nm were chosen for incidenting from the glass side for the measurement at $\text{CH}_3\text{NH}_3\text{PbI}_3/\text{TiO}_2$ interface and at a deeper position within the $\text{CH}_3\text{NH}_3\text{PbI}_3$ layer, respectively. The results are shown in Figure 5.26b and Figure 5.26c. It is observed from Figure 5.26b that there is clear quenching of steady-state PL caused by Ag NPs, indicating improved charge separation at the $\text{CH}_3\text{NH}_3\text{PbI}_3/\text{TiO}_2$ interface and more electrons being trapped into the TiO_2 layer [96]. Correlating this to the above discussion, this can be partly due to the localized surface plasmon resonance (LSP) of the Ag NPs. The quenching effect becomes stronger with increase of Ag NPs' sizes from 11 nm to 36 nm. At 504 nm laser wavelength corresponding to a deeper probing position, the same quenching effect happens for the 36 nm Ag NP sample only while the PL density of the control sample, 11 nm Ag NP sample and 16 nm Ag NP sample are nearly equal. From the two PL measurements, the consistency on 36 nm Ag NP sample and difference on the 11 nm and 16 nm Ag NP samples confirm that the effect of Ag NPs takes place only very near the Ag NPs. This finding agrees with localization of field enhancement due to the LSP effect. The localized surface plasmon resonances of NPs can be used for photocurrent enhancement of perovskite solar cells.

By *J-V* measurements, the effect of Ag NPs on the performance of UTPSCs was investigated. Figure 5.27a shows the schematic structure of UTPSC with integration of Ag NPs at the TiO_2/FTO interface. In all the figures, a schematic structure of the samples used for each measurement is shown to facilitate understanding. Figure 5.27b presents *J-V* curves of the best UTPSCs with and without Ag NPs selected from more than 20 devices. Diameters of Ag NPs varied from 11 nm to 16 nm. In the content afterwards, the UTPSC without Ag NPs is named as control sample while the UTPSCs with 11 nm and 16 nm Ag NPs are named as 11 nm Ag NP sample and 16 nm Ag NP sample, respectively. The control sample exhibited 1.02 V V_{oc} , $J_{sc} = 14.1 \text{ mA/cm}^2$, and FF = 0.58, leading to a PCE of 8.3%. With implementation of different sizes of Ag NPs, V_{oc} of the UTPSCs decreases from 1.02 V to 0.99 V (both 11 nm and 16 nm Ag NP sample). This can be due to the Ag NPs acting as recombination center in the UTPSCs. However, J_{sc} of the UTPSCs first increases from 14 mA/cm^2 of the control sample to 15.9 mA/cm^2 of the 11 nm Ag NP sample (13.5% increase compared to the control sample), then increases less to 15.8 mA/cm^2 for the 16 nm Ag NP sample (12.7% increase compared to control sample). FF of the 11 nm Ag NP sample is 0.58 which is the same as the control sample while for the 16 nm Ag NP sample FF is 0.54 which is a bit lower. The increase of J_{sc} leads to the increase of PCE from 8.3% for the control sample to 9.1% for the 11 nm Ag NP sample and 8.4% for the 16 nm Ag NP sample. The relative increase of PCE by incorporating 11 nm and 16 nm Ag NPs are 10.4% and 1.4%, respectively. Due to the decrease of V_{oc} , the increase of PCE is not as high as the one in J_{sc} .

To ensure the reliability of the enhancement, more than 20 devices were prepared for each configuration in three batches. The average device performance parameters are presented in Figure 5.27c. For the 11 nm Ag NP samples, an average J_{sc} of 13.2 mA/cm^2 was achieved, which is 22.2% higher than the average J_{sc} of 10.8 mA/cm^2 for the control

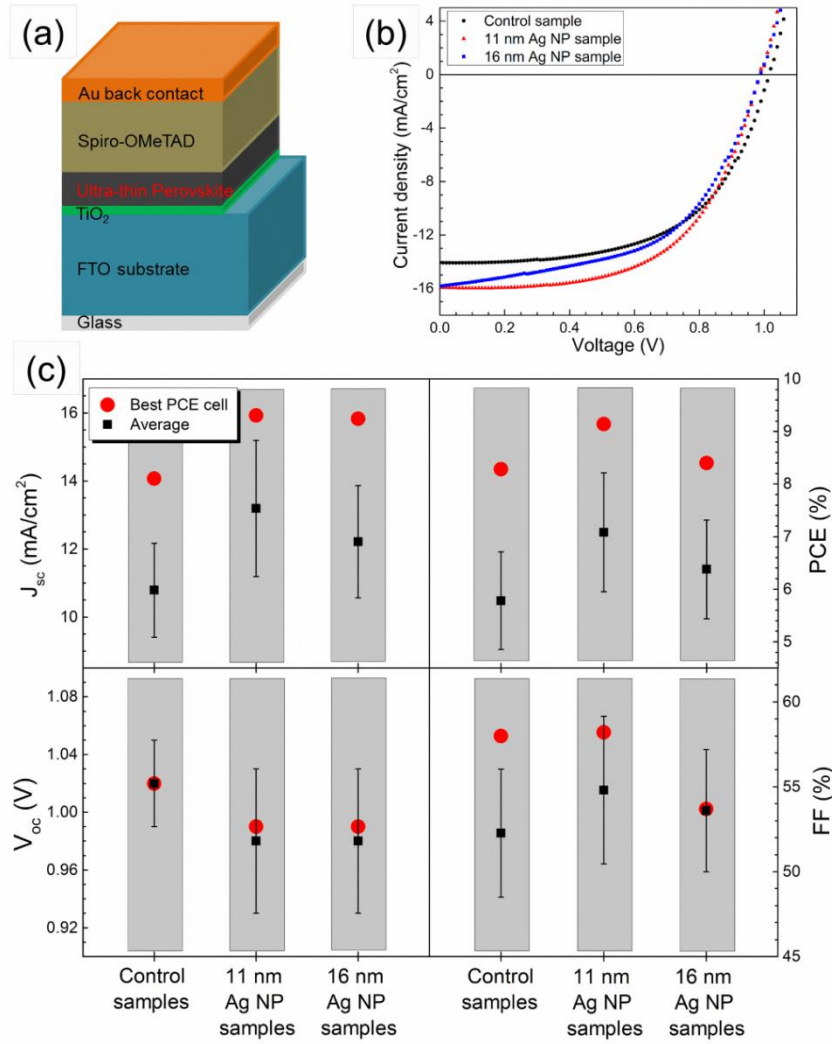


Figure 5.27: (a) Schematic device structure of ultra-thin perovskite solar cell with incorporation of Ag nanoparticles at the TiO₂/FTO interface. (b) *J-V* curves of the best PCE ultra-thin perovskite solar cells without (control sample) and with 11 nm (11 nm Ag NP sample), 16 nm (16 nm Ag NP sample) Ag NPs. (c) Average devices performances of control samples, 11 nm Ag NP samples and 16 nm Ag NP samples measured by reverse scan. For each condition, more than 20 devices were fabricated and measured.

samples. At the same time, the average J_{sc} is 12.2 mA/cm² for the 16 nm Ag NP samples, which is 13.2% higher than that of the control samples. The average FF of 11 nm Ag NP samples is 0.55 while that of 16 nm Ag NP samples is 0.54, both of which are higher than 0.52 for the control samples. The increase of both J_{sc} and FF leads to the improvements of the average PCE from 5.8% for the control samples to 7.1% (22.5% relative) for the 11 nm Ag NP samples and to 6.4% (10.5% relative) for the 16 nm Ag NP samples. Therefore, it's confirmed that the incorporation of Ag NPs can improve the device performance of UTPSC by enhancing the photocurrent. It has to be pointed out that in each batch the enhancement of J_{sc} and PCE by incorporating Ag NPs has the same trend (shown in Figure 5.28). The consistency of the enhancement in different batches confirmed again the influence of Ag NPs on UTPSCs. However, it is also observed that V_{oc} decreased clearly due to the integration of both 11 nm and 16 nm Ag NPs, which lowers the increase of

average PCE for both the 11 nm and 16 nm Ag NPs samples. If the decrease of V_{oc} can be prevented, even higher improvement of PCE can be expected.

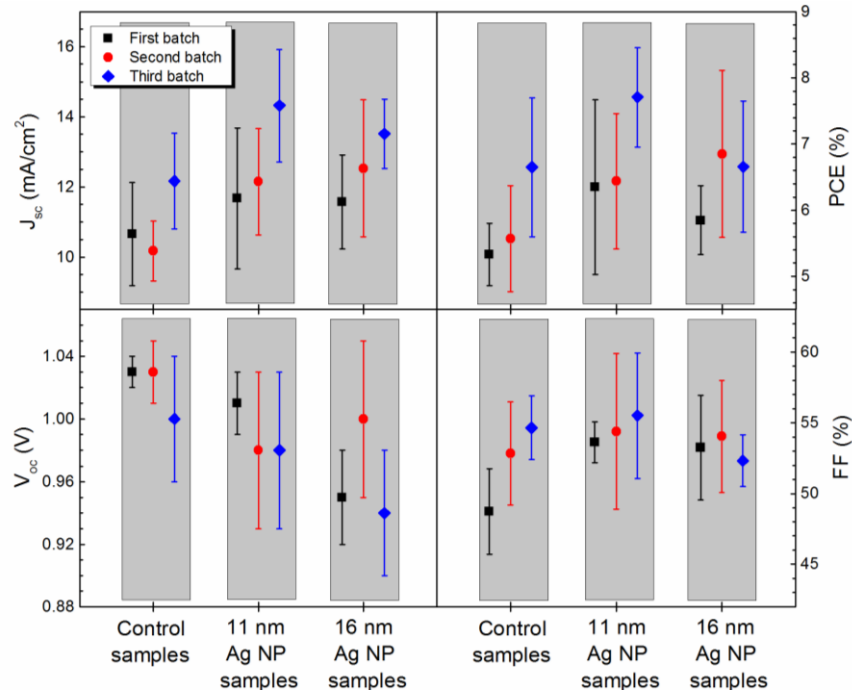


Figure 5.28: Average devices performances in three different batches of control samples, 11 nm Ag NP samples and 16 nm Ag NP samples measured by reverse scan.

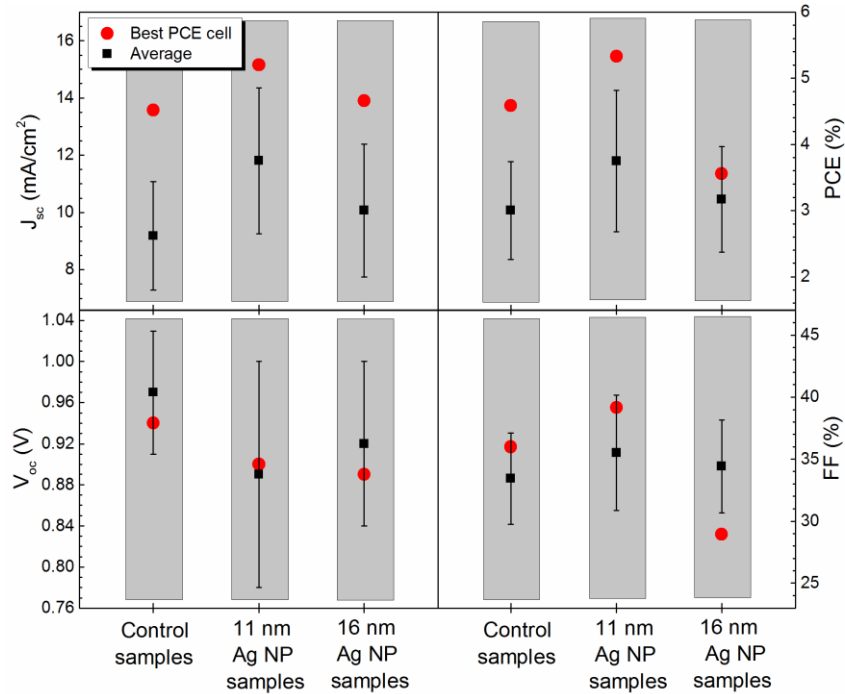


Figure 5.29: Average devices performances of control samples, 11 nm Ag NP samples and 16 nm Ag NP samples measured by forward scan.

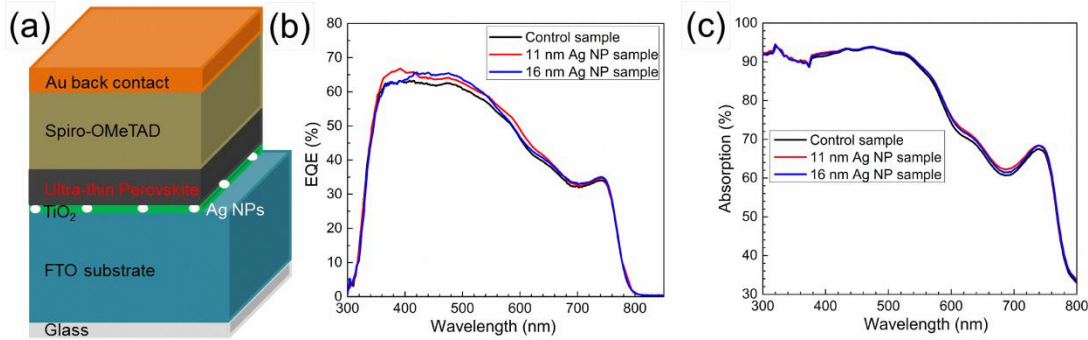


Figure 5.30: (a) Schematic device structure of ultra-thin perovskite solar cell with incorporation of Ag nanoparticles at the TiO₂/FTO interface. (b) EQE of the ultra-thin perovskite solar cells without (control sample) and with 11 nm (11 nm Ag NP sample), 16 nm (16 nm Ag NP sample) Ag NPs. (c) UV-Vis spectra of the ultra-thin perovskite solar cells without (control sample) and with 11 nm (11 nm Ag NP sample), 16 nm (16 nm Ag NP sample) Ag NPs.

Figure 5.27 shows the reverse scan performances of the UTPSCs and Figure 5.29 the average forward scan performances of the same samples shown in Figure 5.27. The differences of which agreed well with the reverse scan behavior.

Figure 5.30b shows the external quantum efficiency (EQE) for typical devices. Architecture of the devices is presented in Figure 5.30a. The EQE spectrum from the 11 nm Ag NP sample and 16 nm Ag NP sample increased in the wavelength range from 350 nm to 700 nm compared to the control sample. The differences on EQE for the three samples indicate the broadband current enhancement by implementation of 11 nm Ag NPs and 16 nm Ag NPs. Absorption spectra of the control sample and the 11 nm Ag NP and 16 nm Ag NP solar cells are shown in Figure 5.30c. It is observed that at wavelengths between 300 nm and 580 nm there is almost no difference for the three devices. At the wavelengths between 580 nm and 700 nm, Ag NPs cause a slight absorption enhancement (in Figure 5.30c) which contributes to the EQE improvement. From Figure 5.22f, the resonance peak of Ag NPs would be expected at wavelengths around 580 nm. The shift of the Ag NPs resonance peak position can be due to the change of medium surrounding the Ag NPs from air to TiO₂, the resonance peak will however redshift which can explain the enhancement between 580 and 700 nm. Therefore, the resonant behavior of the Ag NPs contributes to the absorption and EQE enhancement of UTPSC in the longer wavelength range. But for shorter wavelengths, other effects of the Ag NPs need to cause the enhancement of EQE. Compared to the absorption spectra, there is loss of EQE between 300 nm and 350 nm for all the solar cells. This is because the light is mainly absorbed by FTO/glass substrate and TiO₂ layer. It will be very promising if this part of light can be also contribute to the performance of UTPSCs.

The substance shown above gives clear evidences for the encouraging finding that incorporation of Ag NPs into UTPSCs leads to enhancement of both charge separation and diffusion of electrons into TiO₂ layer surrounding the Ag NPs which will improve J_{sc} of UTPSCs. This is very helpful for explaining how Ag NPs improve the performance of UTPSCs and very important for further improving the performance of UTPSCS. As not fully covered Ag NPs can act as recombination center, electrons which were first trapped in TiO₂ de-trap into Ag NPs and hence recombine with holes from perovskite layer, leading to a decrease of V_{oc} and relatively also J_{sc} . To overcome the drawback of Ag NPs,

increasing the thickness of the TiO_2 layer to fully cover the Ag NPs could be one possible way.

5.4 Summary

In this chapter, incorporation of Ag NPs into ultra-thin perovskite solar cells is described. Optical simulation and experiment on the incorporation of Ag NPs in three different positions are shown in detail.

In section 5.1, ultra-thin perovskite solar cells are fabricated by spray pyrolysis, spin coating and evaporation. The perovskite layer deposited in this work is a continuous film and nearly pin hole free. The thickness of the perovskite layer is around 140 nm which is 53.3% thinner than the standard thickness used in perovskite solar cells. That's the reason it is named as ultra-thin perovskite layer. Due to the thin thickness, the absorption of the layer is poor in wavelengths longer than 550 nm. Incorporation of Ag NPs into the ultra-thin perovskite solar cells is a possible way to enhance the absorption as well as their performance.

In section 5.2, optical simulation of Ag NP incorporation in ultra-thin perovskite solar cells is carried out. Three different positions, i.e., between perovskite layer and spiro-OMeTAD layer, between TiO_2 layer and perovskite layer, between FTO substrate and TiO_2 layer, are used for the incorporation. By variation of different parameters of Ag NPs, the first two positions can cause absorption enhancement of the ultra-thin perovskite layer while the last position can only lead to absorption loss. Details of the optical simulations in the positions are shown following:

- Incorporation of Ag NPs at the interface between perovskite layer and spiro-OMeTAD layer: when the Ag NPs are not fully on top of perovskite layer but have some part cut by it, the absorption of the perovskite layer can be enhanced at the poor absorbing range of the spectrum. The absorption enhancement on the perovskite layer is caused by scattering and localized surface plasmon resonance (LSPR). With increase of particle size, enhancement of absorption increases. However, absorption enhancement caused by Ag NPs larger than 90 nm is less which is due to the red-shift of resonance peak of larger Ag NPs to wavelengths longer than the band gap of perovskite. This decreases the resonance that can be coupled to the perovskite layer. Density of Ag NPs also has an influence: for higher density Ag NPs, their resonance at longer wavelengths can contribute more to absorption of Ag NPs whereas at shorter wavelength can contribute more to scattering; for lower density Ag NPs, their resonance at longer wavelength contributes more to scattering.
- Incorporation of Ag NPs at the interface between TiO_2 layer and perovskite layer: At this position, particle size of Ag NPs is studied systematically. For the Ag NPs equal to or smaller than 30 nm, absorption of the perovskite layer is less than the reference. Ag NPs larger than 30 nm can cause absorption enhancement of the perovskite layer. The reason is smaller Ag NPs prefer to absorb the incident light while the larger one prefer to scatter light according to Mie theory. Since the Ag NPs are surrounded by a perovskite layer, both scattering effect and near field effect of Ag NPs can be contributed to the absorption enhancement.
- Incorporation of Ag NPs at the interface between FTO substrate and TiO_2 layer: Due to the limitation of TiO_2 thickness, only particles smaller than 30 nm are considered. The absorption of all samples with incorporation of Ag NPs is lower

than the reference one. The reason is Ag NPs absorb the incident light prior to perovskite layer. That's also why with decrease of Ag NPs' density, absorption losses of perovskite layer decrease as well.

To check the possibility of incorporation Ag NPs in ultra-thin perovskite solar cells and whether the optical simulation can be used for predicting experiment, Ag NPs are incorporated into the ultra-thin perovskite solar cells by spray-CVD. Three different positions were used in the experiment according to the simulation.

- On top of perovskite layer: From experiment it is found that the perovskite layer is not stable under the deposition conditions of Ag NPs. The instability leads to a property change of the perovskite layer itself and no absorption enhancement can be detected in this case.
- Between TiO₂ layer and perovskite layer: From SEM images, the morphology of perovskite layer can be influenced strongly by Ag NPs. However, absorption enhancement of the ultra-thin perovskite solar cells can be observed in this case. *J-V* measurements were carried out for this series samples, but both V_{oc} and J_{sc} decrease for the solar cells with incorporation of Ag NPs. The reason is that the direct contact between Ag NPs and perovskite leads to the formation of recombination centers.
- Between FTO substrate and TiO₂ layer: With incorporation of Ag NPs in this position, J_{sc} enhancement of around 22.2% was observed, like the average J_{sc} increased from 10.8 mA/cm² for the control sample to 13.2 mA/cm² for the samples with 11 nm Ag NPs. This leads to an increase of average PCE from 5.8% to 7.1%, i.e., 22.5% relative. Quenching of steady-state PL indicated that charge separation and trapping of electrons into the TiO₂ layer were enhanced at the CH₃NH₃PbI₃/TiO₂ interface, which contributes to the enhancement of J_{sc} . Studies of XPS and SPV show that not fully covered Ag NPs can also act as recombination center which leads to the decrease of V_{oc} and J_{sc} . If this problem can be resolved, higher enhancements of J_{sc} and PCE of UTPSC can be expected. It's also expected that plasmonic Ag NPs can be applied for further improvement of UTPSCs.

It is found that incorporation of Ag NPs near the perovskite layer is effective for absorption enhancement. However, the direct contact of metal nanoparticles and perovskite layer can generate recombination center which decrease the performances of the solar cell. In addition, it can also influence the morphology of the perovskite layer. Therefore, nanoparticles with SiO₂ shell are very useful to avoid the direct contact between metal nanoparticles. This part of content will be shown in next chapter.

Chapter 6

Application of Au@SiO₂ core-shell nanorods in perovskite solar cells

From previous chapter and reported work, it is known that direct contact between plasmonic metal nanoparticles and perovskite layer in perovskite solar cells (PSCs) leads to the formation of recombination centers which could strongly decrease the performance of PSCs [32, 33]. This is a significant drawback for incorporating plasmonic metal nanoparticles in the positions which can have direct contact with perovskite layer. To overcome the obstacle, metal nanoparticles with dielectric SiO₂ shell would be a promising way.

In this chapter, pre-synthesized Au@SiO₂ core-shell nanorods (Au NRs) are applied in PSCs for enhancement of photocurrent and power conversion efficiency. Optical simulation results of the incorporation of Au NRs into PSCs are shown in Section 6.1. Section 6.2 presents results of the experimental incorporation of Au NRs into PSCs. Section 6.3 gives the summary of this chapter.

6.1 Simulated incorporation of Au@SiO₂ core-shell nanorods in perovskite solar cells

In this section, an example of the incorporation of Au NRs into PSCs is given in optical simulation. The optical simulation was carried out by JCMsuite. Figure 6.1 shows the schematic structure of PSC with incorporation of Au NRs at the interface between TiO₂ layer and perovskite layer. The perovskite layer in this chapter is referred to CH₃NH₃PbI₃ layer. The PSC includes FTO on top of glass substrate, TiO₂, perovskite, spiro-OMeTAD and Au back contact layers. The respective thicknesses of the layers are 200 nm, 570 nm, 35 nm, 140 nm, 280 nm and 80 nm. Au NRs were set as ellipsoids. Lengths of the half axes of the Au core are 45 nm, 32.5 nm and 32.5 nm and the thickness of the SiO₂ shell is 15 nm in all directions. The density of Au NRs was set as 11.8% and positions of them were on top of TiO₂ and embedded in perovskite layer. It has to be mentioned that the parameters of Au NRs were systematically varied to study the influence of them, but only these specify values are shown here to correlate with the experiment results (in section 6.2). The material data for Au and SiO₂ were taken from literature [174], while other material data, such as TiO₂, CH₃NH₃PbI₃, Spiro-OMeTAD and FTO were obtained reflecting from transmission and reflection measurements performed for our own samples by RefDex software (the same as in Chapter 5). In the simulation, light illuminates from the glass side.

Figure 6.2 shows the absorption spectra of perovskite layers without (black line, reference sample) and with (red line) Au NRs incorporation. For the PSC with Au NRs incorporation, absorption of Au NRs (cyan line) and perovskite layer plus Au NRs (green line) are also shown in Figure 6.2. In PSC with Au NRs, absorption of the perovskite layer is slightly less than the reference perovskite layer at the wavelength range shorter than 580 nm, but higher in the wavelength range between 580 nm and 760 nm. The decrease of the absorption of the perovskite layer at shorter wavelengths is due to the parasitic absorption of Au NRs which can be seen from the absorption of Au NRs [70]. The absorption of perovskite layer plus Au NRs is nearly the same as that of the reference perovskite layer at the same shorter wavelengths. The absorption enhancement of the perovskite layer at longer wavelength range can be attributed to the plasmonic enhancement of Au NRs. Resonance wavelengths of Au NRs can support this explanation.

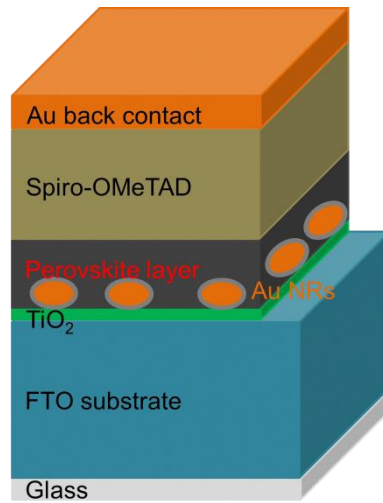


Figure 6.1: Schematic device structure of ultra-thin perovskite solar cell with incorporated Au NRs at the interface between TiO_2 layer and perovskite layer.

To further study the influence of Au NRs on the absorption of the perovskite layer, the near field intensity profiles at $\lambda = 580$ and 620 nm are shown in Fig.6.3a and Figure 6.3b. It is found from Figure 6.2 that the absorption peak of Au NRs is located at $\lambda = 580$ nm and above this wavelength the resonance of Au NRs enhances the absorption of the perovskite layer. When we look at Figure 6.3a, we can find that plasmonic resonance is strongly confined inside the SiO_2 shell and concentrated inside the Au NR's core. This leads to the low cross section of both near field and far field which can be clearly seen from the surrounding of Au NRs in Figure 6.3a. The lower refractive index of SiO_2 than the surrounding perovskite (1.5 of SiO_2 compared to 2.5 of perovskite) is the reason for the resonance observed in figure 6.3a. However, a small part of light can still be coupled into the absorption of the perovskite layer which enhances the absorption of the perovskite layer [108]. A similar effect happens at $\lambda = 620$ nm, too. Moreover a part of the incident light is preferentially scattered forward to the perovskite layer and spiro-OMeTAD layer. This enhances the absorption of the perovskite layer a bit more compared to the reference layer.

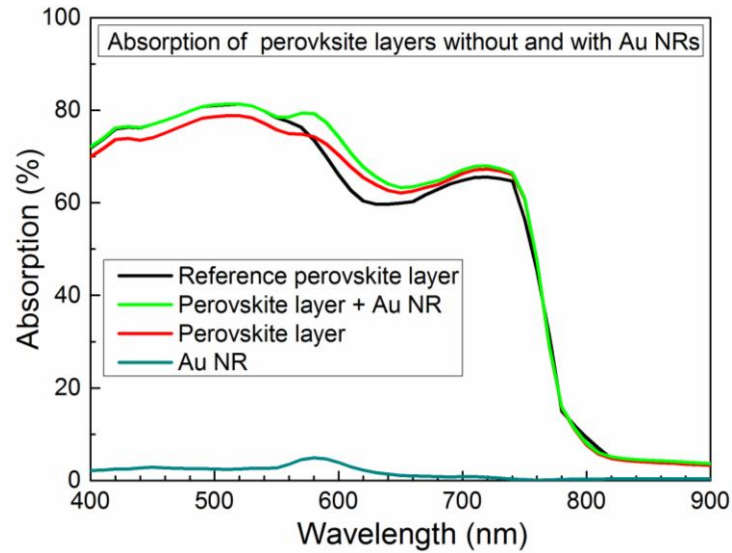


Figure 6.2: PSCs without and with 11.8% Au NRs are simulated. PSC without Au NRs is set as reference while the other named as sample. Absorption spectra of the perovskite layer in reference PSC (black line), perovskite layer in sample PSC (red line), perovskite layer plus Au NRs in sample PSC (green line) and Au NRs in sample PSC (cyan line) are shown.

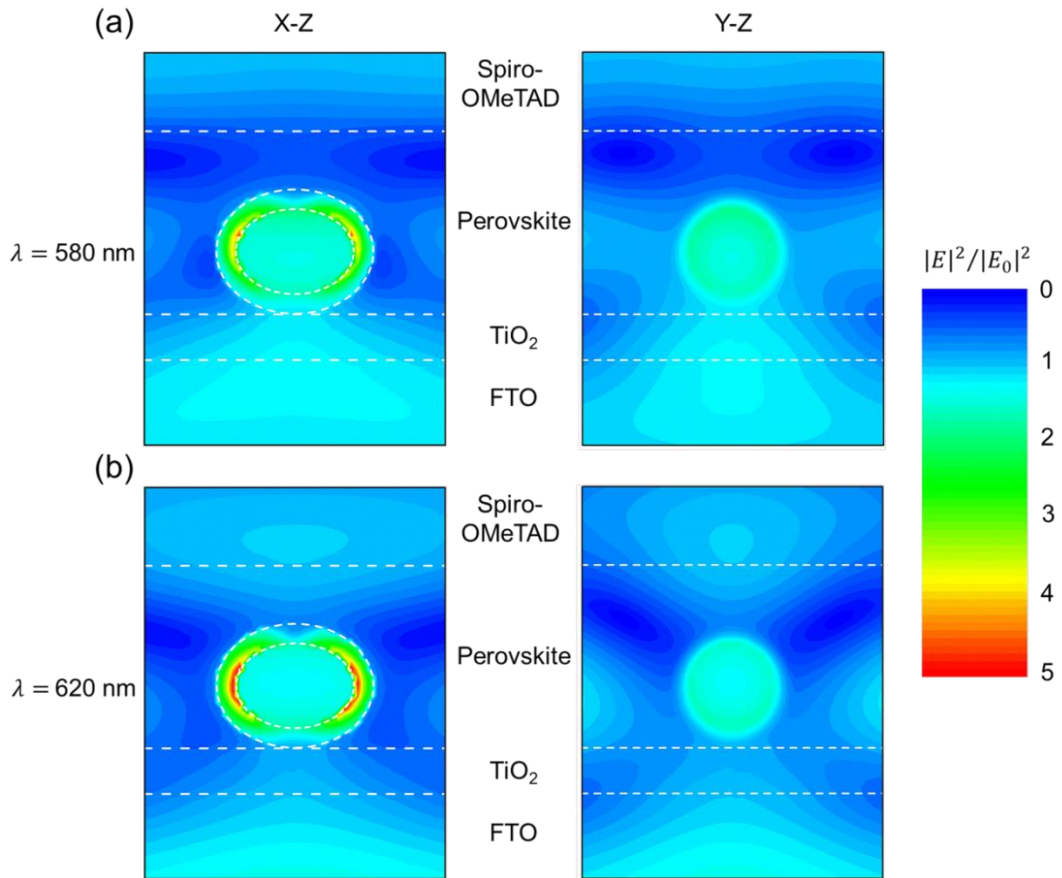


Figure 6.3 The cross sections of electrical field intensity at the middle of Au NRs in both (x-z) and (y-z) planes: (a) at the absorption peak wavelength ($\lambda = 580$ nm); (b) at the resonance wavelength ($\lambda = 620$ nm).

From Figure 6.2 and Figure 6.3, we can conclude that (1) Au NRs can be used for absorption enhancement of PSCs at longer wavelengths but may cause slightly absorption decrease in shorter wavelengths range because of parasitic absorption of Au, (2) plasmonic resonance of Au NRs is strongly confined inside them which lower the absorption enhancement of the perovskite layer. It has to be mentioned that the simulation result shown in this section is not perfect but is just used to illustrate how Au NRs can work in PSC for absorption enhancement. Systematical variation of different parameters would be one possible way to strengthen the absorption enhancement of PSC. Using dielectric nanospheres can decrease the parasitic absorption of them, i.e., SiO_2 spheres, which has been used for absorption enhancement in other solar cells could be another way for absorption enhancement of PSCs.

6.2 Experimental incorporation of Au@ SiO_2 core-shell nanorods into perovskite solar cells

From the simulation shown in the previous section, Au NRs can be used for absorption enhancement of PSCs. In this section, Au NRs will be experimentally incorporated into PSCs to investigate the influence of them on PSCs. Au NRs are synthesized by wet chemical method, e.g., gold core of Au NRs are produced by seed-mediated growth method, a first mesoporous silica shell is coated by a modified Stöber process and a second dense silica shell is generated by layer-by-layer technique. Details of the synthesis of Au NRs can be found elsewhere [175].

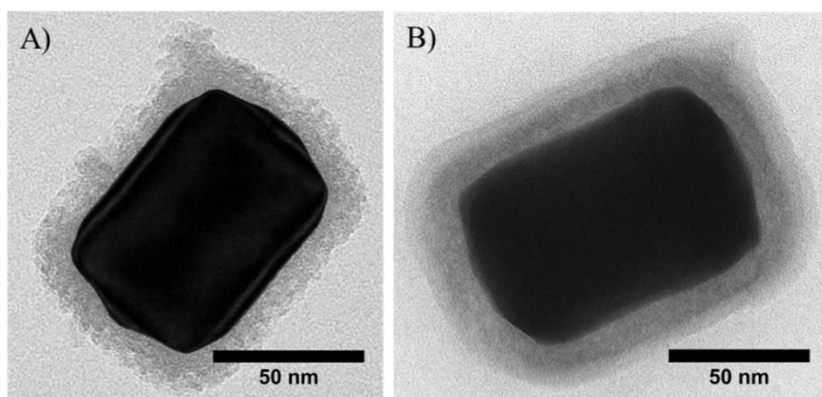


Figure 6.4 TEM images of a gold nanorod with a mesoporous silica shell (a) and a mesoporous plus a dense silica shell (b). [175]

Figure 6.4 shows TEM images of the synthesized (a) Au NR with a mesoporous silica shell as well as (b) Au NR with both mesoporous and dense silica shells. Length and core of Au NRs are 90 ± 9 nm and 65 ± 7 nm, respectively. Thickness of the SiO_2 shell in Figure 6.4B is 15 ± 1 nm. The Au NRs are spin coated onto FTO substrates and SEM images of FTO substrates without and with different coverage (3%, 5.9% and 11.8%) of Au NRs are shown in Figure 6.5. From Figure 6.5, we can find that the distribution of most of the Au NRs on the surface is uniform. Absorption and reflection spectra of the samples mentioned above are measured by UV-Vis and are shown in Figure 6.6. Absorption of the three samples with Au NRs are all stronger than that of FTO substrate. There is a clearly trend that the absorption of the samples increase with the increase of Au NRs' coverage. Two resonance peaks at $\lambda = 540$ nm and $\lambda = 600$ nm can be also observed from the

absorption spectra (Figure 6.6a) which can be attributed to the short and long axis of the Au NRs. Figure 6.6b shows that Au NRs don't increase back scattering of FTO substrates.

After the measurements of optical properties, FTO substrates without and with different coverage of Au NRs were transported into glove box and ultra-thin perovskite layers were deposited on top them using the process described in section 5.1. Optical property characterizations of these samples were carried out again.

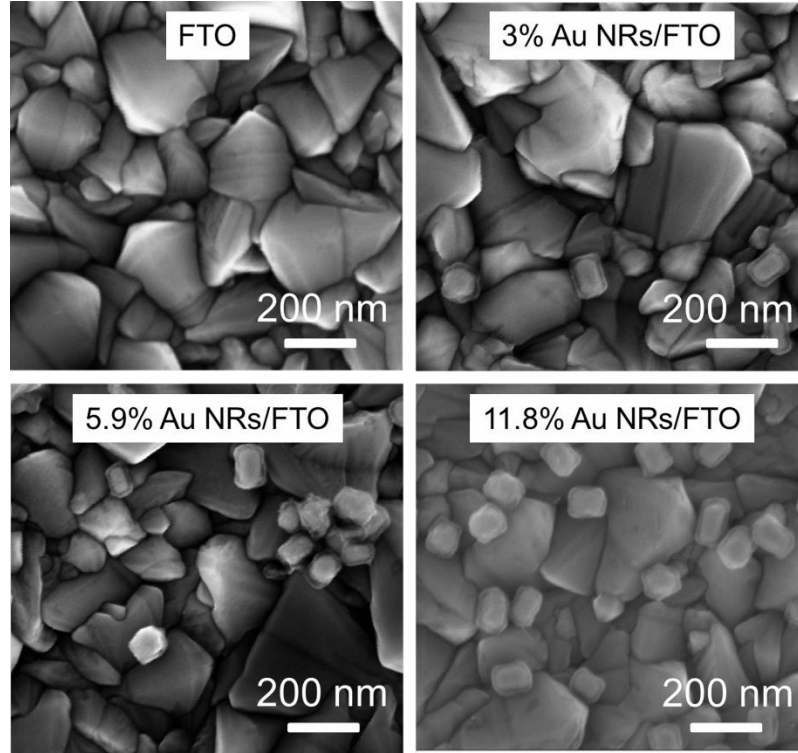


Figure 6.5: SEM images of FTO substrate without and with different coverage of Au NRs on top. SEM image of 11.8% Au NRs/FTO sample has been shown in the thesis of Dr. Andreas Ott [175].

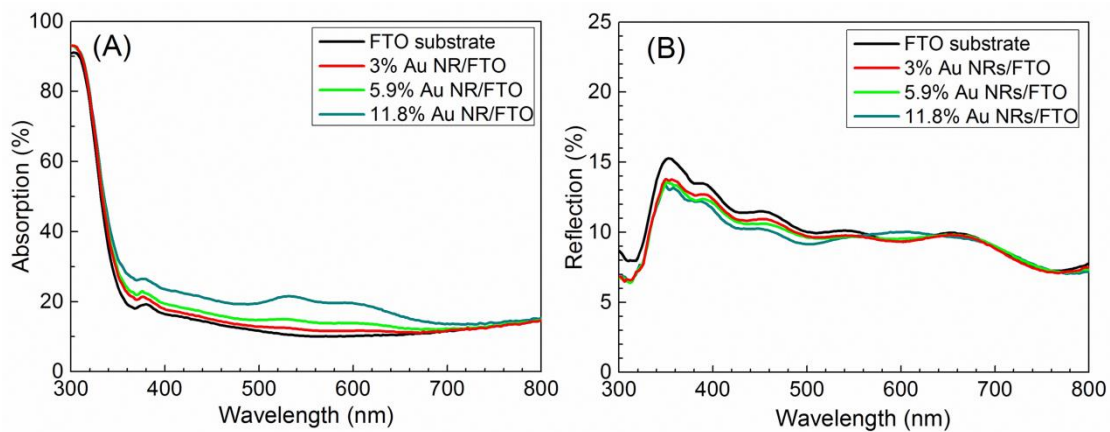


Figure 6.6: Absorption (a) and reflection (b) spectra of FTO substrates without and with different coverage of Au NRs on top. Part of Figure 6.7 has been shown in the thesis of Dr. Andreas Ott [175].

Figure 6.7a and 6.7b show the absorption and reflection spectra of the samples after deposition of perovskite layers. It's observed that absorption of perovskite layers with Au NRs are higher than pure perovskite layer in the wavelength range between 560 nm and 780 nm and it increase with increases of coverage of Au NRs. Reflection spectra of all the samples are nearly the same (Figure 6.7b) which means the incorporation of Au NRs will not increase the loss of incident light from the back scattering side. Figure 6.7c shows the absorption spectra of FTO substrates without and with 11.8% coverage Au NRs as well as the same samples after the deposition of perovskite layer. The resonance wavelengths range of Au NRs on FTO substrate is between 350 nm and 750 nm. However, the absorption of the Au NRs incorporated perovskite sample is higher than the pure perovskite sample at the wavelength range between 550 nm and 1300 nm. The significant red shift of the wavelength range is caused by the increase of the refractive index of Au NRs surrounding medium (from air = 1.0 to perovskite ≈ 2.5).

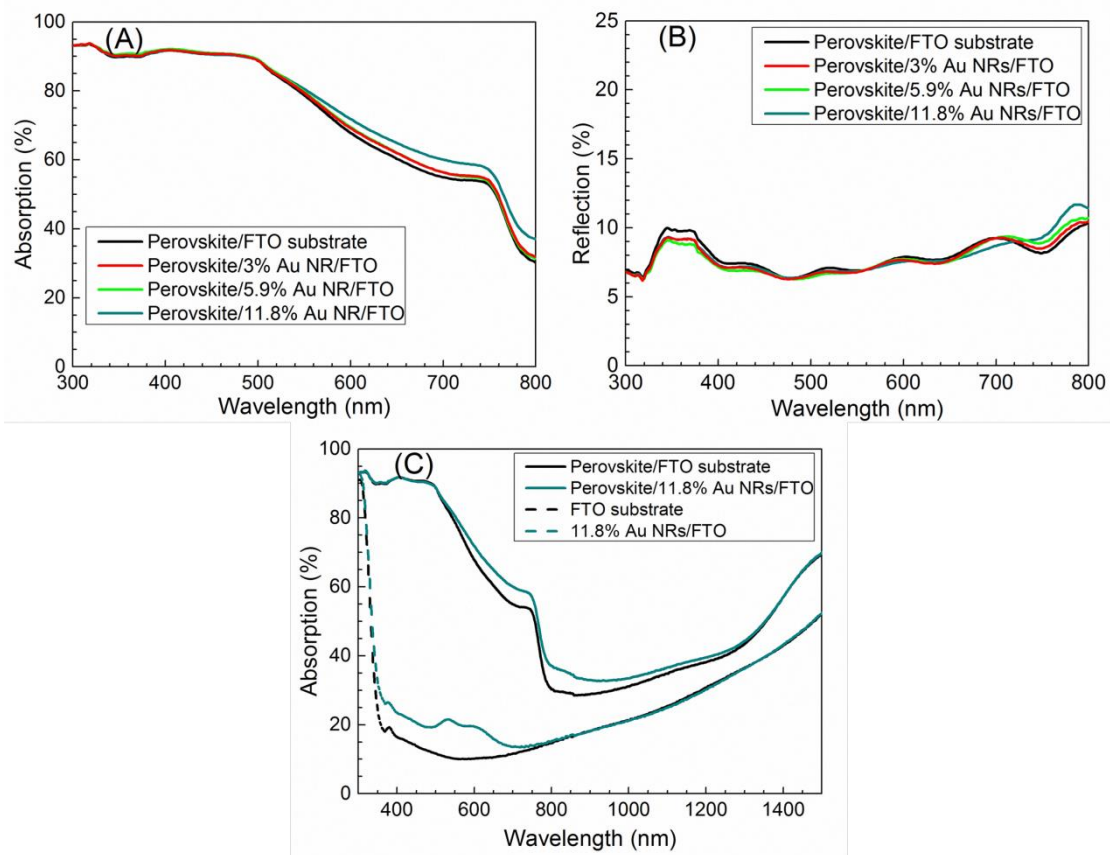


Figure 6.7: Absorption (a) and reflection (b) spectra of perovskite layer coated on top of FTO substrates without and with different coverage of Au NRs. (c) Absorption spectra of FTO substrate without and with 11.8% coverage Au NRs as well as the same samples after deposition of perovskite layers. Part of Figure 6.7 has been shown in the thesis of Dr. Andreas Ott [175].

Besides the investigation of morphology and optical properties of Au NRs, PSCs are fabricated to investigate the effect of Au NRs on the performance of PSCs. It has to be mentioned that in the morphology and optical studies Au NRs were incorporated on FTO substrate directly, but in the fabrication of PSCs Au NRs were incorporated at the interface between TiO_2 and perovskite layer which is the same as in simulation. The method and process described in section 5.1 are used for the fabrication of PSCs. Au NRs are

incorporated by spin coating before the deposition of the perovskite layer. Cross sectional SEM, current density and voltage (J - V) characteristics and external quantum efficiency (EQE) measurements are carried out on the fabricated PSCs.

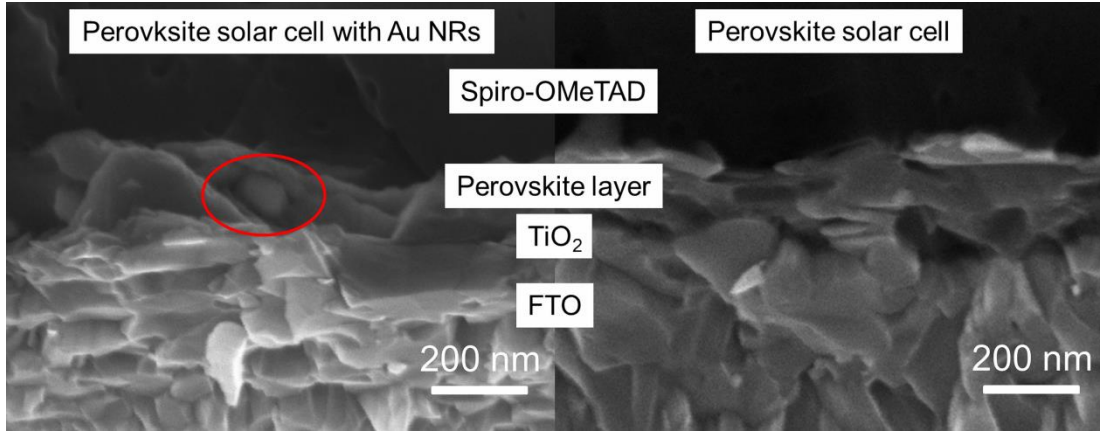


Figure 6.8: Cross sectional SEM images of PSCs with (left) and without (right) incorporation of Au NRs.

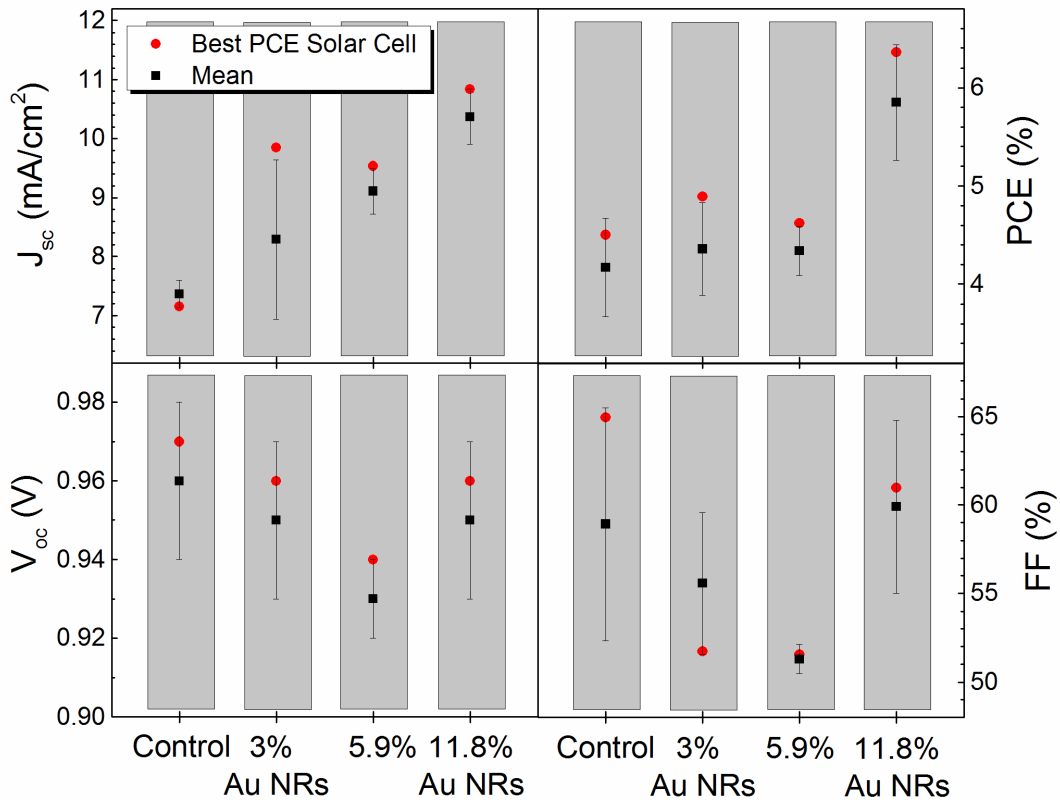


Figure 6.9: Best Average devices performances of PSCs without (control) and with 3%, 5.9%, 11.8% coverage Au NRs measured by reverse scan. For each condition, 3 devices were fabricated and measured.

Figure 6.8 shows the cross sectional SEM images of PSCs without and with 11.8% coverage of Au NRs. The layers shown in the SEM images are (from bottom to top) FTO substrate, TiO₂ layer, perovskite layer and spiro-OMeTAD layer. For both samples,

perovskite layers are continuous films and the thickness of the perovskite layer is similar for the PSCs without and with Au NRs. The red circle in Figure 6.8 points out the embedded Au NR.

Average and best performances of solar cells with different composition (without Au NRs, with 3%, 5.9% and 11.8% Au NRs) are summarized in Figure 6.9. Short current density (J_{sc}) of the PSCs is enhanced significantly by incorporation of Au NRs. With increase of coverage of Au NRs, average J_{sc} increases linearly from 7.4 mA/cm² for the control sample to 8.3 mA/cm² for the 3% Au NRs sample, to 9.1 mA/cm² for the 5.9% Au NRs sample, and to 10.4 mA/cm² for the 11.8% Au NRs sample. Due to the enhancement of J_{sc} , average PCE of PSCs with 11.8% Au NRs exhibits 5.9% which is relatively 41% higher than that of the PSCs without Au NRs (average PCE = 4.2%). However, average PCEs of PSCs with 3% and 5.9% Au NRs are 4.4% and 4.3%, respectively. Both values are similar to the PSCs without Au NRs and do not follow the increase trend of average J_{sc} . The similar values can be explained by the decrease of both average open circuit voltage (V_{oc}) and fill factor (FF) for the PSCs with 3% and 5.9% Au NRs. Among all the samples, PSCs with 5.9% coverage of Au NRs have the lowest V_{oc} and FF. This is the reason of the lowest average PCE for the PSCs with 5.9% Au NRs.

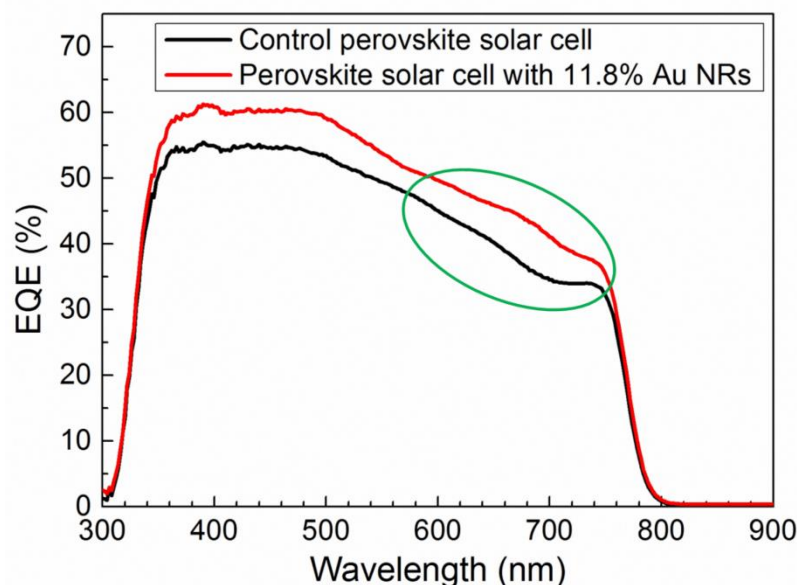


Figure 6.10: EQE spectra of PSCs without (control) and with 11.8% coverage Au NRs. This figure has been shown in the thesis of Dr. Andreas Ott [175].

To further study the influence of Au NRs on the J_{sc} , EQE spectra of the best PCE PSCs without Au NRs and with 11.8% coverage Au NRs are shown in Figure 6.10. An obvious broadband enhancement of EQE can be observed from the EQE spectra. When we compare the EQE spectra shown in Figure 6.10 with the absorption spectra shown in Figure 6.7C, the enhancement of EQE at the wavelength ranges between 580 nm and 760 nm can be attributed to the plasmonic absorption enhancement of the perovskite layer caused by the incorporation of Au NRs. The reason of the enhancement of EQE spectra at other wavelengths is still unclear. It could be that with Au NRs at the interface between TiO₂ layer and perovskite layer, the charge transport properties can be enhanced.

6.3 Summary

In this chapter, the incorporation of Au NRs into ultra-thin perovskite solar cells is described. Optical simulation and experiment of the incorporation of Au NRs at the interface between TiO_2 layer and perovskite layer are carried out.

In section 6.1, optical simulation of PSCs with incorporation of Au NRs (core length 90 nm, width 65 nm, SiO_2 shell thickness 15 nm) is investigated. The results show that Au NRs can be used for absorption enhancement of PSCs in wavelengths longer than 580 nm but may cause slight absorption decrease in shorter wavelengths because of parasitic absorption of Au. The study of the near field intensity revealed that the plasmonic resonance is strongly confined inside of the Au NRs which lowers the absorption enhancement on the perovskite layer. The reason is that the refractive index of the SiO_2 shell is 1.5 which is smaller than that of the surrounding medium perovskite (refractive index 2.5). This can be overcome by using shell materials which have higher refractive index than perovskite.

In section 6.2, Au NRs with similar size as in the optical simulation are synthesized by wet chemical method and incorporated into the ultra-thin perovskite solar cells by spin coating.

- The investigation of optical properties of Au NRs on FTO substrate shows that the resonance wavelength range of Au NRs on FTO substrate is between 350 nm and 750 nm. After deposition of the perovskite layer on top of Au NRs, absorption of the samples with Au NRs are higher than that of the pure perovskite layer at the wavelengths range between 550 nm and 1300 nm. This significant red shift is caused by the change of refractive index of the medium (from air = 1.0 to perovskite ≈ 2.5) surround Au NRs.

The average J_{sc} increases linearly with increase of Au NRs coverage at the interface between TiO_2 layer and perovskite layer. PSCs with 11.8% coverage of Au NRs exhibits 10.4 mA/cm^2 average J_{sc} which is relatively 41% higher than 7.4 mA/cm^2 for the PSCs without Au NRs. Due to the enhancement of J_{sc} , average PCE exhibits 5.9% which is relatively 41% higher than that of the PSCs without Au NRs (average PCE = 4.2%). EQE spectra of the best PCE solar cells without and with 11.8% covered Au NRs show a broadband enhancement of EQE for the latter.

Clarification: The work in this chapter was cooperated with Dr. Andreas Ott in Helmholtz-Zentrum Berlin. The Au NRs preparation and TEM investigation of Au NRs are executed by him. Rest work were done by me. Figure 6.4, Figure 6.10 as well as part of Figure 6.5 and Figure 6.7 have been shown in Dr. Andreas Ott's thesis. For more details of Dr. Ott's work, please refer to Ref: [175].

Chapter 7

Summary

Plasmonic silver nanoparticles (Ag NPs) and gold nanoparticles (Au NPs) are widely used in different kinds of solar cells to enhance their absorption of light and power conversion efficiency (PCE). To improve the performance of extremely thin absorber solar cells (ETA SCs) and ultra-thin perovskite solar cells (UTPSCs) without increasing the thicknesses of absorbers, such nanoparticles are very promising. However, a simple enough, cheap scalable, direct spray based method for producing and incorporating silver nanoparticles is a great challenge. In addition, it is very hard to achieve the performance enhancement of ETA SCs and UTPSCs. In the following, the work has been done which can either solve the problems or give the prospects for further studies will be summarized.

Firstly, a new spray chemical vapor deposition method (spray-CVD) for producing Ag NPs was developed. By that, size and density controlled Ag NPs can be produced at the necessary unusually low temperatures and under atmospheric pressure. A highly volatile material Ag(hfacac)PMe₃ has been chosen as precursor. The lowest temperature for the production of a high quality Ag NP film was shown to be 80 °C which is much lower than other spray based methods. By variation of the deposition parameters such as N₂ flow rate, precursor solution volume and concentration, deposition time and substrate temperature, size and density of Ag NPs can be controlled independently which is a prerequisite for the desired plasmonic properties. The average size of the achieved Ag NPs can be controlled between 5 nm and 120 nm and their coverage between 1% and 60%. By spray-CVD, Ag NPs can be incorporated directly on different kinds of substrates and materials, e.g., FTO, ITO, Mo, c-Si and kapton tape, which widely broaden the application scope of the deposited Ag NPs.

Mechanisms of deposition procedure and particle growth as a function of temperature and precursor concentration were studied by systematical variation of the deposition parameters. Thus, a consistent schematic illustration of the process could be obtained. It was found that a vapor phase formation takes place even at temperatures lower than the melting point of the precursor material. By chemical experiments with the precursor powder a CVD mechanism involving the ethanol evidently explained the high volatility and low decomposition temperature of the precursor in the process. Three temperature sections are clearly distinguished by their slope in the Arrhenius plot. These are with increasing temperature for a high precursor concentration a landing droplets regime (liquid-solid pyrolysis), a kinetically controlled regime and a transport controlled regime (both gas-solid pyrolysis), and for lower concentration a landing droplets regime, a feed

rate limited regime with incomplete evaporation and a feed rate limited regime with complete evaporation, respectively. The respective determining energies such as evaporation enthalpy and activation energy could be attributed to the particular Arrhenius slopes. For the growth of Ag NPs, the interplay between nucleation and growth by integration of fresh material or Ostwald Ripening contribute to the narrow size distribution, absence of much smaller particles and quite homogenous distances to the next neighbors.

Secondly, by the developed spray-CVD, Ag NPs were deposited onto In_2S_3 layers and the resulting layers with Ag NPs were used to investigate the plasmonic enhancement and leading to light trapping and its influence on the solar energy conversion efficiency of ETA SCs. Phase transitions during the deposition of Ag NPs was investigated. With increasing deposition time of Ag, transformations of In_2S_3 into AgIn_5S_8 , orthorhombic AgInS_2 and Ag_2S phases were detected. After the phase transitions, the layer still showed semiconducting properties, which allows further use as absorber in solar cells. Plasmonic absorption enhancement has been demonstrated for the layer after deposition of Ag for 16 min. The phase transition approach for the deposition of Ag NPs on In_2S_3 layers is promising for the application of plasmonic to ETA SCs, as it opens the opportunity not only to tune the size or density of Ag NPs but can also help to solve the problem of stable integration of Ag NPs on top of sulfide absorber layers.

Thirdly, to enhance the performance of UTPSCs, incorporation of Ag NPs produced by spray-CVD and Au@SiO_2 core-shell nanorods (Au NRs) synthesized by a colloidal method was investigated. Prior to the experimental incorporation of Ag NPs and Au NRs, optical simulations were carried out to study the influence of both nanoparticles. It was found that both nanoparticles can cause the absorption enhancement of perovskite absorber layers and the enhancement of incident light originates from localized surface plasmon resonances of Ag NPs and Au NRs.

For experimental incorporation, Ag NPs with diameters of 11 nm, 16 nm and 36 nm were deposited at the interfaces between FTO substrates and TiO_2 layers by simple variation of deposition time. Both 11 nm and 16 nm Ag NPs lead to the PCE enhancement of UTPSCs and 11 nm Ag NPs give the most promising results. Here, a short-circuit current density (J_{sc}) enhancement of 22.2% was observed, i.e., the average J_{sc} increased from 10.8 mA/cm^2 for the control samples (UTPSCs without Ag NPs) to 13.2 mA/cm^2 . This leads to an increase of average PCE from 5.8% to 7.1%, i.e., 22.5% relative. Different characterization methods are used to investigate the reasons of enhancement. Quenching of steady-state photoluminescence indicates that charge separation and trapping of electrons into the TiO_2 layer were enhanced at the $\text{CH}_3\text{NH}_3\text{PbI}_3/\text{TiO}_2$ interface, which contributes to the enhancement of J_{sc} . Studies of XPS and SPV showed that not fully covered Ag NPs can act as recombination centers leading to a decrease of V_{oc} and J_{sc} . If this challenge can be resolved, higher enhancements of J_{sc} and PCE of UTPSCs can be expected. It's also expected that by varying parameters, plasmonic Ag NPs can be applied for further improvement of UTPSCs.

Finally, Au NRs were incorporated into the UTPSCs by spin coating. With increasing coverage at the interface between TiO_2 layer and perovskite layer, the average J_{sc} increase linearly. UTPSCs with 11.8% coverage of Au NRs exhibited 10.4 mA/cm^2 average J_{sc} which is relatively 41% higher than 7.4 mA/cm^2 for the UTPSCs without Au NRs. Due to the enhancement of J_{sc} , the average PCE exhibited 5.9% which is relatively 41% higher than that of the UTPSCs without Au NRs (average PCE = 4.2%).

In conclusion, this work has successfully elaborated a novel, simple, widely applicable and low temperature method for the deposition of tailored, high quality Ag NPs. It solves the challenge of incorporating Ag NPs in ETA SCs and these Ag NPs can be used in UTPSCs for J_{sc} and PCE enhancement. It can be expected that further adjustment achieves even higher enhancement of PCE in ETA SCs and UTPSCs.

Appendix A

Analysis Techniques

This chapter gives a very short overview on the characterization techniques. Details can be found in textbooks [176-178].

A.1 Scanning electron microscope (SEM)

Scanning electron microscope (SEM) is a very powerful tool for characterizing the surface topography and composition of a sample. It generates various signals which contain the information of the sample surface by scanning the sample with focused beam of electrons. Secondary electrons and backscattered electrons are commonly used for imaging the sample surface. Secondary electrons are normally used for imaging the surface morphology and backscattered electrons are for detecting the contrast of sample composition.

In this work, SEM analyses are performed on a LEO GEMINI 1530 scanning electron microscope equipped with a Thermo Noran X-ray detector. The acceleration voltages applied are between 3 kV and 10 kV.

A.2 X-ray Diffraction (XRD)

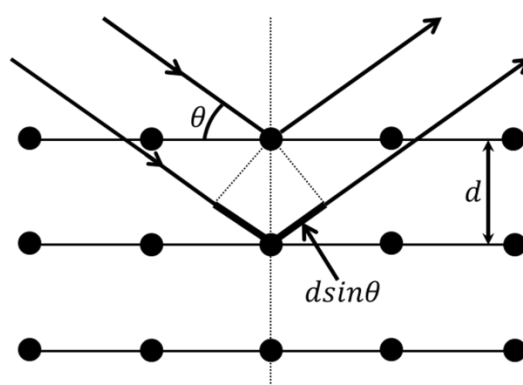


Figure A.1: Representation of Bragg diffraction.

X-ray diffraction (XRD) is a very useful analytical technique for the characterization of crystalline materials. Since wavelengths of X-rays are similar to the spacing between planes in the crystal, crystals can act as a three-dimensional grating for X-ray. When X-rays are incident to a crystal sample, the interaction between X-rays and the sample

produces constructive and destructive interferences. This is the diffraction process. These diffracted X-rays are then collected and the peaks in the diffraction pattern correspond to the atomic structure. The diffraction can be described by Bragg's Law:

$$2d\sin\theta = n\lambda \quad \text{Eq.A.1}$$

In the equation, d is the spacing between two lattice planes in the crystal, θ is the angle between incident X-rays and the crystal lattice plane, n is any integer and λ is the wavelength of incident X-rays. Figure A.1 represents the Bragg's diffraction.

In this work, the crystal phases of the samples are studied by XRD with a Bruker D8 X-ray diffractometer operated in the detector scan mode, with radiation of a Cu K α source (wavelength 0.154056 nm). In the measurements, the acceleration voltage is set to 40 kV and the filament current to 40 mA.

A.3 Laser ablation inductively coupled plasma mass spectrometry (LA-ICP-MS)

Laser ablation inductively coupled plasma mass spectrometry (LA-ICP-MS) is a highly sensitive analytical technique for qualitative and quantitative determination of elements and isotopes from samples. LA-ICP-MS is based on the separation and quantification of the samples' ions which are generated by ionizing the sample vapor by high energy inductively coupled plasma (ICP). A LA-ICP-MS instrument can be divided into three components: laser ablation (LA) system, inductively coupled plasma and mass spectrometer (MS).

The LA system is used for the introduction of the sample which is the first step of the measurement. In this step, a pulsed ultraviolet laser is focused on the sample, upon absorption of the high laser energy the irradiated part of the sample evaporates or sublimates and is then transported to ICP. By controlling the power output and spot size of the laser, a chosen depth and diameter of the sample can be controlled.

In ICP, argon gas flows into the ICP torch and then is heated by an electromagnetic coil and forms argon discharge or plasma. When the sample is introduced to the ICP torch by LA, the compounds are atomized and the atoms are converted first evaporated and then ionized by the plasma.

In MS, the ions from ICP are extracted inside in an electric field through several cones and are separated based on their mass-to-charge ratio. A detector receives a signal proportional to the ion amount which can be determined by the calibration with certified reference materials.

In this work, LA-ICP-MS measurements are performed in multiline scan using a LSX213 laser system built by CETAC (laser wavelength 213 nm, 4 mJ/pulse, 20 Hz pulse frequency, spot size 200 μm , 100 $\mu\text{m/s}$ scan speed for all samples). The NIST610 and NIST612 reference material are used for calibration.

A.4 Ultraviolet–visible spectroscopy (UV-Vis)

Ultraviolet-visible spectroscopy is used to characterize reflection and transmission of the samples. In this works, a Lambda 950 spectrophotometer with an integrating sphere is used for the measurements of reflection and transmission. Absorption spectra are determined by subtracting transmission and reflection from 100%.

A.5 Surface photovoltage (SPV)

Surface photovoltage (SPV) technique is a non-destructive highly sensitive method for characterizing charge separation in semiconductor materials. SPV can be defined as the change of the surface work function caused by illumination-induced charge separation at the surface or interfaces. SPV can be used for determining surface states' distribution, diffusion length of charge carriers, band bending and alignments, formation of charge-selective contacts in bulk semiconductor system, thin-film structures, multilayers as well as in entire devices. [50, 56, 179]

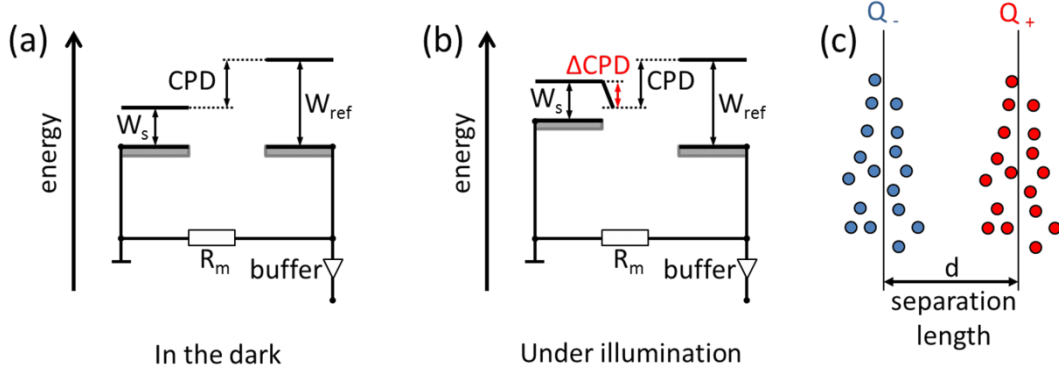


Figure A.2: Schematic illustration of SPV principle (a) in the dark and (b) under illumination for measurement with a high impedance buffer. (c) Separation length between centers of negative and positive charge carriers.

Figure A.2a and A.2b show the schematic illustration of SPV principles for measurement with a high impedance buffer. In the dark condition, when a sample is connected electrically with a reference electrode, electrons are flowing from the sample which has a smaller work function to the reference electrode which has a higher work function for the given case until the Fermi-levels of both are aligned (see Figure A.2a). The difference between the work function of the sample (W_s) and the work function of the reference electrode (W_{ref}) is called contact potential difference (CPD). When the sample is under illumination, free charge carriers generated in the sample induce a change of W_s (see Figure A.2b). A change of W_s can induce a current flow through a large resistance (R_m) between the sample and the reference electrode before the Fermi-levels re-align. The change of CPD (ΔCPD), which is caused by the illumination, can be measured as a voltage drop across the large resistance and is equal to the negative SPV signal. This can be illustrated as:

$$SPV = -\Delta CPD \quad \text{Eq.A.2}$$

Figure A.2c shows the separation length of charge carriers (d) giving together with the number of separated charges (Q), dielectric function of the sample (ϵ) and permittivity of free space ($\epsilon_0 = 8.85 \times 10^{-14} \text{ As/Vcm}$), can determine the SPV signal:

$$SPV = Q \cdot \frac{d}{\epsilon_0 \cdot \epsilon} \quad \text{Eq.A.3}$$

Q and d are influenced by the wavelength of incident light, optical properties and electronic properties of the sample.

In this work, SPV is measured in the fixed capacitor arrangement. A halogen lamp with a quartz prism monochromator is used for illumination. The modulation frequency (frequency of the light chopping) is 8 Hz. The SPV signals are detected by a high impedance buffer and a double phase lock-in amplifier (EG&G 7260DSP). SPV measurements are performed at photon energies in the spectral range between 0.5 eV and 4.5 eV. An in-phase (X) signal and a phase-shifted by 90 ° (Y) signal regarding to the chopped light are measured and the amplitude of SPV signal can be obtained by:

$$SPV_{amp} = \sqrt{X^2 + Y^2} \quad \text{Eq.A.4}$$

Information of the direction of modulated charge separation is contained from the X signal. A positive or negative sign of X signal shows that the illumination induced charges separated towards the internal or external surface, respectively. The Y signal refers to the slow increase or decrease of the SPV signal.

Appendix B

List of Abbreviation & Symbols

List B.1: Abbreviations

AACVD	Aerosol assisted chemical vapor deposition
Ag	Silver
AgInS ₂	Silver indium sulfide
AgIn ₅ S ₈	Silver indium sulfide
Ag(hfacac)PMe ₃	Trimethylphosphine (hexafluoroacetylacetonato) silver
AgNO ₃	Silver nitrate
Ag NPs	Silver nanoparticles
Ag ₂ S	Silver sulfide
ALD	Atomic layer deposition
ALE	Atomic Layer Epitaxy
Al ₂ O ₃	Aluminium oxide
Ar	Argon
Au	Gold
Au NPs	Gold nanoparticles
Au NRs	Gold@SiO ₂ core-shell nanorods
B ₂ H ₆	Diborane
Br	Bromine
CaTiO ₃	Calcium titanate
CdS	Cadmium sulfide
CdSe	Cadium selenide
CdTe	Cadmium telluride
CH ₃ NH ₃ ⁺	Methylammonium

$\text{CH}_3\text{NH}_3\text{PbI}_3$	Methylammonium lead iodide
CIGS	Copper indium-gallium sulfide
CVD	Chemical vapor deposition
Cl	Chlorine
c-Si	Crystalline silicon
$\text{Cu}(\text{In}, \text{Ga})\text{Se}_2$	Copper indium-gallium selenide
CuInS_2	Copper indium sulfide
CuInSe_2	Copper indium selenide
Cu NPs	Copper nanoparticles
CuSCN	Copper thiocyanate
CVI	Chemical vapor infiltration
Dip-ILGAR	Dip ion layer gas reaction
EDX	Energy-dispersive X-ray spectroscopy
ETA SCs	Extremely thin absorber solar cells
EtOH	Ethanol
EVD	Electrochemical vapor deposition
FAVD	Flame assisted vapor deposition
FEM	Finite element method
FTO	Fluorine doped tin oxide
GaAs	Gallium arsenide
GW	Gigawatts
H_2	Hydrogen gas
$\text{H}_2\text{NCHNH}_2^+$	Formamidinium
H_2S	Hydrogen sulfide
I	Iodine
ILGAR	Ion layer gas reaction
$\text{In}(\text{acac})_3$	Indium acetylacetonate
In_2S_3	Indium sulfide
$\text{In}_2\text{S}_3:\text{Ag}$	Silver doped indium sulfide
ITO	Indium tin oxide
JCPDS	Joint Committee on Powder Diffraction Standards
<i>J-V</i>	Current density-voltage
LA-ICP-MS	Laser Ablation Inductively Coupled Plasma Mass Spectrometry

LSPRs	Localized surface plasmon resonances
MAI	Methylammonium iodide
mL	Millilitre
mM	Millimolar
MnS	Manganese sulfide
Mo	Molybdenum
MOCVD	Metal organic chemical vapor deposition
N ₂	Nitrogen gas
NaBH ₄	Sodium borohydride
NaNO ₃	Sodium nitrate
NREL	National Renewable Energy Laboratory
OR	Ostwald Ripening
PACVD	Photo-assisted chemical vapor deposition
Pb	Lead
PbI ₂	Lead iodide
PCE	Power conversion efficiency
PECVD	Plasma enhanced chemical vapor deposition
PMC	Particle migration and subsequent coalescence
PSCs	Perovskite solar cells
PV	Photovoltaic
PVD	Physical vapor deposition
Sb ₂ S ₃	Antimony(III) Sulfide
SEM	Scanning electron microscope
Si	Silicon
SiO ₂	Silicon dioxide
Sn	Tin
spiro-OMeTAD	2,2',7,7'-Tetrakis-(N,N-di-4-methoxyphenylamino) -9,9'-spirobifluorene
SPP	Surface plasmon polaritons
spray-CVD	Spray chemical vapor deposition
spray-ILGAR	Spray ion layer gas reaction
SPV	Surface photovoltage
TACVD	Thermal activated CVD
TCO	Transparent conductive oxide
TiO ₂	Titanium dioxide

TEM	Transmission electron microscopy
UTPSCs	Ultra-thin perovskite solar cells
UV-Vis	Ultraviolet-visible spectrophotometry
VO ₂	Vanadium(IV) oxide
XPS	X-ray photoelectron spectroscopy
XRD	X-ray Powder Diffraction
ZnO	Zinc oxide
ZnS	Zinc sulfide

List B.2: Symbols

a	Radius of metal nanoparticle
A	Diode ideality factor; pre-exponential constant
Abs	Absorption
A_s	Heated area in chemical vapor deposition
B	Constant
C_{abs}	Absorption cross-section
CPD	Contact potential difference
C_r	Molar concentration of gaseous reactant outside the boundary layer
C_{sca}	Scattering cross-section
C_T	Pre-exponential term for the temperature-dependent form of the precursor vapor pressure
d	Spacing between two lattice planes in crystal; separation length of charge carriers
D	Diffusion coefficient
D_0	Diffusion coefficient at reference conditions
E_A	Activation energy
E_{abs}	Onset energy of SPV signal
E_{dpa}	Energy of derivative peak analysis
eV	Electronvolt
FF	Fill factor
F_r	Feed rate of the reactant
h	hour
Hz	Hertz
Im	Imaginary part

J_0	Saturation current density
J_{MPP}	Current density at the maximum power point
J_{ph}	Photo-generated current density
J_{sc}	Short-circuit current density
$J(v)$	Net current density
k	Boltzmann's constant
k_o	Pre-exponential constant
K	Wave vector in the surrounding medium
k_s	Surface reaction rate constant
kV	Kilovolt
L	Thickness of the boundary layer
M	Atomic weight of depositing species
mA	Milliampere
mA/cm ²	Milliampere per Square Centimeter
mJ	Millijoule
nm	Nanometer
p	Total pressure
p_0	Total pressure at reference conditions
P_{in}	Input energy from the sunlight
P_{MPP}	Maximum power point
ppm	Parts per million
p_r	Reactant partial pressure outside the boundary layer
q	Elementary charge
Q	Gas flow rate in volume; number of separated charges
R	Universal gas constant; reflection
R_m	Resistance
SPV_{amp}	Amplitude of SPV signal
T	Absolute temperature; substrate surface temperature; transmission
T_0 substrate	Reference temperature for the gas above the
v	Applied voltage across the p-n junction; volume of deposited species
V_{oc}	Open-circuit voltage

V_{MPP}	Voltage at the maximum power point
W_{ref}	Work function of the reference
W_s	Work function of the sample
X	In phase signals
Y	Phase shifted by 90 °signals
α	Polarizability
δ	Deposition rate
ΔCPD	Change of contact potential difference
ΔH_{vap}	Enthalpy of evaporation of the precursor material
ε	Dielectric function of the metal nanoparticle
ε_0	Permittivity of free space
ε_{Ag}	Emissivity of silver
ε_{FTO}	Emissivity of FTO
ε_m	Dielectric function of the medium
η	Power conversion efficiency
θ	Angle between incident X-ray and the crystal lattice plane
λ	Wavelength of incident light
μL	Microliter
π	Mathematical constant Pi
ρ	Density of the deposited film

References

- [1] Trends in Photovoltaic Applications. 2016. International Energy Agency Photovoltaic Power Systems Programme: <http://www.iea-pvps.org/index.php?id=256>.
- [2] Technology Roadmap: Solar Photovoltaic Energy. 2014. International Energy Agency: <http://www.iea.org>.
- [3] Ferry VE, Verschuuren MA, Lare MC, Schropp RE, Atwater HA, Polman A. Optimized spatial correlations for broadband light trapping nanopatterns in high efficiency ultrathin film a-Si:H solar cells. *Nano Letters*, 2011, 11, 4239-4245.
- [4] Ferry VE, Verschuuren MA, Li HB, Verhagen E, Walters RJ, Schropp RE, et al. Light trapping in ultrathin plasmonic solar cells. *Optics Express*, 2010, 18, A237-A245.
- [5] Ernst K, Belaidi A, Könenkamp R. Solar cell with extremely thin absorber on highly structured substrate. *Semiconductor Science and Technology*, 2003, 18, 475-479.
- [6] Belaidi A, Dittrich T, Kieven D, Tornow J, Schwarzburg K, Kunst M, et al. ZnO-nanorod arrays for solar cells with extremely thin sulfidic absorber. *Solar Energy Materials and Solar Cells*, 2009, 93, 1033-1036.
- [7] Majidi H. Extremely Thin Absorber Solar Cells: Drexel University; 2012.
- [8] Briscoe J, Dunn S. Extremely thin absorber solar cells based on nanostructured semiconductors. *Materials Science and Technology*, 2011, 27, 1741-1756.
- [9] Sum TC, Mathews N. Advancements in perovskite solar cells: photophysics behind the photovoltaics. *Energy & Environmental Science*, 2014, 7, 2518-2534.
- [10] Jung HS, Park N-G. Perovskite Solar Cells: From Materials to Devices. *Small*, 2015, 11, 10-25.
- [11] Kojima A, Teshima K, Shirai Y, Miyasaka T. Organometal Halide Perovskites as Visible-Light Sensitizers for Photovoltaic Cells. *Journal of the American Chemical Society*, 2009, 131, 6050-6051.
- [12] NREL efficiency chart: http://www.nrel.gov/ncpv/images/efficiency_chart.jpg.
- [13] Ono LK, Wang S, Kato Y, Raga SR, Qi Y. Fabrication of semi-transparent perovskite films with centimeter-scale superior uniformity by the hybrid deposition method. *Energy & Environmental Science*, 2014, 7, 3989-3993.
- [14] Lang F, Gluba MA, Albrecht S, Rappich J, Korte L, Rech B, et al. Perovskite Solar Cells with Large-Area CVD-Graphene for Tandem Solar Cells. *The Journal of Physical Chemistry Letters*, 2015, 6, 2745-2750.
- [15] Eperon GE, Burlakov VM, Goriely A, Snaith HJ. Neutral Color Semitransparent Microstructured Perovskite Solar Cells. *ACS Nano*, 2014, 8, 591-598.
- [16] Della Gaspera E, Peng Y, Hou Q, Spiccia L, Bach U, Jasieniak JJ, et al. Ultra-thin high efficiency semitransparent perovskite solar cells. *Nano Energy*, 2015, 13, 249-257.

- [17] Liu Y, Fu Y, Dittrich T, Sáez-Araoz R, Schmid M, Hinrichs V, et al. Phase transitions during formation of Ag nanoparticles on In_2S_3 precursor layers. *Thin Solid Films*, 2015, 590, 54-59.
- [18] Schmid M, Tsakanikas S, Mangalgi G, Andrae P, Song M, Yin G, et al. Nano-optical concept design for light management. *Proceedings of SPIE*, 2015, 9626, 96260E.
- [19] van Lare C, Yin G, Polman A, Schmid M. Light Coupling and Trapping in Ultrathin Cu(In,Ga)Se_2 Solar Cells Using Dielectric Scattering Patterns. *ACS Nano*, 2015, 9, 9603-9613.
- [20] van Lare M, Lenzmann F, Verschuuren MA, Polman A. Mode coupling by plasmonic surface scatterers in thin-film silicon solar cells. *Applied Physics Letters*, 2012, 101, 221110.
- [21] Chen X, Jia B, Saha JK, Cai B, Stokes N, Qiao Q, et al. Broadband Enhancement in Thin-Film Amorphous Silicon Solar Cells Enabled by Nucleated Silver Nanoparticles. *Nano Letters*, 2012, 12, 2187-2192.
- [22] Schmid M, Klaer J, Klenk R, Topič M, Krč J. Stability of plasmonic metal nanoparticles integrated in the back contact of ultra-thin Cu(In,Ga)S_2 solar cells. *Thin Solid Films*, 2013, 527, 308-313.
- [23] Yin G, Steigert A, Andrae P, Goebelt M, Latzel M, Manley P, et al. Integration of plasmonic Ag nanoparticles as a back reflector in ultra-thin Cu(In,Ga)Se_2 solar cells. *Applied Surface Science*, 2015, 355, 800-804.
- [24] Kalfagiannis N, Karagiannidis PG, Pitsalidis C, Panagiotopoulos NT, Gravalidis C, Kassavetis S, et al. Plasmonic silver nanoparticles for improved organic solar cells. *Solar Energy Materials and Solar Cells*, 2012, 104, 165-174.
- [25] Kim S-S, Na S-I, Jo J, Kim D-Y, Nah Y-C. Plasmon enhanced performance of organic solar cells using electrodeposited Ag nanoparticles. *Applied Physics Letters*, 2008, 93, 073307.
- [26] Qian M, Li M, Shi X-B, Ma H, Wang Z-K, Liao L-S. Planar perovskite solar cells with 15.75% power conversion efficiency by cathode and anode interfacial modification. *Journal of Materials Chemistry A*, 2015, 3, 13533-13539.
- [27] Yue L, Yan B, Attridge M, Wang Z. Light absorption in perovskite solar cell: Fundamentals and plasmonic enhancement of infrared band absorption. *Solar Energy*, 2016, 124, 143-152.
- [28] Cobley CM, Skrabalak SE, Campbell DJ, Xia Y. Shape-Controlled Synthesis of Silver Nanoparticles for Plasmonic and Sensing Applications. *Plasmonics*, 2009, 4, 171-179.
- [29] Mock JJ, Barbic M, Smith DR, Schultz DA, Schultz S. Shape effects in plasmon resonance of individual colloidal silver nanoparticles. *The Journal of Chemical Physics*, 2002, 116, 6755-6759.
- [30] Berhe TA, Su W-N, Chen C-H, Pan C-J, Cheng J-H, Chen H-M, et al. Organometal halide perovskite solar cells: degradation and stability. *Energy & Environmental Science*, 2016, 9, 323-356.
- [31] Long M, Chen Z, Zhang T, Xiao Y, Zeng X, Chen J, et al. Ultrathin efficient perovskite solar cells employing a periodic structure of a composite hole conductor for elevated plasmonic light harvesting and hole collection. *Nanoscale*, 2016, 8, 6290-6299.
- [32] Zhang W, Saliba M, Stranks SD, Sun Y, Shi X, Wiesner U, et al. Enhancement of Perovskite-Based Solar Cells Employing Core-Shell Metal Nanoparticles. *Nano Letters*, 2013, 13, 4505-4510.
- [33] Yuan Z, Wu Z, Bai S, Xia Z, Xu W, Song T, et al. Hot-Electron Injection in a Sandwiched $\text{TiO}_x\text{-Au-TiO}_x$ Structure for High-Performance Planar Perovskite Solar Cells. *Advanced Energy Materials*, 2015, 5, 1500038.

-
- [34] Lu L, Luo Z, Xu T, Yu L. Cooperative Plasmonic Effect of Ag and Au Nanoparticles on Enhancing Performance of Polymer Solar Cells. *Nano Letters*, 2013, 13, 59-64.
- [35] Fahrenbruch A, Bube R. *Fundamentals Of Solar Cells: Photovoltaic Solar Energy Conversion*: Elsevier Science; 2012.
- [36] Atwater HA, Polman A. Plasmonics for improved photovoltaic devices. *Nature Materials*, 2010, 9, 205-213.
- [37] Liu M, Johnston MB, Snaith HJ. Efficient planar heterojunction perovskite solar cells by vapour deposition. *Nature*, 2013, 501, 395-398.
- [38] Tao CS, Jiang J, Tao M. Natural resource limitations to terawatt-scale solar cells. *Solar Energy Materials and Solar Cells*, 2011, 95, 3176-3180.
- [39] Fthenakis V. Sustainability of photovoltaics: The case for thin-film solar cells. *Renewable and Sustainable Energy Reviews*, 2009, 13, 2746-2750.
- [40] Belaidi A, Dittrich T, Kieven D, Tornow J, Schwarzburg K, Lux-Steiner M. Influence of the local absorber layer thickness on the performance of ZnO nanorod solar cells. *physica status solidi (RRL) – Rapid Research Letters*, 2008, 2, 172-174.
- [41] Dittrich T, Belaidi A, Ennaoui A. Concepts of inorganic solid-state nanostructured solar cells. *Solar Energy Materials and Solar Cells*, 2011, 95, 1527-1536.
- [42] Fu Y. Spray-ILGAR[®] deposition of controllable ZnS nanodots and application as passivation/point contact at the In₂S₃/Cu(In, Ga)(S, Se)₂ junction in thin film solar cells: Freie Universität Berlin; 2012.
- [43] Gray JL. The Physics of the Solar Cell. *Handbook of Photovoltaic Science and Engineering*: John Wiley & Sons, Ltd; 2005. p. 61-112.
- [44] Würfel P. *Physics of Solar Cells: From Principles to New Concepts*: Wiley; 2008.
- [45] Kieven D, Dittrich T, Belaidi A, Tornow J, Schwarzburg K, Allsop N, et al. Effect of internal surface area on the performance of ZnO / In₂S₃ / CuSCN solar cells with extremely thin absorber. *Applied Physics Letters*, 2008, 92, 1033-1036.
- [46] Tena-Zaera R, Ryan MA, Katty A, Hodes G, Bastide S, Lévy-Clément C. Fabrication and characterization of ZnO nanowires/CdSe/CuSCN eta-solar cell. *Comptes Rendus Chimie*, 2006, 9, 717-729.
- [47] Hu L, Dai S, Weng J, Xiao S, Sui Y, Huang Y, et al. Microstructure Design of Nanoporous TiO₂ Photoelectrodes for Dye-Sensitized Solar Cell Modules. *The Journal of Physical Chemistry B*, 2007, 111, 358-362.
- [48] Grinis L, Dor S, Ofir A, Zaban A. Electrophoretic deposition and compression of titania nanoparticle films for dye-sensitized solar cells. *Journal of Photochemistry and Photobiology A: Chemistry*, 2008, 198, 52-59.
- [49] Gavrilov SA, Dronov AA, Shevyakov VI, Belov AN, Poltoratskii EA. Ways to increase the efficiency of solar cells with extremely thin absorption layers. *Nanotechnologies in Russia*, 2009, 4, 237-243.
- [50] Zabel P, Dittrich T, Funes M, Durantini EN, Otero L. Charge Separation at Pd-Porphyrin/TiO₂ Interfaces. *The Journal of Physical Chemistry C*, 2009, 113, 21090-21096.
- [51] Larramona G, Choné C, Jacob A, Sakakura D, Delatouche B, Péré D, et al. Nanostructured Photovoltaic Cell of the Type Titanium Dioxide, Cadmium Sulfide Thin Coating, and Copper Thiocyanate Showing High Quantum Efficiency. *Chemistry of Materials*, 2006, 18, 1688-1696.
- [52] Cao B, Cai W. From ZnO Nanorods to Nanoplates: Chemical Bath Deposition Growth and Surface-Related Emissions. *The Journal of Physical Chemistry C*, 2008, 112, 680-685.

- [53] Elias J, Tena-Zaera R, L  vy-Cl  ment C. Electrodeposition of ZnO nanowires with controlled dimensions for photovoltaic applications: Role of buffer layer. *Thin Solid Films*, 2007, 515, 8553-8557.
- [54] Nanu M, Schoonman J, Goossens A. Inorganic Nanocomposites of n- and p-Type Semiconductors: A New Type of Three-Dimensional Solar Cell. *Advanced Materials*, 2004, 16, 453-456.
- [55] Ernst K, Sieber I, Neumann-Spallart M, Lux-Steiner MC, K  nenkamp R. Characterization of II-VI compounds on porous substrates. *Thin Solid Films*, 2000, 361-362, 213-217.
- [56] Dittrich T, Kieven D, Belaidi A, Rusu M, Tornow J, Schwarzburg K, et al. Formation of the charge selective contact in solar cells with extremely thin absorber based on ZnO-nanorod/In₂S₃/CuSCN. *Journal of Applied Physics*, 2009, 105, 034509.
- [57] Yin W-J, Yang J-H, Kang J, Yan Y, Wei S-H. Halide perovskite materials for solar cells: a theoretical review. *Journal of Materials Chemistry A*, 2015, 3, 8926-8942.
- [58] Stoumpos CC, Malliakas CD, Kanatzidis MG. Semiconducting Tin and Lead Iodide Perovskites with Organic Cations: Phase Transitions, High Mobilities, and Near-Infrared Photoluminescent Properties. *Inorganic Chemistry*, 2013, 52, 9019-9038.
- [59] Eperon GE, Stranks SD, Menelaou C, Johnston MB, Herz LM, Snaith HJ. Formamidinium lead trihalide: a broadly tunable perovskite for efficient planar heterojunction solar cells. *Energy & Environmental Science*, 2014, 7, 982-988.
- [60] Dittrich T, Lang F, Shargaieva O, Rappich J, Nickel NH, Unger E, et al. Diffusion length of photo-generated charge carriers in layers and powders of CH₃NH₃PbI₃ perovskite. *Applied Physics Letters*, 2016, 109, 073901.
- [61] Stranks SD, Eperon GE, Grancini G, Menelaou C, Alcocer MJP, Leijtens T, et al. Electron-Hole Diffusion Lengths Exceeding 1 Micrometer in an Organometal Trihalide Perovskite Absorber. *Science*, 2013, 342, 341-344.
- [62] Mali SS, Hong CK. p-i-n/n-i-p type planar hybrid structure of highly efficient perovskite solar cells towards improved air stability: synthetic strategies and the role of p-type hole transport layer (HTL) and n-type electron transport layer (ETL) metal oxides. *Nanoscale*, 2016, 8, 10528-10540.
- [63] Jeon NJ, Noh JH, Kim YC, Yang WS, Ryu S, Seok SI. Solvent engineering for high-performance inorganic-organic hybrid perovskite solar cells. *Nature Materials*, 2014, 13, 897-903.
- [64] Liu D, Kelly TL. Perovskite solar cells with a planar heterojunction structure prepared using room-temperature solution processing techniques. *Nat Photon*, 2014, 8, 133-138.
- [65] Sha WEI, Ren X, Chen L, Choy WCH. The efficiency limit of CH₃NH₃PbI₃ perovskite solar cells. *Applied Physics Letters*, 2015, 106, 221104.
- [66] Schuller JA, Barnard ES, Cai W, Jun YC, White JS, Brongersma ML. Plasmonics for extreme light concentration and manipulation. *Nature Materials*, 2010, 9, 193-204.
- [67] Guler U, Shalaev VM, Boltasseva A. Nanoparticle plasmonics: going practical with transition metal nitrides. *Materials Today*, 2015, 18, 227-237.
- [68] Murray WA, Barnes WL. Plasmonic Materials. *Advanced Materials*, 2007, 19, 3771-3782.
- [69] Willets KA, Duyne RPV. Localized Surface Plasmon Resonance Spectroscopy and Sensing. *Annual Review of Physical Chemistry*, 2007, 58, 267-297.
- [70] Maier SA. *Plasmonics: Fundamentals and Applications*: Springer US; 2010.
- [71] Evanoff DD, Chumanov G. Synthesis and Optical Properties of Silver Nanoparticles and Arrays. *ChemPhysChem*, 2005, 6, 1221-1231.

- [72] Zhou J, Ralston J, Sedev R, Beattie DA. Functionalized gold nanoparticles: Synthesis, structure and colloid stability. *Journal of Colloid and Interface Science*, 2009, 331, 251-262.
- [73] Suryanarayana C. Mechanical alloying and milling. *Progress in Materials Science*, 2001, 46, 1-184.
- [74] Mulfinger L, Solomon SD, Bahadory M, Jeyarajasingam AV, Rutkowsky SA, Boritz C. Synthesis and Study of Silver Nanoparticles. *Journal of Chemical Education*, 2007, 84, 322.
- [75] Fu Y, Lu Y, Polzer F, Lux-Steiner MC, Fischer C-H. In-situ Synthesis of Stabilizer-Free Gold Nanocrystals with Controllable Shape on Substrates as Highly Active Catalysts for Multiple Use. *Advanced Synthesis & Catalysis*, 2016, 358, 1440-1448.
- [76] Tan H, Santbergen R, Smets AHM, Zeman M. Plasmonic Light Trapping in Thin-film Silicon Solar Cells with Improved Self-Assembled Silver Nanoparticles. *Nano Letters*, 2012, 12, 4070-4076.
- [77] Broers AN, Molzen WW, Cuomo JJ, Wittels ND. Electron - beam fabrication of 80 - Å metal structures. *Applied Physics Letters*, 1976, 29, 596-598.
- [78] Gu S, Kaiser J, Marzun G, Ott A, Lu Y, Ballauff M, et al. Ligand-free Gold Nanoparticles as a Reference Material for Kinetic Modelling of Catalytic Reduction of 4-Nitrophenol. *Catalysis Letters*, 2015, 145, 1105-1112.
- [79] Creighton JA, Blatchford CG, Albrecht MG. Plasma resonance enhancement of Raman scattering by pyridine adsorbed on silver or gold sol particles of size comparable to the excitation wavelength. *Journal of the Chemical Society, Faraday Transactions 2: Molecular and Chemical Physics*, 1979, 75, 790-798.
- [80] Suh JS, DiLella DP, Moskovits M. Surface-enhanced Raman spectroscopy of colloidal metal systems: a two-dimensional phase equilibrium in p-aminobenzoic acid adsorbed on silver. *The Journal of Physical Chemistry*, 1983, 87, 1540-1544.
- [81] Faraday M. The Bakerian Lecture: Experimental Relations of Gold (and Other Metals) to Light. *Philosophical Transactions of the Royal Society of London*, 1857, 147, 145-181.
- [82] Turkevich J, Stevenson PC, Hillier J. A study of the nucleation and growth processes in the synthesis of colloidal gold. *Discussions of the Faraday Society*, 1951, 11, 55-75.
- [83] Frens G. Controlled nucleation for the regulation of the particle size in monodisperse gold suspensions. *Nature*, 1973, 241, 20-22.
- [84] Sharma N, Bhatt G, Kothiyal P. Gold Nanoparticles synthesis, properties, and forthcoming applications-A review. *Indian Journal of Pharmaceutical and Biological Research*, 2015, 3, 13-27.
- [85] Sau TK, Murphy CJ. Room Temperature, High-Yield Synthesis of Multiple Shapes of Gold Nanoparticles in Aqueous Solution. *Journal of the American Chemical Society*, 2004, 126, 8648-8649.
- [86] Gole A, Murphy CJ. Seed-Mediated Synthesis of Gold Nanorods: Role of the Size and Nature of the Seed. *Chemistry of Materials*, 2004, 16, 3633-3640.
- [87] Waters CA, Mills AJ, Johnson KA, Schiffrin DJ. Purification of dodecanethiol derivatised gold nanoparticles. *Chemical Communications*, 2003, 540-541.
- [88] Chen Y, Gu X, Nie C-G, Jiang Z-Y, Xie Z-X, Lin C-J. Shape controlled growth of gold nanoparticles by a solution synthesis. *Chemical Communications*, 2005, 4181-4183.
- [89] Bridges CR, DiCarmino PM, Fokina A, Huesmann D, Seferos DS. Synthesis of gold nanotubes with variable wall thicknesses. *Journal of Materials Chemistry A*, 2013, 1, 1127-1133.
- [90] Catchpole KR, Mookapati S, Beck F, Wang E-C, McKinley A, Basch A, et al. Plasmonics and nanophotonics for photovoltaics. *MRS Bulletin*, 2011, 36, 461-467.

- [91] Schmid M, Andrae P, Manley P. Plasmonic and photonic scattering and near fields of nanoparticles. *Nanoscale Research Letters*, 2014, 9, 50.
- [92] Hsu H-L, Juang T-Y, Chen C-P, Hsieh C-M, Yang C-C, Huang C-L, et al. Enhanced efficiency of organic and perovskite photovoltaics from shape-dependent broadband plasmonic effects of silver nanoplates. *Solar Energy Materials and Solar Cells*, 2015, 140, 224-231.
- [93] Seweryn M, Manuel JM, Salvatore M, Francesca S, Francesco P, Isodiana C. Self-assembled silver nanoparticles for plasmon-enhanced solar cell back reflectors: correlation between structural and optical properties. *Nanotechnology*, 2013, 24, 265601.
- [94] Lee JH, Park JH, Kim JS, Lee DY, Cho K. High efficiency polymer solar cells with wet deposited plasmonic gold nanodots. *Organic Electronics*, 2009, 10, 416-420.
- [95] Spinelli P, Polman A. Prospects of near-field plasmonic absorption enhancement in semiconductor materials using embedded Ag nanoparticles. *Optics Express*, 2012, 20, A641-A654.
- [96] Lu Z, Pan X, Ma Y, Li Y, Zheng L, Zhang D, et al. Plasmonic-enhanced perovskite solar cells using alloy popcorn nanoparticles. *RSC Advances*, 2015, 5, 11175-11179.
- [97] Rand BP, Peumans P, Forrest SR. Long-range absorption enhancement in organic tandem thin-film solar cells containing silver nanoclusters. *Journal of Applied Physics*, 2004, 96, 7519-7526.
- [98] Westphalen M, Kreibig U, Rostalski J, Lüth H, Meissner D. Metal cluster enhanced organic solar cells. *Solar Energy Materials and Solar Cells*, 2000, 61, 97-105.
- [99] Hägglund C, Zäch M, Kasemo B. Enhanced charge carrier generation in dye sensitized solar cells by nanoparticle plasmons. *Applied Physics Letters*, 2008, 92, 013113.
- [100] Konda RB, Mundle R, Mustafa H, Bamiduro O, Pradhan AK, Roy UN, et al. Surface plasmon excitation via Au nanoparticles in n-CdSe / p-Si heterojunction diodes. *Applied Physics Letters*, 2007, 91, 191111.
- [101] Ferry VE, Verschuuren MA, Li HBT, Schropp REI, Atwater HA, Polman A. Improved red-response in thin film a-Si:H solar cells with soft-imprinted plasmonic back reflectors. *Applied Physics Letters*, 2009, 95, 183503.
- [102] Mapel JK, Singh M, Baldo MA, Celebi K. Plasmonic excitation of organic double heterostructure solar cells. *Applied Physics Letters*, 2007, 90, 121102.
- [103] Heidel TD, Mapel JK, Singh M, Celebi K, Baldo MA. Surface plasmon polariton mediated energy transfer in organic photovoltaic devices. *Applied Physics Letters*, 2007, 91, 093506.
- [104] Zschiedrich L, Burger S, Schäde A, Schmidt F. A rigorous finite-element domain decomposition method for electromagnetic near field simulations. *SPIE Advanced Lithography: International Society for Optics and Photonics*; 2008. p. 692450.
- [105] Pomplun J, Burger S, Zschiedrich L, Schmidt F. Adaptive finite element method for simulation of optical nano structures. *physica status solidi (b)*, 2007, 244, 3419-3434.
- [106] Rockstuhl C, Fahr S, Lederer F. Absorption enhancement in solar cells by localized plasmon polaritons. *Journal of Applied Physics*, 2008, 104, 123102.
- [107] JCMwave: <http://www.jcmwave.com/>.
- [108] Manley P. Simulation of Plasmonic Nanoparticles in Thin Film Solar Cells: Freie Universität Berlin; 2016.
- [109] Yin G. Preparation of Ultra-thin $\text{CuIn}_{1-x}\text{Ga}_x\text{Se}_2$ Solar Cells and Their Light Absorption Enhancement: Technischen Universität Berlin; 2015.
- [110] Choy KL. Chemical vapour deposition of coatings. *Progress in Materials Science*, 2003, 48, 57-170.
- [111] De Lodyguine A. Illuminant for incandescent lamps. Google Patents; 1897.

-
- [112] Gurav A, Kodas T, Pluym T, Xiong Y. Aerosol Processing of Materials. *Aerosol Science and Technology*, 1993, 19, 411-452.
- [113] Pierson HO. *Handbook of Refractory Carbides and Nitrides: Properties, Characteristics, Processing, and Applications*: Noyes Publications; 1996.
- [114] Kodas TTT, Hampden-Smith MJ. *Aerosol Processing of Materials*: Wiley; 1999.
- [115] Pierson HO. 5 - CVD Processes and Equipment. *Handbook of Chemical Vapor Deposition (CVD) (Second Edition)*. Norwich, NY: William Andrew Publishing; 1999. p. 108-146.
- [116] Hampden-Smith MJ, Kodas TT. Chemical vapor deposition of metals: Part 1. An overview of CVD processes. *Chemical Vapor Deposition*, 1995, 1, 8-23.
- [117] Fischer C-H, Allsop NA, Gledhill SE, Köhler T, Krüger M, Sáez-Araoz R, et al. The spray-ILGAR[®] (ion layer gas reaction) method for the deposition of thin semiconductor layers: Process and applications for thin film solar cells. *Solar Energy Materials and Solar Cells*, 2011, 95, 1518-1526.
- [118] Kumar N, Alam F, Dutta V. Deposition of Ag and Au–Ag alloy nanoparticle films by spray pyrolysis technique with tuned plasmonic properties. *Journal of Alloys and Compounds*, 2014, 585, 312-317.
- [119] Shih S-J, Chien IC. Preparation and characterization of nanostructured silver particles by one-step spray pyrolysis. *Powder Technology*, 2013, 237, 436-441.
- [120] Yuan Z, Dryden NH, Vittal JJ, Puddephatt RJ. Chemical vapor deposition of silver. *Chemistry of Materials*, 1995, 7, 1696-1702.
- [121] Genduso G, Inganta R, Sunseri C, Piazza S, Kelch C, Sáez-Araoz R, et al. Deposition of very thin uniform indium sulfide layers over metallic nano-rods by the Spray-Ion Layer Gas Reaction method. *Thin Solid Films*, 2013, 548, 91-97.
- [122] Committee MPD. *ASM Ready Reference: Thermal properties of metals*: ASM International; 2002.
- [123] Yang JK, Liang B, Zhao MJ, Gao Y, Zhang FC, Zhao HL. Reference of Temperature and Time during tempering process for non-stoichiometric FTO films. *Scientific Reports*, 2015, 5, 15001.
- [124] Atkins P, de Paula J. *Atkins' Physical Chemistry*: OUP Oxford; 2010.
- [125] Bryant WA. The fundamentals of chemical vapour deposition. *Journal of Materials Science*, 1977, 12, 1285-1306.
- [126] Gledhill S, Allison R, Allsop N, Fu Y, Kanaki E, Sáez-Araoz R, et al. The reaction mechanism of the spray Ion Layer Gas Reaction process to deposit In₂S₃ thin films. *Thin Solid Films*, 2011, 519, 6413-6419.
- [127] Dryden NH, Vittal JJ, Puddephatt RJ. New precursors for chemical vapor deposition of silver. *Chemistry of Materials*, 1993, 5, 765-766.
- [128] Venables JA, Spiller GDT, Hanbucken M. Nucleation and growth of thin films. *Reports on Progress in Physics*, 1984, 47, 399.
- [129] Hansen TW, DeLaRiva AT, Challa SR, Datye AK. Sintering of Catalytic Nanoparticles: Particle Migration or Ostwald Ripening? *Accounts of Chemical Research*, 2013, 46, 1720-1730.
- [130] Carlow GR, Zinke-Allmang M. Self-Similar Spatial Ordering of Clusters on Surfaces during Ostwald Ripening. *Physical Review letters*, 1997, 78, 4601-4604.
- [131] Lifshitz I, Slyozov V. Kinetics of diffusive decomposition of supersaturated solid solutions. *Sov Phys–JETP*, 1959, 8, 331-339.
- [132] Fischer CH, Henglein A. Photochemistry of colloidal semiconductors. 31. Preparation and photolysis of cadmium sulfide sols in organic solvents. *The Journal of Physical Chemistry*, 1989, 93, 5578-5581.

- [133] Morawiec S, Mendes MJ, Filonovich SA, Mateus T, Mirabella S, Águas H, et al. Broadband photocurrent enhancement in a-Si:H solar cells with plasmonic back reflectors. *Optics Express*, 2014, 22, A1059-A1070.
- [134] Mathew M, Sudha Kartha C, Vijayakumar KP. In_2S_3 :Ag, an ideal buffer layer for thin film solar cells. *Journal of Materials Science: Materials in Electronics*, 2009, 20, 294-298.
- [135] Buecheler S, Corica D, Guettler D, Chirila A, Verma R, Müller U, et al. Ultrasonically sprayed indium sulfide buffer layers for $\text{Cu}(\text{In,Ga})(\text{S,Se})_2$ thin-film solar cells. *Thin Solid Films*, 2009, 517, 2312-2315.
- [136] Hariskos D, Ruckh M, Rühle U, Walter T, Schock HW, Hedström J, et al. A novel cadmium free buffer layer for $\text{Cu}(\text{In,Ga})\text{Se}_2$ based solar cells. *Solar Energy Materials and Solar Cells*, 1996, 41, 345-353.
- [137] Allsop NA, Schönmann A, Muffler HJ, Bär M, Lux-Steiner MC, Fischer CH. Spray-ILGAR indium sulfide buffers for $\text{Cu}(\text{In,Ga})(\text{S,Se})_2$ solar cells. *Progress in Photovoltaics: Research and Applications*, 2005, 13, 607-616.
- [138] Naghavi N, Spiering S, Powalla M, Cavana B, Lincot D. High-efficiency copper indium gallium diselenide (CIGS) solar cells with indium sulfide buffer layers deposited by atomic layer chemical vapor deposition (ALCVD). *Progress in Photovoltaics: Research and Applications*, 2003, 11, 437-443.
- [139] Sáez-Araoz R, Krammer J, Harndt S, Koehler T, Krueger M, Pistor P, et al. ILGAR In_2S_3 buffer layers for Cd-free $\text{Cu}(\text{In,Ga})(\text{S,Se})_2$ solar cells with certified efficiencies above 16%. *Progress in Photovoltaics: Research and Applications*, 2012, 20, 855-861.
- [140] Yousfi EB, Weinberger B, Donsanti F, Cowache P, Lincot D. Atomic layer deposition of zinc oxide and indium sulfide layers for $\text{Cu}(\text{In,Ga})\text{Se}_2$ thin-film solar cells. *Thin Solid Films*, 2001, 387, 29-32.
- [141] Grimm A, Kieven D, Klenk R, Lauermann I, Neisser A, Niesen T, et al. Junction formation in chalcopyrite solar cells by sputtered wide gap compound semiconductors. *Thin Solid Films*, 2011, 520, 1330-1333.
- [142] Strohm A, Eisenmann L, Gebhardt RK, Harding A, Schlötzer T, Abou-Ras D, et al. $\text{ZnO}/\text{In}_x\text{S}_y/\text{Cu}(\text{In,Ga})\text{Se}_2$ solar cells fabricated by coherent heterojunction formation. *Thin Solid Films*, 2005, 480-481, 162-167.
- [143] Hariskos D, Spiering S, Powalla M. Buffer layers in $\text{Cu}(\text{In,Ga})\text{Se}_2$ solar cells and modules. *Thin Solid Films*, 2005, 480-481, 99-109.
- [144] Fischer CH, Muffler HJ, Bär M, Fiechter S, Leupolt B, Lux-Steiner MC. Ion layer gas reaction (ILGAR)—conversion, thermodynamic considerations and related FTIR analyses. *Journal of Crystal Growth*, 2002, 241, 151-158.
- [145] Bär M, Muffler HJ, Fischer CH, Lux-Steiner MC. ILGAR technology IV:: ILGAR thin film technology extended to metal oxides. *Solar Energy Materials and Solar Cells*, 2001, 67, 113-120.
- [146] Koehler T, Gledhill S, Grimm A, Allsop N, Camus C, Hänsel A, et al. An investigation of the dip-Ion Layer Gas Reaction process to produce ZnO films with increased deposition rates. *Thin Solid Films*, 2009, 517, 3332-3339.
- [147] Bär M, Fischer CH, Muffler HJ, Zweigart S, Karg F, Lux-Steiner MC. Replacement of the CBD-CdS buffer and the sputtered i-ZnO layer by an ILGAR-ZnO WEL: optimization of the WEL deposition. *Solar Energy Materials and Solar Cells*, 2003, 75, 101-107.
- [148] Muffler H, Bar M, Fischer CH, Gay R, Karg F, Lux-Steiner MC. ILGAR technology. VIII. Sulfidic buffer layers for $\text{Cu}(\text{In,Ga})(\text{S,Se})_2$ solar cells prepared by ion layer gas reaction (ILGAR). *Photovoltaic Specialists Conference*, 2000. *Conference Record of the Twenty-Eighth IEEE2000*. p. 610-613.

- [149] Allsop NA, Niesen TP, Gledhill SE, Kr M, ger, T K, et al. Up-scaling ILGAR In_2S_3 buffer layers production for chalcopyrite solar modules. Photovoltaic Specialists Conference (PVSC), 2009 34th IEEE2009. p. 000680-000684.
- [150] Fu Y, Allsop NA, Gledhill SE, Köhler T, Krüger M, Sáez-Araoz R, et al. ZnS Nanodot Film as Defect Passivation Layer for $\text{Cu}(\text{In,Ga})(\text{S,Se})_2$ Thin-Film Solar Cells Deposited by Spray-ILGAR (Ion-Layer Gas Reaction). *Advanced Energy Materials*, 2011, 1, 561-564.
- [151] Camus C, Allsop NA, Gledhill SE, Bohne W, Röhrich J, Lauermann I, et al. Properties of Spray ILGAR CuInS_2 thin films. *Thin Solid Films*, 2008, 516, 7026-7030.
- [152] Azarpira A, Lublow M, Steigert A, Bogdanoff P, Greiner D, Kaufmann CA, et al. Efficient and Stable $\text{TiO}_2\text{:Pt-Cu}(\text{In,Ga})\text{Se}_2$ Composite Photoelectrodes for Visible Light Driven Hydrogen Evolution. *Advanced Energy Materials*, 2015, 5, 1402148.
- [153] Allsop NA, Schönmann A, Belaidi A, Muffler HJ, Mertesacker B, Bohne W, et al. Indium sulfide thin films deposited by the spray ion layer gas reaction technique. *Thin Solid Films*, 2006, 513, 52-56.
- [154] Owino Juma A, Azarpira A, Steigert A, Pomaska M, Fischer C-H, Lauermann I, et al. Role of chlorine in In_2S_3 for band alignment at nanoporous- $\text{TiO}_2/\text{In}_2\text{S}_3$ interfaces. *Journal of Applied Physics*, 2013, 114, 053711.
- [155] Jochum KP, Weis U, Stoll B, Kuzmin D, Yang Q, Raczek I, et al. Determination of Reference Values for NIST SRM 610–617 Glasses Following ISO Guidelines. *Geostandards and Geoanalytical Research*, 2011, 35, 397-429.
- [156] Juma A, Kavalakkatt J, Pistor P, Latzel B, Schwarzburg K, Dittrich T. Formation of a disorderd hetero-junction by diffusion of CuI from CuSCN into In_2S_3 layers: A surface photovoltage study. *physica status solidi (a)*, 2012, 209, 663-668.
- [157] Boldish SI, White WB. Optical band gaps of selected ternary sulfide minerals. *American Mineralogist*, 1998, 83, 865-871.
- [158] Chen C, Xie Y, Ali G, Yoo SH, Cho SO. Improved conversion efficiency of Ag_2S quantum dot-sensitized solar cells based on TiO_2 nanotubes with a ZnO recombination barrier layer. *Nanoscale Research Letters*, 2011, 6, 462.
- [159] Shay JL, Tell B, Schiavone LM, Kasper HM, Thiel F. Energy bands of AgInS_2 in the chalcopyrite and orthorhombic structures. *Physical Review B*, 1974, 9, 1719-1723.
- [160] Aguilera MLA, Ortega-López M, Resendiz VMS, Hernández JA, Trujillo MAG. Some physical properties of chalcopyrite and orthorhombic AgInS_2 thin films prepared by spray pyrolysis. *Materials Science and Engineering: B*, 2003, 102, 380-384.
- [161] Ortega-López M, Vigil-Galán O, Cruz Gandarilla F, Solorza-Feria O. Preparation of AgInS_2 chalcopyrite thin films by chemical spray pyrolysis. *Materials Research Bulletin*, 2003, 38, 55-61.
- [162] Yu AA, Koh WS. Resonant and nonresonant plasmonic nanoparticle enhancement for thin-film silicon solar cells. *Nanotechnology*, 2010, 21, 235201.
- [163] Temgire MK, Joshi SS. Optical and structural studies of silver nanoparticles. *Radiation Physics and Chemistry*, 2004, 71, 1039-1044.
- [164] Im J-H, Lee C-R, Lee J-W, Park S-W, Park N-G. 6.5% efficient perovskite quantum-dot-sensitized solar cell. *Nanoscale*, 2011, 3, 4088-4093.
- [165] Lee MM, Teuscher J, Miyasaka T, Murakami TN, Snaith HJ. Efficient Hybrid Solar Cells Based on Meso-Superstructured Organometal Halide Perovskites. *Science*, 2012, 338, 643-647.
- [166] Zhou H, Chen Q, Li G, Luo S, Song T-b, Duan H-S, et al. Interface engineering of highly efficient perovskite solar cells. *Science*, 2014, 345, 542-546.

-
- [167] Salim T, Sun S, Abe Y, Krishna A, Grimsdale AC, Lam YM. Perovskite-based solar cells: impact of morphology and device architecture on device performance. *Journal of Materials Chemistry A*, 2015, 3, 8943-8969.
- [168] Xiao Z, Dong Q, Bi C, Shao Y, Yuan Y, Huang J. Solvent Annealing of Perovskite-Induced Crystal Growth for Photovoltaic-Device Efficiency Enhancement. *Advanced Materials*, 2014, 26, 6503-6509.
- [169] Richardson G, O'Kane SEJ, Niemann RG, Peltola TA, Foster JM, Cameron PJ, et al. Can slow-moving ions explain hysteresis in the current-voltage curves of perovskite solar cells? *Energy & Environmental Science*, 2016, 9, 1476-1485.
- [170] Palik ED. *Handbook of Optical Constants of Solids*: Elsevier Science; 2012.
- [171] Phillip M, Guanchao Y, Martina S. A method for calculating the complex refractive index of inhomogeneous thin films. *J Phys D: Appl Phys*, 2014, 47, 205301.
- [172] Supasai T, Rujisamphan N, Ullrich K, Chemseddine A, Dittrich T. Formation of a passivating $\text{CH}_3\text{NH}_3\text{PbI}_3/\text{PbI}_2$ interface during moderate heating of $\text{CH}_3\text{NH}_3\text{PbI}_3$ layers. *Applied Physics Letters*, 2013, 103, 183906.
- [173] Niu G, Guo X, Wang L. Review of recent progress in chemical stability of perovskite solar cells. *Journal of Materials Chemistry A*, 2015, 3, 8970-8980.
- [174] Babar S, Weaver JH. Optical constants of Cu, Ag, and Au revisited. *Applied Optics*, 2015, 54, 477-481.
- [175] Ott A. *Synthesis and application of hybrid materials based on plasmonic nanoparticles*: Humboldt-Universität zu Berlin; 2016.
- [176] Goldstein J, Newbury DE, Joy DC, Lyman CE, Echlin P, Lifshin E, et al. *Scanning Electron Microscopy and X-ray Microanalysis*: Third Edition: Springer US; 2013.
- [177] Cullity BD, Stock SR. *Elements of X-ray Diffraction*: Pearson Education, Limited; 2013.
- [178] Kronik L, Shapira Y. Surface photovoltage phenomena: theory, experiment, and applications. *Surface Science Reports*, 1999, 37, 1-206.
- [179] Juma A. Copper diffusion in In_2S_3 and charge separation at $\text{In}_2\text{S}_3/\text{CuSCN}$ and $\text{TiO}_2/\text{In}_2\text{S}_3$ interfaces: Freie Universität Berlin; 2013.

List of publications

Journal Publications

- *Phase transitions during formation of Ag nanoparticles on In₂S₃ precursor layers*
Yang Liu, Yanpeng Fu, Thomas Dittrich, Rodrigo Sáez-Araoz, Martina Schmid, Volker Hinrichs, Martha Ch. Lux-Steiner, Christian-Herbert Fischer
Thin Solid Films 590 (2015), p. 54-59 (related to chapter 4)
<http://dx.doi.org/10.1016/j.tsf.2015.07.021>
- *Enhancement of photocurrent in ultra-thin perovskite solar cell by Ag nanoparticles deposited at low temperature*
Yang Liu, Felix Lang, Thomas Dittrich, Alexander Steigert, Christian-Herbert Fischer, Tristan Köhler, Paul Plate, Jörg Rappich, Martha Ch. Lux-Steiner, Martina Schmid
RSC Advances, 7 (2017), p. 1206-1214 (related to chapter 5)
DOI: 10.1039/C6RA25149H
- *Size and density controlled deposition of Ag nanoparticle films by a novel low temperature spray chemical vapour deposition method – research into mechanism, particle growth and optical simulation*
Yang Liu, Paul Plate, Volker Hinrichs, Tristan Köhler, Min Song, Phillip Manley, Martina Schmid, Peter Bartsch, Sebastian Fiechter, Martha Ch. Lux-Steiner, Christian-Herbert Fischer
Journal of Nanoparticle Research, submitted (related to chapter 3)
- *Synthesis and characterization of V-doped β -In₂S₃ thin films on FTO substrates*
Cristina Tapia, Sean P. Berglund, Dennis Friedrich, Thomas Dittrich, Peter Bogdanoff, Yang Liu, Sergiu Levchenko, Thomas Unold, José Carlos Conesa, Antonio L. de Lacey, Marcos Pita, Sebastian Fiechter
Journal of Physical Chemistry C, 120 (2016), p. 28753-28761
DOI: 10.1021/acs.jpcc.6b09601

Conference presentation

- *Spray deposition of Ag nano-dots for absorption enhancement of extremely thin ILGAR[®] absorber layers*
Yang Liu, Yanpeng Fu, Thomas Dittrich, Rodrigo Sáez-Araoz, Martina Schmid, Martha Ch. Lux-Steiner, Christian-Herbert Fischer
2014 Europe Material Research Society Spring Meeting. Lille, France, May 26th-30th 2014. Poster presentation.
- *Modelling and spray deposition of Ag nanoparticles for absorption enhancement of perovskite absorber layers*
Yang Liu, Phillip Manley, Paul Plate, Christian-Herbert Fischer, Thomas Dittrich, Rodrigo Sáez-Araoz, Guanchao Yin, Tristan Köhler, Martha Ch. Lux-Steiner, Martina Schmid.
2015 Material Research Society Autumn Meeting. Boston, USA, November 29th-December 4th 2015. Oral presentation

Curriculum Vitae

For reasons of data protection, the Curriculum vitae is not published in the electronic version.

Statement

I hereby declare that this submission is my work and all forms of aid and help from others are accordingly acknowledged, e.g., some preparation works of chapter 3 were done in cooperation with Paul Plate under my supervision. To the best of my knowledge and belief, it contains no materials previously accepted or judged to be insufficient within the content of previous doctoral studies, except for very minor cooperation overlap where clarification is made in chapter 6.

Berlin..... Signed.....